Modelling, Aging and Optimal Operation of Lithium-ion Batteries

Original
Modelling, Aging and Optimal Operation of Lithium-ion Batteries / Maheshwari, Arpit. - (2018 Oct 19).
[10.6092/polito/porto/2715622]

Publisher:
Politecnico di Torino

Published
DOI:10.6092/polito/porto/2715622

Modelling, Aging and Optimal Operation of Lithium-ion Batteries

PROEFSCHRIFT

ter verkrijging van de graad van doctor aan de Technische Universiteit
Eindhoven, op gezag van de rector magnificus, prof.dr.ir. F.P.T. Baaijens,
voor een commissie aangewezen door het College voor Promoties in het
openbaar te verdedigen op maandag 29 oktober 2018 om 11:00 uur.

door

Arpit Maheshwari

geboren te Bhopal, India

Dit proefschrift is goedgekeurd door de promotoren en de samenstelling van de promotiecommissie is als volgt:

voorzitter:	prof.dr.ir. J.H. Blom
1e promotor:	prof.dr. M. Santarelli (Politecnico di Torino)
2e promotor:	dr. M. Gibescu
copromotor:	dr. N. Paterakis
leden:	prof.dr. J.P.S. Catalão (Universidade do Porto)
	prof.dr.ir. A.J.M. Pemen
	dr. S. Bodoardo (Politecnico di Torino)
adviseur	dr. M. Heck (Hella GmbH, voorheen Fraunhofer ISE)

Het onderzoek of ontwerp dat in dit proefschrift wordt beschreven is uitgevoerd in overeenstemming met de TU/e Gedragscode Wetenschapsbeoefening.

Doctoral Dissertation
Doctoral Program in Energy Engineering (XXX Cycle)

Modelling, Aging and Optimal Operation of Lithium-ion Batteries

Titolo in italiano: Modellizzazione elettrochimica e termica, analisi di invecchiamento e ottimizzazione prestazionale di batterie agli ioni di litio

Arpit Maheshwari

Supervisor I: prof. M. Santarelli (Politecnico di Torino)
Supervisor II: prof. M. Gibescu (Technische Universiteit Eindhoven)
Co-supervisor: dr. N. Paterakis (Technische Universiteit Eindhoven)

Doctoral Examination Committee at Politecnico di Torino:
Referees: prof. J.P.S. Catalão (Universidade do Porto)
prof. J.M.G. Lastra (Danmarks Tekniske Universitet)
Members: prof. G. Chicco (Politecnico di Torino)
prof. P. Mustarelli (Università degli studi di Pavia)
prof. S. Bodoardo (Politecnico di Torino)

Politecnico di Torino
October 2018

SELECT+
Part of Explore Energy

TU/e Technische Universiteit
Eindhoven
University of Technology

The research described in this thesis is performed at the Synergies of Thermochemical and Electrochemical Power Systems (STEPS) group of the department of Energy at Politecnico di Torino in Italy, Battery engineering team of the department of Electrical Energy Storage at Fraunhofer Institute for Solar Energy Systems in Freiburg, Germany and Electrical Energy Systems (EES) group of the department of Electrical Engineering at Eindhoven University of Technology in the Netherlands.

The research is primarily funded by the Erasmus Mundus joint doctorate SELECT+ programme (WP1.3 Innovative and ageing resistant Li-ion batteries for high electric energy storage in a smart grid framework). Additional research and mobility funding is provided by MARS-EV project and Innoenergy PhD school. The research contributed to the successful completion of MARS-EV (EU FP7) and Ca(r)vour (EU ERDF) projects.

Printed by Ipskamp printing, Enschede, The Netherlands

Front cover shows the scanning electron microscope images (750X magnification) of a graphite electrode (top) and a NMC electrode (bottom) extracted from a lithium-ion battery. The electrodes are coated over current collectors which can also be distinguished in the images. Photo courtesy: Daniele, Mauro

Back cover has been designed by Gaurab (chobighar.weebly.com) to depict the plight of cobalt miners in Democratic Republic of Congo. Cobalt is a critical element in many lithium-ion batteries. Seen in the image is the mischievous sprite *Kobold* from german folklore after which the element cobalt has been named.

A catalogue record is available from the Eindhoven University of Technology Library.
ISBN: 978-90-386-4607-7

I hereby declare that, the contents and organisation of this dissertation constitute my own original work and does not compromise in any way the rights of third parties, including those relating to the security of personal data.

Arpit Maheshwari
2018

Abstract

Energy storage has a big role to play in power systems across the world in order to integrate increasing amounts of intermittent renewable sources of energy. Among the different storage technologies, lithium-ion batteries exhibit favourable characteristics that make them suitable for power system applications. However, commercial success of lithium-ion battery based storage is limited not only for grid applications but also for electric vehicles. This is due to three inter-related factors - safety, price-performance ratio and lifetime, which largely offset the advantages that these batteries offer and impede their adoption for potential applications. Any improvement in these factors is tied to better understanding of the functioning and of the limits of these batteries. This work is an attempt to further this understanding using modelling and experimental means, such that the behaviour of these batteries can be predicted over their lifetime, and their operation can be optimized. The contributions of this thesis are three-fold, as described in the following paragraphs.

A battery model that is not only able to accurately estimate the electrochemical but also the thermal behaviour of a lithium ion battery is important in order to keep track of performance and safety indices. To this end, a physics based pseudo 2D electrochemical-thermal model of a lithium iron phosphate battery is developed. Parameters for this model are determined through primary information from manufacturer, literature studies and experimental data analysis. The developed model accurately predicts the electrochemical and thermal behaviour of the battery for both charging and discharging conditions for a wide range of current rates. Heat generation in the cell is investigated using the validated model and the important role of reversible heat and the dominant role of graphite electrode is highlighted. The model is extended to determine thermal behaviour of module, pack and study different thermal management systems.

Given that battery performance degrades over time, long-term accelerated aging tests are used to quantify calendar and cycle aging in commercial lithium nickel manganese cobalt oxide batteries. Capacity and impedance measurements, electrochemical impedance spectroscopy as well as post-mortem analysis are used to study aging. Calendar aging is analysed as a function of temperature and

storage state of charge. In general, low temperatures and low states of charge cause less degradation in the battery. Considerable influence of the periodic characterization process on the calendar aging results is noticed. Cycle aging is analysed as a function of temperature, current rate, depth of discharge and state of charge. In general, fast aging in batteries is observed when they are operated at low temperatures and high current rates. The effects of local potentials at the two electrodes and staging behaviour of graphite in causing capacity fade and increase in the resistances of the cell are elucidated.

Finally, the integration of storage in power systems is investigated. Technically, lithium-ion batteries are found to be suitable for a variety of applications in power systems both at utility scale as well as for home storage. Their economic feasibility is however debatable and dependent on local market conditions. To optimally use batteries in power system applications, an accurate degradation model that takes into account the complex, non-linear dependence of battery aging on operating parameters is developed. A mixed integer linear program is formulated, which produces an optimal charge-discharge schedule for the energy storage when trading in electricity markets. This program optimizes the operation of battery systems considering the twin objectives of maximizing revenue from market transactions and minimizing degradation. Such a multi-objective approach yields a Pareto-front of feasible operating strategies putting the onus on a decision maker to choose a desirable operational strategy for implementation.

Summary

We are in the middle of an energy transition. Multiple challenges such as climate change, air quality and high oil import bill are compelling countries around the world to integrate more renewable sources in their energy mix. The global growth in solar and wind power capacity is slowly outpacing that of fossil fuels. These sources are however intermittent in nature. In order to integrate more solar and wind sources in the energy mix while maintaining the stability and reliability of our energy supply, electrical energy storage (EES) technologies are vital. Among the different EES technologies, lithium-ion batteries are the most promising. This is due to their high efficiency, location-independence and fast response time combined with greater energy and power densities compared to most other EES technologies. However, their high price-performance ratio along with the challenges of safety and lifetime have resulted in an underwhelming deployment of storage systems based on these batteries. In this doctoral dissertation, through modelling and experimental means, an enhanced understanding of the behaviour of these batteries is obtained and used to optimize their operation. The dissertation has been structured into three parts. The first part details the process of developing an accurate model for a lithium-ion battery, employing it to further the understanding of these batteries. The second part describes experimental data analysis of aging in the batteries. It delivers new insights into the degradation processes. In the third part, this understanding of degradation is exploited to develop strategies to operate these batteries optimally especially in power system applications.

Part I: Modelling
For a safe and optimum operation of batteries, their behaviour must be predictable under different conditions. In other words, an accurate model of the battery technology that can predict its electrochemical and thermal behaviour is necessary. In Chapter 2, different ways to model lithium-ion batteries are briefly discussed. A Pseudo 2D (P2D) electrochemical modelling approach is chosen for simulating the battery in this part of the thesis because of its ability to incorporate the underlying physical phenomena in different cell layers of the battery and simulate entire charge-discharge cycles with accuracy. A 3D lumped thermal model is also simultaneously developed and coupled to the

electrochemical model. The battery's electrochemical performance is substantially dependent on the operating temperature and the coupling ensures that the simulations are accurate for operating conditions that lead to significant changes in temperature of the battery. The P2D electrochemical 3D thermal modelling framework has been discussed in detail focussing on all dominant phenomena in the battery. Laws of conservation of mass and charge and theories of kinetics, diffusion, porous electrode, concentrated solution and heat transfer provide the necessary framework for the model.

To ensure that the P2D electrochemical 3D thermal model represents the battery, it must be accurately parametrized. This necessitates knowledge of different electrochemical, thermal and geometrical parameters of the battery. In Chapter 3, the parametrization of such a model for a lithium iron phosphate pouch cell is carried out. To determine the parameters for the model, literature study of the battery technology and ad hoc experiments on these cells are performed. Inverse determination of some of these parameters has been discussed. The developed model is validated electrochemically and thermally for a wide range of operating conditions. The validated model is used to investigate the source of the differences in the thermal behaviour between charge and discharge. Reversible heat is attributed for this difference. The contribution of the graphite electrode is found to dominate the thermal behaviour of the cell. The accuracy, flexibility and modular nature of the developed model is demonstrated in Chapter 4, where the modelling is scaled to design and investigate thermal management systems for battery packs. Different designs of such systems have been simulated for a fixed battery pack design.

Part II: Aging

The performance of lithium-ion batteries reduces with time and operation. Different physical and chemical changes are responsible for this aging of the batteries. They have been discussed in Chapter 5. A nickel manganese cobalt oxide-based battery is investigated to analyse the effect of operating and environmental conditions such as depth of discharge (DOD), state of charge (SOC), current and temperature on the aging of this battery. The analysis has been divided into aging as a function of time (calendar aging) and aging as a function of operating conditions (cycle aging). Experimental procedure including the equipment and the electrochemical techniques used have been described in this chapter. Extensive analysis of electrochemical impedance spectra using equivalent circuit models has been a highlight of this part of the dissertation.

Calendar aging, which is the loss of performance of an idle cell with time, is analysed in Chapter 6. For the tested cells, it is noticed that high temperature and high SOC cause faster decline of cell capacity and greater increase in cell impedance. The dominant effect in the cells is the increase in polarization resistance with time, which can be attributed to the growth of solid-electrolyte interphase (SEI). The results of calendar aging were found to be significantly influenced by the unavoidable process of characterizing the cells to collect data for analysis. This characterization process entails the cell experiencing a charge throughput. Comprehensive analysis of the effect of charge throughput due to cell operation on the long-term performance of the cell, also known as cycle aging, is carried out in Chapter 7. It is observed that cell function is compromised early when cycling at low temperature irrespective of other conditions. At higher temperatures, greater decrease in cell capacity is noticed when cycling at high currents and both in the high and the low SOC region. The capacity fade for a given condition is seen to be slow at first and is attributed to the growth of SEI. However, after the SEI resistance surpasses a critical value, the cell capacity fades rapidly. Staging behaviour in graphite electrode and activation of different reaction mechanisms at very high voltage are responsible for the non-monotonicity observed in cycle aging behaviour.

Part III: Optimal Operation

Large-scale integration of storage based on lithium-ion batteries is being widely considered in power systems. Chapter 8 looks at the different possible applications of these batteries in power systems from the point of view of technical and economic feasibility. Analysing the current scenario, it is concluded that while technically lithium-ion batteries are well-poised to provide a host of on-grid and off-grid services, their economic viability depends on the specific battery technology (cost and performance), application and the market conditions. They are already seen to have a viable business case in certain markets and for certain applications. It is expected that improved utilization of the battery through smart short-term operational strategies can lower their lifetime costs, further hastening their commercial deployment. This has been explored in Chapter 9 through a case study of a storage system participating in an electricity market. Here, a multi-objective approach that maximizes the revenue from the market and minimizes the degradation of the storage system has been proposed. Since, traditional approaches to model the degradation behaviour of batteries in market studies were found to be inadequate in representing the observed experimental behaviour, a more accurate model has been developed using the data described in Part II of the dissertation. This model of the storage system participating in the energy market is cast as mixed integer linear program and yields Pareto optimal strategies for the operation of storage highlighting the revenue vs. degradation trade-off. A temporal decomposition technique has also been proposed and demonstrated that extends the applicability of the developed model to more computationally intensive optimization studies.

The research findings detailed in the three parts of this dissertation are summarized in Chapter 10. A non-exhaustive list of suggestions to take this research further has been proposed. The dissertation concludes with a glimpse of the future of batteries by listing the different alternatives, both lithium and non-lithium based, being investigated around the world.

Contents

List of Figures

List of Tables

The storage battery is, in my opinion, a catchpenny, a sensation, a mechanism for swindling the public by stock companies. The storage battery is one of those peculiar things which appeals to the imagination, and no more perfect thing could be desired by stock swindlers than that very self-same thing. … Just as soon as a man gets working on the secondary battery it brings out his latent capacity for lying.

Thomas Alva Edison in 1883

Chapter 1

Introduction

Electrical energy storage (EES) technologies are vital for de-carbonization of the global economy. They are seen as the enabling technology by which intermittent renewable sources of electricity can provide a greater contribution to the total electricity production than is possible with conventional grids.

Renewable energy is on the rise globally. In 2016, renewable sources accounted for almost two-thirds of new global power capacity [1]. At the European level, the impetus to renewables is driven by policy and targets set by the European Union. A binding target of 20% of final energy consumption and 10% of transport fuels from renewable sources has been set for 2020. The target for 2030 has recently been set at 32% with an upwards revision clause by 2023 [2, 3]. Multiple reasons such as concerns of climate change, air quality and high energy import bill provoke these targets and policies from the European Union.

Renewables, especially solar and wind, are intermittent with diurnal and seasonal variations. This, combined with the stochastic nature of electricity demand and the economic reasons for ensuring a reliable 24/7/365 supply, means that power systems are set for a big challenge. EES technologies can provide a range of services to offset many concerns arising in such a situation. Simply speaking, the role of EES is to decouple the instantaneous balance between supply and demand which is a requisite of a stable power system.

1.1 Batteries

Energy storage is possible through various means such as mechanical, electrical, chemical and electrochemical storage. For more than a century, energy storage in the power sector has been dominated by pumped hydro-power energy storage (PHES). In the last decades, many new EES technologies have been developed such as compressed air energy storage (CAES), flywheels, superconducting magnetic energy storage (SMES), super-capacitors, rechargeable batteries, fuel cells, etc.

These EES technologies have widely varying characteristics. One common way

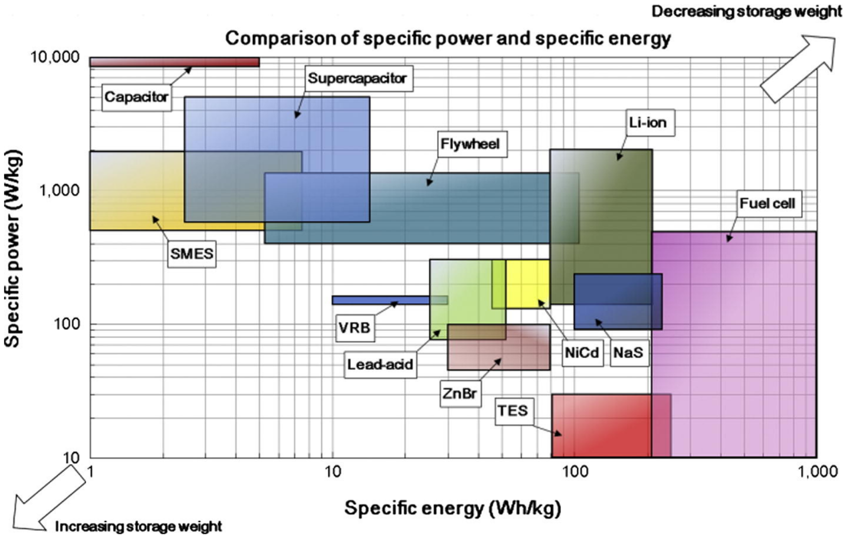

Figure 1.1. Ragone plot: comparison of storage technologies based on specific power and specific energy [4]

to compare storage technologies is to use a Ragone plot such as the one in Figure 1.1 or its counterpart in Figure 1.2. While Ragone plot compares technologies on the basis of the weight, the graph in Figure 1.2 measures them on the basis of volume. Both these plots focus on performance, which paints an incomplete picture of the suitability of an energy storage device to an application.

A battery stores energy electrochemically. It comprises of three major components: the positive electrode, the negative electrode and the electrolyte. Energy is stored as the difference of the electric potentials between the two electrodes. Some characteristics set batteries apart from the other storage options for many applications. Unlike PHES and CAES, batteries are modular and location independent. They have no moving mechanical parts unlike flywheels. Compared to CAES, they have a fast response time. Where costs and efficiencies are considered, they do much better than fuel cells. In terms of market maturity, they are much ahead of super-capacitors or SMES.

Their energy and power densities combined with other favourable characteristics make them an attractive option for electrical energy storage. Together these properties of batteries also open up other avenues for their application, over and above grid services. These include use in island systems, off-grid systems, in rural areas, as emergency power modules and in electric vehicles.

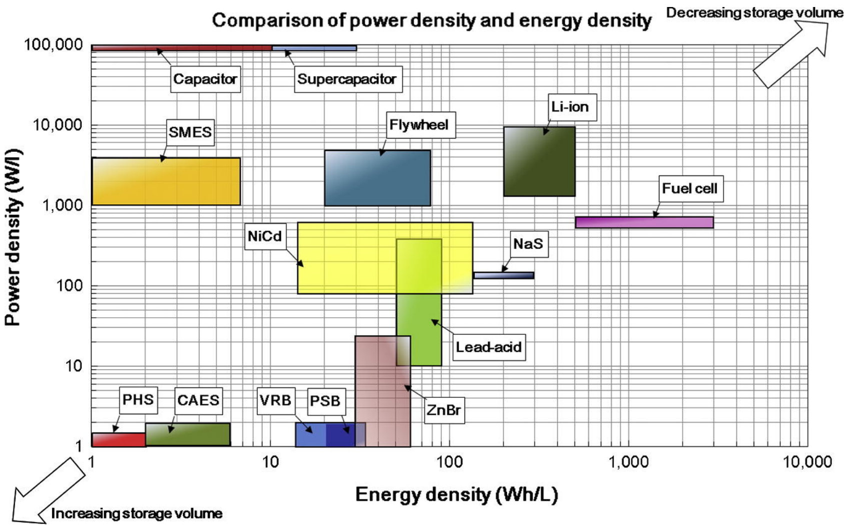

Figure 1.2. Comparison of storage technologies based on energy and power densities [4]

1.2 Lithium-ion batteries

Chemical batteries have a long history. Alessandro Volta is usually attributed as the inventor of the first battery around the year 1800. Since then, several different kinds of batteries with widely different characteristics have been developed. These include lead-acid, nickel-cadmium, nickel-metal hydride, lithium-ion, sodium-sulphur, vanadium redox, zinc-bromine, metal-air, etc.

Among these, rechargeable lithium-ion batteries are the subject of focus in this work. This technology powers almost all mobile phones and laptops currently in use today [5]. They are also used in portable electric tools, garden tools, e-bikes, etc. Recent spurt in demand comes from their consideration in electric vehicles (EVs) where the use of these batteries will soon exceed their use in personal electronic goods [6]. According to a BCG report [7], 20.4 % of all cars sold in 2020 will partially or fully run on these batteries. For electric energy storage applications in power systems, their demand is also slowly ramping up and the total manufacturing capacity of lithium-ion batteries is expected to exceed 250 GW h by 2020 compared to the 100 GW h in 2016 [8].

The success and popularity of these batteries vis-à-vis other battery technologies is due to a combination of characteristics that makes them more suitable for vehicle electrification and power system applications. Unlike lead acid batteries and nickel based batteries, they have higher efficiencies, energy and power densities. They enjoy high technological and market maturity unlike metal-air batteries or vanadium batteries. The energy densities of lithium-ion batteries are much higher than flow batteries such as vanadium red-ox or

Table 1.1. Technical characteristics of storage technologies [9, 10]

	Power rating (MW)	**Storage duration**	**Lifetime (years/cycles)**	**Self discharge %**	**Efficiency %**	**Response time**
PHS	100 - 1000	4 - 12h	30 - 60 years	0 - 0.02	70 - 85	sec - min
CAES	10 - 1000	2 - 30h	20 - 40 years	0 - 1	40 - 75	sec - min
Flywheels	0.001 - 1	sec - hours	100000 - 1000000	1.3 -100	70 - 95	10 - 20 ms
NaS battery	10 - 100	1 min - 8h	1000 - 10000	0.05 - 1	70 - 90	10 - 20 ms
Li-ion battery	0.1 - 100	1 min - 8h	1000 - 10000	0.1 - 0.36	85 - 98	10 - 20 ms
Flow battery	0.1 - 100	1 - 10h	12000 - 14000	0 - 1	60 - 85	10 - 20 ms
Super-capacitor	0.01 - 1	ms - min	10000 - 100000	20 - 40	80 - 98	10 - 20 ms
SMES	0.1 - 1	ms - sec	100000	10 - 15	80 - 95	<100 ms
Hydrogen	0.01 - 1000	min - weeks	5 - 30 years	0 - 4	25 - 45	sec - min

zinc-bromine. They are also much more compact and easy to install than flow batteries. Also very few battery technologies have a lifetime more than lithium-ion batteries. Their properties can be compared with other storage and battery technologies from Figure 1.1, Figure 1.2 and Table 1.1.

Lithium-ion batteries is an umbrella term used to classify many different kinds of batteries such as lithium iron phosphate (LFP), lithium nickel manganese cobalt (NMC), lithium manganese oxide (LMO), lithium nickel cobalt aluminium (NCA), lithium cobalt oxide (LCO), etc. The different chemistries can have different performances and costs. However in this work, rather than studying the differences among lithium-ion batteries, the commonalities have been the focus. A further lower level classification of a particular chemistry of lithium-ion battery is also possible. This is based on differences at the atomic levels.

Given the long history of batteries, lithium-ion batteries can be considered as a new entrant. In 1991, Sony became the first commercial entity to manufacture and sell them.

1.3 Challenges

Continuous developments, improvements and cost reductions have led to the application base of lithium-ion batteries expand from small portable devices to more energy and power intensive devices such as power tools. But commercial success of lithium-ion battery based storage technologies in both vehicle and grid applications is still limited.

Three different paths can help move these batteries from their status quo. These are: scaling up the technology, optimizing existing technology and researching breakthrough new technology. The first path avoids the uncertainty of R&D and works through the principle of economies of scale to bring down the costs of production. This is currently happening. The prices of lithium-ion batteries are falling rapidly as supply chains are getting increasingly stabilized and mega factories around the world begin large scale production. The last path instead places its bet on an important new discovery or development such as in materials. The potential gains over the current state of art can be big but so is the uncertainty of any favourable outcome. Moreover, every new development has usually a long technology life-cycle to traverse before it becomes commercially viable. The middle path is that of extracting the most value from the already existing and market-mature lithium-ion technology. It also relies on R&D but with much less uncertainty in outcome than the last path. Operational experience and improved understanding lead to incremental improvements in the already existing lithium-ion technology.

An 18650 lithium-ion cylindrical cell had a capacity of 800 mA h in 1992 which increased to about 2900 mA h in 2006 [5]. In 2018, capacities between 3350 mA h to 3500 mA h are available from reputable manufacturers for 18650 cells [11, 12]. Apart from energy density, other characteristics of batteries have similarly improved. This progress from the first generation lithium-ion batteries to the current state-of-the-art has been due to a combination of all these three paths. If these batteries are to maintain and increase their competitive viability for a long time horizon also in the future, continued progress through all three paths will be essential.

This work treads the middle path, which is that of optimizing the current technology by furthering the understanding of how these batteries function. The first step to this approach is to recognise the deficiencies of present day lithium-ion batteries that impede their adoption in vehicle and grid applications. Three areas have been identified for these batteries where improvements are desired:

(i) Safety: this has been a long term challenge for lithium-ion batteries, right from their inception. Most issues arise due to heating of the batteries caused by their operation causing runaways in temperature, fires and sometimes explosions. While considerable improvements have been made on this front, these batteries are still considered dangerous goods on air planes and as cargo [13].

(ii) Price-performance ratio: though costs of lithium-ion batteries are decreasing fast and the performance is improving, the price-performance ratio is still high enough to prevent their use for certain applications, such as electric vehicle adoption where batteries still constitute on an average 48 % of the total cost of the vehicle (2016 figures) [14] and as energy storage for grid applications. While the operating and maintenance costs of battery based storage system are low, the initial capital and the replacement costs are prohibitively high.

(iii) Life: the service lifetime of most lithium-ion batteries is a few years or a few thousand cycles at maximum. While lithium-ion battery lifetimes have prolonged over time through research efforts mainly in materials, they are still short for many applications. Sudden unexpected failures and rapid loss in performance have moreover raised doubts over their reliability and feasibility for grid applications.

These three areas discussed above are not independent from each other. The interrelation between them can be understood through an example. A safer operation of the battery can be achieved by using intrinsically safer materials to build batteries or by using an external cooling system. But either of these options usually adds to the cost of the total system. A safer operation can also be achieved through a less stressful operation of the battery which may extend its life as well. But it will lead to a lower price-performance ratio for the battery.

1.4 Research questions

The research presented in this thesis is inspired by the quest for getting the most out of lithium-ion batteries but in a manner that is safe and causes the least degradation.

Recognizing the shortcomings of the state-of-the-art of lithium-ion batteries, it was evident that improvement in any of the three areas mentioned before without a corresponding decrease in any of the other two is not straight forward. Thus the need for an enhanced understanding and prediction of the behaviour and limits of these batteries was felt.

In order to operate batteries in a safe way, it is important to understand their behaviour under different load conditions. Accurate models that can predict electrochemical and thermal behaviour of the batteries in wide operating conditions are then necessary to track these performance and safety indices. This led to the first research question:

1) How to parametrize accurate physics based models for batteries?

Battery performance degrades with time and usage. An aged battery not only performs worse but also heats up more than a fresh battery making it a bigger safety challenge. Replacing old batteries add to their total cost of ownership. It is therefore imperative to not only be able to predict the behaviour of a new battery, but also to understand how it behaves over its lifetime. In order to have a qualitative and quantitative grip over the degradation processes in the battery, the research answers the following question:

2) How does battery performance degrade over time and with use?

Armed with quantitative knowledge of battery degradation in different operating and environmental conditions, new strategies on how to operate batteries more efficiently for real world applications could be evaluated. A practical way to use the knowledge of degradation in these batteries in order to optimize the operation of a storage unit is sought. The final research question expresses this idea:

3) How can battery operation be optimized when integrated in real world applications?

1.5 Layout of the work

The research has been organized into three parts. Each of these parts addresses one of the topics in the title of the thesis - modelling, aging and optimal operation and answers the corresponding research question.

Part I: Modelling
Lithium-ion batteries are reintroduced providing details on the electrochemical reactions. Next, the different ways to model these batteries are summarized. The choice of the Pseudo 2D model (P2D) for this work is justified. Following that, the P2D model is explained mathematically introducing the coupling between the electrochemical and the thermal model. Details on parametrization and validation of the physics based model for LFP battery follows. The developed model is shown to accurately simulate the battery electrochemical and thermal behaviour for a wide range of currents. Lastly, the model is extended to modules and packs and cooling systems are designed and analysed.

Part II: Aging
An overview of the current understanding of degradation processes in lithium-ion batteries is presented. The design of the experiments to investigate the effect of operating and environmental conditions on the calendar and cycle aging of the batteries is explained. The calendar aging results are presented first. The effect of characterization procedure on calendar aging results is elucidated. Cycle aging results are then presented along with new insights gained into the degradation processes.

Part III: Optimal operation
Technical and economic feasibility of lithium-ion batteries in real-world power system applications is discussed. The traditional battery degradation models applied to market studies are looked into and found to be inadequate in representing the nature of degradation in lithium-ion batteries. A new degradation model for lithium-ion batteries is developed that captures the non-linear nature of degradation. A case study demonstrates this new model and its utility in optimizing operation of a storage unit participating in an energy market. A temporal decomposition technique has also been proposed for more complicated cases.

Part I
Modelling

With four parameters I can fit an elephant, and with five I can make him wiggle his trunk.

John von Neumann

Some of the work described in this part has been previously published in [15] and [16].

Chapter 2

Electrochemical-thermal modelling

Rechargeable lithium-ion batteries, also known as secondary lithium batteries, have been around since 1991 when the first commercial battery was introduced by Sony. Interest and research into lithium based batteries is however older than that. Among all metals, lithium is the lightest, has the lowest reduction potential and the highest energy density making it an attractive material for electrochemical cells. Primary lithium cells were already commercialized by 1970s. These included chemistries such as lithium-sulphur dioxide (Li/SO_2) and lithium-thionylchloride (Li/$SOCl_2$) [17].

It was with the discovery of fast ion conduction of lithium ions in an electronically conducting lattice containing transition metal atoms in mixed valence state that progress towards rechargeable batteries could made. Commercialization efforts for lithium-titanium sulphide (Li/TiS_2) and lithium-molybdenum sulphide (Li/MoS_2) batteries were seen in 1970s and 1980s [17, 18]. But continued use of metallic lithium as the negative electrode in these batteries limited their commercial success. These metal electrodes had the tendency to form dendrites and powder deposits. Short circuit phenomena were common. Attention soon shifted to the use of lithium-intercalation material as the negative electrode instead of metallic lithium. H. Ikeda of Sanyo patented the intercalation material graphite in an organic solvent in June 1981 (Japanese Patent No. 1769661). This was closely followed by S. Basu of Bell Laboratories who filed the US Patent 4423125 in 1982 based on lithium intercalation into graphite at room temperature [18].

Metal oxides (Li_xMO_2) where M = Ni, Mn, Co were discovered about the same time, the use of which as positive electrodes lead to higher voltages in these batteries. Goodenough filed the patent for using $LiCoO_2$ as an intercalation positive electrode material in 1980. These research efforts on positive and negative electrodes culminated in the first commercial lithium-ion battery launched in 1991 by Sony which was based on a graphite negative electrode and a $LiCoO_2$ positive electrode [5].

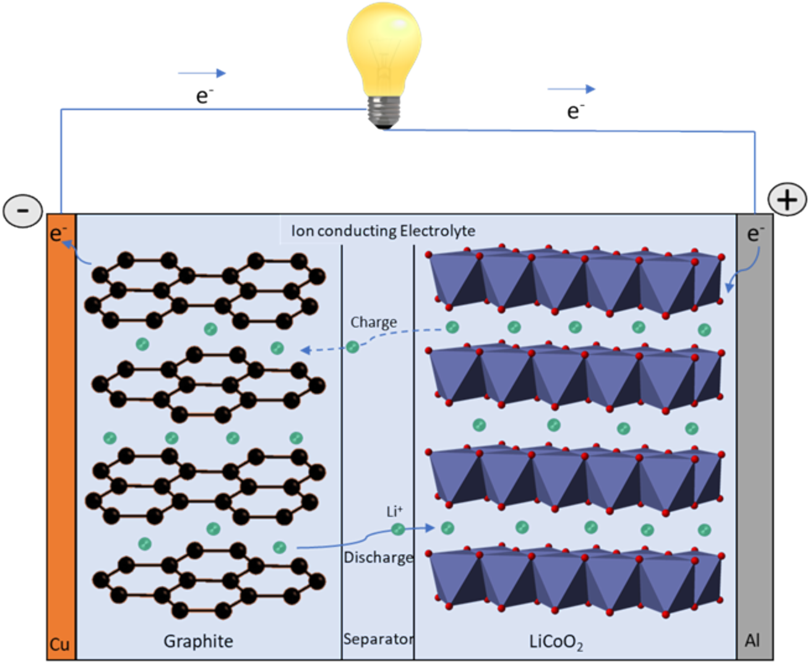

Figure 2.1. Electrochemical unit representation of a lithium-ion battery

2.1 Electrochemical basics of lithium-ion batteries

At the outset of this chapter and work, it is necessary to clarify the definitions of electrochemical cell, cell and battery. An electrochemical cell is a basic unit consisting of electrodes, electrolyte and separator and exhibits a voltage across its two terminals. Cells and batteries have been used interchangeably in this work and refer to one or more electrochemical cells connected electrically.

A battery consisting of electrochemical cells with lithium insertion compounds as both negative and positive electrodes is called a lithium-ion battery. These two electrodes are electrically insulated from each other by a separator. An electrolyte permeates the two electrodes and the separator providing a conductive medium for lithium ions but not for electrons. Lithium ions shuttle between the two electrodes, while electrons are conducted upon connecting the two electrodes externally. The shuttling of lithium ions is often referred to as “rocking-chair” mechanism. The direction of movement of the lithium ions depends on whether the cell is charging or discharging. A representation of an electrochemical unit of a lithium-ion battery can be seen in Figure 2.1.

In battery parlance, anode and cathode are more commonly used terms than negative and positive electrode. Anode is the electrode where oxidation takes place.

During the discharge process, the negative electrode is the anode and the positive electrode is the cathode. The names get switched during the charging process. In this work, considering the considerable confusion that might result from this, positive and negative electrodes terminology has been adopted.

During charging, lithium is inserted into the negative electrode. The choice of the negative electrode is such that the insertion takes place at a higher voltage than the deposition of lithium, thereby preventing the problem of lithium deposition. The problem of lithium deposition was the reason in the delay of the commercial arrival of these batteries and it is still not completely resolved. It will be seen later in Part II of this work that lithium deposition is a major factor affecting battery life. Graphite is the most common negative electrode used in commercial lithium-ion batteries accounting for more than 90% of negative electrodes in 2015 [19].

The reaction at the graphite electrode (as the negative electrode) is:

$$\mathrm{Li}_{x-y}\mathrm{C}_6 + \mathrm{yLi}^+ + \mathrm{ye}^- \underset{\text{discharge}}{\overset{\text{charge}}{\rightleftharpoons}} \mathrm{Li}_x\mathrm{C}_6 \tag{2.1}$$

The same quantity of lithium ions that intercalate into graphite are extracted from the positive electrode during charging. Lamellar oxides of lithiated transition metals, spinels of manganese or iron phosphates are generally used positive electrode materials. These differences in the positive electrode chemical composition are the major reason for the variance seen in the properties of the different lithium-ion batteries. Because of this reason, these batteries are often referred to by the positive electrode chemical composition such as Lithium Nickel Cobalt Aluminium Oxide or NCA batteries ($\mathrm{LiNiCoAlO_2}$), Lithium Iron Phosphate or LFP batteries ($\mathrm{LiFePO_4}$), Lithium Nickel Manganese Cobalt Oxide or NMC batteries ($\mathrm{LiNiMnCoO_2}$), etc. Ideally, positive electrodes with a high potential vs. Li^+/Li are preferred, however in reality the working potentials are often limited by the stability of the electrolyte.

The reaction at the positive electrode (considering a generic positive electrode material Mp) is:

$$\mathrm{Li}_z\mathrm{Mp} \underset{\text{discharge}}{\overset{\text{charge}}{\rightleftharpoons}} \mathrm{Li}_{z-y}\mathrm{Mp} + \mathrm{yLi}^+ + \mathrm{ye}^- \tag{2.2}$$

The two electrodes have a porous morphology and are pervaded by liquid electrolyte. This is usually a alkyl carbonate such as ethylene carbonate (EC), dimethyl carbonate (DMC), di-ethyl carbonate (DEC) or their combination in which a lithium salt is dissolved. The most commonly used salt is lithium hexafluorophosphate ($\mathrm{LiPF_6}$).

2.2 Cell chemistries - focus on NMC and LFP

As discussed in chapter 1, there are many kinds of lithium-ion batteries. The differences mainly arise because of their chemical compositions which in turn cause differences in performance, cost and safety characteristics. Although these factors are also affected by the cell geometry, the dominant role is played by the positive electrode composition. The market share of lithium-ion batteries is currently dominated by lithium cobalt oxide (LCO), lithium manganese oxide (LMO), lithium nickel cobalt aluminium oxide (NCA), lithium nickel manganese cobalt oxide (NMC) and lithium iron phosphate batteries (LFP). Their relative market shares can be seen in Figure 2.2a. In this work, modelling and experiments on NMC and LFP batteries are carried out.

Lithium iron phosphate (LFP) entered the battery scene in 1997 [20] when it was shown as a viable positive electrode material. However it differed from other positive electrode materials due to its olivine structure and the phase change that it underwent. The advantages of LFP batteries are that they have good thermal stability, cycle life and power capability. Being based on iron, they also have lower costs. The disadvantage is that they have a lower energy density. The nominal voltage of these batteries is 3.3 V and they typically cycle between 2.5 V to 4 V.

Research in nickel manganese cobalt (NMC) based lithium-ion batteries was inspired by the high costs, short life span, low power capability and low thermal stability of the first lithium-ion battery based on cobalt (LCO). Efforts concentrated on replacing cobalt by nickel and manganese lead to their development. Like the original LCO, NMC is also a layered oxide. Since their commercial introduction in 2008, NMC based lithium-ion batteries have become one of the most used battery type for a wide range of applications. This is because they offer a good package of energy, power, cycle life and thermal stability. NMC combines the advantages of nickel and manganese to replace a part of energy dense but expensive cobalt. Nickel is thermally unstable but has a high energy density, manganese on the other hand is thermally stable and has a low internal resistance but has a low energy density [19, 21].

The nominal voltage of a typical NMC cell is 3.7 V and it is usually cycled between 2.5 V to 4.2 V. NMC111 and NMC532 are the two most commercial and researched compositions, the numbers representing the relative amounts of each metal in the electrode. A qualitative comparison between LFP and NMC can be seen in Figure 2.2b.

2.3 Cell geometry and format

Lithium-ion batteries can be adapted for different devices and applications by varying the cell geometry and format. Cell geometry refers to the internal dimensioning (length, width and thickness) of the different layers such as the negative, positive electrodes. Cell format refers to the overall packaging of the

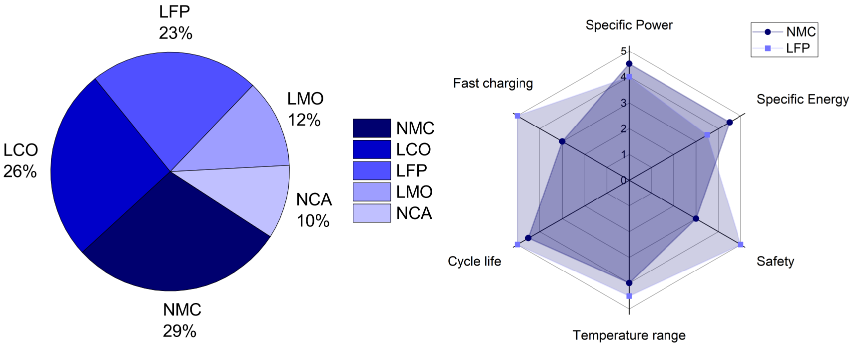

(a) Market demand of different lithium-ion batteries in 2015 [19]

(b) Qualitative comparison between LFP and NMC [18]

Figure 2.2. Different lithium-ion batteries

different layers. These include cylindrical, button, prismatic and pouch formats. They can be seen in Figure 2.3. For each format, units of different dimensions exist based on the internal geometry.

Both cell geometry and format affect the current, potentials and thermal distributions inside the cell and influence their performance, safety and lifetime. For example, using the same electrode materials but varying the thickness of the electrodes, a high power or a high energy cell can be realized. Battery pack architecture also depends on the individual cell format and geometry. Thus they also dictate the overall pack energy density, power density and cost. The format and dimensions additionally affects the choice, sizing and economics of cooling system design for battery packs.

In this work, modelling of a pouch format and experimental testing on both cylindrical and pouch formats have been carried out. The cylindrical cell used is an 18650 cell. The name comes from the external dimensions of the cell with the diameter being 18 mm and the length about 65 mm. Cylindrical cells have high specific energy and mechanical stability. They are also easy to manufacture. The different cell layers are rolled up inside the cylindrical structure. This format is commonly used in laptops and also in some electric vehicles.

A pouch cell is a comparatively newer invention which makes more efficient use of space. The cell layers are stacked up inside the pouch covering. A pouch cell is more flexible and lighter (for the same capacity) than 18650 cells and the shape allows for easy stacking. These kind of cells are also called laminate cells or coffee bag cells. They have mainly been adopted for use in electric vehicles. B5 format pouch cells are used in this work. B5 refers to the external dimensions of the pouch (176 mm x 250 mm), following the same convention as paper sizes.

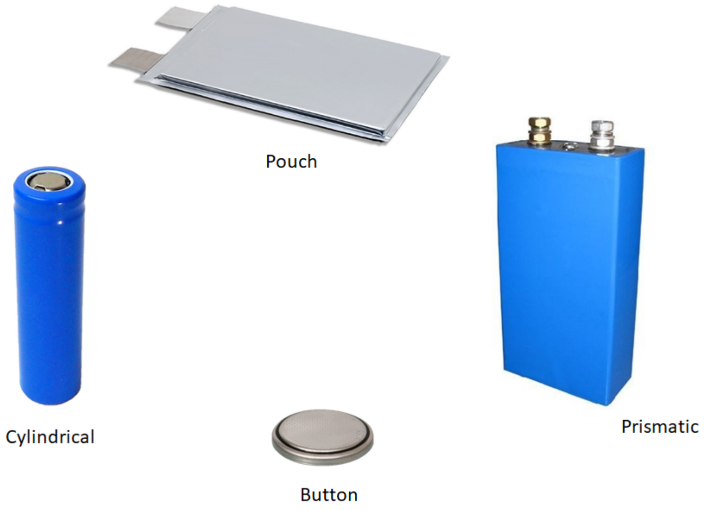

Figure 2.3. Different formats of lithium-ion batteries (not to scale)

2.4 Lithium-ion battery models

As was true for the first models of lithium-ion batteries, the current objectives of modelling batteries are to aid understanding, help designing and enable scale up of these batteries. The principles of model development are usually to start with a simple model and progressively add more details until the model predictions are sufficiently accurate for the objective of the modelling. Various types of mathematical models for lithium-ion batteries have been developed over the last years and a summary of them can be seen in Figure 2.4, highlighting the trade-off between computational requirements and prediction accuracy.

A third axis, that of modelling effort can also be added to Figure 2.4 but generally speaking, a model that requires more modelling effort is also computationally more demanding. This modelling effort comes from determining the value of parameters in the model.

Empirical models are the most simple and the least accurate. Linear, polynomial, exponential and other commonly used functions or their combinations are used to fit experimental data directly to get parameters for the model. This simplicity allows for fast computation and these models are best suited for real-world applications such as in battery management systems (BMS). Their prediction capability, especially when extrapolating from the usual operating conditions is poor [22, 23].

The next two levels of modelling include the single particle model (SPM) and the pseudo two dimensional (P2D) model. These two models incorporate kinetics and

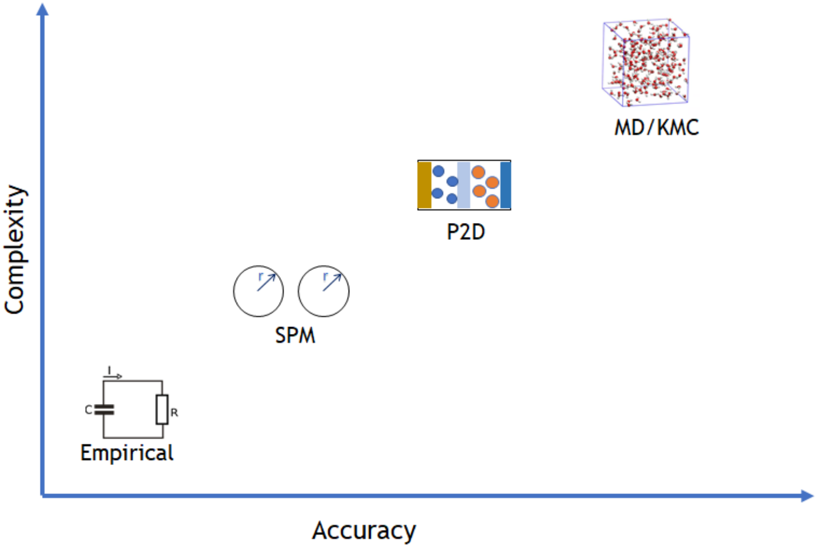

Figure 2.4. Types of models

diffusion phenomena in the electrolyte and the electrodes using partial differential equations (PDE). Finite element analysis (FEA) is usually carried out to solve these coupled PDEs. In the SPM, each electrode is considered as a single particle with the same surface area as the electrode. Diffusion and insertion kinetics are considered in the model but no variance in concentration or potential is considered in the solution phase. The SPM model simulates thin electrode and low current conditions reasonably well but fails at high current conditions [24, 25].

P2D model takes into account diffusion both in electrolyte and solid electrode phases. Kinetics of insertion/extraction is described using Butler-Volmer equations. This model is more accurate than SPM at the cost of more parametrization effort and more computing resource requirement [26, 27]. Both the P2D model and the SPM are able to simulate entire charge-discharge cycles in lithium-ion batteries within seconds.

The most advanced models simulate battery behaviour at the molecular/atomic level. Kinetic Monte Carlo (KMC) method can help predict thermodynamic properties of materials, mobility of lithium inside the crystal structure, etc. [28, 29]. Molecular dynamics provides information on phenomena at the molecular scale such as the growth of passivating film on the graphite electrode. The use of these advanced models is restricted to studying one specific process taking place in a very small fraction of a second [30, 31].

Apart from parametrization, an important aspect of modelling is to experimentally validate the model to ensure that the experimental data can be

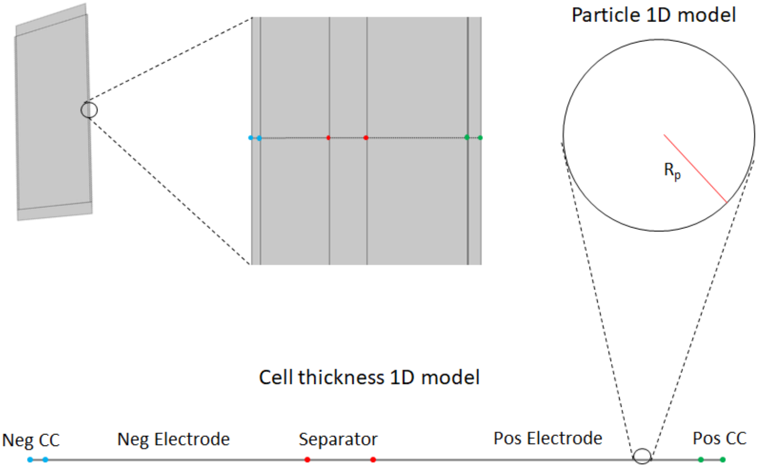

Figure 2.5. Representation of P2D model

reasonably simulated through the model. The more the number of variables being validated, greater is the confidence in the model.

2.4.1 Details on P2D modelling approach

In this work, a Pseudo 2D modelling approach has been followed. This approach enables good prediction of the electrochemical behaviour of batteries for complete charge-discharge cycles in different operating conditions within a reasonable computation time. While parametrization is a challenge, the advantage of a P2D model lies in its accuracy precisely because of inclusion of dominant physical phenomena along with the details of cell layer and particle geometry. The P2D model is also flexible and other phenomenon such as thermal behaviour, stress and strain in components can be coupled with this model.

The P2D model consists of two disparate but connected 1D realms (hence pseudo 2D). One 1D realm models processes along the thickness of the cell and the other 1D realm models the particles of the active material (see Figure 2.5). The first realm models charge and mass transport in porous electrodes and electrolyte along with the electrochemical reactions happening at the interface between the electrode and the electrolyte. Current collectors are also modelled for the sake of accuracy. The other realm models one-dimensional diffusion based transport in the particle. These two realms are coupled based on the law of conservation of species.

The first pseudo 2D model of a lithium battery using porous electrode theory [32], particle diffusion and concentrated solution theory [17] was already developed in 1993 borrowing from modelling approaches developed for non-lithium based batteries. In the porous electrode theory, the exact positions and shapes of all the particles and pores in the electrode are not specified rather the properties are averaged. Particles are generally considered as perfect spheres. Though P2D models have undergone big changes in terms of complexity and account for more phenomena happening in the batteries compared to the first models, the basic approach and structure still borrows a great deal from the first models made by Newman and his associates [33–35].

2.4.2 P2D modelling equations

P2D model includes all dominant phenomena happening in the lithium-ion battery. Law of conservation of mass and of charge and ohm's law combined with theories of kinetics and diffusion provide the necessary framework for the P2D model.

Porous electrodes consist of solid phase (electrodes) and the solution phase (electrolyte). Electrochemical reaction takes place at the interface of these two phases. The rate of this reaction is described by Butler-Volmer kinetics:

In electrolyte phase,

$$\nabla \cdot i_l = a_v \cdot i_0 \cdot \left[\exp\left(\frac{\alpha_a \cdot F \cdot \eta}{R \cdot T}\right) - \exp\left(\frac{-\alpha_c \cdot F \cdot \eta}{R \cdot T}\right)\right] \tag{2.3}$$

In electrode phase,

$$\nabla \cdot i_s = -a_v \cdot i_0 \cdot \left[\exp\left(\frac{\alpha_a \cdot F \cdot \eta}{R \cdot T}\right) - \exp\left(\frac{-\alpha_c \cdot F \cdot \eta}{R \cdot T}\right)\right] \tag{2.4}$$

where
i_l is the current density in the solution ($\mathrm{A\,m^{-2}}$)
i_s is the current density in the solid ($\mathrm{A\,m^{-2}}$)
i_0 is the exchange current density ($\mathrm{A\,m^{-2}}$)
T is the temperature (K)
α is the dimensionless charge transfer coefficient
η is the surface over-potential (V)
R is the gas constant equal to $8.314\,\mathrm{J\,K^{-1}\,mol^{-1}}$
F is the Faraday constant approximately equal to $96\,485\,\mathrm{C\,mol^{-1}}$

The exchange current density, i_0, is given by

$$i_0 = F \cdot k_c^{\alpha_a} \cdot k_a^{\alpha_c} \cdot (c_{s,max} - c_s)^{\alpha_a} \cdot c_s^{\alpha_c} \cdot \left(\frac{c_l}{c_{l,ref}}\right)^{\alpha_a} \tag{2.5}$$

where
k is the rate constant of the electrochemical reaction ($\mathrm{m\,s^{-1}}$)
$c_{s,max}$ is the maximum concentration of lithium in the solid particle ($\mathrm{mol\,m^{-3}}$)

c_s is the instantaneous concentration of lithium in the solid particle ($\mathrm{mol\,m^{-3}}$)
c_l is the instantaneous concentration of lithium in the solution ($\mathrm{mol\,m^{-3}}$)
$c_{l,ref}$ is the reference concentration of lithium in the solution

The difference, $(c_{s,max} - c_s)$, is the concentration of unoccupied sites in the insertion electrode material. When c_s is 0 or $c_{s,max}$, the exchange current density becomes 0. The anodic and the cathodic transfer coefficients given by α_a and α_c decide the preference of the applied potential towards the anodic and cathodic directions of the overall reaction.

The specific inter-facial area of each electrode, a_v, is given

$$a_v = \frac{(3 \cdot \epsilon_s)}{r_p} \tag{2.6}$$

where
ϵ_s is the volume fraction of the solid active material
r_p is the radius of the spherical particle (m)

The surface over-potential (η), is the deviation of the actual potential difference between the solid and solution from the equilibrium potential of the solid determined with respect to reference lithium electrode.

$$\eta = \phi_s - \phi_l - E_{eq} \tag{2.7}$$

where
ϕ_s is the potential at the solid surface (V)
ϕ_l is the potential in the solution (V)
E_{eq} is the equilibrium potential of the electrode material (V)

For the reaction to take place at the interfaces, there should be a flux of ions and electrons at the reaction sites. The conduction of electrons in the solid phase can be described by the ohm's law:

$$i_s = -\sigma_s \cdot \nabla \phi_s \tag{2.8}$$

where
σ_s is the conductivity in the solid phase ($\mathrm{S\,m^{-1}}$)

Concentrated solution theory describes the processes in the electrolyte phase [33]. Here the ion is mobile and the current density can be calculated using,

$$i_l = -\sigma_l \cdot \nabla \phi_l + \frac{2 \cdot \sigma_l \cdot R \cdot T}{F} \cdot \left(1 + \frac{\partial \ln f_\pm}{\partial \ln c_l}\right) \cdot (1 - t_+) \cdot \nabla \ln c_l \tag{2.9}$$

where
σ_l is the conductivity of the solution ($\mathrm{S\,m^{-1}}$)
$f_\pm$ is the mean molar activity coefficient
t_+ is the transference number

This equation is similar to ohm's law with the added second term on the right that accounts for concentration differences in the solution phase. It introduces two new concentration dependent transport parameters, mean molar activity coefficient $f_{\pm}$ and transference no (t_{+}). The mean molar activity coefficient determines the voltage polarization resulting from the concentration gradient [36]. The term $(1 + \frac{\partial \ln f_{\pm}}{\partial \ln c_l})$ is called the thermodynamic factor and can be determined from the mean molar activity coefficient $f_{\pm}$. The transference number (t_{+}), also called the transport number takes into account concentration gradients that form under load.

A mass balance in the electrolyte phase gives,

$$\epsilon_l \cdot \frac{\partial c_l}{\partial t} = \nabla \cdot (D_l \cdot \nabla c_l) - \nabla \cdot \left(\frac{i_l \cdot t_{+}}{F} \right) + \frac{\nabla \cdot i_l}{F} \tag{2.10}$$

where
ϵ_l is the volume fraction of the solution phase
D_l is the diffusivity of the electrolyte $(\mathrm{m^2\,s^{-1}})$

Any change in the concentration of lithium in the electrolyte is due to diffusion, migration and convection. The contribution of convection can be assumed to be zero in the battery as the velocity of the solvent is not significant in lithium-ion batteries [17]. The first term on the right of Equation 2.10 accounts for the contribution of the diffusion, the others terms for that of migration.

Corrections in diffusivity and conductivity to include the effect of tortuosity are effectuated through Bruggeman coefficient [37]. The effect of film resistance is taken into account in the over-potential by modifying Equation 2.7 as follows:

$$\eta = \phi_s - \phi_l - E_{eq} - R_{film} \cdot i \tag{2.11}$$

where R_{film} is the film resistance. This resistance is mainly due to the formation of the Solid Electrolyte Interphase (SEI). This layer formation is an important phenomena that has a profound influence not only on the performance but also the safety and life of the battery. It will be described and analysed in more detail in subsequent chapters.

The active electrode material is assumed to be made of spherical particles of radius r_p. Transportation of lithium in and out of the active material particle take place through the mechanism of diffusion. It is described as follows,

$$\frac{\partial c_s}{\partial t} = \nabla \cdot (-D_s \cdot \nabla c_s) \tag{2.12}$$

where
D_s is the diffusion coefficient in the solid particle $(\mathrm{m^2\,s^{-1}})$

The boundary conditions in the solid particle are:

$$\frac{\partial c_s}{\partial r} = 0|_{r=0} \tag{2.13}$$

$$-D_s \cdot \left.\frac{\partial c_s}{\partial r}\right|_{r=r_p} = -\frac{\nabla \cdot i_s}{F \cdot a_v} \tag{2.14}$$

The boundary conditions ensure that calculations of the mass balance in the solid is coupled to the reaction rate, connecting the two 1D realms of the P2D model. It is assumed that the active material is a good electronic conductor and volume changes in the solid are negligible. No interaction within particles has been assumed which is justified by the much larger distances between particles compared to the length scale within particles. For the sake of accuracy, the current collectors have also been modelled in this work even if the potential drop across them is negligible.

2.4.3 Inclusion of thermal model

Batteries are not 100% efficient. The insertion-extraction and transport of lithium during charging and discharging invariably cause heat to be produced due to irreversible processes in the cells. Moreover, changes in the crystal structure order due to lithium insertion/extraction in either electrode may also cause heat to be generated or absorbed. The first kind of heat is called irreversible heat and it is generated in the cell due to limitations in physical processes, such as ohmic losses, activation over-potential and mass transport limitations. The second kind, due to changes in the crystal order, is called reversible heat. The total heat generated in the cell can be calculated considering all the reversible sources/sinks and irreversible sources of heat in the cell. Further details on thermal behaviour in lithium-ion batteries can be found in [38–40]

Total heat generation is given by,

$$Q = Q_{irr} + Q_r \tag{2.15}$$

Total irreversible heat, Q_{irr}, is given by

$$Q_{irr} = i_l \cdot \nabla\phi_l + i_s \cdot \nabla\phi_s + (\nabla \cdot i_l) \cdot \eta \tag{2.16}$$

where the first two terms denote heat generated due the ohmic losses in electrolyte and solid phases while the last term quantifies the polarization heat.

Reversible heat, Q_r, is given by

$$Q_r = (\nabla \cdot i_l) \cdot T \cdot \frac{dE_{eq}}{dT} \tag{2.17}$$

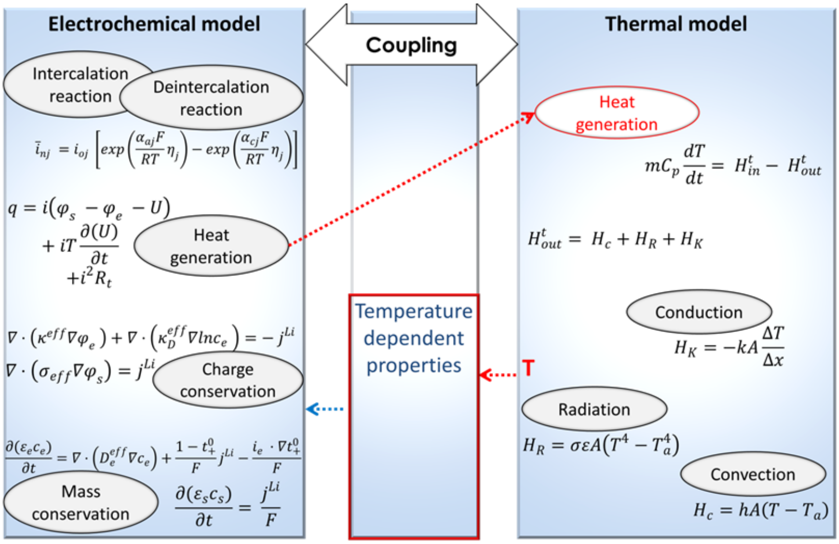

Figure 2.6. Coupled electrochemical and thermal models

A cell consists of active as well as inactive regions. Heat is generated only in the active regions such as in the electrodes and the electrolyte. However, heat can be conducted to and from the active region to the inactive regions which include the separator, the encasing material, etc. Also a battery can gain or lose heat by conduction, convection and radiation with the environment it is placed in. The general equation for heat balance of the cell considering also the environment can be written as:

$$\rho\cdot C_p\cdot\frac{\partial T}{\partial t} = Q + \nabla\cdot(k_T\cdot\nabla T) - \nabla\cdot(h\cdot(T - T_a)) - \nabla\cdot(\sigma_T\cdot\epsilon_T\cdot(T^4 - T_a^4)) \quad (2.18)$$

where
ρ is the density ($\mathrm{kg\,m^{-3}}$)
C_p is the specific heat capacity ($\mathrm{J\,kg^{-1}\,K^{-1}}$)
k_T is the thermal conductivity ($\mathrm{W\,m^{-1}\,K^{-1}}$)
h is the heat transfer coefficient ($\mathrm{W\,m^{-2}\,K^{-1}}$)
σ_T is the StefanBoltzmann constant equal to $5.67\times10^{-8}\,\mathrm{W\,m^{-2}\,K^{-4}}$
ϵ_T is the emissivity
T_a is the ambient temperature (K)

There are two main reasons for developing the thermal model along with the P2D electrochemical model. First, safety in battery is largely a thermal issue and studying the heat generation behaviour and the temperature increase is necessary to ensure that the cell remains in its optimum temperature operating range. Secondly, there is the strong dependence of some physico-chemical parameters of materials on temperature. These include the thermodynamic factor, ionic conductivity of the electrolyte, diffusivity of the electrodes and the electrolyte and the reaction rate constants. The electrode potentials are also temperature dependent. Thus accurate simulations of battery behaviour necessities inclusion of the dependence of temperature on these properties. For the sake of accuracy, heat generation in current collectors is also taken into account. In Figure 2.6, the couple electrochemical-thermal model can be seen.

Chapter 3

Parametrization of LFP model

Physics based approaches such as P2D electrochemical model that are based on physical laws are more complicated and CPU intensive than empirical models. The upside being more flexibility, reliability and accuracy of prediction in a wide range of operating conditions and applications. However to ensure the accuracy of these models, knowledge of different electrochemical and geometrical parameters of the battery is imperative. At least 30 different values of parameters apart from the equilibrium potentials of the electrodes are needed as input just for a P2D model. Additionally, the thermal model necessities knowledge of other properties such as density, heat capacity and thermal conductivities of the active and non-active layers of the cell. The properties needed for building a coupled P2D electrochemical-thermal model are listed in Appendix A.

In this chapter, a coupled P2D electrochemical-3D thermal model for a LFP pouch cell is developed. $LiFePO_4$ material presents an additional modelling challenge compared to the electrodes for which the P2D model was originally developed due to its olivine structure and by undergoing a phase change. In order to include this behaviour of $LiFePO_4$ in the P2D model, a shrinking core model was developed in 2004 [41]. Subsequently the model has been refined and revised. A rectangular geometry of $LiFePO_4$, volume change, rate of phase transformation have been since considered [42]. An improvement of the previous model by also considering the alpha phase was then developed [43]. A multi-scale approach (crystal, particle, electrode) for modelling is presented in [44]. Atomistic simulations revealed insufficiency of shrinking core model and its more sophisticated versions in explaining the physical nature of diffusion in the $LiFePO_4$ particle and a phase field model was developed [45]. It is also been reported that phase separation is suppressed during battery operation at very low over potentials [46], due to surface reactions that are far from equilibrium [47], and also when the particle is nano-sized [48].

Asymmetry between charge and discharge in $LiFePO_4$ electrode has been well documented [49–53]. Path dependence and hysteresis phenomena in $LiFePO_4$ are now generally accepted to have a thermodynamic origin. However, there is no consensus on the theory explaining the asymmetry. The theories that satisfactorily explain it include core-shell model [49, 54] and the many particle system model [51]. Experimental evidence that validates both these theories is also found [52, 55]. A constant value of 20 mV of hysteresis for $LiFePO_4$ is reported by [51]. Though considerable, this is much less than other chemistries such as Li_2FeSiO_4 and TiO_2 which are known to have large hysteresis behaviour, of the order of tens of millivolts [51].

3.1 Experimental

B5 format prototype lithium-ion pouch cells with a nominal capacity of 6 A h manufactured by Lithops S.r.l (Figure 3.1a) were tested during this work and used to collect experimental data for their modelling. These lithium-ion cells were prepared using artificial graphite (IMERYS, D50 about 6 mm) as negative electrode active material and lithium iron phosphate ($LiFePO_4$) (BASF, D50 about 11 mm) as positive electrode active material. The electrodes were obtained by a comma bar roll coating over common commercial Cu (Schlenk, 16 mm thickness) and Al (Showa Denko, 20 mm thickness) metal foils. A 25 µm thick polypropylene membrane was used as separator (Celgard). For these cells 1 M $LiPF_6$ in ethylene carbonate: diethyl carbonate (2:3 w/w) + 1% vinylene carbonate liquid electrolyte was used. The resultant pouch cells have an operational voltage between 2.5 V to 4.0 V and 6 A h rated capacity. After activation by Lithops S.r.l, cells were delivered at 30 % SOC (about 3.1 V) for testing. The cell's nominal capacity was verified via galvanostatic cycling at 0.1 C. The current applied was therefore 0.6 A. In these conditions the measured capacity was around 6 A h, corresponding to the nominal one given by Lithops S.r.l. The external dimensions of the pouch cell are 250 mm x 164 mm x 4 mm.

Starting at a completely discharged state (2.5 V, cut-off voltage), the cell was charged repeatedly using constant current constant voltage (CC-CV) procedure till 4.0 V and current cut-off of 10 mA at 0.1 C, 0.2 C, 1 C, 2 C, 5 C and 10 C rate. After each charge, it was discharged again with the same conditions as charge. Moreover, after every charge and discharge step a 5 min rest period was adopted in order to let the cell stabilize, thereby preventing safety problems due to high current switches and ensuring that the cell is near the ambient temperature. The minor differences in temperatures and SOC at the beginning of different charge discharge steps were accounted for in the model. The temperature was monitored during the whole charge-discharge test by means of a thermocouple placed in contact to the surface of the cell case near the negative electrode tab while the front surface was monitored through a thermal camera (Figure3.1b).

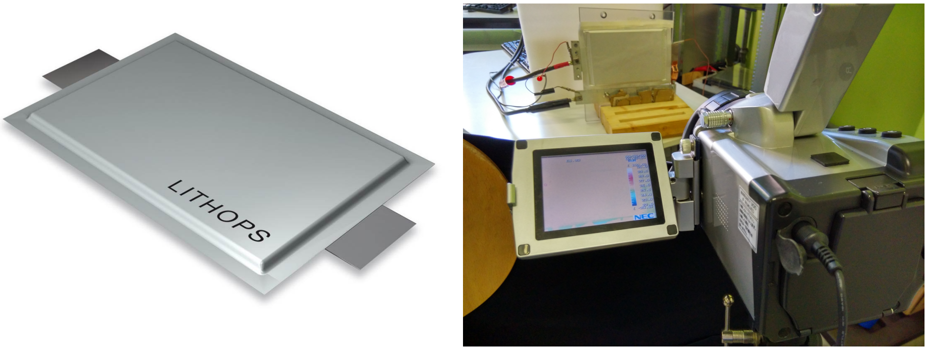

(a) Rendered image of pouch cell from Lithops S.r.l

(b) Actual battery under testing being monitored by thermal camera

Figure 3.1. Battery and experimental testing

3.2 Modelling philosophy

The basic modelling framework for the complete battery except for the $LiFePO_4$ electrode is based on the traditional pseudo 2D model (Section 2.4.2). For $LiFePO_4$ electrode, the modelling philosophy was to start from a standard P2D approach such as for a generic insertion electrode and modify it progressively until a good match between experiment and simulation is found. Similar approach where no special features of the two phase process of $LiFePO_4$ are included but instead charge discharge curves are used to determine correlations for diffusion coefficient and rate constant in the $LiFePO_4$ electrode is seen in [56]. Here, a good match between simulations and experiments until 1 C for charge and discharge curves is seen. The approach in [27] is also similar, but here instead diffusion coefficients and rate constants are held constant and radius is current dependent. Their electrochemical model is not a P2D model but a simpler electrochemical model. This model is validated for both charge and discharge current rates until 8 C.

The difference from [27] in this work is that a P2D modelling approach is the basis of the electrochemical model and a wider range of charge and discharge rates from 0.1 C to 10 C is simulated and validated against experimental data. The equivalence of current dependent diffusion coefficient and a current dependent radius is also shown. As in [27] but with a more detailed thermal model, an additional validation, that of temperature rise, is done by reproducing in the model the actual thermal conditions for the pouch cell when it was being experimentally tested. Critical discussion on every choice of correlation and values for parameters is made in this work given that some of them are not easily determined, or available in literature, or if available there is no consensus. An inverse mode for determination of some of them is also discussed in the text.

A 3D thermal model is simultaneously developed with the P2D model and

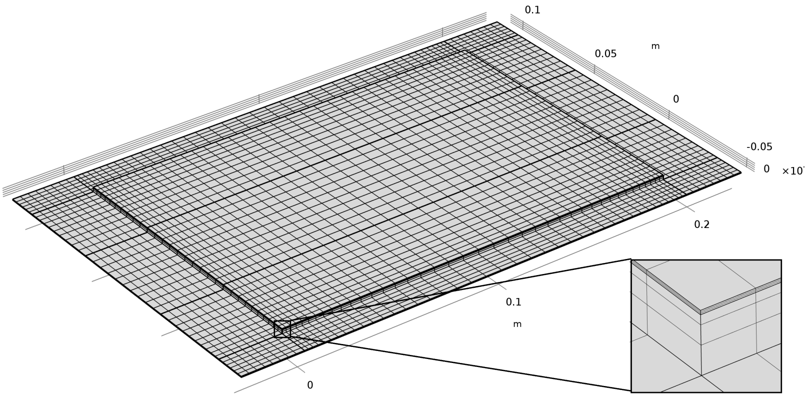

Figure 3.2. Mesh for the pouch cell

they are coupled together (Section 2.4.3). A 3D thermal model is necessary, since geometry and surface area play an important role in heat transfer. The testing set-up is asymmetric, such that the pouch cell is insulated on one side, while the other side is open to natural convection cooling. In the 3D thermal model of the battery, non-active battery component, the pouch, is also modelled since it plays a significant role in the thermal profile due to its thermal properties such as emissivity, thermal conductivity and heat capacity. To simplify calculations, composite thermal properties of the active parts of the battery are considered instead of modelling each thin layer separately. The pouch is however modelled as a separate layer.

The P2D electrochemical and the 3D thermal model are developed and coupled using the battery module of COMSOL Multiphysics®modelling software. MUMPS direct solver with a relative tolerance of 0.0001 is used for simulations. The maximum size of the mesh element in the thickness direction is 1.6×10^{-6} m, and the particle dimension has been discretized with ten elements in the radial direction. For the thermal model, a rectangular mapped mesh swept in the thickness direction of the pouch cell, with at least three elements for each layer in the thickness direction, is employed. The resulting hexahedral elements can be seen in Figure 3.2. The high aspect ratio of the elements cause the overall mesh quality to be low necessitating the use of the direct solver.

3.3 Model Parameters

Given the importance of accurate determination of parameters in the model, the values provided directly by the cell manufacturer, Lithops S.r.l have been fixed in the model. Experimentally determined values obtained from literature study are

Table 3.1. Properties known from manufacturer and literature review

Quantity		**Unit**	**Values**				
			Negative current collector	**Negative electrode**	**Separator/ Electrolyte**	**Positive electrode**	**Positive current collector**
Maximum concentration solid phase		$\mathrm{mol\,m^3}$		31370		22806	
Initial electrolyte salt concentration		$\mathrm{mol\,m^3}$			1000		
Activation Energy	Diffusion	$\mathrm{kJ\,mol^{-1}}$		35		35	
	Reaction	$\mathrm{kJ\,mol^{-1}}$		20		20	
Conductivity		$\mathrm{S\,m^{-1}}$	5.998×10^7	100	0.771	6	3.774×10^7
Bruggeman coefficient				1.5	1.5	1.5	
Transport number					0.363		

also fixed in the model whenever a good agreement is seen among the different sources. The literature obtained values that were inconsistent, are modified during the calibration stage of the model with the literature values as first guess.

3.3.1 Physico-chemical properties

Current collector: copper and aluminium are the current collectors used for the negative and the positive electrode, respectively. These materials have well studied properties and no ambiguity exists as regards their values. Current collectors ensure that that the current distribution inside the active layers is uniform. They are materials with high electrical conductivity which ensures that the resistance from the current collectors is low.

Maximum concentration in the solid phase: maximum concentration of lithium in the solid phase for the negative electrode is taken to be $31\,370\,\mathrm{mol\,m^{-3}}$ [57]. A slightly different value in [58] has been estimated as $30\,555\,\mathrm{mol\,m^{-3}}$. For the positive electrode, calculations of crystal density ($3600\,\mathrm{mol\,m^{-3}}$) and molecular mass ($157.76\,\mathrm{g\,mol^{-1}}$) gives a value for the theoretical maximum capacity of around $22\,800\,\mathrm{mol\,m^{-3}}$. The value in the model taken from [57].

Activation energy: kinetic activation energies for $LiFePO_4$ and graphite are both input as $20\,\mathrm{kJ\,mol^{-1}}$ after comparing values from [27, 57, 59] whereas diffusion coefficient activation energies for $LiFePO_4$ and Graphite are inputted as $35\,\mathrm{kJ\,mol^{-1}}$ after comparing values from [27, 57, 60, 61]. A good review on the $LiFePO_4$ diffusivities and activation energies is available in [62].

Bruggeman coefficient: it is assumed to be 1.5 in the separator as well as in the two electrodes to account for tortuosity of these porous media. Any incorrect

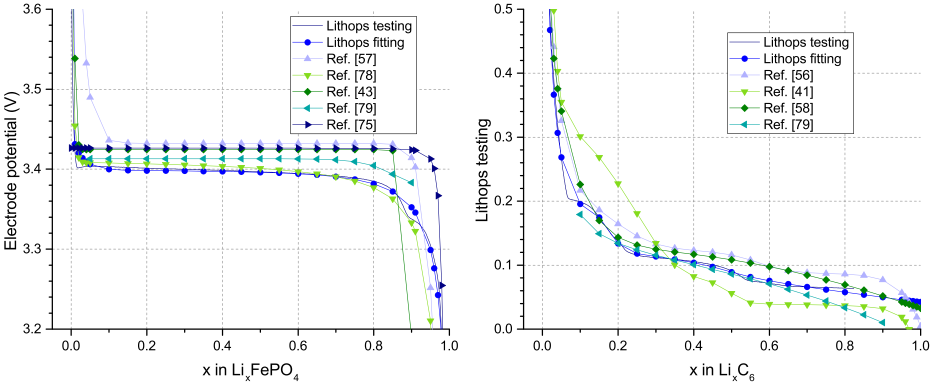

(a) Positive electrode potential (b) Negative electrode potential

Figure 3.3. Electrode potential

assumption for this coefficient is compensated by the values of diffusivities and conductivities which are estimated from experimental charge discharge curves.

Equilibrium electrode potentials: there are significant differences in literature in the measured values of the electrode potentials at equilibrium as can be seen in Figure 3.3. These differences can arise because of different electrode compositions in these studies. Usually the potential measured at low current rate is assumed to be equal to the equilibrium electrode potential. However differences can arise based on the value of this low current rate or whether the potential was measured during charge or discharge or if an average value is used (hysteresis effect [41, 56, 63]). The value of the maximum theoretical capacity assumed for the electrode can also make a difference. Moreover the differences at the beginning and end of the curve for $LiFePO_4$ (Figure 3.3a) can probably be explained by the difference in solid solution ranges for $LiFePO_4$ obtained from different sources [43]. Difference in the values of the potential found in literature is as high as 0.06 V for $LiFePO_4$ (0.1 - 0.85 x range, see Figure 3.3a) and 0.12 V (0.05 - 0.8 x range, see Figure 3.3b) for graphite. The differences are larger near the beginning and the end of the curve.

The shape of the equilibrium electrode potential has a large effect upon the simulation results, and accurate data for this property measured with respect to a lithium reference electrode are important, especially when one is comparing full-cell-sandwich simulations with experimental data. Given the error that can be induced using incorrect correlation for the determination of the potential, experimental data for electrode potential were obtained from the manufacturer. Curve fitting of the potential curves of the electrodes is carried out in MATLAB R2014b to yield the following equations.

LiFePO$_4$ electrode potential at 25 °C:

$$\begin{aligned} E_{eq} = 3.399 + h - 1.239 \cdot \exp\left(-7.903 \cdot \left(1-x\right)^{0.3821}\right)\right) \\ - 3.644 \times 10^{-10} \cdot \exp\left(21.12 \cdot (1-x)^{30.37}\right) \\ + 8.249 \times 10^{-12} \cdot \exp\left(22.39 \cdot (1-x)^{1.56}\right) \end{aligned} \quad (3.1)$$

where
h is the hysteresis factor
x is the relative local concentration of lithium in the electrode given by the ratio of the lithium concentration to the maximum lithium concentration for the electrode.

This 10 parameter equation fits the experimental curve with a R-squared value of 0.9823. The electrode potential curve is calculated from a slow rate (0.1 C) discharge of a LiFePO$_4$ electrode vs. a reference lithium electrode. The value of h is assumed to be zero during discharge and is then determined to be 50 mV from the charge curve. The actual hysteresis, an average of the distance between these low rate charge and discharge potentials, is thus 25 mV. This is slightly greater than the value reported in the literature where smaller particles are used [51]. However, hysteresis depends on particle size [48, 50] such that smaller particles are seen to have a lower hysteresis. LiFePO$_4$ particles in the battery used in this study are in the µm range.

Graphite electrode potential at 25 °C:

$$\begin{aligned} E_{eq} = 0.2033 + 0.6613 \cdot \exp\left(-68.63 \cdot x\right) \\ + 0.026\,74 \cdot \tanh\left[-\frac{x-0.1814}{0.03031}\right] - 0.006\,943 \cdot \tanh\left[\frac{x-0.4895}{0.0854}\right] \\ - 0.009\,25 \cdot \tanh\left[\frac{x-0.0317}{0.053}\right] - 0.075 \cdot \tanh\left[\frac{x-0.5692}{0.875}\right] \end{aligned} \quad (3.2)$$

The graphite potential equation, fitted using 15 parameters, has an R-squared value of 0.9924.

Entropy coefficient: electrode potentials are temperature dependent. The dependency is expressed as

$$E_{eq}^{T} = E_{eq} - (T - 298.15) \cdot \frac{dE_{eq}}{dT} \quad (3.3)$$

where
E_{eq}^{T} is the electrode potential at temperature T (K)
E_{eq} is the electrode potential at 298.15 K given by Equation 3.1 and Equation 3.2
$\frac{dE_{eq}}{dT}$ is the entropy coefficient

Entropy coefficient for graphite has been adopted from [64]. A different

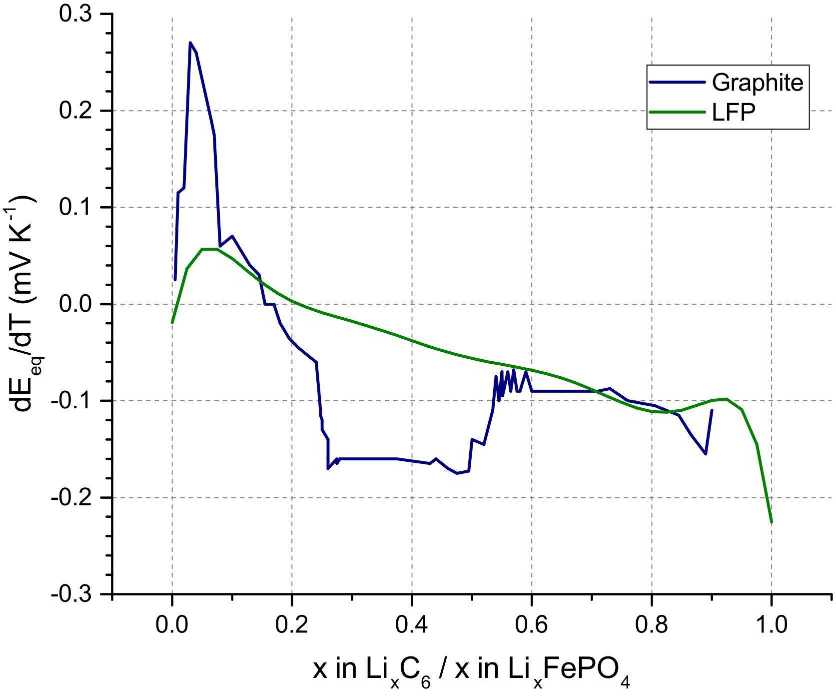

Figure 3.4. Entropy coefficients

correlation from the data in [65] is also widely used in literature [66–69] but it has been determined with fewer experimental data and its accuracy is suspect over the wider range of x. Entropy coefficient for $LiFePO_4$ has been determined in [63, 70, 71]. It is observed that between $x = 0.1$ to $x = 0.9$ there is not a significant difference in the determined values between the different sources. In view of this, in this work the correlation determined from [63] is used for the model. The entropic coefficients used for both electrodes have been plotted in Figure 3.4.

The graphite entropic coefficient is input as a set of data points while the $LiFePO_4$ entropic coefficient as the following equation:

$$\begin{aligned}\frac{dE_{eq}}{dT} &= -0.35376 \cdot x^8 + 1.3902 \cdot x^7 - 2.2585 \cdot x^6 + 1.9653 \cdot x^4 \\ &\quad + 0.28857 \cdot x^3 - 0.046272 \cdot x^2 + 0.0032157 \cdot x - 1.9186 \times 10^{-5} \qquad (3.4)\end{aligned}$$

Transport number: in [36], the transport number of different electrolytes were compared and values between 0.325 and 0.47 is seen. In [72], a temperature and concentration dependent transport number and thermodynamic factor is used. The low sensitivity of the discharge curve on the transport number can be in seen in

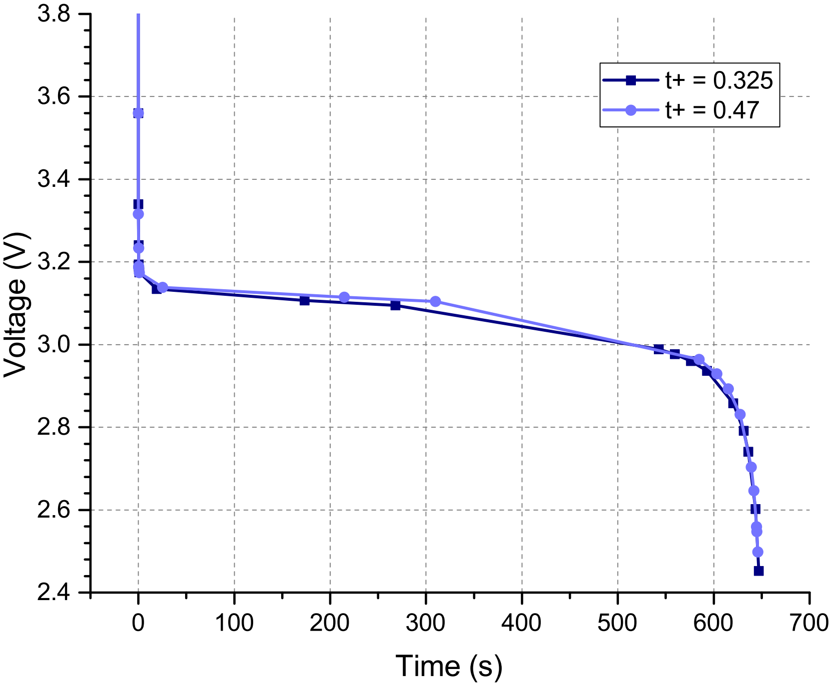

Figure 3.5. Effect of transport number on discharge at 5 C

Figure 3.5 for 5 C rate. In view of this, a constant transport number of 0.363 [73] is used in this work. Though the error of assuming a constant transport number is higher at 10 C, no dependence of transport number is assumed in the absence of data.

For temperature and concentration dependence of thermodynamic factor, an unmodified correlation for thermodynamic factor from [36] is used as is. This correlation is strongly sensitive to concentration and weakly to temperature. It is given by:

$$\left(1+\frac{\partial \ln f_{\pm}}{\partial \ln c_l}\right)\cdot(1-t_+) = 0.601\cdot[(1-0.399334\cdot c_l^{0.5} \\ +1.63394\cdot(1-0.0052\cdot c_l^{1.5}\cdot(T-294))] \quad (3.5)$$

Conductivity: electronic conductivity of the negative electrode has been assumed as 100 S m^{-1}. Graphite has a high electronic conductivity which ensures that the electronic conductivity of the negative electrode is not a limiting factor. This value has been measured and used in multiple references [74–76].

Positive electrode material, $LiFePO_4$, by itself is an electronic insulator with an inherent poor electrical conductivity of the order of $10^{-7}\,\mathrm{S\,m^{-1}}$. An effective way to increase the electrical conductivity is by carbon coating of the particles. In the cells used in this work, the positive electrode particles are not only carbon coated but some amount of conductive carbon is further added to the electrode to improve the conductivity. The conductivities depend on the carbon content of the electrode and increases to $2.1\,\mathrm{S\,m^{-1}}$ at 2.5 % carbon and $16\,\mathrm{S\,m^{-1}}$ at 4.75 % carbon with negligible temperature dependence [77]. In the present work, even with 8 % added carbon, a conservative value of $6\,\mathrm{S\,m^{-1}}$ is assumed for the conductivity. It is seen in literature that with widely different values of conductivity, the discharge curves have been fitted well. In the lower range such as in [78], a value of $3.3 \times 10^{-4}\,\mathrm{S\,m^{-1}}$ is used (fitted up to 5 C) while in [41] a value of $5 \times 10^{-3}\,\mathrm{S\,m^{-1}}$ is used (fitted upto 5 C). At the higher range, a value of $11.8\,\mathrm{S\,m^{-1}}$ is used in [79] (fitting up to 2 C). The effect of electronic conductivity on the charge discharge curves is similar to other parameters such as total ohmic resistance or reaction rate constants, which makes it difficult to determine the value accurately. The conservative value chosen, ensures that it is not a limiting factor, in the range of current rates studied.

Ionic conductivity of electrolyte (with $LiPF_6$ salt) depends on the specific electrolyte composition used. In [36] a temperature and concentration dependent correlation for PC:EC:DMC (10:27:63 v/v/v) is determined, which has a value of around $1.2\,\mathrm{S\,m^{-1}}$ at 1 M and 298.15 K. In [80], this equation was modified for EC:DMC (2:1 v/v), which gives a conductivity of $1.4\,\mathrm{S\,m^{-1}}$ for the same conditions. While in [72], using their correlation a value of $0.89\,\mathrm{S\,m^{-1}}$ is found for EC:EMC (3:7 w/w) under the same conditions. A concentration dependent correlation at 21 °C for EC:DMC (2:1 v/v) is used in [76], which gives a value of about $1\,\mathrm{S\,m^{-1}}$ at 1 M. While in [27] for EMC:DMC (1:1 w/w), the value is about $0.25\,\mathrm{S\,m^{-1}}$. In the present work, the electrolyte is 1 M $LiPF_6$ in EC:DEC (2:3 w/w) and a value of $0.771\,\mathrm{S\,m^{-1}}$ at 298.15 K and 1 M is given by the manufacturer. This solvent system was chosen taking into account working conditions below 0 °C. The content of EC is usually less than 50 vol%, and preferably around 30 vol%, because higher EC content causes its precipitation at low temperatures. The absence of DMC in the electrolyte is suspected to be the reason for its low conductivity. The temperature dependency of the electrolyte comes from [36]. The following correlation is used:

$$\begin{aligned}\sigma_l = 0.055 \cdot c_l \cdot [1.12 \cdot (&-8.2488 + 0.053248 \cdot T \\ &- 0.000029871 \cdot T^2 + 0.26235 \cdot c_l - 0.0093063 \cdot c_l \cdot T \\ &+ 0.000008069 \cdot c_l \cdot T^2 + 0.22002 \cdot c_l^2 - 0.0001765 \cdot c_l^2 \cdot T)]\end{aligned} \tag{3.6}$$

3.3.2 Thermal properties

Lumped thermal properties are calculated for the internal layers of the pouch cell. This approach, while less detailed than a full thermal model, ensures sufficient accuracy as will be seen later. Thermal conductivity (K) in the cell layers is anisotropic due to the effect of the stacking of cell layers. In the directions parallel to the cell layer, it is given by Equation 3.7, while in the direction perpendicular to cell layers (cell thickness direction), it is calculated using Equation 3.8.

$$K_{\parallel} = \frac{(L_{NC} \cdot K_{NC} + L_{NE} \cdot K_{NE} + L_S \cdot K_S + L_{PE} \cdot K_{PE} + L_{PC} \cdot K_{PC})}{L_{tot}} \tag{3.7}$$

$$\frac{L_{tot}}{K_{\perp}} = \frac{L_{NC}}{K_{NC}} + \frac{L_{NE}}{K_{NE}} + \frac{L_S}{K_S} + \frac{L_{PE}}{K_{PE}} + \frac{L_{PC}}{K_{PC}} \tag{3.8}$$

where
NC is the negative current collector
NE is the negative electrode
S is the separator
PE is the positive electrode
PC is the positive current collector

The density (ρ) and the specific heat capacity (C_p) of the composite is calculated as a volume average of the different cell layers through Equation 3.9 and Equation 3.10, respectively. In these equations using the thickness dimension (L) is equivalent to using volume as the other two dimensions are the same for all cell layer components. Lumped thermal properties for internal cell layers are tabulated in Table 3.2. Individual properties for each cell layer are discussed below.

$$\bar{\rho} = \frac{\sum_i \rho_i \cdot L_i}{L_{tot}} \tag{3.9}$$

$$\bar{C}_p = \frac{\sum_i C_{p,i} \cdot L_i}{L_{tot}} \tag{3.10}$$

Thermal conductivity: for the negative electrode graphite, a range of values from 1.04 $\mathrm{W\,m^{-1}\,K^{-1}}$ to 5 $\mathrm{W\,m^{-1}\,K^{-1}}$ [68, 69, 80, 81] are seen in the literature. The actual value of thermal conductivity should consider the presence of electrolyte in the pores. Thus, the value 4.21 $\mathrm{W\,m^{-1}\,K^{-1}}$ from [80] is used in the model. For the positive electrode, the range of values found are from 0.2 $\mathrm{W\,m^{-1}\,K^{-1}}$ to 5 $\mathrm{W\,m^{-1}\,K^{-1}}$ [68, 69, 82]. For this electrode, the additives affect this property. The value used in the model is from [82] as the composition of the the electrode in that work ($LiFePO_4$ + 7.5% PVDF + 7.5% C) is similar to the electrode used in this study (LiFePO4 + 8% PVDF + 8% C). For the separator, thermal conductivity is also taken from [80] because it considers an electrolyte filled value. In literature, values range from 0.3344 $\mathrm{W\,m^{-1}\,K^{-1}}$ to 1.21 $\mathrm{W\,m^{-1}\,K^{-1}}$ [68, 69, 80, 81].

Table 3.2. Thermal properties

Property	Unit	Negative current collector	Negative electrode	Separator	Positive electrode	Positive current collector
Thermal conductivity	$\mathrm{W\,m^{-1}\,K^{-1}}$	400	4.21	1.21	0.27	238
Density	$\mathrm{kg\,m^{-3}}$	8700	1861	1043	2300	2700
Heat capacity	$\mathrm{J\,kg^{-1}\,K^{-1}}$	385	845	1688	750	900

Densities: for the negative electrode, a range from $1347\,\mathrm{kg\,m^{-3}}$ to $2500\,\mathrm{kg\,m^{-3}}$, for positive electrode, from $1500\,\mathrm{kg\,m^{-3}}$ to $2310\,\mathrm{kg\,m^{-3}}$ and for separator, from $900\,\mathrm{kg\,m^{-3}}$ to $1200\,\mathrm{kg\,m^{-3}}$ are seen in literature [68, 69, 80–82]. The values chosen for simulation are from [80] for both negative electrode and separator. For the positive electrode a value of $2300\,\mathrm{kg\,m^{-3}}$ from [82] is chosen as the electrode composition is similar.

Heat capacities: a range of values from, $641\,\mathrm{J\,kg^{-1}\,K^{-1}}$ to $1437\,\mathrm{J\,kg^{-1}\,K^{-1}}$ for the negative electrode, $700\,\mathrm{J\,kg^{-1}\,K^{-1}}$ to $800\,\mathrm{J\,kg^{-1}\,K^{-1}}$ for the positive electrode and $700\,\mathrm{J\,kg^{-1}\,K^{-1}}$ to $1978\,\mathrm{J\,kg^{-1}\,K^{-1}}$ for the separator are seen in the literature [68, 69, 80–82]. The values used in the model come from [80] for the separator and negative electrode and from [82] for the positive electrode for the same reasons as discussed before.

3.3.3 Pouch properties

Pouch material is modelled consisting of three layers: polyethylene terephthalate (PET), aluminium and cast polypropylene (CPP). The properties for the pouch are determined from the individual values of these standard components in an approach similar to the lumping of the properties of the cell layers. Anisotropic conductivity in the parallel and perpendicular directions as well as the average density and heat capacity can be seen in (Table 3.3). The emissivity value is obtained from the calibration of the thermal camera with the thermocouple.

3.3.4 Parameters determined from charge and discharge experimental data

It is possible to determine some parameters mathematically from experimental data. The procedure to determine them has been described in the following paragraphs.

Table 3.3. Pouch properties

Pouch properties (calculated/measured values)	**Unit**	**Value**
Thickness	µm	150
Thermal Conductivity (length and breadth direction)	$\mathrm{W\,m^{-1}\,K^{-1}}$	79.45
Thermal Conductivity (thickness direction)	$\mathrm{W\,m^{-1}\,K^{-1}}$	0.26
Density	$\mathrm{kg\,m^{-3}}$	1645
Heat capacity	$\mathrm{J\,kg^{-1}\,K^{-1}}$	1233
Emissivity		0.95
Heat transfer coefficient on surface	$\mathrm{W\,m^{-2}\,K^{-1}}$	5

Volume fraction of the active material in the positive electrode: to determine this, it is assumed that at the end of discharge when the cut-off voltage (2.5 V) is reached, the lithium concentration in the positive electrode is maximum ($x = 1$). Thus, the positive electrode x changes from 0 to 1 during the battery discharge process. This is true in the case of the tested batteries for a battery as the negative electrode is oversized. For each electrode, the following equation holds true:

$$c_{s,max} \cdot \epsilon_s \cdot d \cdot \Delta x \cdot F = i \cdot t \tag{3.11}$$

where

$c_{s,max}$ is the maximum permissible concentration of lithium in the electrode
ϵ_s is the volume fraction of the solid phase
d is the thickness of the electrode
F is the Faraday constant
i is the current density
t is the duration of charge/discharge

Volume fraction for the positive electrode active material is determined to be 0.1805 based on experimentally determined time of discharge using the above equation using the data for discharge at 0.1 C.

Initial concentration and volume fraction of the negative electrode: the battery is charged using a CC-CV charging procedure. It can be assumed that at the end of this charging procedure, the lithium concentration in the positive electrode is zero ($x = 0$). The positive electrode has an non-varying potential for a large range of x while the negative electrode potential shows characteristic stage behaviour in graphite. At very low C rates such as 0.1 C the effect of polarization and ohmic resistance is low and it can also be assumed that the voltage curve of 0.1 C is approximately equal to the difference of the positive electrode equilibrium potential curve and the negative electrode equilibrium potential curve. With this assumption, the initial x and volume fraction are determined comparing graphically the equilibrium electrode potential curves with the discharge curve at 0.1 C and using Equation 3.11. A value of 0.46 for the volume fraction and 0.5 for the initial x is determined in an iterative process.

Some parameters are also determined from comparison between experimental and simulated discharge curves:

Diffusion coefficient: different values are found in literature for the graphite electrode. In [83] a concentration based diffusion coefficient is seen, which is also used in [84] with a good prediction of experimental results. Elsewhere concentration independent diffusion coefficient are used (in $\mathrm{m^2\,s^{-1}}$) : 9×10^{-14} [75] (worst value of [83]), 8×10^{-14} (model fit) [79], 3.9×10^{-14} [58], 3×10^{-15} [27], 2×10^{-14} [57] (fitted, temperature dependence), 5.5×10^{-14} [85].

In this work, this diffusion coefficient is determined by fitting the simulation for 10 C discharge to the experimental discharge curves at 10 C for the pouch cell. The effect of diffusion are apparent at high current rates. A value of 3.9×10^{-14} ($D_{n,0}$) is determined by parametric sweep. No concentration dependence is considered in the model but Arrhenius equation models dependence of the diffusion coefficient on temperature. The activation energy value is given in Table 3.1.

The negative electrode diffusion coefficient is given by:

$$D_n = D_{n,0} \cdot \exp\left(\frac{Ea_n}{R}\right) \cdot \left(\frac{1}{T_{ref}} - \frac{1}{T}\right) \tag{3.12}$$

Diffusivity of the electrolyte: electrolyte diffusivity depends on the electrolyte composition. Values (in $\mathrm{m^2\,s^{-1}}$) of 3×10^{-10} (EC:DMC:EMC 1:1:1, 1 M $\mathrm{LiPF_6}$) [79], 2×10^{-10} (EMC:DMC 1:1, 1.2 M $\mathrm{LiPF_6}$) [27] with temperature dependence, 7.5×10^{-10} (EC:DMC, $\mathrm{LiPF_6}$) [58], 1.3×10^{-10} (at 1 M $\mathrm{LiPF_6}$, 298K, EC:EMC) with temperature and concentration dependence [72] are seen in literature.

The temperature and concentration dependent equation given by [36] is used in this work. The correlation below simulates the results accurately and gives a value of $1.3 \times 10^{-10}\,\mathrm{m^2\,s^{-1}}$ at 1 M $\mathrm{LiPF_6}$ and 298.15 K

$$D_l = \frac{0.4 \cdot \left(10^{-4.43} - \frac{54}{T-(229+5\cdot c_l)} - 0.22 \cdot c_l\right)}{1000} \tag{3.13}$$

Diffusion coefficient of the positive electrode: diffusion coefficient of the positive electrode shows a much wider variation in literature, over eight orders of magnitude. One reason suggested in [56] is the difference in measuring technique. Various methods such impedance spectroscopy, current pulse, potentiostatic intermittent titration technique, galvanostatic intermittent titration technique, capacity intermittent titration technique, cyclic voltammetry have been used to measure it and the reported values in the literature range from $10 \times 10^{-14}\,\mathrm{m^2\,s^{-1}}$ to $10 \times 10^{-22}\,\mathrm{m^2\,s^{-1}}$. For simulations a constant value of $8 \times 10^{-18}\,\mathrm{m^2\,s^{-1}}$ is seen in [41], obtained through fitting of experimental data. Two different particle sizes are used in their work. In [56] a fitted value of $1.18 \times 10^{-18}\,\mathrm{m^2\,s^{-1}}$, with concentration and temperature dependence, is used. Prada et al.[27] used the value from [86] of $5.9 \times 10^{-20}\,\mathrm{m^2\,s^{-1}}$ even for high rate simulations even if in the original paper the value had been determined only for C/25 rate. Probably this low value is balanced by using a fitted values of current dependent radius. This idea is supported by the very small particle size values obtained by them using fitting. In [79] a constant value $6 \times 10^{-18}\,\mathrm{m^2\,s^{-1}}$ is used. A concentration and temperature dependent diffusion coefficient is used in [56, 57]. In this work, a concentration independent value of the diffusion coefficient ($D_{p,0}$), determined to be $2.2 \times 10^{-14}\,\mathrm{m^2\,s^{-1}}$ by comparing experimental and simulated curves. With the the activation energy value as in Table 3.1, the temperature dependent diffusion coefficient is given by:

$$D_p = D_{p,0} \cdot \exp\left[\frac{Ea_n}{R} \cdot \left(\frac{1}{T_{ref}} - \frac{1}{T}\right)\right] \tag{3.14}$$

Radius of the electrode particle size: in the cells in this study, where the negative electrode is over-designed, the positive electrode is the more critical electrode deciding battery performance and capacity when the limiting factor is diffusion of lithium in and out of the particles. Thus, in order to fit the simulation results to the experimental ones, only the radius of the positive electrode particle is adjusted for each C-rate for fitting purposes. This is unlike the approach followed in [27] where the radii of both positive and negative electrode particles are adjusted. The value of radius at 1 C discharge is arbitrarily fixed to the value provided by the manufacturer. This value is high compared to other $LiFePO_4$ electrode particle values found in literature. No current dependency of radius is required for the negative electrode to ensure a good fit. The value of radius of the graphite particle during discharge is fixed to the manufacturer's provided value. During charge, the fitted value of radius of the negative electrode is about 13% less than the one of discharge. All radii values can be seen in Table 3.4.

C-rate dependent radius is explained in [27] and [86] with the mosaic concept, first proposed in [87]. The trend of radii seen in this work, is similar to these published works, with a counter intuitive decrease in radius with increase in C-rate. Employing a current dependent radius can be understand as equivalent to simulating the actual particle size distribution (modelled in [41, 78]) that is present in the electrode. As current densities increase, smaller particles undergo large changes in concentration faster than bigger particles and hence influence the potential more. The cell may reach the cut-off potential due to increased over-potentials from the smaller particles [41, 87]. The large particles may also become unusable at high rates due to forming a lithium rich shell due to low diffusion rate inside the particle. The apparent average size of the particles seen at high rates is consequently smaller. This is further equivalent to using a current dependent diffusion coefficient [86] and this is shown in section 3.5.

Table 3.4. Radii of the electrode particles

Parameter	C-rate	Discharge	Charge
Radius negative electrode (µm)	all	4.5	3.9
Radius positive electrode (µm)	0.1 C	6.95	6.95
	0.2 C	6.95	6.5
	1 C	5.75	5.75
	2 C	5.12	5
	5 C	3.35	2.6
	10 C	3.25	2

The radius determined with this method is thus the apparent radius value that accounts for the particle size distribution (PSD). Since, PSD follows a bell shaped curve, one would expect a levelling off in the value of apparent radius at both very high and very low current densities. At high current densities it is because only the smallest particles are used up and the cut-off voltage is reached when they get filled up while at low current densities it is because all the particles of all sizes are completely used up. This behaviour is noticed in the curve in Figure 3.6, where its slope keeps decreasing as the current increases such that the radius determined at 5 C and 10 C are almost similar. Here the negative log of the current is plotted on the x-axis to visualize the ratio difference between the currents. The classic sigmoid nature of the particle size distribution can be observed in the nature of the curve.

Reaction rate constant: reaction rate constant of negative electrode: intercalation mechanism in graphite electrodes is well studied [88, 89]. In literature values range from $8.9 \times 10^{-12}\,\mathrm{m\,s^{-1}}$ to $5 \times 10^{-11}\,\mathrm{m\,s^{-1}}$ [57, 69, 79, 90]. A value of $6 \times 10^{-11}\,\mathrm{m\,s^{-1}}$ ($k_{n,0}$) is found to fit the discharge curves at both 0.1 C and 10 C. The temperature dependence is accounted for by the Arrhenius equation. With the activation energy value seen in Table 3.1, the reaction rate constant is given by:

$$k_n = k_{n,0} \exp\left[\frac{Ea_n}{R} \cdot \left(\frac{1}{T_{ref}} - \frac{1}{T}\right)\right] \tag{3.15}$$

The exact value of this variable is difficult to determine with the experimental charge discharge curves as its influence on the curves is similar to the total resistance or conductivities.

Reaction rate constant of positive electrode: For $LiFePO_4$ electrodes, rate constant is seen in literature to vary up to seven order of magnitude [27, 41, 56, 57, 63, 69]. Values of the order of 10^{-13} $\mathrm{m\,s^{-1}}$ were found in [57, 63]. An

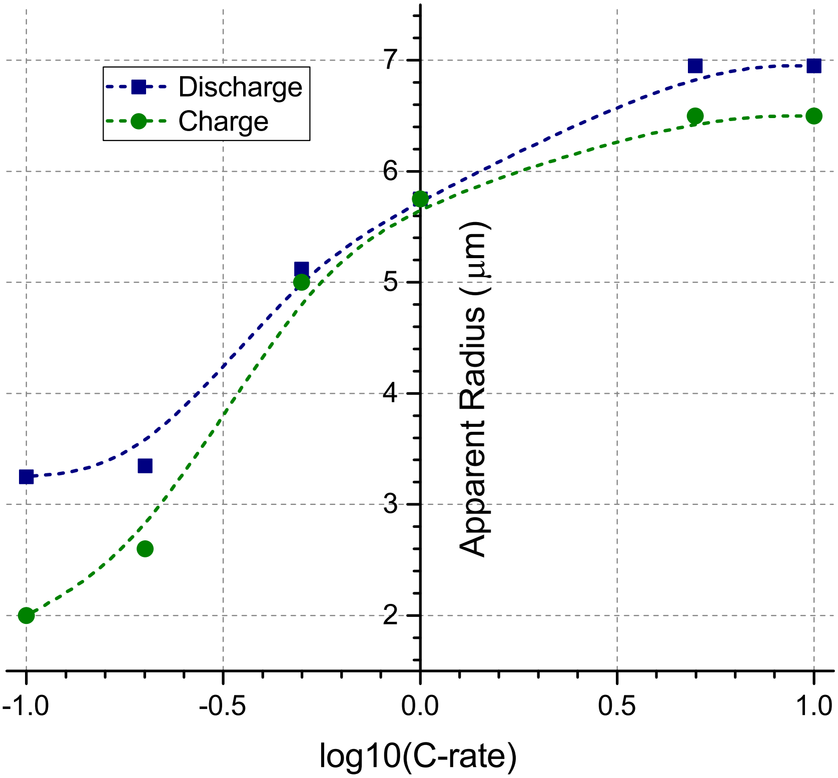

Figure 3.6. Apparent radius as a function of C-rate during charge and discharge

empirical current dependent correlation is used in [56]. A concentration dependent value is used in [69], which makes the rate constant vary from $1.4 \times 10^{-14}\,\mathrm{m\,s^{-1}}$ at $x = 0$ to $6.97 \times 10^{-14}\,\mathrm{m\,s^{-1}}$ at $x = 100$.

In this work, no concentration dependence is modelled. Simulations with the values found in literature do not fit the discharge curve at 10 C discharge current. Reaction rate constant value of $1 \times 10^{-9}\,\mathrm{m\,s^{-1}}$ is determined from parametric sweep by comparing experimental and simulated discharge curves. The temperature dependence is modelled through the Arrhenius equation using the activation energy value seen in Table 3.1. The reaction rate constant is given by:

$$k_p = k_{p,0} \exp\left[\frac{Ea_n}{R} \cdot \left(\frac{1}{T_{ref}} - \frac{1}{T}\right)\right] \tag{3.16}$$

Fast kinetics of lithium ion transfer reaction is suggested in [91] where an area independent value of about $2 \times 10^{4}\,\mathrm{s^{-1}}$ is found as the rate constant which yields a value of the order of 10^{-9} $\mathrm{m\,s^{-1}}$ for the porosity and particle size of the $LiFePO_4$ electrode used in this study.

Table 3.5. Calibrated values

Quantity	**Unit**	**Negative electrode**	**Electrolyte**	**Positive electrode**
Diffusion coefficient	$m^2\,s^{-1}$	3.9×10^{-14}	1.3×10^{-10}	2.2×10^{-14}
Reaction rate constant	$m\,s^{-1}$	6×10^{-11}		1×10^{-9}
Initial SOC (Fully charged)		0.5		0.00001
Solid phase volume fraction		0.46		0.1805
Total ohmic resistance	$\Omega\,m^2$	0.037		

Total resistance: to account for the contact resistances and the film resistances at both the electrodes, an additional resistance is used as the final fitting parameter. It represents the film resistance on the negative electrode given that the dominant resistance effect is from the SEI growth at this electrode. As discussed before, this resistance gives an additional potential drop in the cell and is a heat source in the thermal model. The fitted value of this parameter can be seen in Table 3.5.

3.4 Model validation

Electrochemical validation of the battery model is carried out using the set of properties determined through prior knowledge and literature, experiments and fitting. These properties are tabulated in Table 3.1, Table 3.2, Table 3.3, Table 3.4 and Table 3.5. The fitted values are mostly determined using only discharge curves except for the current dependent radii and hysteresis factor. Moreover, even in case of discharge, except for the current dependent radii, only the 0.1 C and the 10 C curves are sufficient to fully parametrize the model.

A battery generates significant heat at higher C rates leading to an increase in temperature. To check if the temperature dependence is properly accounted for the different parameters, thermal validation is carried out for 2 C, 5 C and 10 C rates along with the electrochemical validation for 0.1 C, 0.2 C, 1 C, 2 C, 5 C, 10 C. Thermal validation is also an additional check for other parameters used for modelling. It increases the confidence level in the value of some parameters and thermal correlations used in the model of the cell. This will be demonstrated later in the chapter.

3.4.1 Discharge and charge validation

From Figures 3.7a, 3.7b, 3.7c, a good match between experimental and simulated discharge curves at all C rates can be seen. At low rates (0.1 C and 0.2 C), the voltages seen are very near to the difference in the electrochemical potentials of the two electrodes. The simulated curves follow the experimental curves closely throughout the full discharge. The nature of the experimental curve not captured in the model is the step change in the potential that are visible around 10 000 s in

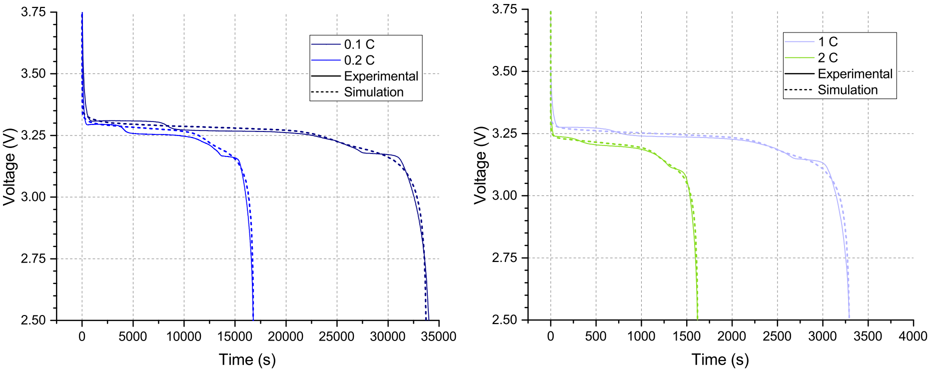

(a) Electrochemical validation at 0.1 C and 0.2 C

(b) Electrochemical validation at 1 C and 2 C

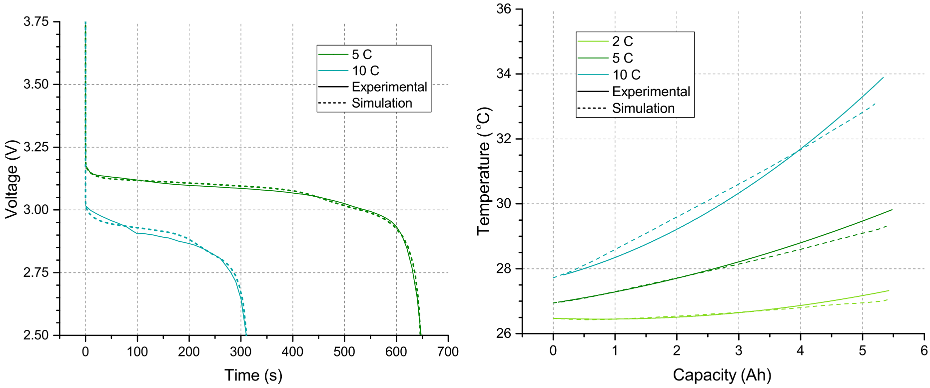

(c) Electrochemical validation at 5 C and 10 C

(d) Thermal validation at 2 C, 5 C and 10 C

Figure 3.7. Discharge curve validation results

0.1 C and 5000 s in 0.2 C, respectively. This is due to a smoothed negative electrode potential fitting curve given by Equation 3.2. The $FePO_4$ to $LiFePO_4$ phase transition leads to a flat potential plateau so all the steps observed in the discharge curve of the pouch cell can be ascribed to the negative electrode. One of the most important characteristics of graphite is the stage intercalation of lithium. The stages that are observed in the curve of the experimental data are due to the typical multi-step lithium intercalation/de-intercalation process within the graphene planes of graphite [92, 93]. The potential of de-intercalation (during cell discharge) differs depending on the stage. The phase boundary movement is initially determined by the rate of the inter-facial electrochemical reaction and is controlled thereafter by a diffusion process. Lithium diffusion from the interior of the negative electrode to the electrode-separator interface is rate-limiting. As a consequence, the stages are more evident at low C-rates and tend not to be

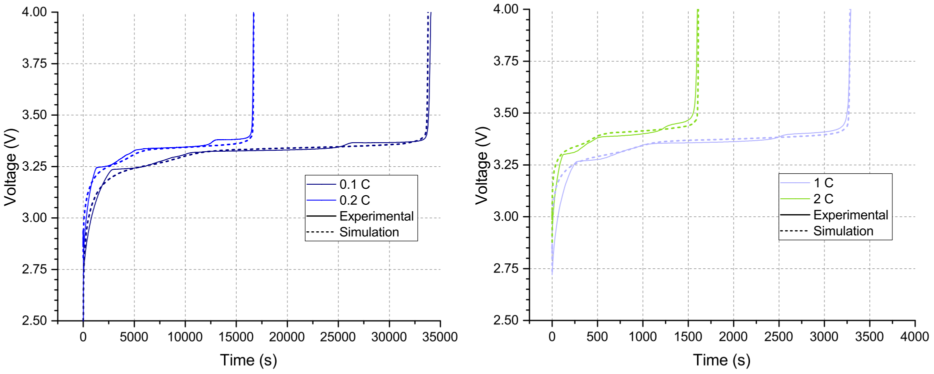

(a) Electrochemical validation at 0.1 C and 0.2 C

(b) Electrochemical validation at 1 C and 2 C

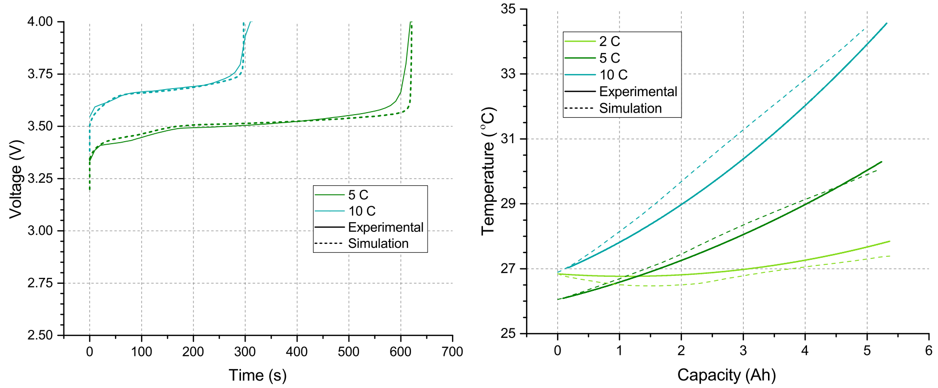

(c) Electrochemical validation at 5 C and 10 C

(d) Thermal validation at 2 C, 5 C and 10 C

Figure 3.8. Charge curve validation results

evident at higher rates. At medium rates (1 C and 2 C), effects of over potentials and resistance are seen on the discharge curve where the voltage is reduced from the equilibrium value. The simulated discharge curves match the experimental curves well, not only during the constant potential phase, but also towards end of the discharge. The model predicts the voltage satisfactorily also at 5 C and 10 C rate however deviation from the experimental curve becomes greater with increasing current rate. During discharge, the heat generated by the reactions and the current flow causes the temperature to go up. Arrhenius dependence of diffusion and reaction rate phenomena on temperature causes these properties to change during the discharge process. Good high rate electrochemical predictions of the model increase the confidence in the thermal correlations chosen for these properties of the cell.

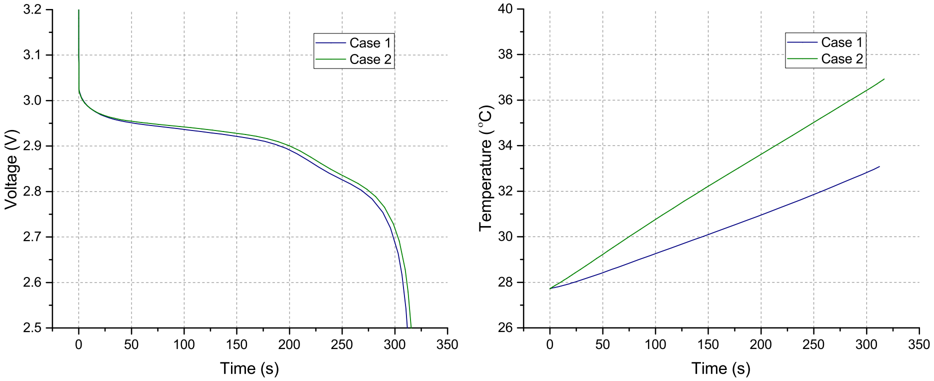

(a) Voltage during discharge (b) Temperature during discharge

Figure 3.9. Additional validation from the thermal model

Validation results during charging can be seen in Figure 3.8 . All parameter values except radii of the electrodes and hysteresis factor h are the same as discharge. The simulated voltage curves in Figures 3.8a, 3.8b, 3.8c follow the experimental ones closely for all C rates and the total charge times are also predicted well. One interesting detail to notice in the case of 5 C and 10 C is the shape of the curve towards the end of charge. While at lower C rates, in experiments, the voltage shoots up immediately, at 5 C and 10 C, the voltage rise is less sharp. The voltage, simulated by the model, however shoots up sharply also for 5 C and 10 C as for the other C rates. In case of high C rates, the reason for the slope at the end of charge needs to be better investigated. However apart from this, the voltages are predicted well by the model for all C rates. The steps seen in the experimental curves specially at low C rates caused due to staging in graphite electrodes is not captured in the model due to the smoothing process caused by the curve fit of graphite potential as also seen during discharge.

The additional validation from the thermal model is seen in Figure 3.7d and Figure 3.8d. The rise in temperature of the complete pouch, based on the actual conditions of the testing environment, is predicted quite well. An under-prediction is seen towards the end of discharge at all C rates, and a slight over prediction is noticed at the end of charge. Though the thermal modelling is at best a limited approximation of the real process of heat transfer, the predictions of temperature during charge and discharge are quite accurate.

3.4.2 Validity of Parameters

Volume fraction and initial concentration values for the electrodes used in the model are expected to be quite accurate as they can be logically determined from the experimental curves by a combination of graphical and analytical methods.

Due to their similar effect on the voltage curve, the values of total resistance as well as rate constants are difficult to entangle from each other. However, thermal validation gives more confidence in the parameter values selected for the model. To demonstrate this, consider that with $k_{neg} = 6 \times 10^{-12}\,\mathrm{m\,s^{-1}}$, a value at the lower spectrum of literature values along with a lower value of resistance $= 0.019\,\Omega\,\mathrm{m}^2$, a discharge curve similar to the one (Case I) with optimized parameters (Figure 3.9a) is obtained. However, the temperature increase seen with these parameters (Case II) is much higher than Case I (Figure 3.9b). Thus, the values chosen for the total resistance and k_{neg} in the optimized model are a more accurate choice due to the additional thermal validation.

Regarding the diffusion coefficient of the negative electrode, most values in literature are of the order of 10^{-14} $\mathrm{m\,s^{-1}}$. The fitted values falls into the range as well, assuring its validity. Moreover, the charge and discharge curves when simulated with values of this order of magnitude do not vary, signifying that it is not the limiting factor for this cell at the current rates tested. With smaller $LiFePO_4$ particles or larger graphite grain size or greater thickness of negative electrode or at high C rates, the cut-off voltages can be due to diffusion limitation in the negative electrode [75].

Electrolyte diffusivity values in literature are of the order of 10^{-10} $\mathrm{m^2\,s^{-1}}$. The value determined is also in this range though at the lower end. This low value is due to choosing a EC:DEC based electrolyte for low temperature performance, instead of a one based on DMC [94].

Values of parameters of the $LiFePO_4$ electrode, namely diffusion coefficient and rate constant, which have a large range of values in literature, were seen to be on the higher side of the literature median. This can be due to ignoring the physical process of phase separation in the positive electrode and approximating it with the P2D approach. Often, nano-sized $LiFePO_4$ are used in batteries to ensure short diffusion lengths [50, 95]. In the cell modelled here, the particle size is in micrometer range. The experimental evidence of the cell being able to sustain high rate charge and discharge even with a large particle size, points to $LiFePO_4$ having an intrinsically high diffusion coefficient and high rate constant. The low rate capability of this material, reported in some works [49, 75], is due to low conductivity of pure $LiFePO_4$. To resolve the problem of low conductivity, the $LiFePO_4$ particles used in this work are carbon coated. Moreover additional carbon has been added to the electrode.

The radii of the electrode particles are not considered as a constant value in the model for the purpose of fitting of curves. D50 values of the particles of the electrodes obtained from the manufacturer were arbitrarily fixed for 1 C discharge. The apparent values of positive electrode radii determined from fitting do not represent the actual radius value of particles but instead, as explained before, represent the particle size distribution present in the positive electrode.

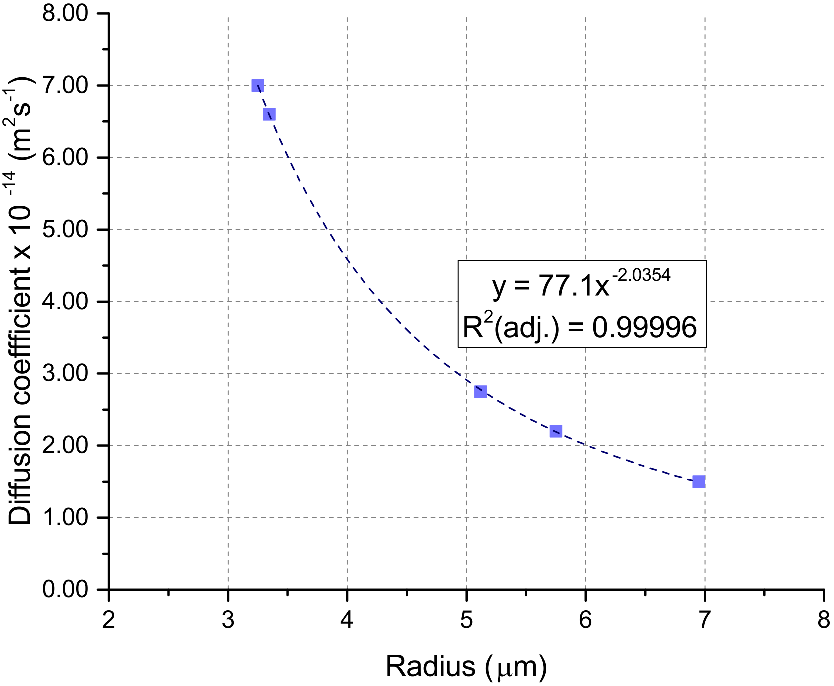

Figure 3.10. Correlation between current dependent radius and current dependent diffusion coefficient

3.5 Equivalence between current dependent radius and diffusion coefficient

It is found that the model simulated with a fixed value of radius of positive electrode particle but with a current varying diffusion coefficient value for this electrode is equivalent to the approach used in the work, which is to fix the diffusion coefficient and vary the particle radius. On plotting the unique values of diffusion coefficient during discharge at each current rate in this new approach with the radii values obtained in the original approach, a power 2 correlation is seen in the nature of the values (see Figure 3.10). Similar behaviour is expected for charge simulations.

This power correlation can be explained looking at the particle boundary condition:

$$-D_s \cdot \left.\frac{\partial c_s}{\partial r}\right|_{r=r_p} = -\frac{\nabla \cdot i_s}{F \cdot a_v} \tag{3.17}$$

where,

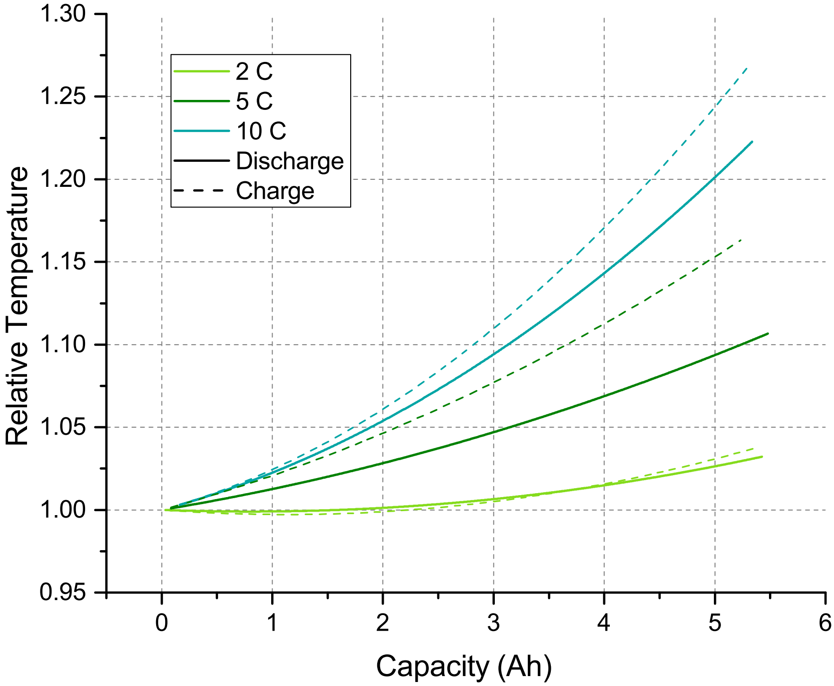

Figure 3.11. Relative temperature difference between charge and discharge from experimental data

$$a_v = \frac{3 \cdot \epsilon_s}{r_p} \tag{3.18}$$

Thus, there is equivalence in using a current dependent radius with constant diffusion coefficient and a current dependent diffusion coefficient with a constant radius value. In [86], it is seen that only particle radius can be independently adjusted, if constant values of diffusion coefficient and surface resistance are set.

3.6 Thermal behaviour during charge and discharge

Analysing the experimental data of charge and discharge, it is noticed that at high C rates (5 C and 10 C) the pouch cell is at a higher temperature during charge compared to discharge (Figure 3.11). This is unlike other lithium-ion chemistries where temperature during discharge is higher than temperature during charge. This emphasizes the importance of having an accurate charge model for $LiFePO_4$ as it represents a worse thermal condition than discharge of the battery.

P2D models allows the heat generation to be studied separately for all cell

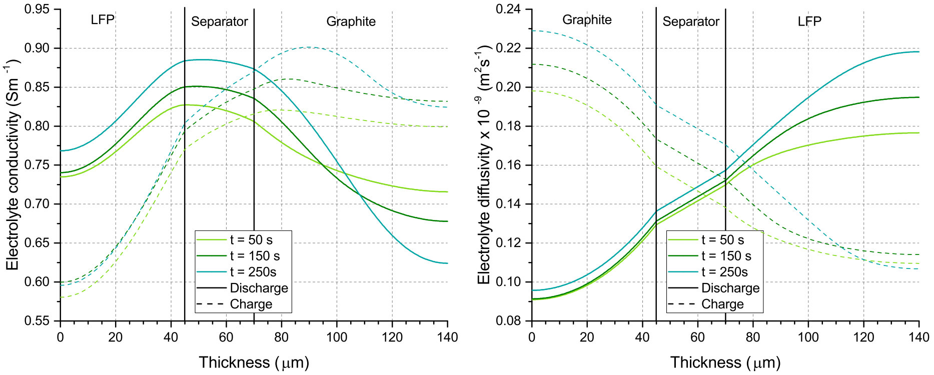

(a) Conductivity (b) Diffusivity

Figure 3.12. Variation of electrolyte properties along thickness for three different times during 10 C charge and 10 C discharge

layers and from all sources inside the cell. In the current collectors, the only source of heat is from ohmic heat due to conduction of electrons from the tabs to the electrodes. This remains the same during charge and discharge. Thus, the discussion on thermal behaviour in this work takes into account the heat generation only in the porous electrodes and the separator layers of the battery. In the separator region, the source of heat is irreversible in nature due to conduction of ions through the electrolyte from one electrode to another. However, due to different electrolyte concentration and overall temperature difference between charge and discharge, the generated heat during charge and discharge are different. Properties of the electrolyte such as electrolyte conductivity and diffusivity which are dependent on concentration and temperature can vary significantly between charge and discharge. Figures 3.12a and 3.12b show the variation of electrolyte conductivity and diffusivity, respectively at three moments (50 s, 150 s, 250 s) during a 10 C charge and discharge in the three battery layers. This variation in electrolyte properties affects not only the heat generation in the separator but also in the porous electrodes.

In the electrode region, apart from the difference in electrolyte properties affecting heat generation, kinetics of reaction and solid phase diffusion coefficients are different during charge and discharge[84, 96]. As lithium is exchanged between the electrodes, it causes ever changing lattice arrangements of the electrode particles with different entropies. The first phenomenon due to kinetics and diffusion coefficients in the electrodes gives rise to irreversible heat and is exothermic. The different radii fitted for charge and discharge in the model account for this difference of irreversible heat between charge and discharge. The other heat source that is due to changes in the order/disorder of the crystal

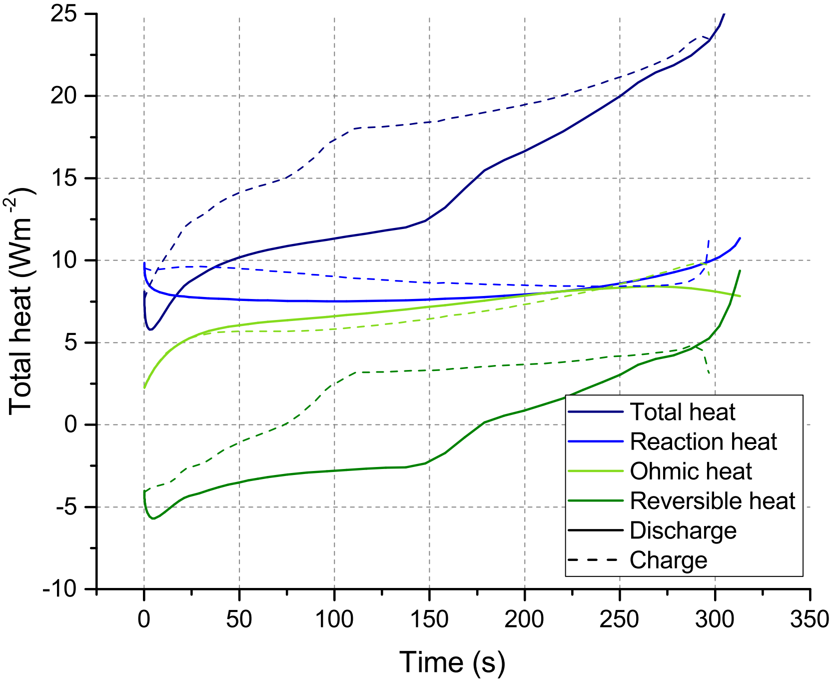

Figure 3.13. Instantaneous heat generation in cell at 10 C during charge and discharge

lattice is a thermodynamic property of the material and is reversible. It can be both exothermic and endothermic. This is included in the model through entropic coefficients of the electrodes.

In Figure 3.13, the relevant contributions of reversible and irreversible heats (further divided into ohmic heat and reaction heat) from the battery layers, as well as their sum (the total heat) are plotted for 10 C charge and discharge. The total heat for both charge and discharge is positive, which signifies that the process is exothermic. It is consistent with the rise in temperature measured for the battery (Figure 3.11). It can also be noticed that the curve for total heat for charge is for the most part higher than that for discharge, also consistent with the higher temperature seen for charge as compared to discharge. Looking at individual processes, reaction heat contributes the maximum to the exothermic heat for both charge and discharge. However, the difference between charge and discharge is not very high. The same is true for ohmic heat, which is low in the beginning but catches up with reaction heat towards the end of both charge and discharge.

A clearer view can be obtained from Table 3.6 where the area under the curve for Figure 3.13 is tabulated. The area is the summation of the heat generated during the whole duration of charge and discharge. For irreversible heat, the difference in

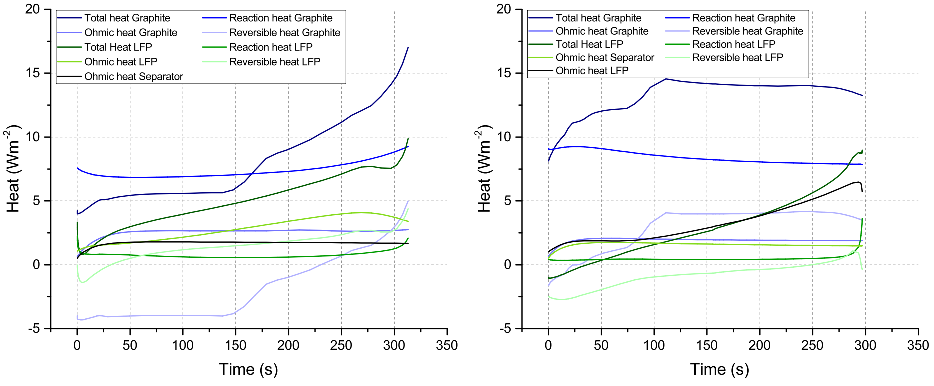

(a) Discharge (b) Charge

Figure 3.14. Instantaneous heat generation in cell layers at 10 C

Table 3.6. Total heat generation at 10 C

10 C	Reversible heat (J m^{-2})			Irreversible heat Reaction + Ohmic (J m^{-2})				Total heat (J m^{-2})
	Graphite	LFP	Total	Graphite	LFP	Separator	Total	
Discharge	-582	453	-129	2309+801	237+880	0+533	4760	4631
Charge	866	-246	620	2497+571	142+970	0+469	4649	5269

the area under the curve for discharge and charge is about +2.3 %. All numbers compared here are calculated relative to discharge process and the plus sign signifies that the discharge value is larger than the charge value. Considering the area under the curve for the total heat, it can be seen that 10 C charge produces about 13.8 % more heat than 10 C discharge leading to a temperature difference of about 1 °C for the specific battery tested in this work. The difference in the percentages can thus be ascribed to the reversible heat. Reversible heat, through much less in magnitude than irreversible heat, casts a substantial influence on the total heat generation even dictating the shape of the curve for total heat generation. It can be seen that the reversible heat for both charge and discharge is endothermic at first but becomes exothermic at a certain point. However, the switch from heat consumption to heat generation is sooner for charge than for discharge. In fact, due to the nature of the lithium arrangement in these electrodes, the total reversible heat during discharge is endothermic, while in the case of charging it is exothermic.

Further investigation into individual electrode behaviour (seen in Figure 3.14) reveals that the graphite electrode produces more heat than $LiFePO_4$ electrode for both charge and discharge. The difference is much more for charge. Ohmic heat production difference between charge and discharge is not highly variable with time. A difference of +12 % for separator, +28.7 % for graphite and -10.2 % for

$LiFePO_4$ is seen between charge and discharge, with the total difference for the battery being +9.2 %.

Reaction heat generation in graphite is much more than in $LiFePO_4$ for both charge and discharge. The kinetics of $LiFePO_4$ electrode are seen to be faster compared to the graphite electrode for this cell. Though pure $LiFePO_4$ is known to have low rate capability because of its intrinsic low conductivity [75], modified electrodes such as nano-structured particles, carbon added and carbon coated $LiFePO_4$ electrodes have been found to show good rate capability at high C rates [97, 98]. The difference in reaction heat between charge and discharge is -8.1 % for graphite and +4 % for $LiFePO_4$.

Looking at the reversible heat, it can be seen that during discharge, graphite electrode consumes heat for half of the time, leading to a net negative value seen in Table 3.6. During charge, even though $LiFePO_4$ consumes heat almost throughout the whole duration of charge, the greater exothermic process of graphite intercalation leads to a net positive value for the cell. At lower C rates, this battery chemistry produces very less heat, leading to very little rise in temperatures from the ambient. The entropy change at low C-rates in different electrodes and electrode pairs is studied in [70] and the $LiFePO_4$-graphite combination is found have low overall heat generation because of cancellation of reversible heats of both electrodes. The relative contribution of reversible heat due to entropy changes gets weaker as C-rate increases, and irreversible losses increase much more in comparison to reversible losses. This is the reason why temperature difference between charge and discharge is higher at 5 C than at 10 C.

Chapter 4

Application of the electrochemical-thermal model

Lithium-ion batteries are sensitive to temperature and have a narrow optimal operating range of temperature. At low temperatures, their performance suffers due to slower rate of kinetic and diffusion phenomena [99]. Propensity for lithium plating also increases at lower temperature [100, 101]. At high temperatures, although these batteries have a better performance, their lifespan gets compromised [102, 103]. This is because of increase in the rate of undesirable side reactions in the cell as well as the faster growth of the surface layers such as the SEI layer [100, 103, 104]. At very high temperatures, there is a risk of thermal runaway [105]. Organic electrolytes normally used in these batteries are inflammable. An overview of the different thermal issues in a lithium ion battery can be seen in [106], while quantification of aging at different temperatures has been carried out in part II of this work for a NMC battery.

To ensure safety and long term performance, lithium ion batteries must be kept within their optimal temperature range. A control over temperature ensures a balance between performance and service life, which in turn dictates the costs and safety of using this technology. This control is made possible using thermal management systems (TMS). TMS can be classified into active and passive systems depending on whether they need an energy input or not [38, 107–110].

4.1 Module, packs and thermal management systems

For many applications of lithium-ion batteries such as grid storage and electric vehicles, a number of cells are connected in series and parallel in modules and packs to cater to the energy and power needs of the application. Thermal issues can get aggravated in case of modules and packs where thermal gradients between different cells also need to be minimized in addition to keeping the individual cells in the optimal temperature range. Large thermal gradients between cells cause

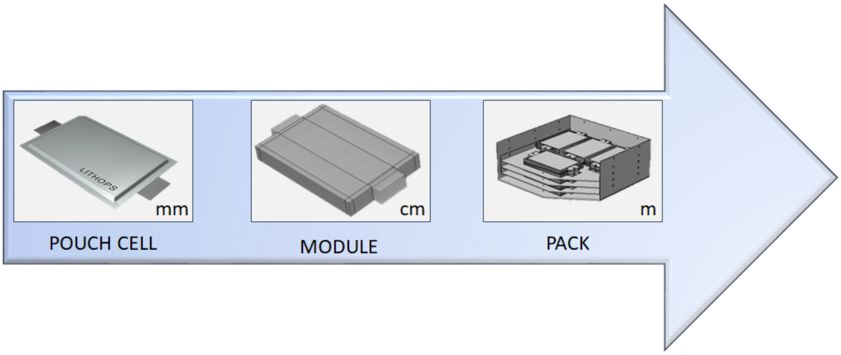

Figure 4.1. Bottom-up modelling direction

them to have different performances, which in turn leads to electrical balancing issues and overall greater degradation in these cells [107]. There is a need for accurate heat generation models applied at this scale to ensure good prediction of the temperatures and gradients in the modules and the packs, not only in order that the TMS can take corrective action during the operation but also to make sure that the TMS is properly sized and designed.

There are different approaches to calculate heat generation in the battery. These approaches are empirical, semi-empirical and theoretical [38, 111–113] depending on how much of the model is based on physical laws. The choice of the thermal model for any application depends on the requirements of accuracy and computation speed.

An online thermal management system such as in a vehicle or a home storage system needs quick estimates of the temperatures. The computing resources that are made available for such systems are limited due to cost and size restrictions. Thus, such systems usually rely on simple empirical models. For the purpose of designing a TMS, computation costs are less important while accuracy takes centre-stage. Here, the semi empirical [114–116] and the theoretical approaches [38, 117] offers the most benefit due to the ability to simulate transient nature of battery operation.

In this chapter, the focus is on demonstrating the utility of the P2D model developed in the last chapter to design and evaluate different cooling system solutions. The physics based electrochemical model of the cell has been coupled with a thermal and fluid-dynamics model in order to study pack thermal behaviour. The challenge of this approach is to adapt the physics based model developed at the cell level to the pack level. Some physics based multi-scale modelling approaches in literature can be found in literature. In [118], the particle to the cell domain are modelled. In [119], modelling extends from pore to the battery stack level. An electrochemical model and a lumped thermal model for a cell are used to simulate a battery pack in [120].

In this work, the P2D electrochemical model developed and validated in the last chapter is used to estimate the heat generation for the pack. The accuracy of this model at the pouch cell level has been demonstrated in the last chapter. The thermal model is extended from pouch cell to module and pack level. The extent of the scale of modelling is shown in Figure 4.1.

Apart from the higher accuracy, the advantage of this modelling approach is that it allows simulations for any design change in the model. Possible changes can be made at any level of modelling, be it battery chemistry at the particle level or thickness (or any other dimension) of any layer of the battery or the number of batteries in a module or the pack design or the TMS design. Different environmental or operating conditions can also be simulated to see their effect on the performance of the complete pack.

4.2 Scope of the study

The modelling approach followed for pack simulations allows a lot of flexibility in modifying the model. The case study presented in this chapter is restricted in its scope to designing and studying different cooling system solutions. The module and the pack designs are fixed in the study. However, to demonstrate the flexibility of the model, an example with low level changes at the module level is shown later in the chapter. The cell used in the study is the one modelled in the last chapter.

To allow comparability, the operating and the environmental conditions for all simulations presented in this chapter are the same. Worst-case operating condition for the pouch cell is chosen for the simulations. As discussed before, it is for 10 C charge. Simulating a 10 C charge from 0 to 100 % SOC represents a realistic goal for cases such as in electric vehicles. Fast charging is an important feature for the success of these vehicles as it alleviates range anxiety. A 10 C charge would mean getting the batteries charged from zero to full in 6 min. From a thermal point of view in an electric vehicle, continuous high rate charging represents a more demanding case than any typical transient charge discharge driving cycle. The ambient temperature for all simulations in this study is 25 °C.

4.3 Module modelling

A module consists of a number of cells connected together in series and parallel. In this case study, the module consists of six pouch cells stacked on top of each other as seen in Figure 4.2a. Electrically, they are connected in parallel. In order to simulate the thermal behaviour of the module in a reasonable time, first the geometry of the module in the model is simplified. Second, the equivalent thermal properties of the simplified module are calculated using an optimization procedure.

One way to determine the equivalent properties is analytically as in the case of pouch cells (see Section 3.3.1). However, a different approach is developed here to determine properties for the equivalent module which accurately simulates the

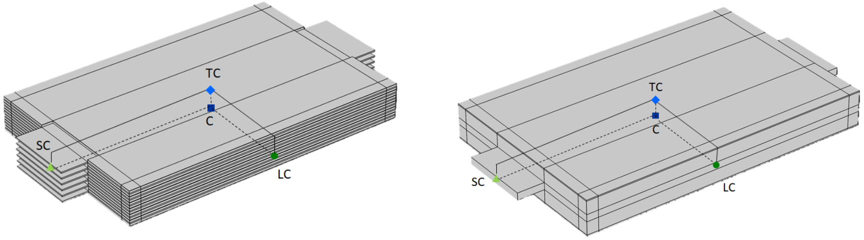

(a) Full module (b) Equivalent module

Figure 4.2. Module with probe elements

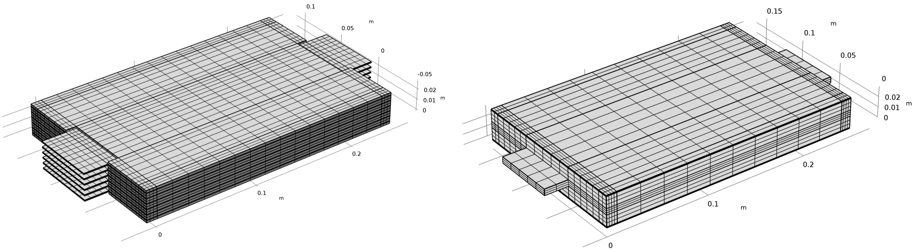

(a) Full module mesh (b) Equivalent module mesh

Figure 4.3. Mesh and dimensions

full module. The equivalent module can be seen in Figure 4.2b. It has the same major dimensions as the full module. The current tabs at the ends in the equivalent module are pressed together unlike the full module.

In order to determine the equivalent thermal properties of the module, first the 10 C charge conditions are simulated for the full module in an ambient temperature of 25 °C assuming only heat losses by radiation. Here each pouch cell of the module is considered as a separate thermal unit. Temperature is probed in some points of the domain of the full module during the simulation. The chosen probe points are placed the middle of the module (C), in the middle of the top surface (TC), the middle of the long side face (LC) and in the middle of the short size face (SC), just before the connecting tabs. This configuration is chosen in order to best represent the temperature distribution in the module surface and interior. In Figure 4.2a the placement of the probe points for the temperature for the full module can be seen.

Since the overall dimensions of the full module and equivalent modules are the same, the probe points are placed in the same positions also for the equivalent module (Figure 4.2b). The electrochemical-heat transfer problem is solved for the same environment and operating conditions with volume-averaged density, heat

Table 4.1. Equivalent properties for the simplified module

Property	**Unit**	**Value**
Conductivity x	$\mathrm{W\,m^{-1}\,K^{-1}}$	103.15
Conductivity y	$\mathrm{W\,m^{-1}\,K^{-1}}$	49.6
Conductivity z	$\mathrm{W\,m^{-1}\,K^{-1}}$	1.9744
Specific heat capacity	$\mathrm{J\,kg^{-1}\,K^{-1}}$	1284.7
Density	$\mathrm{kg\,m^{-3}}$	2142.4

capacity, and thermal conductivities (anisotropic) of the equivalent module. The mesh for the full module and the equivalent module can be seen in Figure 4.3.

An objective function is defined as follows:

$$f(k_x, k_y, k_z, C_p, \rho) = \left(T_C^{eq} - T_C^{full}\right)^2 + \left(T_{TC}^{eq} - T_{TC}^{full}\right)^2 + \left(T_{LC}^{eq} - T_{LC}^{full}\right)^2 + \left(T_{SC}^{eq} - T_{SC}^{full}\right)^2 \quad (4.1)$$

where
f =objective function
k = conductivity in 3 directions (x,y,z)
C_p = heat capacity
ρ = density
T = temperature at probe point in equivalent/full model

The optimization problem is to minimize the objective function by varying the volume-averaged density, heat capacity, and thermal conductivities (anisotropic) of the equivalent module. Optimization is carried out using Nelder-Mead method. The equivalent properties found out are seen in Table 4.1 This process is carried with the following two assumptions:

(A) The four probe points are enough to accurately capture the thermal behaviour of the the battery module. The choice is motivated by the fact that these points represent the highest temperature of the module (usually at the centre of the module) as well as the gradients in all directions (the other three points that are located on the peripheries).

(B) The full and equivalent modules have similar thermal behaviour also in conditions different than the ones used for the optimization. This assumption needs to be further investigated in order to ensure its applicability. Since in the present case, the operating conditions of the optimization and the ones used for final pack level simulations are similar, this assumption is obviated.

In Figure 4.4, results for a temperature increase for 10 C charge rate are

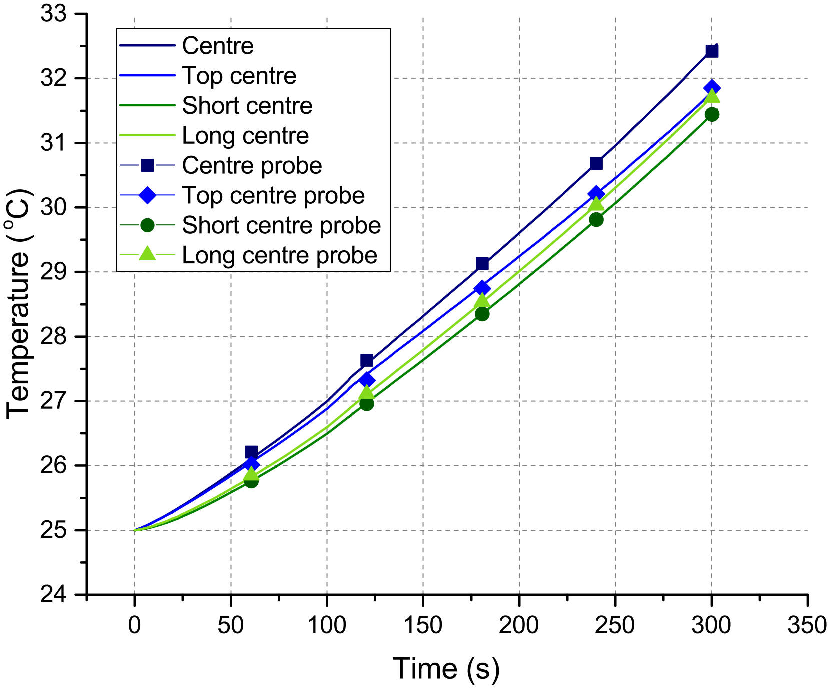

Figure 4.4. Probe temperature comparison for the full and the equivalent modules - symbols represent the probes in the equivalent module

compared for a full model and an equivalent model. As can be seen, the equivalent model captures the behaviour of the full module at the four probe points accurately.

The four probe point optimization procedure is effective in capturing the temperature profile of the full module not just at the four points where the temperature is probed, but over the entire module as can be seen in Figure 4.5. With this reduction approach, the simulation time is reduced by 75% with little decrease in accuracy of the temperature predictions.

4.4 Pack modelling

A battery pack is assembled by connecting modules together in series or parallel. The pack architecture (CAD) used for this case study can be seen in Figure 4.6a. The pack design comes from the project Ca(r)vour [1]. No cables and auxiliary battery systems are simulated in this study.

---

[1] Automotive Project financed by European Regional Development Fund 2007/2013 for Piedmont

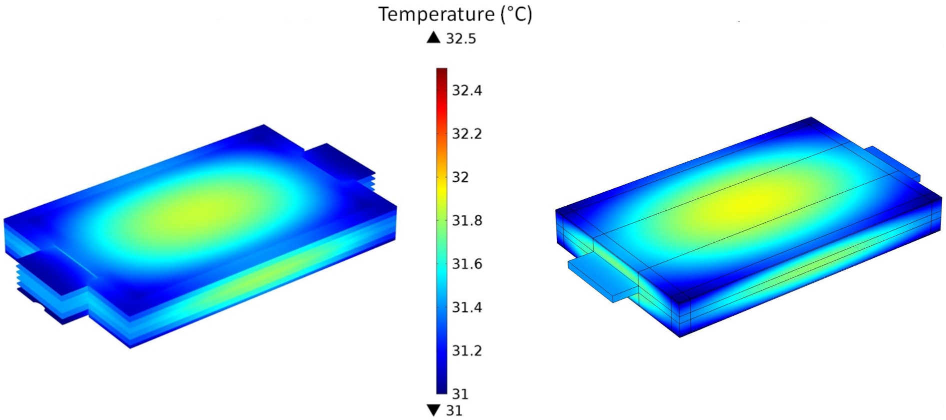

(a) Full module

(b) Equivalent module

Figure 4.5. Module temperature comparison

The pack consists of 16 modules divided in 4 similar compartments stacked one on top of the other. Each compartment is separated by another using aluminium plates. The middle two compartments are thermally more isolated from the environment than the ones at the periphery and are more critical for the TMS. Hence in certain TMS design cases only one of these compartments are simulated with symmetry conditions imposed on the top and bottom surface. This allows faster computation of the temperature profiles in the battery pack.

The pack design is also simplified in order to facilitate meshing and computation. The overall dimensions and the weight of the pack are kept the same. The modules are replaced by their equivalent. Other surfaces are smoothed for easier meshing. The simplified pack design can be seen in Figure 4.6b.

To mesh the simplified pack design, a combination of hexahedral and prism elements are used. Hexahedral elements are used to mesh the modules while triangular prism elements are used for the support plates and the external casing. The mesh for the pack can be seen in Figure 4.7. Similar to the case of the pouch cell, the high aspect ratio causes the mesh quality to deteriorate. A direct solver is used to ensure robustness of the solution.

4.5 Cooling system simulations

The most popular cooling systems currently being used for battery packs in electric vehicles are air cooling and liquid cooling. Natural air cooling has been used in Nissan Leaf. Forced air cooling is seen in Peugeot iOn and Renault Zoe. Tesla Model S, Chevrolet Spark and BMW i3 all use liquid cooling [121].

In this work, three air cooling systems and one water cooling system has been

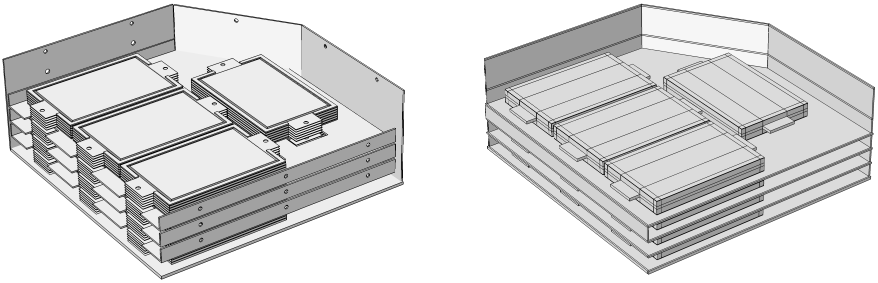

(a) Full pack (b) Simplified pack

Figure 4.6. Battery Pack used in the vehicle design of Ca(r)vour project. The external aluminium casing has been removed to visualize the interior design

simulated. The simulated air cooling strategies are natural air cooling on the outside of the pack, forced convection cooling on the outside of the pack and forced convection cooling on the inside of the pack. All simulation results presented in this section are for the end of charge. No attempt has been made to optimize the cooling in the battery pack by tweaking the flow parameters. The objective of this section is only to demonstrate the application of the P2D model coupled with a thermal and fluid-dynamics model for simulating battery pack behaviour in the presence of a TMS. The simulation results, though, have been presented and the working of the different cooling systems has been qualitatively discussed.

4.5.1 External Air Cooling Simulations

In Figure 4.8 the results of the external air cooling cases can be seen. In Figure 4.8a, natural air convection cooling (heat transfer coefficient $h=5\,\mathrm{W\,m^{-2}\,K^{-1}}$) is simulated at the surface of the pack, while in Figure 4.8b forced air convection cooling ($h = 25\,\mathrm{W\,m^{-2}\,K^{-1}}$) at the surface of the battery pack is simulated.

The maximum temperature in the modules in both cases is the same. This temperature is seen inside the modules and demonstrates that the cooling applied at the external surface of the pack does not reach the core of the modules. On the other hand, the minimum temperature of the modules is slightly lower for the forced cooling case indicating that the effect of cooling reaches the surface of the modules. The overall consequence of this is that there is a greater temperature gradient in the modules in the case of forced convection cooling.

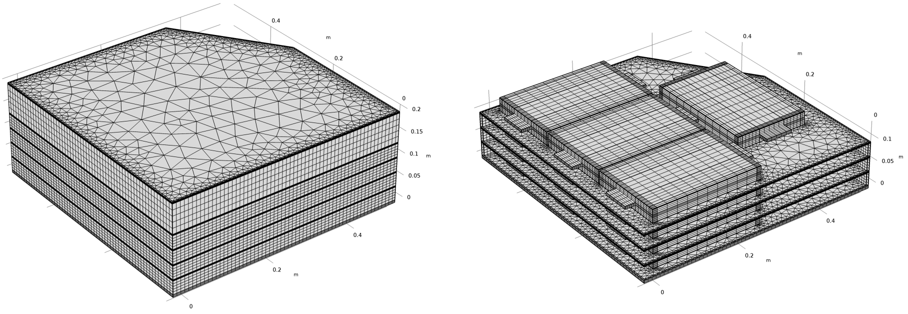

(a) External view (b) Internal view

Figure 4.7. Pack mesh

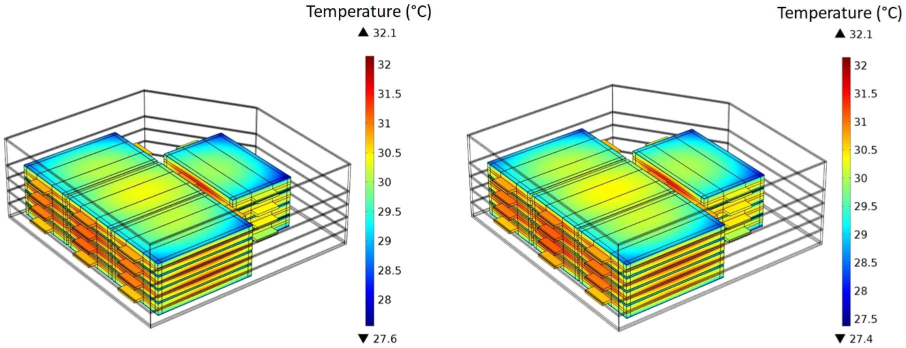

(a) Natural convection cooling (b) Forced convection cooling

Figure 4.8. Simulation results for external air cooling applied to pack at end of charge

4.5.2 Internal Air Cooling Simulations

In Figure 4.9, air cooling inside the pack is implemented. Only one compartment, in the middle of the pack is shown here. This compartment is thermally in a more critical position being surrounded by other compartments. In Figure 4.9a, the air flow established inside the pack is represented and the air velocity distribution can be seen. Air direction is from the left towards the right. The flow rate of air is $10\,\mathrm{cm\,s^{-1}}$ and the temperature of the inlet air is 25 °C. It is seen that the air velocity increases in the narrower regions of the compartment. The temperature distribution in the modules and the flowing air at the end of charge is seen in Figure 4.9b. The effect of air cooling is more visible in this case. However, given the directionality of the air flow, low temperatures are seen at the air inlet. As the air passes over the warm modules, it gets heated up. Because of the structure

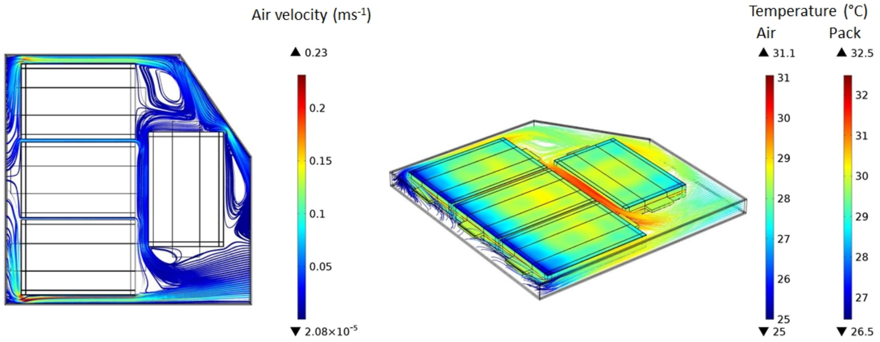

(a) Air flow profile (b) Temperature profile

Figure 4.9. Simulation results for internal air cooling applied to pack at end of charge

of the pack and the chosen direction of air inlet and outlet, a central region of high air temperature is created. This leads to higher maximum temperature in the pack compared to external cooling cases and also greater intra and inter module temperature inhomogeneity.

4.5.3 Liquid Cooling Simulations

In Figure 4.10, water cooling solution can be seen. One compartment of the pack is shown. This compartment is one of the two in the middle of the pack. A network of tubes sandwiches the modules. Water flows in from one side of the pack through the three tubes. It passes over the modules and then flows out on the same side as the entry. The initial water velocity in this simulation is $0.5\,\mathrm{m\,s^{-1}}$ and the water temperature is 25 °C.

In Figure 4.10a, water velocity inside the tubes can be seen. Homogeneous geometry for the three tubes ensures that the velocities are similar. In Figure 4.10b the temperature distribution in the tubes and the modules can be seen after the end of charging of the packs at 10 C current rate. A quite uniform surface distribution of temperature is seen in the modules. Also the overall temperature increase in low. Water leaving the modules is seen at a higher temperature especially in the inner most tube that passes close to the core of the modules. Liquid cooling as an effective means to cool down the battery pack is established in [109] and its effectiveness over other methods is seen in [122].

4.5.4 Simulations after Structural Changes in Pack

The different cooling systems simulated until now had the same pack structure. However, the bottom-up modelling approach is capable of lower level changes. In order to demonstrate the flexibility of the modelling approach, a new module design

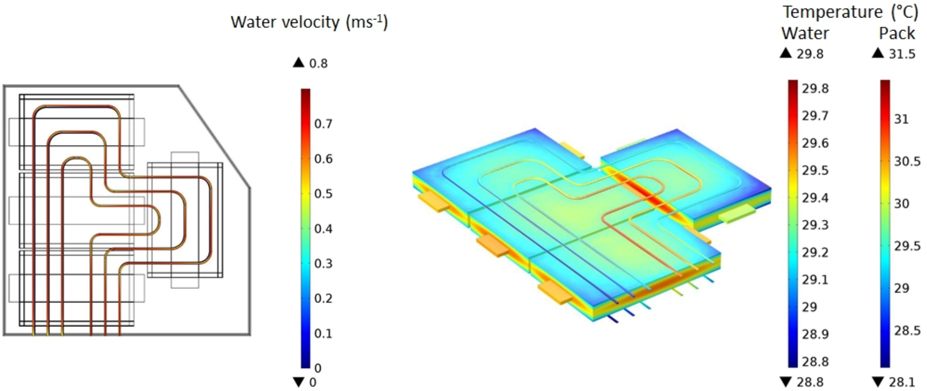

(a) Water flow profile (b) Temperature profile

Figure 4.10. Simulation results for water cooling applied to pack at end of charge

Table 4.2. Pack simulations

	Maximum temperature (°C)	**Minimum temperature (°C)**	**Maximum gradient (°C)**
Natural convection	32.1	27.6	4.5
Forced cooling - external	32.1	27.4	4.7
Forced cooling - internal	32.5	26.5	6
Liquid cooling	31.4	28.1	3.3
Structural change	31.4	28.6	2.8

is simulated for the battery pack. This module consists of only three pouch cells instead of six as in the original design (Figure 4.11a). This design change is inspired from the finding in the previous simulations that it is difficult to cool down the core of the modules. By halving the thickness of the module, a better thermal profile inside the pack is expected. In order that the results are comparable with the previous simulations, care is taken to not modify the heat capacity of the new pack design. This is ensured by also resizing the aluminium separator plates. The total mass of the pack and hence the total heat capacity remains the same as in the previous cases.

The result of the simulations carried out with this arrangement and natural convection cooling on the outer surface of the pack can be seen in Figure 4.11b. A much more uniform distribution of temperature in the modules can be seen. The thermal profile is homogeneous than even the liquid cooling case. Since there is no direct flow of fluid over the modules, the temperature gradients are lower. Thus not only the maximum temperature but also the temperature inhomogeneity in the

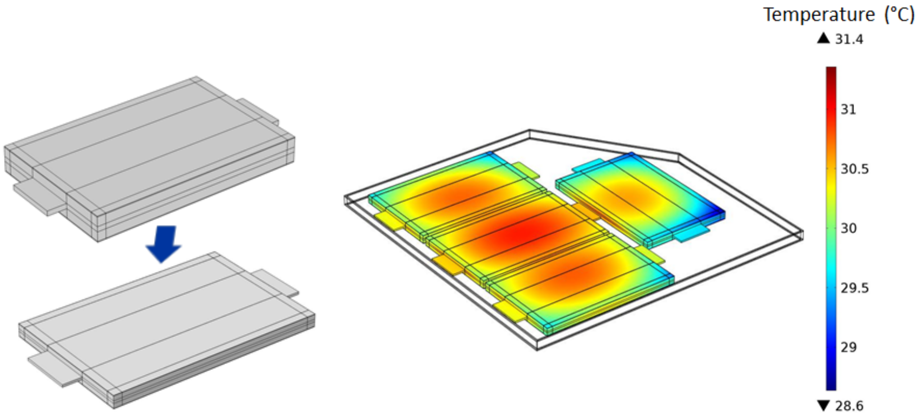

(a) 3 pouch cell module (b) Simulation results for structural changes at end of charge

Figure 4.11. Structural changes in the battery pack

pack is reduced in this case. All simulation results for the different cooling systems discussed can be seen in Table 4.2.

The actual cooling system design is an optimization process based on a number of factors which includes the battery technology used, costs of the system, weight and volume of the pack and the TMS, reliability and control, the application needs, etc. Several parameters can be varied just at the cooling system level to ensure that the application needs are served. For example, changing the air flow rate or the liquid flow rate will give different results than what have been presented in this work. The choice of the fluid also affects the thermal behaviour. The same is true for the inlet temperatures for the fluids. Lower level changes, such as the one demonstrated at the end, give many more options to optimize the design of the pack.

The bottom-up modelling approach developed in this chapter has been demonstrated to be a powerful tool for designing the pack architecture and the cooling system solution. Using the P2D electrochemical model in these simulations ensures that the heat generation data is accurate. The bottom-up approach gives the model the necessary flexibility to incorporate changes at any level of the design and simulate the thermal profile for any operating and environmental condition.

Part II

Aging

The only thing that is constant is change.

Heraclitus

Some of the work described in this part has been previously published in [123] and [124].

Chapter 5

Introduction to aging in batteries

In the previous chapters it is seen that electrochemical and thermal behaviour of lithium-ion batteries can be estimated accurately through a coupled electrochemical-thermal model. Such models take into account the dependence of some battery parameters on the concentrations and the temperature and predict the performance of the battery for any operating condition. However, the variation of parameters over the lifetime of the battery is not taken into account in such models as they are used for simulating the charge discharge behaviour at a particular state of the battery. The parameters of the battery model are valid only for this state. During the lifetime of a battery, its performance degrades. In battery parlance, it “ages” or its “health” deteriorates. This happens due to physical and chemical changes inside the battery irrespective of whether it is being operated or not. When the performance has decreased to a certain level such that it cannot serve the needs of the application, the service life of the battery is over.

The requirements and expectations on the lifetime of battery packs for electric vehicles and stationary energy storage systems are usually much higher than for consumer products, especially because the cost of the battery pack represents a significant share of the cost of the whole product. Good understanding of degradation processes in batteries and knowledge of how their performance decreases in different operating conditions are essential for evaluating how these batteries can be optimally operated or improved. Reliable forecasts on the lifetime of these batteries can help analyse the business cases for this technology in different vehicle and stationary storage applications.

5.1 Classification of aging processes

The most important aging effects occurring in lithium-ion batteries are usually measured in terms of capacity fade and power fade by a storage systems engineer. Capacity fade refers to the loss in discharge capacity that a battery demonstrates over time [125]. Power fade is the decrease of the power capability caused by an increase in the internal resistance/impedance of the cell [126]. These effects have been intensively studied by many groups [105, 127–133].

It is a common approach to distinguish between calendar and cycle aging of lithium-ion batteries [129, 130, 132, 134]. Calendar aging refers to the degradation in the cell during storage, i.e. when the battery is idle, while cycle aging refers to the cell degradation which occurs during charging and discharging of batteries. This differentiation is based on the assumption that there are aging mechanisms which occur independently of whether the cell is cycled (calendar aging) and additional mechanisms which only arise if the cell is operated (cycle aging).

In this work, calendar and cycle aging studies have been carried out to determine the influence of temperature, state of charge, current and depth of discharge on cell performance.

5.2 Aging mechanisms

Degradation in batteries is a non-stop process. The magnitude of degradation depends on the operating and environmental conditions. These often interact in causing degradation, making the aging mechanisms complicated to characterize. Furthermore, the different battery layers also interact in complex ways making it difficult to entangle cause and effect. Different degradation mechanisms occur in the electrolyte as well as the positive and the negative electrodes causing loss of active material in the electrodes and the loss of active lithium. The underlying origin of each of these phenomena can be mechanical or chemical in nature. Aging phenomena in each battery layer have been summarized below based on current knowledge.

5.2.1 Aging phenomena in the negative electrode

Graphite is the most commonly used negative electrode and the aging caused in this electrode is due to physical and chemical properties of graphite. The main aging factor is the initial formation and subsequent growth of a solid electrolyte interphase (SEI) on the graphite surface in contact with the electrolyte [135]. This occurs because the commonly used electrolyte components are not stable against the potential at the graphite electrode. The formation of the SEI layer is not undesirable as once formed it isolates the graphite and prevents further decomposition of the electrolyte. However, the actual SEI that is formed over the electrode is imperfect and grows slowly over time and with operation.

Reduction of electrolyte components with active lithium provides the raw materials for SEI layer. It leads to a change in the composition of the electrolyte as well as loss of active lithium. According to An et al. [136], at low anode potentials more inorganic SEI is formed (Li_2CO_3), while higher anode potentials lead to more organic SEI (ROLi and $ROCO_2Li$). Inorganic SEI is more conductive to lithium ions, which is desirable. Lu et al. [137] find that at low electrode potentials, the SEI layer has less resistance per unit of thickness and the SEI formed at high potential is more porous. At very low potentials, a denser SEI layer is formed that prevents electrolyte from reaching the surface of electrode and protects the negative electrode.

Volume change in graphite during intercalation-deintercalation processes causes mechanical stresses in the electrode [138]. It is suspected to be the reason behind loss of electrical contact and increased impedances of the cell over its lifetime. Co-intercalation of solvent in graphene planes is also known to cause structural damage to graphene sheets of graphite [139].

In low temperature conditions and at low negative electrode potentials, the negative electrode is also susceptible to lithium plating [101]. This happens when the local conditions at the graphite surface are electrochemically more favourable for lithium plating rather than lithium intercalation.

5.2.2 Aging phenomena in the positive electrode

Degradation mechanisms in the positive electrode are reported to have a minor impact on the overall cell aging. They vary depending on the positive electrode material [140]. In case of NMC electrodes, formation of surface layers on the electrode has been investigated [141]. Mechanical stress related degradation in this electrode caused by volume change and phase transitions during cycling is also reported [142]. A high lithiation degree is found to lead to irreversible structural changes (rock salt structure) causing irreversible capacity loss [140, 143]. Cation mixing phenomena wherein the similar ionic radius of Li^+ and Ni^{2+} causes the latter to displace the former in the crystal structure is also known to be a cause of degradation [144]. Jahn-Teller distortion of Mn^{3+}, Ni^{3+} and Co^{2+} is also a suspected cause for degradation in NMC electrode [145, 146].

5.2.3 Aging phenomena in the electrolyte

Electrolytes, which are usually mixtures of organic compounds with added inorganic salt, can be consumed through different side-reactions [147]. Reduction of electrolyte at the negative electrode to form the SEI over the anode is one major cause of aging in cells. As explained before, SEI is made up of different compounds and its composition depends on the electrolyte composition and the local electrode potential and temperature. A surface layer can also be formed over the positive electrode through oxidation of the electrolyte [140]. After prolonged operation or time, lack of electrolyte can lead to increased resistance inside the cell. Development of new electrolytes with greater electrochemical stability over wider voltage ranges is a critical research area in order to realize better performing lithium-ion batteries.

Table 5.1. Battery characteristics

Property	**Value**
Chemistry	Nickel Manganese Cobalt
Type	18650
Rated Capacity (Ah)	2.15
Nominal Voltage (V)	3.7
1C current (A)	2.15
Weight (g)	43.6
Cycle performance at 5A discharge	88% of initial capacity at 500 cycles

5.3 Battery under study

The batteries tested and analysed for their aging characteristics are commercially available 18650 cylindrical cells of the type US18650V3 manufactured by Sony Energy Devices Corporation. These have graphite as their negative electrode and $Li(NiMnCo)O_2$ as their positive electrode material. The characteristics of these cells are tabulated in Table 5.1. The upper and lower voltage cut-off are 4.2 V and 2.5 V, respectively. The specific energy density of these cells is $182.6\,\mathrm{W\,h\,kg^{-1}}$.

5.4 Definitions

The analysis carried out in this part of the thesis is largely quantitative. To leave no room for ambiguity, the definitions of some battery terms have been reiterated here to reflect how they were interpreted during this quantitative study for the battery.

Capacity (Q): cell capacity is the amount of electrical charge that can be released to an external electrical load during discharge under specified conditions. It is measured in ampere-hours (A h). The capacity is determined by the amount of active material inside the cell. However, a direct measurement of the cell capacity via determination of the amount of active materials is not practical. Moreover, in a real cell, not all of the electrode material is active because of electrically disconnected regions in the electrode. There is also usually an excess of negative electrode active material due to practical reasons.

In this thesis the cell capacity is defined by the following measurement procedure: The cell capacity Q is the actual amount of charge which can be extracted from a fully charged cell during discharge at a current rate of 0.1 C at an ambient temperature of 20 °C. Besides that, there is a nominal capacity Q_N which is specified by the cell manufacturer and signifies the amount of charge which can be extracted from a fresh cell under a set of standard conditions specified by the manufacturer.

Current rate ($\mathbf{C_{rate}}$): as in other published studies on battery aging, current rates are used for establishing the effect of current on aging instead of current amplitudes. Current rate is defined as:

$$C_{rate} = \frac{I}{Q_N} \tag{5.1}$$

where
I is the current measured in A
Q_N the nominal capacity measured in A h.

Thus, C_{rate} has the dimension of t^{-1} and is usually given in h^{-1}. Discharging at 1 C means that the nominal capacity of the cell can be discharged in exactly one hour.

Charging methods: constant current charging (CC-charging) entails charging the cell with a constant current rate of 1 C until the maximum cut-off voltage is reached. This maximum cut-off voltage is a upper limit specified by the manufacturer. Usually, this procedure is followed by constant voltage charging (CV-charging) where the cell is held at the upper cut-off voltage until the current rate has dropped to 0.05 C or for a maximum of 108 min. These two steps together are called CCCV-charging. The cell is hereafter considered as fully charged. This is the charging method recommended by the manufacturer. When the current rate during the constant current charging phase is not 1 C, it is given as additional information.

State of charge (SOC): the state of charge is a measure for the remaining charge of a battery and is calculated as follows:

$$SOC(t) = SOC(t_0) - \frac{1}{Q}\int_{t_0}^{t} I(t)dt \tag{5.2}$$

where
Q is the capacity
$SOC(t_0)$ is the initial SOC.

SOC is often expressed in percentage. The SOC of a fully charged battery is defined to be 100 %. The method of estimating SOC given by Equation 5.2 is called Coulomb counting.

Cycle: the term cycle denotes the process of charging and discharging a cell following a specified procedure. The SOC at the end of the cycle is the same as at the beginning. Another term, equivalent full cycle (EFC), is often used in degradation studies. EFC is not a cycle per se, but it is used to account for charge throughput of partial cycles relative to a full cycle. A full cycle has a charge throughput of 4.3 A h for a new cell (section 5.3), twice its nominal capacity. Thus, for e.g., a partial cycle consisting of a transition from a SOC of 25 % to 75 % and back, has a charge throughput of 2.15 A h and an EFC count of 0.5.

Depth of discharge (DOD): expressed usually as a percentage, it has different and sometimes conflicting definitions in literature. DOD is used in at least five different ways in published literature. These are:

1. Inverse of SOC [48]. For example, a state of charge of 20 % is equivalent to saying that the depth of discharge is 80 %.
2. The ratio of the net ampere-hours discharged from a battery at a given rate to the rated capacity [148]. For example, if 1.6 A h are discharged from a battery with a rated capacity 2 A h, the DOD is 80 %.
3. Measure of discharge since last charge expressed as a percentage [149]. For example, when the SOC changes from 50 % to 40 %, the DOD is 10 %. However when it changes from 40 % to 50 %, the DOD is 0 %.
4. The difference of maximum SOC and minimum SOC during an event consisting of one equal charging and discharging procedure [150]. For example a DOD of 100 % means going from 100 % SOC to 0 % and back.
5. One half of the fraction of the full cell capacity that is used during one cycle. For example, starting with a SOC of 50 %, charging until 100 %, then discharging completely to 0 % and charging back to 50 % is a cycle with a DOD of 100 % [129].

Only definition four and five are relevant when talking about cycle aging in batteries. This work follows definition five. Mathematically, it is given by:

$$DOD = \frac{1}{2Q} \int_{t_0}^{t_1} |I(t)| dt \tag{5.3}$$

where
t_0 is the time at the start of the cycle
t_1 is the time at the end of the cycle.

5.5 Experimental procedure

In the section, the instruments and procedure used for characterizing aging in batteries are introduced.

5.5.1 Testing equipment

To ensure homogeneity in external resistances during cell testing and safe and quick connections, each cell was mounted by connectors. At each battery pole,

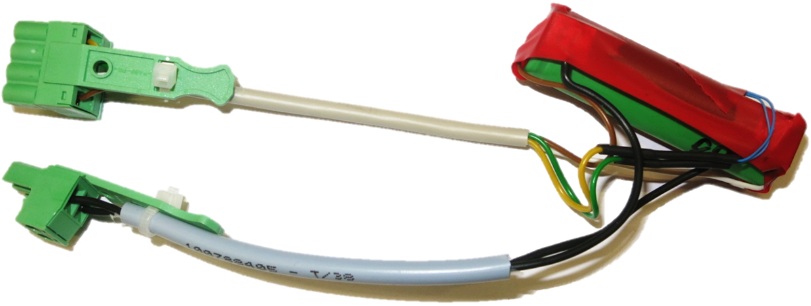

Figure 5.1. Tested 18650 cylindrical cell with mounting

two copper wires were soldered. One pair was used for current flow and the other for voltage sensing. In addition, a thermistor was attached to the cell surface to monitor the temperature. This arrangement can be seen in Figure 5.1.

Electrochemical characterization denotes all types of measurements, where an external current or voltage is applied to an electrochemical system and the response from the battery is measured.

A BaSyTec CTS Battery Test System frrm BaSyTec GmbH was used for periodic characterizations and cycling. The instruments relative accuracy for both voltage and current measurements is specified as 0.05 %. The minimal sampling period is 20 ms. Electrochemical Impedance Spectroscopy (EIS) was conducted with a Digatron EIS-Meter 2-20-2 from Digatron Industrie-Elektronik GmbH.

During the testing procedure, controlled ambient temperature conditions were ensured using three different climatic chambers. A TC 203-1 climatic chamber from Tritec was used for batteries kept at 0 °C. Batteries kept at 20 °C were stored in a Vötsch VT 3050 climatic chamber from Vötsch Industrie-Elektronik GmbH. A Memmert 100-800 climatic chamber from Memmert GmbH + Co. KG was used for batteries kept at 45 °C.

Some analysis also consists of opening the cells in a glove box and analysing samples. Two main analysis carried out were using Scanning Electron Microscope (SEM) and Energy Dispersive X-ray Spectroscopy (EDX). A SU-70 Schottky emission SEM from Hitachi with an accelerating voltage of 10 kV was used to take images of the extracted negative electrode and positive electrode samples. The EDX detector was incorporated in the SEM. It was used to investigate the chemical composition of the samples. An accelerating voltage of 20 kV was used for EDX.

5.5.2 Reference characterization procedure

For both, calendar and cycle aging, aging mechanisms are usually investigated by alternating electrochemical characterizations at a reference condition with storage or cycling periods at predefined conditions. The aim of the reference characterization procedure is to collect coherent comparable data on aging at different aging states. Electrochemical techniques that are part of this periodic characterization procedure are: capacity tests, pulse tests and electrochemical impedance spectroscopy. The cells are subjected to the reference characterization procedure every 30 days during the calendar aging tests and every 100 EFC during the cycle aging tests. This procedure is however is not a standardized procedure to study aging, In literature, different reference characterization procedures have been employed to study aging [129, 134, 151, 152]. The procedure followed in this work is as follows:

1. The cell temperature is first stabilized at 20 °C. This step may include transfer to the 20 °C climatic chamber from other climatic chambers. All periodic reference characterization procedures are always conducted at an ambient temperature of 20 °C to obtain comparable results.

2. The cell is then fully charged using constant current charging up to 4.2 V at a current rate of 1 C followed by constant voltage charging until the current has decreased to 0.05 C (CCCV charging). Thereafter it is held at open circuit conditions for 30 min to let transient processes inside the cell relax.

3. Two cycles consisting of constant current discharging to 2.5 V at 1 C (CC discharging) and CCCV charging are conducted. The discharge capacity during the second cycle is regarded as actual cell capacity $Q_{1\mathrm{C}}$. The cell is kept at open circuit conditions for 30 min after every charge and discharge.

4. The cell is then CC discharged and CCCV charged with a current rate of 0.1 C. The cell is kept at open circuit conditions for 1 min after discharge and for 30 min after charge. The charge withdrawn during this discharging step is denoted as actual cell capacity $Q_{0.1\mathrm{C}}$ which is used for analysing the capacity decrease. The cell is at 100 % SOC after this step.

5. Pulse tests are thereafter applied to the cell. These consists of a discharge pulse at a current rate of 2 C and a duration of 20 s and a charge pulse at a current rate of 1 C and a duration of 40 s. The resting period after the discharge pulse is 40 s and after the charge pulse is 5 min. The change in the SOC after one discharge and charge pulse is zero. The pulses were applied at each 10 % SOC step between 100 % SOC and 0 % SOC. The SOC levels were set by discharging 10 % of the capacity $Q_{1\mathrm{C}}$ at 1 C followed by a pause of 30 min. The pulse tests provide information on cell impedance.

6. The cell is CCCV-charged with a current rate of 1 C. Thereafter, 50 % of capacity $Q_{1\mathrm{C}}$ is discharged with a current rate of 1 C so that the cell is at 50 % SOC at the end of this step.

7. Electrochemical impedance spectroscopy is then carried out. For EIS, 8 points of measurement per decade are taken from 2.0 kHz down to 10 mHz. The ideal voltage response is set to 10 mV and the maximum exciting current amplitude is set to 0.2 A. All EIS measurements are also conducted at an ambient temperature of 20 °C.

5.6 Electrochemical techniques

The non-destructive techniques used to quantify and analyse aging in cells are described below.

5.6.1 Capacity measurement

Capacity measurement is the most basic of techniques used to characterize a battery and also one of the most important. This is because capacity is the leading health indicator of a battery. Most batteries are retired from their primary application when their capacity decreases to around 70 % - 80 % of the original capacity. As described in the previous section, it is measured by discharging the cell at 0.1 C from a fully charged state until the lower cut-off voltage is reached. The advantage of using a low current rate is to minimize the effect of resistance that may cause the cell to reach the cut-off voltage earlier. This is especially important for aged cells that have a higher internal resistance. A low rate measurement of capacity is thus a good measure of the active material in the cell.

5.6.2 Pulse tests

The internal resistance of a cell, R, (defined at some SOC) is derived from the over-voltage due to a current pulse with current amplitude I,

$$R = \frac{U_{OCV} - U_t}{I} \tag{5.4}$$

where
U_{OCV} is the equilibrium voltage before the pulse
U_t is the terminal voltage after a time t.

If the pulse is of a short duration, it can be assumed that the SOC does not change significantly and open circuit voltage can be assumed to be constant. Though pulse tests are conducted at different SOC in the experimental phase, only internal resistance calculated at 50 % SOC is discussed in this work. The trend of resistances with aging is similar at other SOC.

5.6.3 Differential voltage analysis

The derivative of voltage with respect to capacity, dV/dQ, is well suited to analyse battery as well as individual electrode data. The advantage of using dV/dQ as opposed to dQ/dV for analysis is because the contributions of negative electrode and positive electrode add linearly:

$$\left(\frac{dV}{dQ}\right)_{cell} = \left(\frac{dV}{dQ}\right)_{\substack{positive\\electrode}} - \left(\frac{dV}{dQ}\right)_{\substack{negative\\electrode}} \tag{5.5}$$

Additionally, when using a constant charge or discharge current, dQ is never zero and thus dV/dQ is defined everywhere.

dV/dQ curves can be used to study different aging processes in the cell [153]. The analysis is usually visual where dV/dQ is plotted against capacity or SOC. The peaks in a dV/dQ curve represent phase transitions. The loss of active material is manifested as a decrease in distance between transition peaks. Loss of active lithium may lead to extinction of peaks [154].

5.6.4 Electrochemical impedance spectroscopy

Electrochemical impedance spectroscopy (EIS) is one of the most successful non-destructive characterization techniques for delving deeper into understanding the individual processes and process changes of an electrochemical cell. It has been extensively used in this work to analyse data for both calendar and cycle aging tests.

Basic principles of EIS

The fundamental approach of all impedance methods is to apply a small amplitude sinusoidal excitation signal to the system under investigation and measure the response (current or voltage or another signal of interest). The impedance of a circuit is formed from the capacitive, inductive and resistive components and whose magnitude and phase change with the frequency. Therefore by varying the frequency of the applied signal one can get the impedance of the system under study as a function of frequency.

Thus if the input signal is:

$$i(\omega, t) = \bar{i} \exp(j\omega t) \tag{5.6}$$

And the output signal is:

$$u(\omega, t) = \bar{u} \exp(j\omega t + \phi) \tag{5.7}$$

where

$\bar{i}$ = AC current amplitude
$\bar{u}$ = AC voltage amplitude
ω = frequency
ϕ = phase angle

The impedance is given by the ratio of voltage to current, and can be expressed as:

$$Z(\omega, t) = \frac{u(\omega, t)}{i(\omega, t)} = \bar{Z} \exp(j\phi) \tag{5.8}$$

There is more than one way to illustrate the measured impedance data. A Bode plot may be used, wherein the phase angle and impedance are plotted as a function of frequency. A Nyquist plot, where the imaginary and the real parts of the impedance are plotted, is also an alternative. In a Nyquist plot, the frequencies are not explicitly plotted. The EIS spectra shown in this study are all Nyquist plots, keeping in line with other studies on battery aging.

EIS applied to batteries

EIS can be carried out in both galvanostatic and potentiostatic modes. For batteries, EIS is preferably carried out in galvanostatic mode as the battery voltage does not define the SOC well [155]. A large change in state of charge of the battery may lead to only a small change in voltage. However, if care is taken to ensure that system does not evolve during EIS, then these approaches are equivalent. To ensure this, the exciting current amplitude for EIS is capped to a maximum of 0.2 A while the ideal voltage response is set to 10 mV. Other details have been described in Section 5.5.2.

EIS spectrum of a new cell is shown in Figure 5.2a. Examples of EIS spectra of a calendar aged and a cycle aged cell are also seen here. The graphite and NMC electrode spectra are seen in Figure 5.2b and Figure 5.2c, respectively. Note that impedance for NMC is seen to be highly voltage dependent and the electrode processes are at lower frequencies (slower) compared to graphite.

Generally, EIS spectra are analysed to study dependence of electrode processes on SOC and temperature [155, 156]. To study aging, qualitative analysis of EIS spectra has also been carried out [157–160]. Quantitative studies through fitting of EIS spectra with an equivalent circuit model is seen in only some publications [131, 161–163]. In this work, a quantitative study of EIS spectra has been carried out for both calendar and cycle aging. The change of fitting parameters of the equivalent circuit with cell aging has been analysed.

Equivalent circuit model

The convoluted spectrum obtained through EIS is representative of overlapping electrical and electrochemical processes happening in the cell. An equivalent

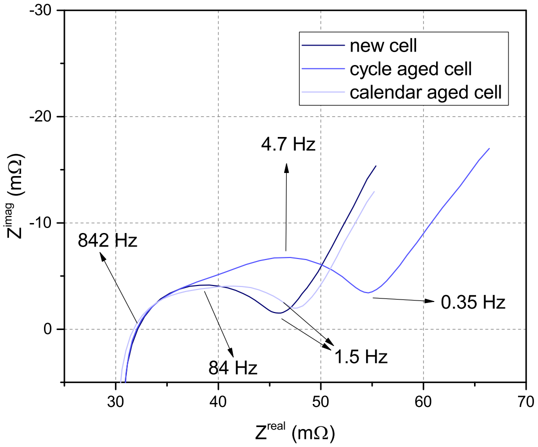

(a) new and aged cells

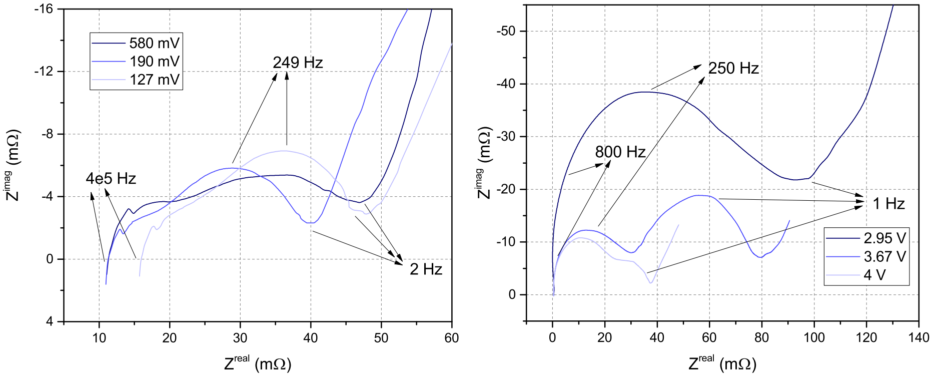

(b) Graphite electrode

(c) NMC electrode

Figure 5.2. EIS spectra

circuit model helps analyse it by breaking it down into parameters representing physical processes. The behaviour of the cell is represented by "classical" electrical components such as resistors, capacitors and inductors as well as specialized electrochemical components such as Warburg element, constant phase element, etc. Once, a equivalent model has been built to represent the cell processes as a series parallel combination of the above mentioned elements, an optimization routine best fits the spectrum with the equivalent circuit and determines these parameters of the model. To avoid over fitting, only the dominant processes happening inside the cells are considered during fitting.

For the cell, inductive effects are observed at frequencies greater than 840 Hz. These effects are caused by cables, geometry and cell windings [164]. Parameter L represents this inductance. The intersection of the spectra with the real axis represents mainly ohmic resistance of the electrolyte (R_s) [157]. Electrode electrochemical processes such as charge transfer and transport through the SEI layer are manifested between 840 Hz and 1 Hz in the form of a semicircle, which is slightly depressed. Processes at porous electrodes show both resistance and capacitance behaviour [87, 165].

The dominant processes in an electrode can be represented by one ZARC element which is a combination of a constant phase element (CPE) with a resistance in parallel [155]. CPE models the behaviour of the double layer, which is formed at the surface of the electrodes and is an imperfect capacitor. It is given by the generalized capacitance K and the depression factor α. CPE has both capacitive and resistive characteristics and the unit of $\mathrm{t}^{\alpha}\,\Omega^{-1}$. α is a measure for the distribution of the time constants due to the porous structure or roughness of the electrode [155, 166] associated with polarization processes and can take values between 0 (for a purely resistive K) and 1 (for a purely capacitive K). The resistance in parallel in the ZARC element accounts for the charge transfer resistance of the electrochemical reaction. Representation of the electrode processes using a ZARC element is accurate as long as the diffusion tail is separated from the charge transfer loop [155]. This is seen to be valid for most part of the calendar and cycle life of the cells in this study.

A new cell is expected to have a small SEI resistance and thus the semicircle seen in its spectrum is primarily due to the charge transfer resistance of the two electrodes. However, even in the calendar aged cells, the cell spectra consisted of mostly only one depressed semicircle. An example of a calendar aged cell spectrum can be seen in Figure 5.2a. Some other calendar aged cells demonstrate an incomplete separation into two semicircles. This signifies that processes at the two electrodes largely overlap even in a extensively aged cell. Thus, for analysing the spectra of calendar aging, only one ZARC element is used for representing processes for both electrodes. Fitting with two ZARC elements causes the parameters representing the ZARC elements to oscillate. The fitting parameters obtained using a single ZARC element represent the total polarization resistances and capacitances.

In case of the cycle aged cell, comparing the spectrum of the fresh cell with the cycled cell in Figure 5.2a, secondary characteristics such as greater separation of semicircles can be noticed in the latter. The magnitude of the separation of the two semicircles depends on the aging state and the cycling conditions. Thus, for the cycle aging spectra analysis each of these electrodes is represented by one ZARC element. The first ZARC element represents the SEI layer (R_{SEI}) on graphite, which has the dominant effect on the electrochemical processes at the negative electrode, and the capacitance and porosity of the negative electrode through $K_{dl,a}$ and $\alpha_{dl,a}$, respectively. The second ZARC element represents processes at the NMC electrode. $K_{dl,c}$ and $\alpha_{dl,c}$ represent the double layer capacitance and the porosity of the NMC electrode while the R_{CT} represents the charge transfer resistance at this electrode.

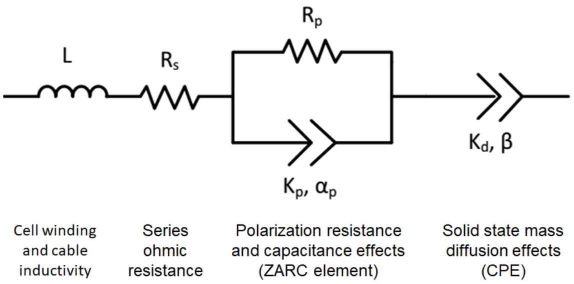

(a) Calendar aged cells

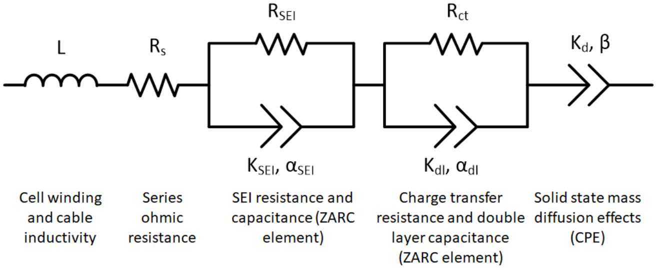

(b) Cycle aged cells

Figure 5.3. Equivalent circuits used for fitting EIS spectra

Solid state diffusion process is manifested as a sloped line in the spectra [155]. In Figure 5.2a, at frequencies below 1 Hz for a new cell, the sloped line can be seen. Usually in literature, Warburg element is used to represent diffusion processes. However this is only valid when the slope of diffusion tail is about 45°, representative of semi-infinite diffusion [155]. The slopes for the cells tested in this work are found to be substantially greater than 45°. Hence the assumption of semi-infinite diffusion is not valid and a CPE element represents this process in the equivalent circuit model.

The circuit used for fitting the calendar aged cell spectra is shown in Figure 5.3a. The cell impedance of this equivalent circuit is given by:

$$Z(\omega) = \mathrm{i}\omega L + R_s + \frac{R_p}{1 + R_p \cdot K_p(\mathrm{i}\omega)^{\alpha_p}} + \frac{1}{K_d(\mathrm{i}\omega)^{\beta}} \tag{5.9}$$

The mean time constant for polarization processes can be defined as $\tau = (R_p{\cdot}K_p)^{1/\alpha_p}$ which has units of time (s) and allows a more intuitive physical interpretation. With this substitution, the impedance is given by:

$$Z(\omega) = \mathrm{i}\omega L + R_s + \frac{R_p}{1 + (\mathrm{i}\omega\tau)^{\alpha_p}} + \frac{1}{K_d(\mathrm{i}\omega)^{\beta}} \tag{5.10}$$

This circuit used for analysing calendar aging spectra consists of seven fitting parameters.

For cycle aging, the equivalent circuit seen in Figure 5.3b is used for fitting the spectra. It consists of ten fitting parameters. Mathematically, it is given by the following equation:

$$Z(\omega) = \mathrm{i}\omega L + R_s + \frac{R_{SEI}}{1 + R_{SEI} \cdot K_{dl,a}(\mathrm{i}\omega)^{\alpha_{dl,a}}} + \frac{R_{CT}}{1 + R_{CT} \cdot K_{dl,c}(\mathrm{i}\omega)^{\alpha_{dl,c}}} + \frac{1}{K_d(\mathrm{i}\omega)^{\beta}} \tag{5.11}$$

As for calendar aging, the mean time constant for polarization processes defined as $\tau = (R \cdot K)^{1/\alpha}$ is substituted in the above equation:

$$Z(\omega) = \mathrm{i}\omega L + R_s + \frac{R_{SEI}}{1 + (\mathrm{i}\omega\tau_a)^{\alpha_{dl,a}}} + \frac{R_{CT}}{1 + (\mathrm{i}\omega\tau_c)^{\alpha_{dl,c}}} + \frac{1}{K_d(\mathrm{i}\omega)^{\beta}} \tag{5.12}$$

In order to fit the EIS spectra to the respective equivalent circuits for all cell characterizations starting from the new cell, a code was developed in Octave [167]. This code employs the Levenberg-Marquardt non-linear algorithm for curve fitting. For any test case, the first spectrum is that of a new cell. The parameters for this cell are roughly estimated from a visual inspection of the spectrum. They are subsequently refined after carrying out fitting. Thereafter, the resulting parameters from the least squares fit become the guess parameters for the next spectrum in chronological order.

Due to individual differences in the cells, the resulting parameters of the initial fit vary a little. Thus, the parameters are normalized to the values extracted from the fit to the spectra measured at the beginning of the experiments. Most tests in this study is performed on three cells to check for reproducibility of results. The average of the parameters of the three cells that are similarly aged is presented in this work. All fitted data for calendar aging and cycle aging EIS spectra are presented in Appendix B and Appendix C, respectively.

Chapter 6
Calendar aging

Calendar aging is the loss of performance of a cell caused by degradation processes that occur in an idle cell. It is sometimes studied together with cycle aging as a special case of cycling when the current rate is zero. The approach in this work has been to analyse it independently. This is based on the assumption that some degradation mechanisms that occur when the cell is idle are independent of degradation mechanisms that occur during cycling the cell. Even though calendar aging is usually considered as a slow process compared to cycle aging in lithium-ion batteries, study of calendar aging is worthwhile and important for several applications where operation periods are substantially shorter than idle periods. These include electric vehicles, emergency power supply systems, reserves in power systems, etc.

6.1 Review of calendar aging mechanisms

The loss of active lithium is reported to be the dominant mechanism causing capacity fade in calendar aging conditions [56, 130, 132, 133]. Its contribution in leading to capacity fade is much more than degradation of both the positive and negative electrodes' active material. Active lithium is mostly lost through electrolyte reduction at the negative electrode surface which leads to the formation of an insulating solid electrolyte interphase (SEI) adjacent to the negative electrode surface [168, 169].

The SEI is initially built during cell formation but keeps on growing at a much slower rate afterwards [160, 169]. Different theories for the processes that limit the rate of SEI growth have been discussed. Some authors describe an electron current through the SEI as rate limiting factor which can be described by electron diffusion, migration or tunnelling [128, 168]. Ploehn et al. [127] described the process as being limited by the diffusion of reactive solvent molecules through the SEI which are then reduced at the SEI/graphite interface. All of these theories suggest a continuous decrease of the SEI growth rate due to the increase of SEI thickness. The capacity fade during calendar aging is thus often described by a square root of time dependence [134, 168, 170].

This behaviour is modelled by Equation 6.1 where a_1 and a_2 are offset and square root aging parameters, respectively and t the storage time in days:

$$\frac{C^{\text{act}}(t)}{C^{\text{ini}}} = a_1 - a_2 \cdot \sqrt{t}. \tag{6.1}$$

Christensen et al. [169] assume the capacity to decrease linearly with time at the beginning and with square root of time at a later stage. Belt et al. [171] found a linear capacity decrease with time for cells stored between 30 °C and 50 °C and a square root of time decrease with time for cells stored at 60 °C.

Linear capacity fade with time, with b_1 and b_2 as offset and linear aging parameter, respectively is given by Equation 6.2:

$$\frac{C^{\text{act}}(t)}{C^{\text{ini}}} = b_1 - b_2 \cdot t. \tag{6.2}$$

Schmalstieg et al. [172] discussed a superposition of linear and square root dependence and used a power law function with exponent 0.75 to achieve a consistent description of this behaviour. Baghdadi et al. [173] described the calendar capacity fade by an exponential function.

Besides capacity fade, changes in the cell impedance during calendar aging of lithium-ion batteries have been discussed in the literature [129, 133, 134, 153, 171, 174]. In most cases, an increase of the overall internal resistance is found, which is attributed to the growth of surface films on both electrodes. The dominant effect is that from the SEI.

The OCV of lithium ion cells are also affected due to loss of lithium and loss of active material [175, 176]. While, this can also be used to analyse degradation, in this work, the change in cell OCV with time has not been studied.

6.2 Outline of this chapter

The results of calendar aging studies on the commercial 18650 lithium-ion cells (Table 5.1) are presented in this chapter. The changes of both cell capacity and cell impedance with time are discussed. The description of changes in cell impedance is based on pulse tests and electrochemical impedance spectra analysis. EIS spectra have been fitted with the equivalent circuit given by Figure 5.3a. Calendar aging of the cells is studied by quantifying the change in the different parameters of the model and associating them with changes in the physical phenomena caused due to degradation.

From the analysis of aging in reference cells it is shown that the reference characterization procedure carried out during the calendar aging tests significantly influences the determined capacity fade and impedance rise. These periodic electrochemical characterizations lead to charge throughput in the cells causing additional degradation over and above the calendar aging. This has been qualitatively discussed in the text. Some additional analysis on calendar aging is also presented in the next chapter after analysing the cycle aging results.

6.3 Method of characterization

The methods for characterizing calendar aged cells are not standardized and depend on the desired application and the type of lithium-ion battery. The storage duration interval between electrochemical characterizations is found to vary from 20 days [177], 42 days [129, 178], 49 days [153], 60 days [128], 90 days up to 2 to 9 month [133]. As discussed in Section 5.5.2, the electrochemical characterizations that are part of the reference characterization procedure can also vary from one study to another. In the articles [128, 133, 153, 177], the influence of additional charge throughput from characterization on the capacity fade and the impedance rise is not mentioned. Calendar aging tests have been conducted at both open circuit conditions and constant voltage conditions [129, 153, 178].

6.3.1 Calendar aging tests

Calendar aging of the cells used in this work is studied by storing the cells under controlled climatic conditions and characterizing them using the reference characterization procedure described in Section 5.5.2 approximately every 30 days.

The combinations of tested temperatures and SOC during storage is shown in Table 6.1. In order to see statistical effects, each test was performed with three cells. After the characterization procedure, the cells were set to a defined storage SOC. For the cell tests at 50 % SOC, no resetting was needed for all storage temperatures as the cells were already at 50 % SOC at the end of the EIS measurement. For cell tests at 100 % SOC, the cells were fully charged using CCCV charging at 1 C. For setting other storage SOC levels, the cells were CCCV charged and subsequently CC discharged with 1 C. They were then CCCV charged and using CC discharging at 1 C, the SOC was set by withdrawing a corresponding part of the charge measured through the preceding discharging step. Afterwards, the cells were disconnected from the test system and stored in climatic chambers at defined temperatures for 30 days. The results shown in this work are based on approximately 470 days of observed aging. EIS results are presented for 360 days of calendar aging.

6.3.2 Reference cells

In order to study the influence of the characterization procedure on cell degradation, four cells were used as reference. They were initially characterized and set to

Table 6.1. Tested combinations of SOC and ambient temperature are marked with 'x'

SOC	$T = 0\,°\text{C}$	$T = 20\,°\text{C}$	$T = 45\,°\text{C}$
25 %		x	
50 %	x	x	x
75 %		x	
100 %	x	x	x

25 %, 50 %, 75 % and 100 % storage SOC by the same procedure as the other cells. Afterwards, they were kept at open circuit conditions at 20 °C. The cells' open-circuit voltage was checked every 30 days in order to monitor self-discharging. If the open-circuit voltage was found to be lower than the one directly after the initial setting of the SOC, the cell was CCCV charged to the initial open-circuit voltage in order to compensate self-discharging. The amount of charge transferred during these procedures was found to be very small in comparison with cell capacity. Self-discharging is therefore negligible for the tested cells during the tested time intervals. Besides these controls, the reference cells were stored without any further characterization until they were finally characterized after 186 days.

6.4 Results and discussion

The results of calendar aging analysed through different electrochemical techniques are discussed in this section.

6.4.1 Capacity fade

In Figure 6.1, the actual cell capacity determined at 0.1 C discharge rate $Q^{\text{act}}_{0.1\text{C}}$ relative to the initial capacity $Q^{\text{ini}}_{0.1\text{C}}$ is plotted versus storage time . Each data point corresponds to the arithmetic mean of the actual relative capacity of three cells tested under the same conditions. The variation in capacity between the cells was low during the testing period, hence no information on variance has been provided in the graphs. The mean initial cell capacity is 2.164 Ah with a standard deviation of only 0.006 Ah, which is a measure of high homogeneity and build quality of the commercial cells.

The cell capacity is seen to decrease with storage time for all tested cells. This decrease of the cell capacity with time, which has been established to be mainly due to the loss of active lithium [56, 130, 132, 133, 170], is a strong function of temperature of storage and the state of charge during storage.

Temperature dependency: the temperature dependency of capacity fade shows a clear trend. At 50 % storage SOC, the rate of capacity fade is slightly higher at 20 °C compared to 0 °C (Figure 6.1). The rate of capacity decrease at 45 °C is more than twice the rate at 20 °C. A similar trend is observed at 100 %

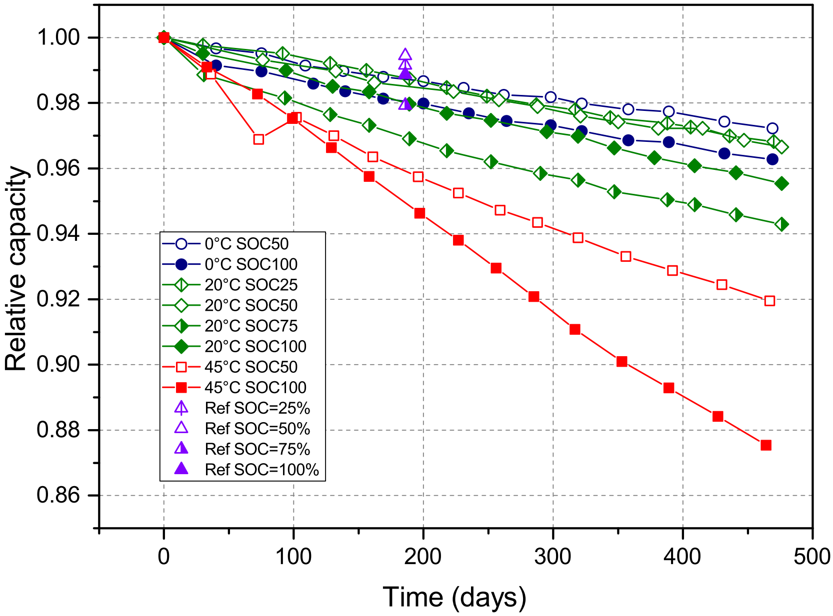

Figure 6.1. Relative cell capacity

storage SOC. Higher capacity fade at higher temperature is an expected behaviour due to the greater rate of reactions, both desirable and undesirable at higher temperatures [133, 153, 171]. A physical interpretation of this temperature behaviour is increased electronic conductivity of the SEI at elevated temperatures, which leads to a higher electronic current across this layer and finally results in a higher rate of electrolyte decomposition at the SEI/electrolyte interface.

SOC dependency The rate of capacity decrease is significantly higher for cells stored at 100 % SOC compared to cells stored at 50 % SOC at all tested temperatures as illustrated in Figure 6.1. Accelerated capacity fade at high SOC is reported in many studies [105, 129, 132, 133, 153, 172]. Keil et al. [133] show that low graphite negative electrode potentials at high SOC facilitate electrolyte reduction and SEI growth and thus lead to accelerated loss of active lithium during calendar aging. The cells stored at 25 % SOC and 75 % SOC at 20 °C do not follow this trend. The 25 % SOC cells lose their capacity slightly faster than the cells stored at 50 % SOC. The cells stored at 75 % SOC show the fastest capacity decrease of all tested SOC levels. This behaviour will be discussed in Section 6.4.3.

6.4.2 Cell impedance

The cell impedance is studied via current pulse measurements and EIS. Current pulses allow the determination of an overall resistance at a certain SOC, temperature and current magnitude. EIS is only conducted at open circuit voltage (OCV) but gives more detailed information than pulse tests about changes in electrochemical phenomena inside the cell including the effect of different resistances.

Pulse tests

The change of internal resistance can be seen in Figure 6.2. Here, the internal resistance based on the voltage response after discharging the cells for 20 s with a current rate of 2 C is shown. This resistance, R_{20s}, is a measure for the overall cell resistance including slow processes like solid state diffusion. The relationship can approximately be described as a linear function of time. Increase of internal resistance during calendar aging is often explained with increased ionic resistance due to the formation of surface layers such as the SEI layer [168, 172]. The rate of resistance increase is significantly higher for cells stored at 45 °C compared to cells stored at lower temperatures. In addition, a general trend of faster resistance increase for cells stored at higher SOC can be observed from Figure 6.2. In particular, the resistance increases significantly faster for cells stored at 100 % SOC than for cells stored at 50 % SOC at the same temperature. Belying the trend, the internal resistance for cells stored at 20 °C with 50 % SOC and for cells stored at 0 °C with 50 % SOC initially decreases and only starts increasing after about 200 days while the actual capacity continuously decreases. Käbitz et al. [129] proposed that cycling can lead to increased anode porosity resulting in a decrease of internal resistance. The only cycling calendar aged cells are subjected to is during the periodic reference characterization procedure.

Electrochemical Impedance Spectroscopy

EIS analysis presented in this work is carried out for a period of about one year starting with fresh cells. The initial impedance spectra show very little variation among the different cells, indicating good cell quality. The spectra were fitted with the equivalent circuit shown in Figure 5.3a. This model contains seven fitting parameters, out of which the four R_s, R_p, α and τ are analysed in this work. Fitted data for all cells is tabulated in Appendix B. The inductance L, which is partially due to external influences such as connecting cables, has no significant importance to cell performance and aging. It is used as a fitting parameter for the very high frequency part of the curve. Analysis of the slow diffusion processes in the impedance spectra is not carried out in this work due to the difficulty of physically interpreting the CPE element. From the fitting analysis, a large scattering of the diffusion parameters Q_d and β is noticed. No bounds could be set on these

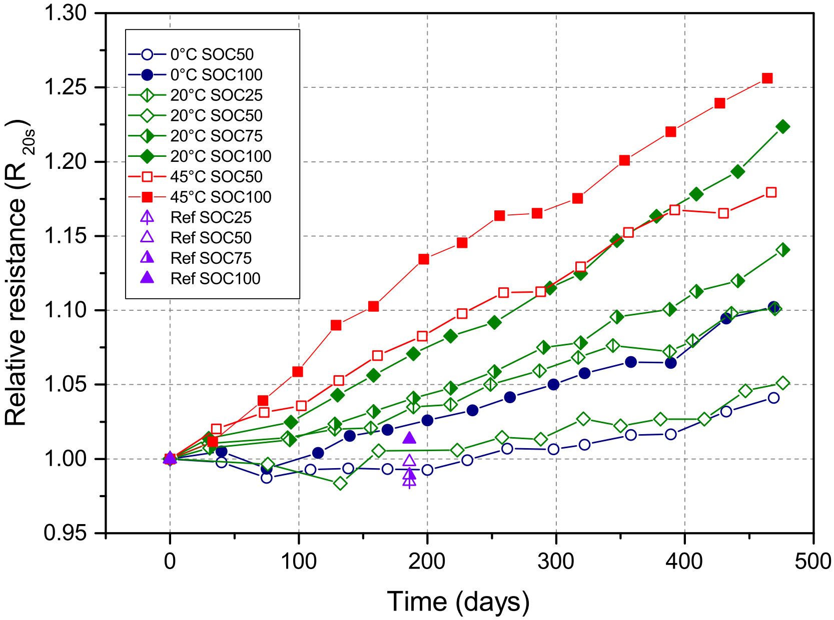

Figure 6.2. Relative cell resistance

parameters during fitting as no published studies define their limits and ranges. The only important aspect worth mentioning is that a generalized CPE element is chosen for fitting the low frequency diffusion tail and not a Warburg element (with $\beta = 0.5$) because the assumption of semi-infinite diffusion [155] is not valid for the cells in this work [95, 179]. Throughout the analysis period of about one year, β hovers around a value of 0.7 (± 0.07).

Calendar aging tests were carried out for periods longer than one year, however the EIS spectra were only analysed using the equivalent circuit model for about 360 days of storage time. This limit is imposed due to the increasing error of fitting that is seen with more aged cells. The equivalent circuit of Figure 5.3a is insufficient in representing the spectrum seen for older cells.

Series resistance ($\mathbf{R_s}$): the general trend of the series resistance (Figure 6.3a and Figure 6.3b) is an increase during aging under all conditions of temperature and SOC. This is consistent with Waag et al. [157] and Stianzny et al. [177]. The cells in [157] are tested for typical electric vehicle (EV) usage with significant storage time, and thus can be compared with the calendar aged cells in this work. From Figure 6.3a and Figure 6.3b, two effects are apparent. First, the increase of series resistance is greater with higher temperature and second, the growth rate of R_s is higher for cells stored at 100 % SOC compared to 50 % SOC. The nature of the increase is quite regular in all cases.

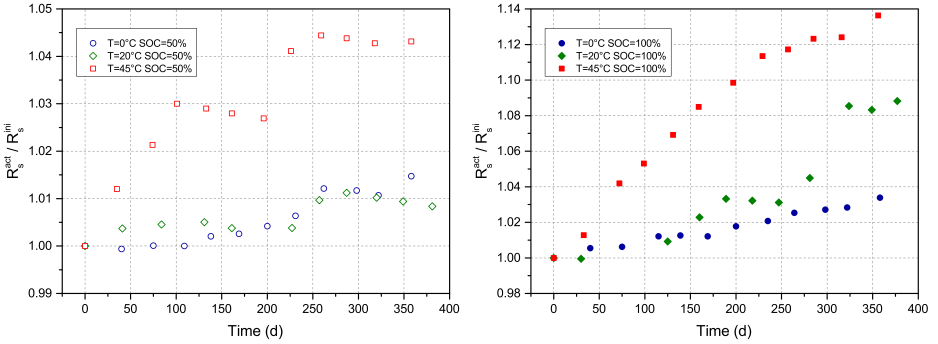

(a) Series resistance at 50 % SOC (b) Series resistance at 100 % SOC

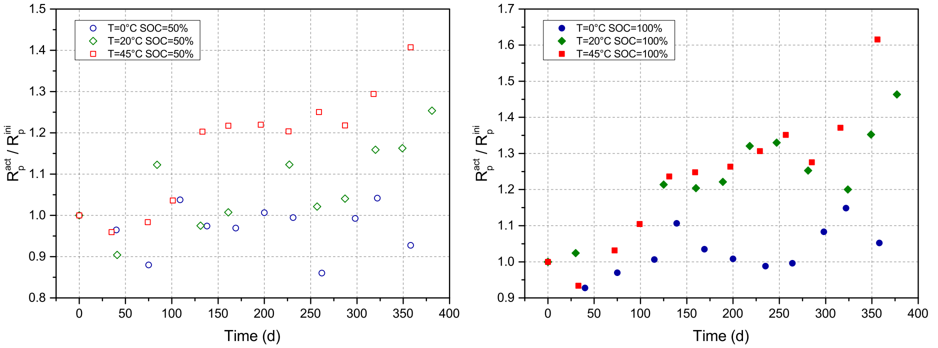

(c) Parallel resistance at 50 % SOC (d) Parallel resistance at 100 % SOC

Figure 6.3. Evolution of resistances from equivalent circuit model at different storage SOC

The series resistance is a measure of the ohmic resistance in the cell, predominantly caused due to the conduction of lithium ions in the electrolyte [131, 139]. Thus, an increase in R_s points to a degradation reaction of the electrolyte, which is faster at higher voltages (or higher SOC) as well as at higher temperatures. This irreversible reaction of electrolyte with lithium contributes to cell degradation and is manifested not only through an increased resistance of the electrolyte (measured by increase in R_s), but also through loss of active lithium (causing capacity fade) and formation of SEI (estimated by change in R_p).

Parallel resistance ($\mathbf{R_p}$): the parallel resistance, representing the total polarization resistance, shows a general upward trend for all cases except the batteries stored at 0 °C, 50 % SOC (Figure 6.3c and Figure 6.3d). In cases of high temperature and high storage SOC (45 °C, 50 % and 100 % SOC; 20 °C, 100 %

SOC), the upward trend is unambiguous and demonstrates that both temperature and SOC affect this parameter. The relative change is much higher for R_p than for R_s. For some cases, fluctuations are seen in the fitting results. The overall trend from Figure 6.3c and Figure 6.3d is that at 0 °C, very little increase in R_p is seen, while the increase at 100 % SOC is more than the increase at 50 % SOC.

The R_p element represents the combined resistances of the SEI (R_{SEI}) as well as the charge transfer resistances (R_{CT}). The dominant effect at the negative electrode is the formation of the SEI layer and R_{CT} represents the charge transfer resistance mainly at the positive electrode. A change in R_p can be physically related to changing chemical composition of the electrodes such as growth of SEI/passivating layer, loss of metallic components of the positive electrode and/or changing crystal structure. R_{SEI} and R_{CT} may not change at the same rate for similar storage conditions of the battery. This could be one reason for the irregular nature of R_p. Increase in positive electrode charge transfer resistance and decrease in negative electrode charge transfer resistance is seen by Stiasnzy et al. (experiments at high temperature 60 °C) [177]. In their results, both the SEI and positive electrode resistance increased substantially at 100 % SOC (much more than the minute drop in negative electrode resistance) compared to the lower SOC case. The overall effect at high temperature and SOC is thus an increase in resistance, which is consistent with the result seen in this work.

The major contribution to polarization resistance, however, can be attributed to the growth of SEI layer. The evidence of this comes from an increase in R_s, which suggests a continuous breakdown of electrolyte. The electrolyte is known to react with the graphite negative electrode forming the SEI [128]. Higher voltages and temperatures, which were seen to increase the degradation rate of the electrolyte, lead to more reaction at the graphite-electrolyte interface and more SEI formation. Moreover, the SEI formed is unstable at high temperatures, leading to a continuous increase by rebuilding itself [180]. This in turn leads to a higher increase in R_p at higher SOC and higher temperatures. Röder et al. found out studying half cells, that SEI growth is the dominant capacity fade mechanism [178]. Käbitz et al. also attributed the main aging mechanism to the SEI formation on the negative electrode [129].

In order to understand the relationship between the two methods of determining resistances, pulse tests and EIS, the sum of series and parallel resistance ($R_s + R_p$) obtained from fitting is plotted along with $R_{1\mathrm{s}}$ obtained from the current pulses versus storage time in Figure 6.4. The reason for this comparison is that the frequency just before the diffusion branch of EIS is 1 Hz for this cell (Figure 5.2a). Thus, ($R_s + R_p$) obtained from EIS spectra fitting corresponds to $R_{1\mathrm{s}}$ calculated from pulse tests. Instead $R_{20\mathrm{s}}$ with the corresponding frequency 0.05 Hz, also takes into account the diffusion resistances as can be observed from the EIS spectra in Figure 5.2a.

Resistances calculated through the two methods are similar in magnitude and nature as can be seen in Figure 6.4. Charge transfer resistance is a function of

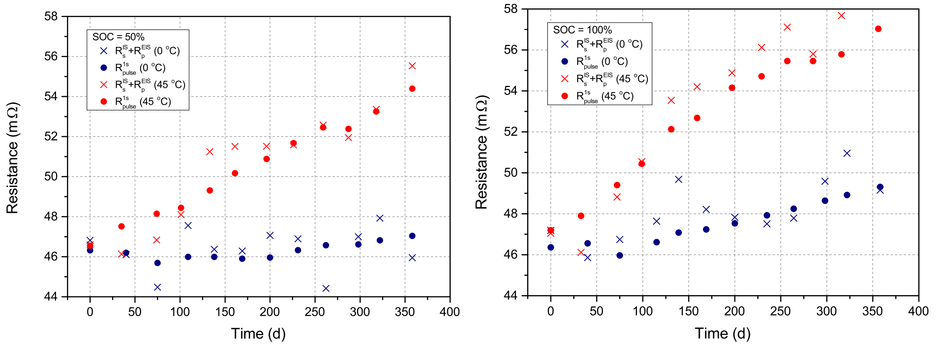

(a) 50 % SOC (b) 100 % SOC

Figure 6.4. Evolution of resistances during calendar aging determined via EIS (around 1 Hz) and pulse test (after 1 s pulse)

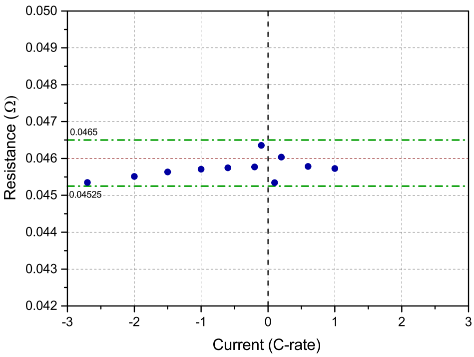

Figure 6.5. Instantaneous resistance calculated at different current rates using pulse tests (horizontal lines drawn only to emphasize the low range of the resistance)

current (Butler-Volmer equation). However, the results of impedance measured at OCV and the pulse measurement at 2 C discharge pulse are similar, clearly showing that the resistance is not a strong function of current for the tested battery chemistry within the tested range of currents. This was investigated in more detail by applying pulses of different current magnitude, and checking the resistance at around 1 s for a new cell at 50 % SOC. In all cases, a very low current dependency of resistance was seen (Figure 6.5). The values are always found to be around 46 mΩ for a new cell.

Resistances calculated using pulses in the works of Belt et al. [171] at 30 °C, for Käbitz et al. [129] at 25 °C and 40 °C and Baghdadi et al. [173] for VL6P batteries at 30 °C and 45 °C for batteries stored at 30 % SOC show a fluctuating nature similar to what is observed for the low temperature data for the cells in

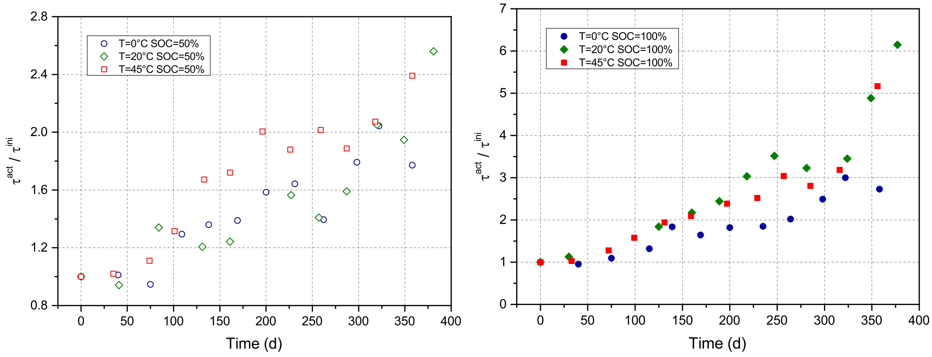

(a) Time constant at 50 % SOC (b) Time constant at 100 % SOC

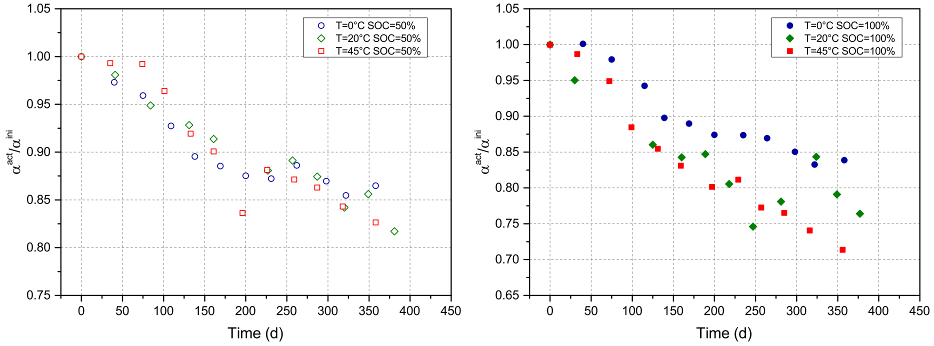

(c) Depression factor at 50 % SOC (d) Depression factor at 100 % SOC

Figure 6.6. Evolution of ZARC parameters

this study. Their high temperature data is more linear and regular, as is also seen here. Stiaszny et al. [177] also conducted tests at high temperature and high SOC storage conditions where a more linear increase with time is seen. In such cases, the average increase in R_p is many times compared to the increase in R_s. Consistent to this, for cells in this study that are stored at 45 °C with a storage SOC of 100 %, R_p is about $0.7\,R_s$ at the initial characterization but is equal to R_s after 360 days of storage.

Mean time constant (τ): the mean time constant is interpreted as a measure of the dynamical behaviour of the battery [157]. Since different surfaces on the electrode have different electrochemical activation energies, they give rise to a distribution of time constants. Hence, a mean time constant needs to be defined, while the roughness of surfaces is given by α. A greater time constant signifies a slower response of the battery to the current pulse. Hence, the voltage change due to a current pulse is slower in case of a higher time constant. The increase in time constant is found to be a strong function of storage SOC and has a weak temperature dependence, as can be seen from Figure 6.6a and Figure 6.6b. The nature of increase of time constant is exponential with storage time. An increase in time constant is also seen in the results presented in [157] through the lowering of the frequencies in the Nyquist plot.

Depression factor (α): the depression factor is the measure of depression of the semicircle given by the ZARC element, which arises due to the porous microstructure of the electrodes and as such it is a measure of the non-uniformity of the electrode surfaces [166]. In all cases of temperature and SOC, a decrease in α is seen with storage time (Figure 6.6c and Figure 6.6d). Change in α is dependent on storage SOC with greater decrease at 100 % SOC than at 50 % SOC. Also, a stronger temperature dependency is noticed at 100 % SOC than at 50 % SOC. Decreasing α represents greater depression of the semicircle, which in turn could represent an increasing non-uniformity of electrode surfaces probably due to an increasing porosity. Particle fracture, which can cause an increase of porosity in the NMC particles, was observed by Stiaszny et al. [177]. This was more prominently seen at high voltage (or high SOC), consistent with the results of the cell tested in this work. A decrease of α, pointing to an increase of active surface area, could also affect the charge transfer resistance by decreasing it, as noticed in the case of graphite negative electrode by Stiaszny et al. [177].

The decrease in α should be considered keeping in mind that the SEI and the charge transfer semicircles separate with aging as the charge transfer semicircle moves towards lower frequencies. The two separated processes, when fit by only one ZARC element, can lead to an exaggerated apparent decrease in the value of α especially for aged cells.

6.4.3 Influence of electrochemical characterization

Reference cells

Four cells are characterized initially and only after 186 days of storage at 20 °C unlike the other cells that were characterized every 30 days. These four cells are referred to as reference cells. Their relative capacity fade is displayed in Figure 6.1 along with the capacity fade of the cells that were characterized every 30 days. The reference cells are used to study the influence of the characterization procedures on cell degradation. It is seen that the capacity fade after 186 days is significantly smaller for the reference cells compared to the corresponding cells stored at the same conditions that where characterized every 30 days. The capacity fade of the reference cells follows the same SOC dependency as the other cells and thus, the capacity fade for the reference cell stored at 75 % SOC is greater than for the cell stored at 100 %.

A significant difference between regularly characterized cells and reference cells can also be observed for the change of internal resistance with time as depicted in

Figure 6.2. R_{20s} only increases by about 2 % after 186 days for the reference cell stored at 100 % SOC, while R_{20s} of the regular cells stored at this SOC increases by about 7 % during the same time. The other reference cells even show a decrease in R_{20s} after 186 days.

The aging of the regularly characterized cells seen is thus partly due to the additional degradation they undergo due to the electrochemical characterization. The regular characterization procedure (Section 5.5.2) and the process of resetting the SEI (Section 6.3.1) entail charging and discharging of the cells. It is commonly accepted that cycling lithium-ion cells leads to enhanced degradation compared to calendar aging [134, 172]. Additional mechanical degradation resulting from volume changes of the graphite negative electrode during charging and discharging [181], can lead to cracking of the SEI. The subsequent repair results in additional lithium consumption and therefore capacity loss [168].

While reference cells have not been further quantitatively analysed, there is strong evidence that charge throughput causes additional capacity fade and impedance increase. The non-negligible impact that regular characterization procedure and the resetting of SOC has on calendar aging results also hints on the relative magnitude of cycle aging vis-à-vis calendar aging. The cycle aging results are documented in the next chapter.

Calendar aging considering the effect of charge throughput

The charge throughput experienced by a cell due to characterizations can be quantified in equivalent full cycles (EFC). One EFC corresponds to two times the rated capacity (1 EFC = 4.3 Ah). After the regular characterization procedure, the SOC is reset (see Section 6.3.1), which causes additional charge throughput in the cells, the magnitude of which depends on the storage condition. This too can be quantified in EFC. During the test period, the cells stored at 50 % SOC and 100 % SOC and 20 °C experienced approximately 60 equivalent full cycles due to the characterizations and resetting of SOC. The cells stored at 25 % SOC and 75 % SOC and 20 °C experienced approximately 100 and 92 equivalent full cycles during the same time period, i.e. more than 50 % of the charge throughput experienced by the cells stored at 50 % SOC and 100 % SOC.

In Figure 6.7a, the residual cell capacity is plotted as a function of EFC instead of time as in Figure 6.1. As discussed in Section 6.4.1, the cells stored at 25 % SOC and 75 % SOC show an unexpected fast capacity fade compared to the cells stored at 50 % SOC and 100 % SOC, respectively when capacity fade is regarded as a function of time. But when capacity fade is regarded as a function of charge throughput, the cells stored at 25 % SOC show the slowest rate of capacity decrease followed by the cells stored at 50 % SOC which is as expected. It can thus be inferred that the relatively high rate of capacity fade of the cells stored at 25 % SOC when compared to cells stored at 50 % SOC is due to the additional cycling these cells experienced during resetting of the SOC.

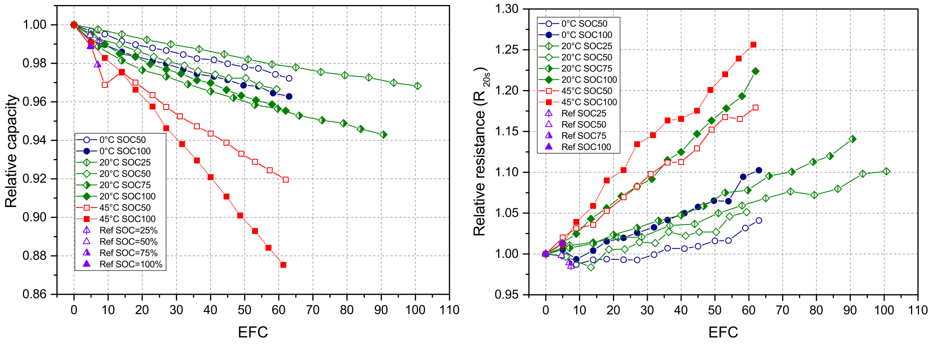

(a) Capacity fade (b) R_{20s}

Figure 6.7. Aging parameters plotted vs. EFC

Even for cells stored at 75 % SOC, when the data is plotted against charge throughput, they show a similar rate of capacity fade as the cells stored at 100 % SOC, as depicted in Figure 6.7a. These cells exhibit the fastest capacity decrease as a function of time, as seen from Figure 6.1.

In Figure 6.7b, the change of internal resistance $R_{20\mathrm{s}}$ is plotted as a function of charge throughput. The resistance of the cells stored at 50 % SOC still rises the slowest but the difference to the cells stored at 25 % SOC is much smaller than in the case of using time as independent variable. The resistance increase of the cells stored at 100 % SOC is the highest.

The internal resistance of the reference cells does not rise significantly faster than the internal resistance of the cells which were characterized regularly as shown in Figure 6.7b. This suggests that the rise of internal resistance during calendar aging actually might be mainly due to the cycling during characterizations and resetting of SOC.

EIS analysis

Until now EIS results were presented only for cells that were stored at 50 % SOC and 100 % SOC in Figure 6.3. Greater increase of R_s, R_p and τ as well as greater decrease in α is seen for the 100 % SOC case compared to 50 % SOC. This is as expected, as greater SOC or greater voltage is known to enhance calender aging [133, 153]. However, looking at the parameters R_s, R_p, τ and α for cells stored at 25 % SOC and 75 % SOC at 20 °C in Figure 6.8, it can be clearly seen that 50 % SOC has the least increase of R_s, τ and the least decrease of α instead of 25 % SOC as would be expected. The nature of change in the value of R_p is not smooth. The change in fitting parameters for cells stored at 100 % SOC is the greatest followed by the cells stored at 75 % SOC.

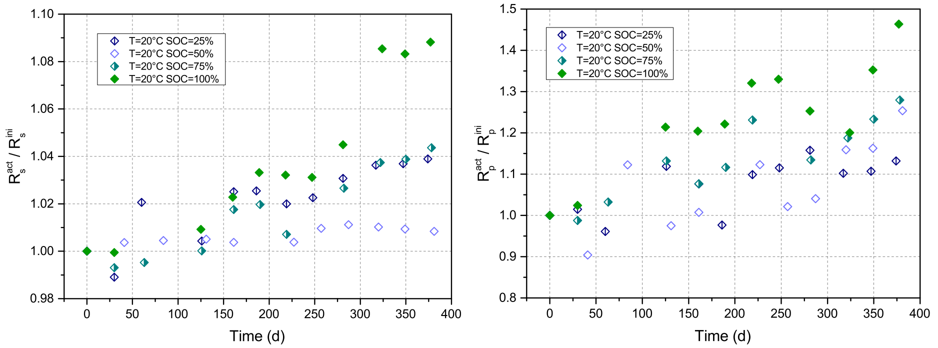

(a) Series resistance (b) Parallel resistance

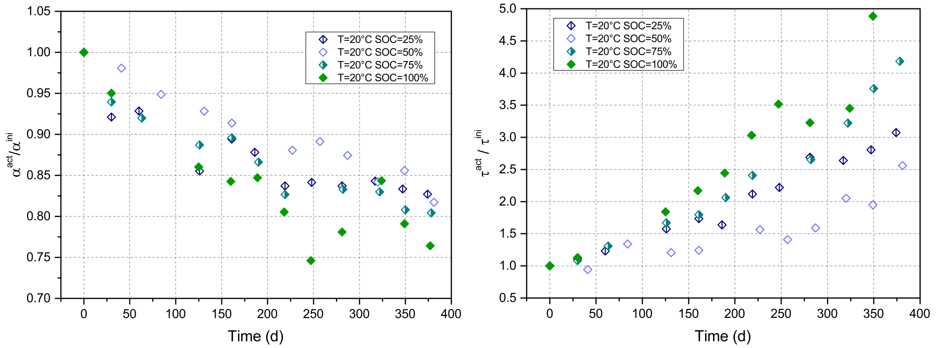

(c) Depression factor (d) Time constant

Figure 6.8. Fitted equivalent circuit parameters from EIS analysis of batteries calendar aged at 20 °C at different SOC plotted versus storage time

In Figure 6.9, EIS fitting results have been plotted versus EFC. Cell stored at 50 % SOC have the slowest increase in R_s and τ, however the difference from 25 % SOC is much reduced as compared to the fitting results plotted versus storage time in Figure 6.8. The change in parameters is still the greatest for cells stored at 100 % SOC. Comparing the fitted parameters results in Figure 6.8 and Figure 6.9, the additional degradation seen for cells stored at 25 % compared to cells stored at 50 % can be largely attributed to the extra charge throughput experienced by the former due to the process of resetting the SOC. Extra charge throughput is also experienced by the cells stored at 75 % SOC. However, the change in fitting parameters for cells stored at 100 % SOC is much greater even after considering the effect of charge throughput.

While plotting the calendar aging results versus EFC instead of time gives a more correct picture of the relative differences in calendar aging between these cells, it still does not completely explain the slow impedance rise for cells stored at 50 %

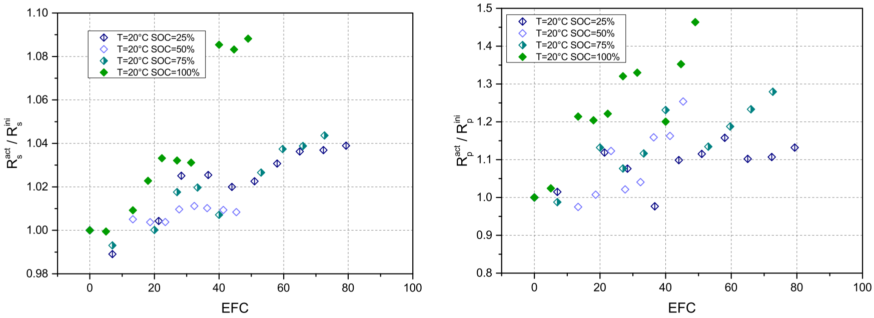

(a) Series resistance (b) Parallel resistance

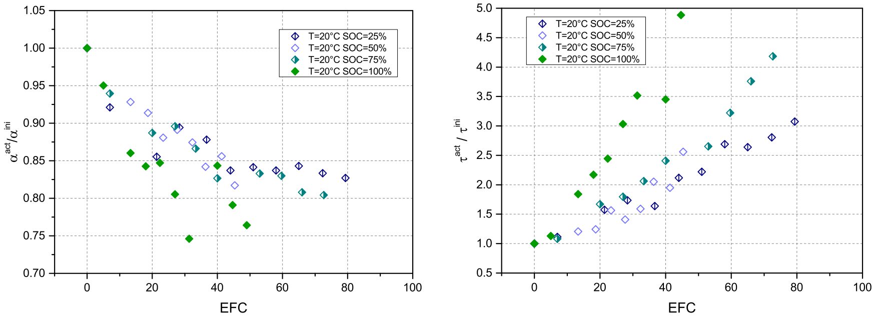

(c) Depression factor (d) Time constant

Figure 6.9. Fitted equivalent circuit parameters from EIS analysis of batteries calendar aged at 20 °C at different SOC plotted vs. EFC

SOC compared to 25 % SOC stored cells as well as the slow capacity fade of the cells stored at 100 % SOC compared to cells stored at 75 % SOC. Calendar aging in these cases has been revisited after considering the insights from cycle aging results in the next chapter.

Chapter 7

Cycle aging

Cycle aging is the loss in performance of the cell due to degradation processes occurring during its operation. Operating a battery essentially means that the battery experiences charge throughput and as is already evident from the last chapter, charge throughput has a strong influence on degradation processes. The reference procedure used for characterization of calendar aging is observed to cause sizeable degradation in the cell affecting the measurement of calendar aging, reminiscent of the "Observer effect"[1]. All applications of storage whether in consumer devices, electric vehicles or power system applications entail charging or discharging the cell. The study of cycle aging under different operating conditions is thus important to understand and quantify degradation caused due to charging and discharging. Analysing cycle aging behaviour can also help optimize the operation of the battery and to estimate its life.

7.1 Review of cycle aging mechanisms

The degradation during cycle aging is usually studied as a function of temperature, state of charge (SOC), current amplitude and depth of discharge (DOD).

Temperature affects cycle aging mainly because of the Arrhenius dependence of desirable and undesirable reactions on temperature. It has been found that higher temperature leads to greater capacity fade [129, 182] in NMC - graphite batteries. Leng et al. [104] found that degradation mechanism in graphite is enhanced at high temperatures. Instead An et al. [136] suggest a more stable SEI at high temperature. Schuster et al. [183] even found a lower capacity fade at 50 °C than at 25 °C, with an optimum at 35 °C for a NMC-graphite battery.

The dependence of capacity fade on DOD and SOC is studied due to its importance in deciding the usable capacity of the battery as well as the operating strategy. For batteries with NMC as positive electrode and graphite as negative

---

[1] the theory that simply observing a situation or phenomenon necessarily changes that phenomenon.

electrode, Schuster et al. [183] found that at higher DOD, a higher capacity fade is seen. Higher DOD means that the cell reaches high and low SOC states, leading to more SEI formation and greater active material loss in graphite, respectively. Similar results are found by Wang et al. [130] but in their case at higher rates this dependence is not clear. Schmalstieg et al. [172] discovered that mean SOC around which the cell is cycled is important to understand DOD dependence. Capacity fade for 10 % DOD was found to be fastest at high and low SOC and lowest at 50 %. Ecker et al. [153] found that at 50 % SOC, the deeper the cycle (greater DOD), the higher the capacity fade is.

Studying the dependence of cycle aging on current rate is especially relevant for high power applications such as in power tools or fast charging in electric vehicles. Higher rates are found to cause faster degradation due to more stress in cells [130, 135, 184]. Wang et al. [130] discovered that with increasing temperature, the dependence of capacity fade on current rate decreases. Schuster et al. [183] found out that more capacity fade is seen at higher charge rates than at higher discharge rates which they attributed to lithium plating. An et al. [136] discovered that the SEI formed at higher current densities has a higher porosity and electronic conductivity, which are undesirable properties for SEI.

Spotnitz [105] identified 4 different stages of capacity fade during cycle life, with the first three stages often indistinct and slow and the last one conspicuously steep. This rapid decline in capacity loss is well documented in batteries [105, 128, 153, 177, 183, 185, 186].

7.2 Outline of this chapter

The results of cycle aging studies conducted on the commercial 18650 lithium-ion cells (Table 5.1) are presented in this work. Capacity and impedance changes are discussed. Electrochemical impedance spectroscopy data is analysed to study the changes in impedance with cycle aging. New insights into the cycle aging behaviour of the cells as a function of the studied parameters result from statistical data analysis of these non-destructive characterizations. Detailed investigation into the rapid capacity fade phenomena has been conducted. Its importance in end-of-life determination has been emphasized. A deeper analysis using SEM and EDX is carried out in order to understand chemical and morphological changes in the battery layers at different stages of aging. The concept of critical SEI resistance has been suggested as a possible metric for battery operation regulation. Degradation parameters for the studied cells have been quantified and presented in this chapter.

7.3 Methods of characterization

Alternating cycling periods with reference characterization procedures is widely used as a technique to study cycle aging. But just like calendar aging, there is not a standardized method for studying and quantifying cycle aging for a cell.

Different studies vary one or more parameters (among DOD, SOC, temperature and current) to study the effect of them on aging. Even the duration between the characterizations vary. Käbitz et al. [129] varied DOD, SOC and temperature. Their cycling duration interval between the characterizations is 6 weeks. Jalkanen et al. [131] instead characterized their batteries after every 100 EFC and studied the dependence on cycle aging only on temperature. In [153] and [172] the characterizations are performed every 3 weeks and the effects of temperature and current rate are not studied.

7.3.1 Cycle aging tests

In this work, cycle aging dependence on DOD, SOC, temperature and discharge current rate is studied. The combinations of tested temperatures, DOD, charge and current rate CxDy and mean SOC for cycling are shown in Table 7.1. If the operating conditions of a cell are DOD = 50 % with a (mean) SOC = 75 %, it means that the cell is cycled between 50 % and 100 % SOC. To ensure repeatability, most tests were performed with three cells. Because of the high repeatability of the data, an average is presented in this work (unless otherwise mentioned). After each reference characterization procedure (Section 5.5.2) the charge and discharge capacities have to be adapted, since the actual cell capacity $C_{1\mathrm{C}}$ reduces with aging. The sequence of one cycle for each cell was as follows:

(i) Charging by 1 C to the upper SOC limit defined by the case

(ii) pause of 30 min

(iii) CC discharging at defined current rate to the lower SOC limit defined by the case

(iv) pause of 5 min

In step (i), for cases with upper SOC limit $< 75\,\%$, the charging process was limited by charge throughput while for cases with upper SOC limit $> 75\,\%$ and for aged cells, a CV-charging phase was necessary.

The cells were cycled at defined conditions until the total (charge and discharge) capacity reaches 100 equivalent full cycles (EFC). Some cycle tests needed to be stopped before 100 EFC due to technical issues. After cycling, if required, the cells were placed in a 20 °C temperature chamber.

Additional aging tests for studying cross correlation between the two parameters, temperature and DOD, are tabulated in Table 7.2. The cells were first operated at the operating conditions (T_1, DOD$_1$) for 200 EFC and then switched to (T_2, DOD$_2$). The cell testing for these cells also began about two years later than the other cells.

Table 7.1. Test matrix of studied cycle conditions around the mean SOC in %. The parameter CxDy represents (C)harge and (D)ischarge with current rate x and y, respectively.

	T = 0 °C		T = 20 °C		T = 45 °C	
CxDy DOD / %	C1D1	C1D2	C1D1	C1D2	C1D1	C1D2
25			50	50		
50	50	50	25/50/75	50	50	50
60/80/90			50			
75			50	50		
100	50	50	50	50	50	50

Table 7.2. Test matrix for correlation studies with charge and discharge currents of C1D1 and 50 % mean SOC. The arrow indicates the change to different operating conditions.

T_1/ °C	DOD$_1$ / %		T_2/ °C	DOD$_2$ / %
20	50	⇒	45	50
45	50	⇒	20	50
20	50	⇒	20	100
20	100	⇒	20	50

7.3.2 Other cell tests

Electrode materials, both graphite and NMC, were also recovered from unused cells by opening them. Coin cells (of type 2032) with glass fibre Whatman GF/A double layer separator (diameter 1.8 cm and thickness 0.3 mm) and T-cells (1 cm electrode diameter) with glass fibre Whatman GF/A double layer separator (diameter 1 cm and thickness 0.3 mm) of these electrodes vs. lithium metal (reference/counter) were prepared for further analysis. The electrolyte used was 1 M LiPF$_6$ in EC:DMC 1:1 v/v + 1 % VC. Additional analysis performed on these cells are described in the relevant sections.

7.4 Results and discussion

7.4.1 Cell capacity

In discussing results, to refer to a certain test case, the temperature, DOD, current rate and SOC of the test case are used in that order as identifier. For example, the cells cycled at 20 °C, with a DOD of 50 % with a charge and discharge rate of 1 C around a mean SOC of 75 % is referred to as 20 °C DOD50 C1D1 SOC75 case.

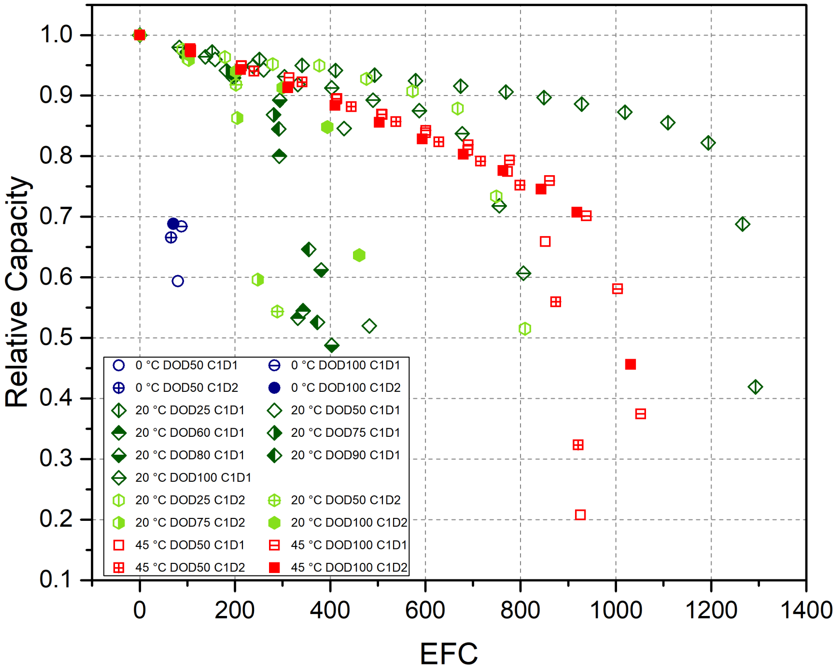

Figure 7.1. Capacity fade

Only in cases where the mean SOC around which the cell is cycled is not 50 %, the SOC is mentioned in the identifier. This is because, most cells were cycled around this SOC value.

In Figure 7.1, relative capacity fade has been plotted for the cells of Table 7.1 that were cycled around the mean SOC of 50 % to present an overall picture of cycle induced aging. For all experimental tests performed, the fastest rate of capacity fade is seen in the case of 0 °C with almost no DOD or current rate dependence. Their capacity decreases below 70 % of the initial capacity in less than 100 EFC. No quantitative analysis can thus be made for cells cycled at this temperature. On the other hand, the slowest decrease in capacity is seen for 20 °C DOD25 C1D1 case, where more than 1200 EFC are measured. The cells cycled at 20 °C have a strong dependency on the DOD and current rate, while at 0 °C and 45 °C negligible dependency is observed.

Most cells also show a clear distinction into two capacity fade stages: a slow linear capacity fade initially that is followed by a rapid capacity fade. The transition between these two stages depends strongly on the operating conditions of the cell and does not happen at the same capacity for all cells. However, once in the rapid capacity fade stage, the capacity declines dramatically within a few EFC for all cells.

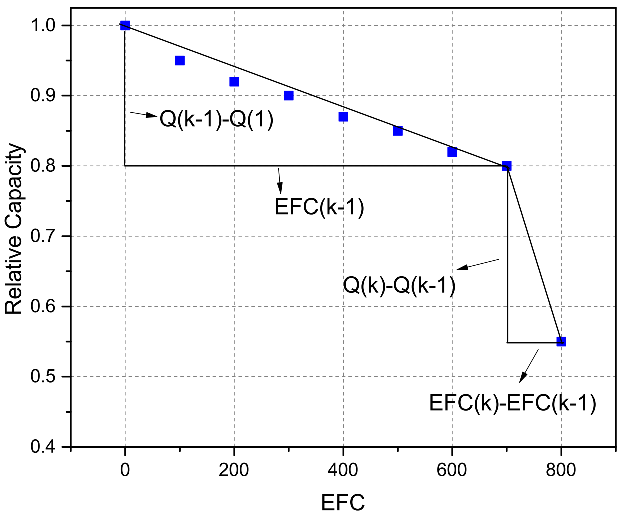

Figure 7.2. Illustration to explain quantities used to define cycle life based on transition from slow linear capacity fade to rapid capacity fade.

Generally it is assumed that once the batteries have 70 % or 80 % remaining capacity, they should be retired from their primary application [105, 187]. However, as seen here, capacity of some cells fades rapidly even before reaching 80 % relative capacity while others continue the slow linear capacity fade beyond 80 % relative capacity. Thus, in this work transition to non-linear aging stage is chosen as the criteria for deciding end-of-life (EOL) and consequently cycle life. The mathematical formulation of cycle life based on this criteria is explained below.

Transition to rapid capacity fade: the transition to the rapid capacity fade is calculated using the following method. A battery has reached the rapid capacity fade aging stage, when the local slope of capacity decrease per EFC step is larger than twice the overall slope of capacity decrease per EFC (see Figure 7.2). This means, the k^{th} point of measurement of an cycle aging test is considered to lie in the rapid capacity fade aging stage if

$$\frac{Q(k) - Q(k-1)}{EFC(k) - EFC(k-1)} \geq 2 \cdot \frac{Q(k-1) - Q(1)}{EFC(k-1)} \tag{7.1}$$

where $Q(k)$ is the capacity and $EFC(k)$ are the number of EFC at the k^{th} measurement point. Based on this definition, the cycle life in the slow linear aging stage $\mathrm{EFC_{life}}$ is defined as follows:

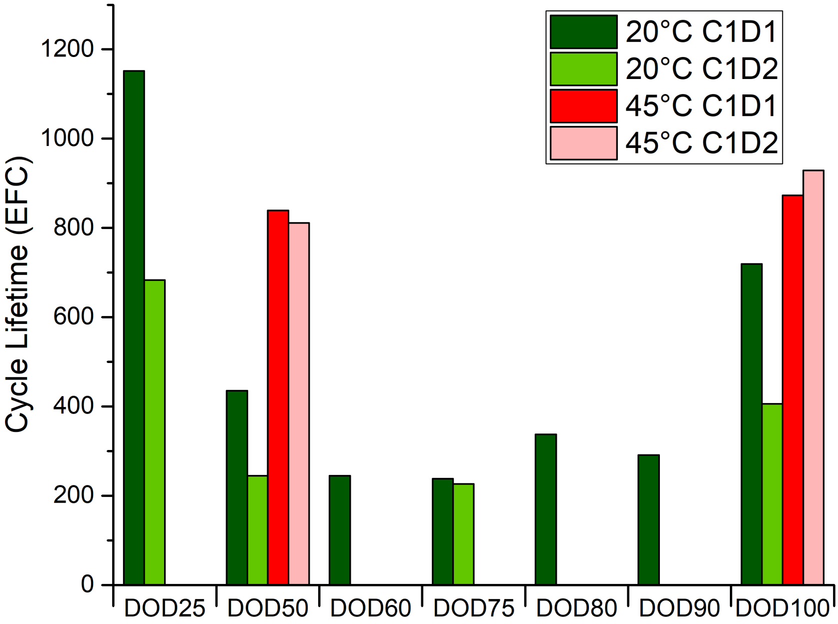

Figure 7.3. Cycle life

$$EFC_{life} = EFC(k-1) + \frac{EFC(k) - EFC(k-1)}{2} \tag{7.2}$$

where $EFC(k)$ is the EFC at the k^{th} point of measurement and k is the number of the first point of measurement that is inside the non-linear aging stage.

Based on this definition the cycle life are plotted in Figure 7.3 for the cases presented in Figure 7.1.

Temperature dependency: capacity fade dependence on temperature shows a clear trend. The cells cycled at 0 °C show dramatic capacity fade and are already below 70 % of their initial capacity before completing 100 EFC. The dominant phenomena here causing such rapid capacity fade is understood to be lithium plating which is accelerated by greater polarization of the negative electrode at low temperatures [100]. This arises because of slow diffusion through the SEI at low temperatures and low ionic conductivity. Once lithium gets deposited over the negative electrode, it reacts rapidly with the electrolyte causing irreversible loss of cyclable lithium manifested by the sudden capacity fade seen.

Between 20 °C and 45 °C, a longer cycle life is seen in the latter case independent of the current rate and the DOD. Looking closely at Figure 7.1, one can see that in all cases of cells cycled at 20 °C, a rapid capacity fade is observed even before the capacity fade reaches 80 %, while at 45 °C, the linear aging stage continues

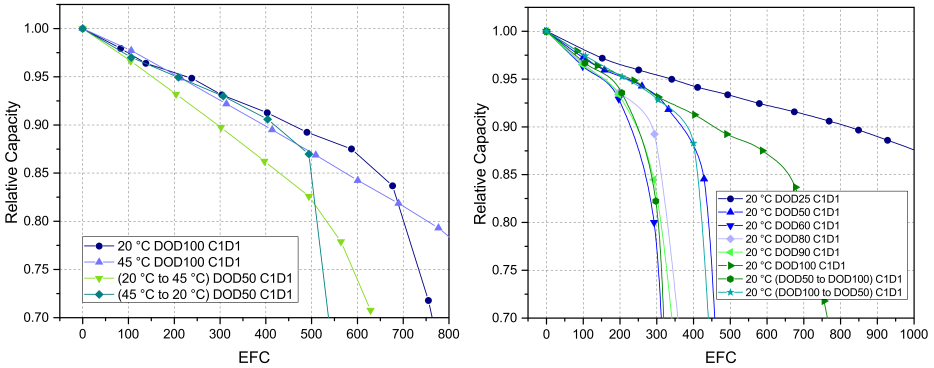

(a) 20 °C and 45 °C for 1 C charge rate and 1 C discharge rate

(b) different DOD for 1 C charge and 1 C discharge rate at 20 °C

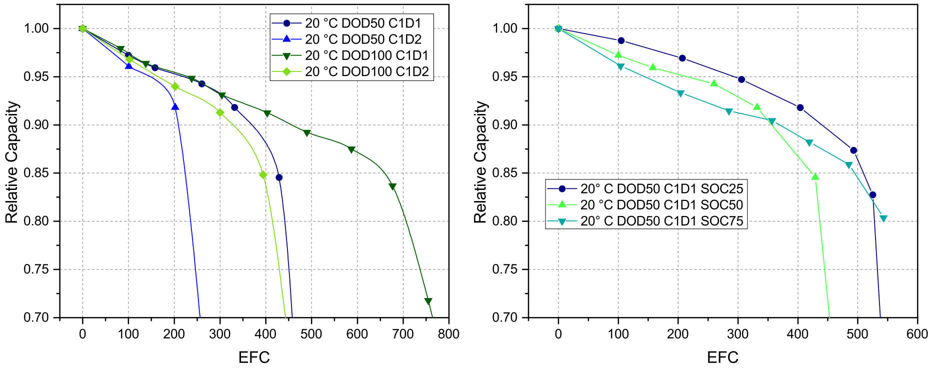

(c) two different discharge rates cycled at 20 °C for DOD of 50 % and 100 %

(d) different mean SOC for 50 % DOD and 1 C charge rate and 1 C discharge rate

Figure 7.4. Capacity fade vs. EFC at different conditions

even after reaching the 80 % mark. Also the longer cycle life in the case of 45 °C can be despite the higher rate of linear capacity fade as can be seen for the case of C1D1 DOD100 case (Figure 7.4a). In general, the onset of rapid capacity fade is retarded at higher temperatures. Figure 7.4a also shows the behaviour of cells whose operating temperature are switched at 200 EFC. The cell which is initially cycled at 45 °C has a similar capacity fade as the DOD100 cases. The cycle life in this case is extended but it is still much shorter compared to the cycling at only 45 °C. The cell cycled initially at 20 °C shows a much faster capacity fade.

DOD dependency: in the case of 20 °C C1D1 it can be noticed that low DOD of 25 % (cycled between 37.5 % SOC and 62.5 % SOC) has particularly low capacity fade and a long cycle life. Capacity fade for cells cycled for DOD of 50 % to 90 % is higher and cycle life shorter, but not in an obvious orderly manner with respect to the DOD (Figure 7.3 and Figure 7.4b). Greater DOD is reported to cause higher capacity fade, a direct consequence of more undesirable reactions at high voltages and thickening SEI at low negative electrode potentials [130, 153, 183]. While this reasoning works when looking only at DOD values that are well separated such as 25 %, 50 % and 75 %, the dependence on DOD is much more complex if more intermediate DOD values are considered. This has been investigated in depth by EIS analysis and explained in Section 7.4.3.

An anomaly to consider is the specific case when the cell undergoes full cycling (DOD = 100 %). Notice in Figure 7.3, the cycle life is counter-intuitively extended for this DOD independent of current rate or temperature. This is despite the local potentials at both negative and positive electrodes being at their extremes. The DOD100 case has been further discussed in Section 7.4.5. The dependence of capacity fade on DOD decreases at 45 °C where only a slightly increased cycle life can be noticed for DOD of 100 % compared to 50 %.

Another interesting behaviour is seen for the correlation test cells (Table 7.2), shown in Figure 7.4b. The cell which is initially cycled at DOD100 and later switched to DOD50 shows lower capacity fade and longer cycle life than the cell initially cycled at DOD50 and switched to DOD100.

Current rate dependency: at 20 °C, a greatly reduced cycle life and substantial increase of capacity fade is seen (Figure 7.3 and Figure 7.4c) as the discharge current increases from 1 C to 2 C. This is consistent with literature [130, 135]. A higher ionic current density requires faster reaction and diffusion kinetics in the electrodes. This causes greater mechanical stresses especially in the negative electrode, resulting in cracks and fissures and leading to increased SEI formation. The loss of reversible lithium in repairing the SEI is manifested as capacity fade.

At 45 °C, cycle life shows no significant dependence on the current rate. Wang et al. [130] also noticed that current rate has a lower impact on capacity fade at higher temperatures. The detrimental influence of high rate is possibly mitigated by an increase in the reaction rate kinetics as well as ion diffusion kinetics in the particle at higher temperature, reducing the surface stress on the particle.

Mean SOC dependency: Figure 7.4d shows the aging results of the cells cycled with DOD 50 % around the mean SOC of 25 %, 50 % and 75 % at 20 °C. For the first 300 EFC, higher the mean SOC values, greater is the rate of capacity fade. This is a direct consequence of high voltages causing greater undesirable reactions as noted in the previous section also for high DOD. The cycle life of these cells are, however, not in this order and the rapid capacity fade stage is reached the latest for the cell cycled around a mean SOC of 75 %. This is explained later in Section 7.4.5.

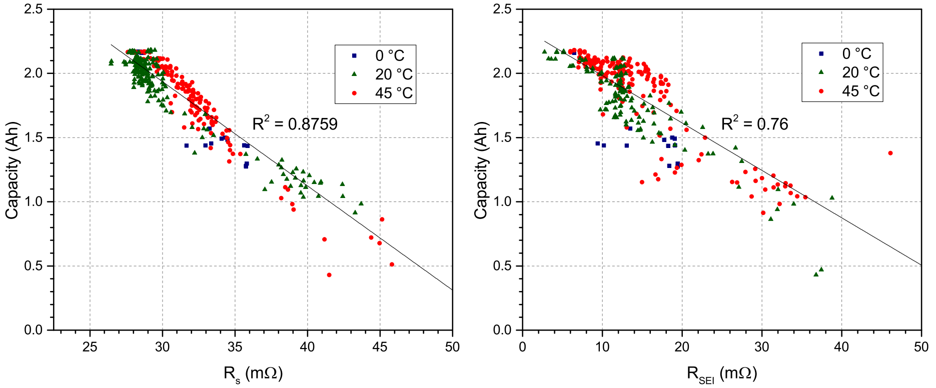

(a) Series resistance (b) SEI resistance

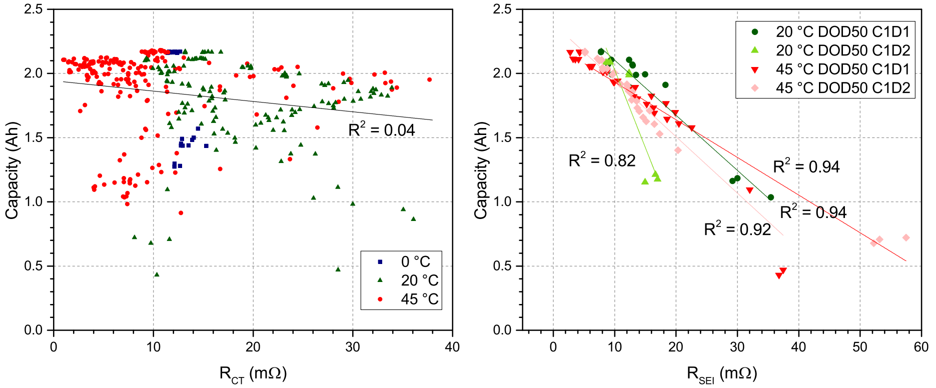

(c) Charge transfer resistance (d) Individual SEI resistances

Figure 7.5. Correlation of capacity fade with resistances determined from equivalent EIS circuit

7.4.2 Cell impedance

Unlike calendar aging, cell impedance has only been studied using electrochemical impedance spectroscopy. Out of the 10 fitting parameters, the values of resistances (R_s, R_{SEI} and R_{CT}) extracted from the fitting of the equivalent circuit (Figure 5.3b) have been analysed in this work. All fitting parameters are tabulated in Appendix C.

Capacity fade correlation

Capacity fade is a consequence of loss of lithium ions and loss of active material in the electrodes. On plotting the fitted values of series resistance R_s with capacity fade (Figure 7.5a), a strong correlation (adjusted R-squared = 0.88) is found between the two. The value of adjusted R-squared value for the correlation between capacity and R_{SEI} is slightly lower at 0.76 (Figure 7.5b). The correlation of capacity with R_{CT} has an R-squared value of 0.04 (Figure 7.5c). This suggests that the major cause of capacity fade is the loss of the electrolyte mainly caused by its reaction with lithium to form the SEI. This is consistent with literature where capacity fade is attributed to SEI formation in NMC based chemistries [130, 163, 182, 186]. It can also be inferred from the results that the capacity fade is not correlated to processes at the positive electrode.

The slightly lower correlation between capacity fade and R_{SEI} compared to the correlation between capacity fade and R_s may be explained by the fact that the SEI formed is a mixture of compounds whose composition depends on the operating conditions (temperature, DOD and current rate). This means that the same quantity of electrolyte can react to form SEI with different properties. Evidence for this reasoning can be seen in the plot between R_{SEI} and capacity (Figure 7.5d) for some operating conditions. A much better correlation coefficient is seen for each individual operating case. Schuster et al. [183, 188] also recommend using R_s as indicator for state of health rather than $R_{SEI} + R_{CT}$, which they found to be sensitive to operational conditions.

Onset of rapid capacity fade

Cells in this study (and elsewhere [125, 128, 153, 177, 183, 185, 186]) are observed to have a slower linear capacity fade followed by a rapid capacity fade. The transition point (and hence the cycle life of the cells) from the slow linear to the rapid capacity fade varies widely for the different operating conditions. EIS combined with SEM and EDX analysis is used to investigate the rapid capacity fade phenomena in detail.

Consider the capacity fade for cells shown in Figure 7.6a. The cells have been cycled with the same DOD (50 %) around the same mean SOC (50 %) and the same rate (C1D2) but at two different temperatures. While the cell at 45 °C has a long slow linear aging stage lasting more than 600 EFC, the cell at 20 °C undergoes a transition to rapid capacity fade stage between 200 EFC and 300 EFC. Scanning Electron Microscopy (SEM) and Energy Dispersive X-Ray spectroscopy (EDX) were performed at the four states numbered in Figure 7.6a for both the graphite and the NMC electrode. The graphite electrodes at these four aging states are shown in Figure 7.6b for the same magnification. In the case of the cell at 45 °C, at around 300 EFC (State 3), the graphite electrode looks very similar to the pristine negative electrode (State 1). Individual particle boundaries can be easily noticed. There is an occasional amorphous deposit, which can be the binder. It can be expected that the SEI has grown in the cycled state, however the growth is in the nm range or lower [136, 137, 189], too small to be detected by SEM. For about the same number of EFC, the graphite electrode of the cell cycled at 20 °C shows a rough surface deposition covering the entire electrode surface facing the separator

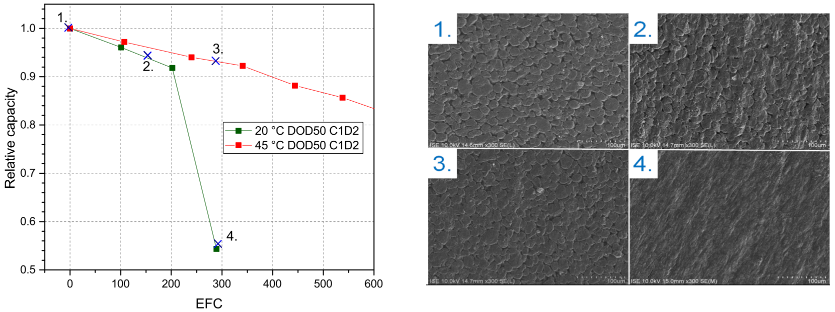

(a) Capacity fade depicted at four states for 2 cells cycled at 20 °C and 45 °C

(b) SEM images of top view of the negative electrode at the four states

Figure 7.6. Rapid capacity fade behaviour

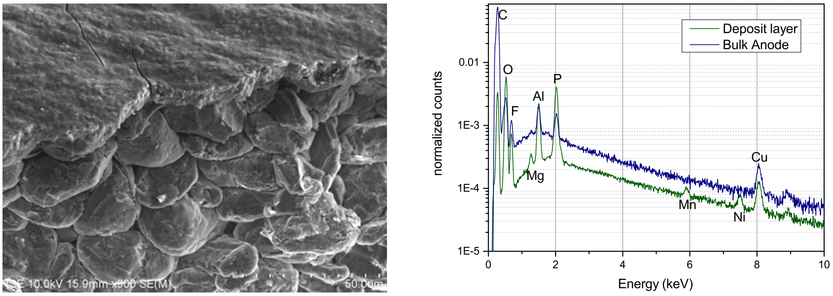

(a) Cross-sectional SEM of the negative electrode in the rapid capacity fade region

(b) EDX for the bulk negative electrode region and the deposit layer

Figure 7.7. Investigation of state 4 through SEM and EDX

(State 4), and no particles can be individuated. The difference being that this cell is in the rapid capacity fade stage. In the slow linear fade stage of this cell, at an intermediate EFC (State 2, about 150 EFC), the graphite electrode looks very similar to the pristine negative electrode.

In Figure 7.7a, the cross-section of the negative electrode sample for State 4 can be seen. The rough deposition observed over the electrode now appears as a distinctive layer of a few μm between the agglomerate of graphite particles that form the electrode and the separator. The graphite morphology underneath the deposition is largely preserved. EDX is carried out for both the deposit layer and the graphite particles below the layer (Figure 7.7b). Mainly X-rays from the K-shell of the atoms are observed in spectra. For State 4, the spectrum taken from the region below the surface deposit layer is similar to that of the pristine

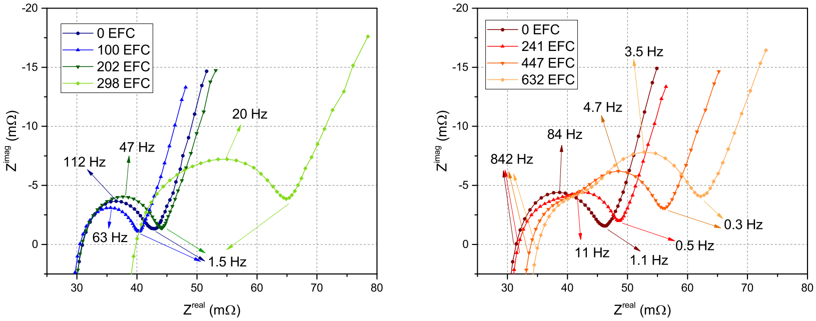

(a) 20 °C DOD50 C1D2 (b) 45 °C DOD50 C1D2

Figure 7.8. EIS spectra for cells at different aging states

negative electrode sample. Instead, the spectrum of the surface layer shows higher counts of oxygen and phosphorous. Clearly the layer is formed from the breakdown components of the organic electrolyte and the inorganic salt $LiPF_6$, commonly present in the electrolyte. Aluminium is used as the positive electrode current collector and is considered stable in the presence of $LiPF_6$ salt [190, 191]. Thus, its presence in the graphite layer needs further investigation. It is outside the scope of this work. Also note the presence of positive electrode materials such as manganese and nickel in the deposit layer. Magnesium is also detected in the deposit layer. However, no magnesium was seen in the EDX of the positive electrode. Thus, the source of magnesium can only be conjectured as being from an additive to the electrolyte [192], the composition of which is not known. EDX spectra of the positive electrode (not shown) for all four states are also similar, confirming no drastic changes in composition with cycle aging.

Parts of the deposit layer were metallic golden under argon when the cell was opened up for post-mortem and then became matt silver on exposure to air. This behaviour has been observed in many studies and is known to be plating of lithium [128, 131, 153, 193, 194]. The observed rapid capacity fade can be attributed to deposition of lithium considering also that the bulk electrode morphology and composition has not changed for both graphite and NMC. Positive electrode's minimal role in rapid capacity fade phenomenon is further substantiated by the fact that rapid capacity fade and deposit layer phenomena have also been seen for chemistries other than NMC [128, 152].

Role of negative electrode and electrolyte

The role of electrolyte and graphite in rapid capacity fade phenomenon is further investigated using EIS. EIS spectra for the cells discussed in the previous section can be seen in Figure 7.8a and Figure 7.8b. It can be seen that for the cell cycled at 20 °C, the spectrum does not change much but instead after a few hundred EFC

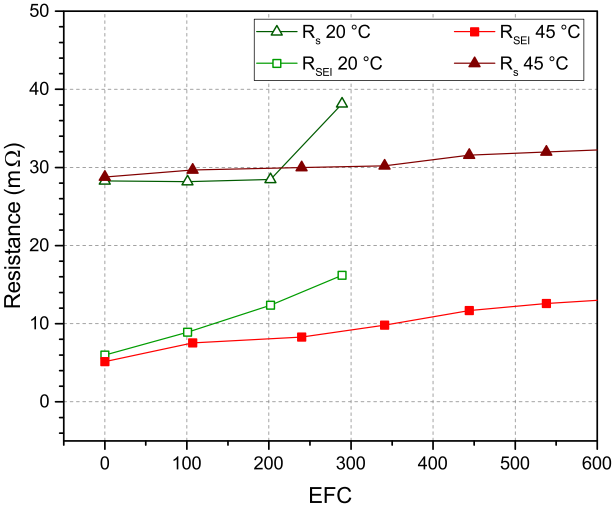

Figure 7.9. Evolution of series and SEI resistance with EFC for cells cycled at 20 °C and 45 °C

is horizontally shifted towards higher impedance. The spectrum at 45 °C shifts and enlarges gradually and electrode processes become more distinct as the cell ages. There is a also a shift towards low frequencies. The fitting results for series and SEI resistance are seen in Figure 7.9. There is a faster growth of R_{SEI} at 20 °C than at 45 °C. The onset of rapid capacity fade for the 20 °C cycled cell in Figure 7.6a is here seen to be accompanied by a jump in the value of R_s. In other test cases, a simultaneous jump is the value of R_{SEI} is also clearly distinguishable.

Considering and combining the evidence from EIS, capacity fade results and post-mortem analysis, the sudden increase in values of R_s and R_{SEI} indicates a change in process in the cell. In the slow linear capacity fade stage, the SEI resistance increase is also slow and gradual. Instead, in the rapid capacity fade stage, the SEI resistance is seen to increase dramatically due to the formation of the several μm thick deposit layer. The probable reason why this deposit layer does not show as a separate process in the spectra may have to do with the similarity in charge transfer process across this deposit layer and the SEI layer. The EDX of the deposit layer confirms the presence of electrolyte degradation products [185]. Moreover, this deposit layer is known to be not very lithium conductive [177] and to cause impediment to ion movement [194]. Fu et al. [185] even suggest that this deposit layer leads to active material loss which shows up as capacity fade.

Electrolyte reduction, confirmed by the presence of electrolyte decomposition products in the deposit layer, causes a rapid decrease in ionic conductivity of the electrolyte. This shows up as the simultaneous jump in R_s. Drying of the separator has been reported in conjunction with the formation of the deposit layer [131, 182, 185].

Since the sudden jumps in values of R_s and R_{SEI} are concurrent, a possible mechanism to explain it is as follows. As the SEI layer becomes thicker and increasingly resistive with cycling, at a certain moment the local potential on the surface of the negative electrode drops below 0 V causing lithium deposition [195]. According to Broussely et al. [128] this happens when progressive clogging of pores of graphite by the growth of the SEI layer leads to a reduction in active surface area of graphite such that reduction rate of lithium-ion is greater than the maximum possible diffusion rate of lithium in graphite. This process can be accentuated due to inhomogeneous current and potential distribution in the cell [131, 139, 186]. Deposited lithium reacts rapidly with the electrolyte [139] whose decomposition is evidenced by the increase in R_s. Electrolyte's reaction with the deposited lithium initiates the formation of the deposit layer which causes a further increase in R_{SEI}. A positive feedback loop is set into motion as the local negative electrode potential decreases further due to increased resistance of the deposit layer leading to more lithium deposition, more electrolyte decomposition and the tremendous growth of deposit layer to micrometer dimensions in a matter of a few EFC.

7.4.3 Critical SEI resistance

Arguments in the previous section point to the existence of a critical value of SEI resistance. With cycling, the SEI resistance increases and at one point becomes equal to the critical SEI resistance value. At this point, the potential at the negative electrode is exactly 0 V. Any further cycling causes SEI resistance to increase more than the critical value, and the local potential at the negative electrode drops below 0 V. This leads to lithium deposition over the negative electrode, causing the positive feedback loop of electrolyte decomposition and deposit layer formation which is manifested as the rapid capacity fade.

Further evidence of this comes from considering the cycle life for the cells cycled at 20 °C at 1 C charging and 1 C discharging current in Figure 7.3. As discussed before in Section 7.4.1, the nature of dependence of cycle life on DOD is complex if one looks at DOD values from 50 % to 90 %. In descending order, the cycle life is for case DOD50 > DOD80 > DOD90 > DOD60. Consider now the growth of R_{SEI} for these cases as shown in Figure 7.10a. It can be noticed that the resistance increase rate corresponds inversely to the cycle life i.e. greater the growth of SEI resistance, less is the cycle life noticed or faster is the onset of rapid capacity fade. A faster increase of SEI resistance leads to a earlier attainment of the critical SEI resistance value, beyond which the cell degrades rapidly due to lithium plating.

The transition from the gradual increase to the rapid increase of SEI resistance is concurrent to the transition from the slow linear like increase in capacity fade to the rapid fade stage. The transition happens between 15 mΩ to 19 mΩ for the cells shown in Figure 7.10a indicating that the critical SEI resistance value is in this range. Because of the regular characterization test interval of 100 EFC, a more precise value cannot be estimated.

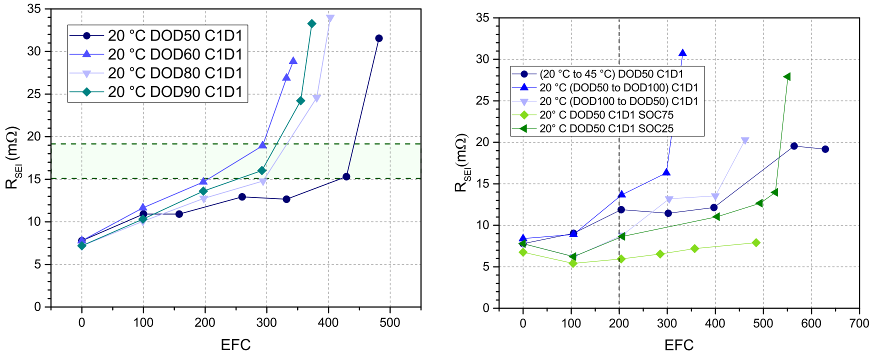

(a) cells cycled at 20 °C C1D1 for different DOD around a mean SOC of 50 %. The highlighted area is meant only as a visual aid

(b) cases in Table 7.2 and cases with a mean SOC not equal to 50 %. The black dashed line indicates the EFC where the switch in the operating conditions is effectuated for the relevant cases

Figure 7.10. SEI resistance vs. EFC for different test cases

A critical SEI resistance value will also be a function of DOD, temperature and current rate. This arises due to the degree of polarization at the graphite electrode that depends on the above factors. The local potential of the graphite electrode is lower at higher SOC. Thus, the critical value of SEI is also lower at higher DOD for the same mean SOC. This behaviour is however not linear, due to the staging behaviour observed in graphite.

As for the effect of temperature on critical SEI value, at high temperatures, the local graphite potential is higher, the transport properties of electrodes and electrolyte are enhanced and thus the critical SEI value is expected to be higher. The range of SEI values at 45 °C at which the transition to rapid capacity fade takes place for the tested cells is noticed to be between 20 mΩ to 27 mΩ which is higher than those seen at 20 °C. The rapid capacity fade is consequently later and cycle life longer at 45 °C as seen in Figure 7.4a and Figure 7.6a. The low cycle life of cells cycled at 0 °C can also be explained by the concept of SEI resistance.

Since lithium plating takes places during the charge cycle, no difference in values for critical resistance are expected between the C1D1 and the C1D2 cases since the charging current is the same in these two cases. This is observed in the experimental data where the range of transition for 45 °C C1D1 case is between 21 mΩ to 23 mΩ and for 45 °C C1D2 case it is between 20 mΩ to 27 mΩ. Similarly, at 20 °C, for C1D1 case, it is between 12 mΩ to 20 mΩ and for C1D2 case, it is between 12 mΩ to 18 mΩ. Some examples of evolution of R_{SEI} and its transition from slow to rapid increase can be noticed in Figure 7.10b for the cases in Table 7.2 and cases where the mean SOC is not 50 %.

The onset of rapid capacity fade due to lithium plating is a function of the operating conditions (DOD, temperature, current rate) which not only affects the resistance of the formed and reformed SEI but also influences the value of critical SEI resistance. In real life applications, the operating conditions are not constant current, constant temperature or fixed DOD conditions such as in this experimental study. Thus a critical SEI resistance will not be a constant value but will vary depending on the immediate operating conditions of the cell. By keeping track of the critical SEI resistance value, the cell can be more optimally used in applications.

7.4.4 Increase of SEI resistance and degradation parameter calculation

In this section reasons for difference in the increase of SEI resistance for different operating conditions are discussed. Furthermore, the cycling data is crunched to yield degradation parameters that illustrate the role of electrodes and electrolyte in causing capacity fade.

SEI consists of a variety of chemical species and is formed from the reduction of the electrolyte at the graphite electrode. Its composition depends on the local graphite potential. Ideally, SEI should be lithium-ion conductive and electronically insulating in order to prevent further electrolyte reduction and lithium ion consumption. Bilayer structure represents the complex SEI layer. The layer near the interface of the electrolyte is more organic and porous. The inner layer, adjacent to graphite particles, is denser, conductive and more inorganic [136].

SEI transforms from organic to inorganic as the potential at the negative electrode is lowered [136, 137, 196]. According to An et al. [136], elevated temperatures lead to more stable SEI formation, while at higher current densities the SEI formed is more porous with high electronic and ionic conductivity. For the batteries tested in this work, the SEI resistance growth is slow at 45 °C (Figure 7.9). This combined with the higher critical SEI value due to higher temperature, cause the cells cycled at 45 °C to have a longer cycle life irrespective of the DOD. Lu et al. [137] further found that lower the negative electrode potential lower is the resistance/thickness ratio of the SEI layer. Thus thickness is not the only factor deciding SEI resistance as is usually assumed. The SEI formed at high graphite potential is more porous. As the cell is cycled from a higher to a lower SOC, a multi-layered structure of SEI is formed which leads to depression of semicircle seen for the first semicircle in the EIS spectra. The evolution of the SEI resistance at a constant current rate and temperature is a function of the DOD since the layer composition depends on the local graphite potential.

Volume expansion in graphite is known to be higher than NMC [142, 177, 183]. This volume change is not uniform over a charge/discharge cycle. Ecker et al. [153] observe that crossing of certain SOC levels causes greater lattice parameter changes and hence higher volume changes and more stresses. These stresses lead to micro-cracks in graphite particles leading to more SEI formation. Higher degradation is seen when the cycle crosses transitions between

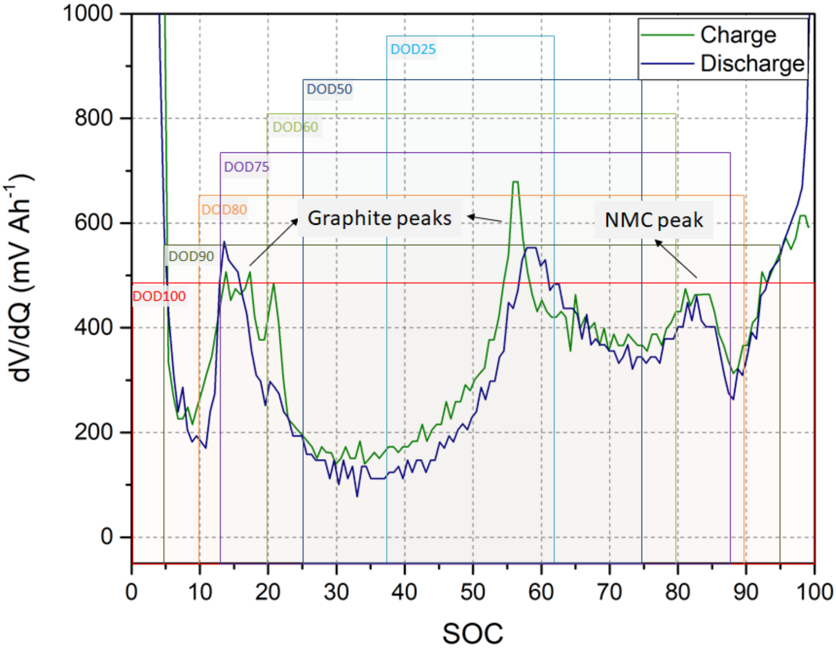

Figure 7.11. dV/dQ curve for the full cell for slow rate charge and discharge conditions with individual peaks recognized and DOD regions highlighted

voltage plateau of graphite. Oh et al. [197] also show that macroscopic swelling of a NMC-graphite battery is dominated by the graphite electrode. Moreover, swelling of the battery corresponded to the voltage plateaus where in the plateau region, the swelling rate is low. The galvanostatic method for electrochemical characterization of the Sony cell is shown in Figure 7.11 as a differential voltage $dV/dQ-$curve. The peaks in the $dV/dQ-$curve have been assigned to the negative and positive electrodes from galvanostatic measurements as plotted in Figure 7.12. During cycling the stresses generated per EFC depend on the count of traversing voltage peaks per EFC. More crossing of voltage peaks should lead to more volume changes in the electrodes, causing greater stresses, leading to more SEI repair and hence more resistance increase.

Determination of degradation parameters: as discussed before, growth of the SEI layer and increase of the SEI resistance are the leading cause of capacity fade. These depend on the local potential at the graphite electrode and crossing of voltage peaks. In order to associate capacity fade to the SOC, keeping in mind the role of local potentials and crossing of voltage peaks in the evolution of the SEI, the battery SOC is divided into ten equal segments. As any charge throughput causes a loss in capacity in the cell, each of these segments are associated with a

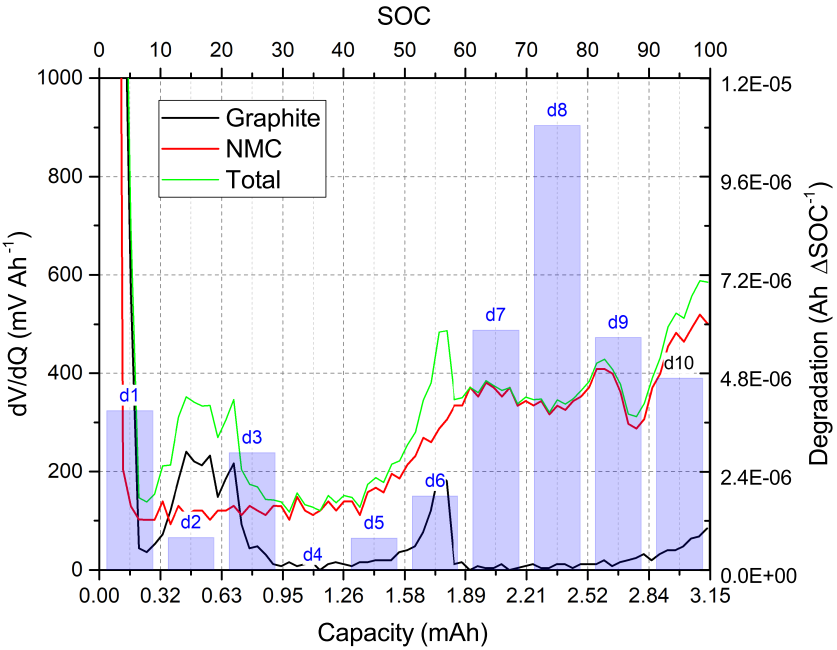

Figure 7.12. dV/dQ curves of negative and positive electrodes from characterization during charging plotted along with degradation parameters

degradation rate (d_1, d_2,..., d_{10}) with units $\mathrm{Ah} \cdot \Delta\mathrm{SOC}^{-1}$. It is assumed that the degradation rate is constant within each segment. The choice of ten segments is not completely arbitrary but has been motivated by the fact that smaller segments may lead to over-fitting while larger segments may not reveal useful information.

The capacity after any number of EFC is assumed to be given by the following equation:

$$Q_f = Q_o - \left(\sum_i d_i \cdot R_i\right) \cdot EFC \cdot N \tag{7.3}$$

where
Q_f is capacity in A h after cycling for a certain number of EFC
Q_o is initial capacity in A h
i is the segment number
d_i is the degradation in $\mathrm{Ah} \cdot \Delta\mathrm{SOC}^{-1}$ in segment i
R_i is the ΔSOC in segment i (max = 10)
N is the number of times a cell crosses the SOC range of a cycle in one EFC

To illustrate how the equation values are inputted consider the case DOD50 SOC50 case. The transition is from SOC25 to SOC75 in this case, thus

$$\sum_i d_i \cdot R_i = d_3 \cdot 5 + d_4 \cdot 10 + d_5 \cdot 10 + d_6 \cdot 10 + d_7 \cdot 10 + d_8 \cdot 5 \tag{7.4}$$

Parameter N keeps track of how many times a particular region is traversed during cycling. The transition SOC25 to SOC75 is crossed 4 times in one EFC for the case DOD50 SOC50, thus $N = 4$. The other variables C_f, C_o and EFC are experimentally determined.

Experimental capacity fade data until the capacity (Q_f) of the cell decreases to 2 A h for C1D1 20 °C for all cells (except for the cells cycled until 4.2 V) are fitted with this equation with the following methodology. First, the limit of 2 A h that corresponds to approximately a relative capacity of 0.93, is set. This ensures that the fitting is only done for the slow linear capacity fade region for all cells (see Figure 7.1). Additionally, this also minimizes the error caused due to changing potentials experienced by the electrodes as the cell ages [163]. Secondly, the data for the cells cycled until 4.2 V are not used for fitting due to additional effects, discussed later in Section 7.4.5, that are observed in these cells.

The error function is defined by reformulation of Equation 7.3:

$$f_e = \mid Q_f - Q_o - \Big(\sum_i d_i \cdot R_i\Big) \cdot EFC \cdot N \mid \tag{7.5}$$

The objective function is the total error for all tested cells. This total error is given by a summation of the average error for each group of cells. A group corresponds to cells that have been subjected to the same operating conditions.

The optimization problem is to minimize the objective function by varying the degradation parameters representing the different SOC segments. Forty five error functions for the different test cases are used to determine the ten degradation parameters with the method detailed above. The entire problem is formulated using Excel Professional Plus 2016 Solver add-in and solved by an evolutionary algorithm with a convergence of 0.0001, a mutation rate of 0.08, population size of 200 and with 2 random seeds.

The optimized solution provides the value of the parameters d_1 to d_{10}. It fits the data with an average error of 0.0081 A h and a maximum error of 0.0145 A h for every group of cell. For C1D2 cases, the optimization problem is modified to yield a scaling factor for the parameters d_1 to d_{10} calculated for C1D1 cases. A scaling factor of 1.2986 fits the experimental data for C1D2 cases with an average error of 0.0138 A h and a maximum error of 0.0168 A h for each group.

The determined degradation parameters serve the purpose of quantifying the role of transition of SOC states on capacity fade. They implicitly consider the effect of DOD. Cycling between SOC states where the degradation parameters are high will lead to a faster capacity fade. The parameters can be seen in Figure 7.12 where they have been superimposed on the dV/dQ curves. High degradation parameters are seen at higher SOC. Higher SOC corresponds to higher voltages across the electrolyte and lower potentials at the negative electrode. As discussed before, this leads to greater SEI formation. It can be noticed that in the SOC range between 60 % to 100 % the degradation parameter is a factor 3-5 higher compared to region from 30 % SOC to 50 % SOC. On the dV/dQ curve, it can be noticed that the region from 30 % SOC to 50 % SOC is a wide plateau region which is surrounded by graphite peaks on either side. High degradation parameters are also noticed at very low SOC. Ecker et al. [153] and Schmalstieg et al. [172] also noticed a low degradation around 50 % SOC and faster capacity fades for cycling around low and high SOC. The degradation parameters provide evidence that not only potentials but also graphite staging behaviour has an influence on capacity fade.

7.4.5 Behaviour of cells cycled with DOD100

DOD100 cases were omitted from discussion until now because a counter-intuitive longer cycle life is observed for these cells compared to other cases as discussed before in Section 7.4.1 and as seen in Figure 7.3. In Figure 7.13a, SEI resistance and series ohmic resistance extracted from the EIS spectra fitting are plotted for the cases 20 °C C1D1 DOD100 and 20 °C C1D1 DOD50. It is seen that after an initial increase, the SEI hardly increases for hundreds of cycles for DOD100 case, unlike the SEI resistance for DOD50 case where the SEI resistance growth is more uniform and linear. A stable SEI resistance for DOD100 case is also seen in some other works [131, 198]. In the previous section on onset of rapid capacity fade and critical SEI resistance, it was discussed that breaching a critical R_{SEI} causes lithium plating and rapid capacity fade. Even though the critical R_{SEI} value will be low in the case of DOD100, but because of the slow rate of SEI resistance increase, the cell completes more EFC before lithium plating can begin. This results in a longer linear capacity fade and a longer cycle life.

The fact that there is a big difference between the increase of SEI resistance and consequently also the cycle life between cells cycled at DOD of 90 % and 100 %, indicates that stable SEI formation is highly voltage (or local potential) dependent. At very low negative electrode potentials (less than 25 mV), a dense SEI layer is known to form that prevents electrolyte from reaching the surface of graphite, hence protecting the negative electrode [137]. Such low electrode potentials are likely at DOD100.

To investigate further the reason for the slow increase of R_{SEI}, another cell was cycled with only constant current during charging and discharging within the entire cut-off voltage range. Thus to distinguish it from the DOD100 case at which a CV charging phase at 4.2 V was applied, it is referred to as DOD100n case in the text. The series and SEI resistances extracted from EIS fitting for this case are also shown in Figure 7.13a. This cell has a longer cycle life than DOD50 case but less than DOD100 case, hence it also shows improved cycle life compared to DOD90 case. The SEI resistance growth for DOD100n case is faster and more uniform than the DOD100 case. The difference between DOD100 and DOD100n cases, is the constant CV phase, indicating that holding the cell at 4.2 V leads to a stabler

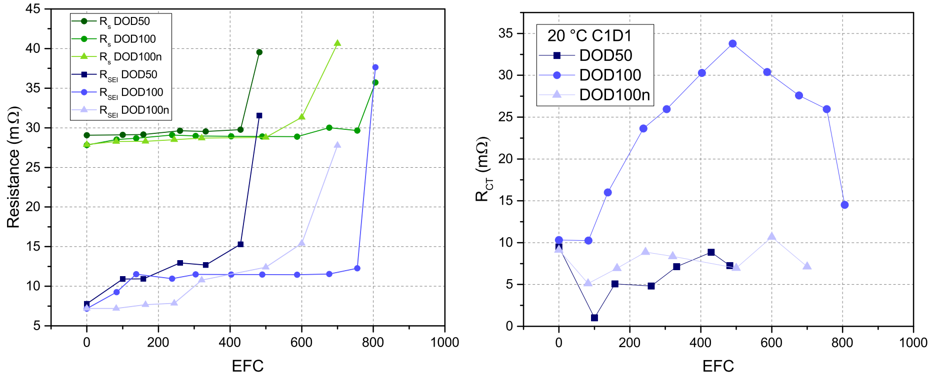

(a) Series and SEI resistance

(b) Charge transfer resistance

Figure 7.13. Evolution of resistances vs. EFC for DOD50, DOD100 and DOD100n cases at 20 °C C1D1 conditions

and more conductive SEI formation. This suggests that the process of conversion of SEI organic layers to inorganic is not only thermodynamically activated (occurring at very low negative electrode potentials) but also kinetically slow. However, once formed this kind of SEI is very stable and greatly immune to the stresses caused by volume changes during the cycling. Other cases, including the 20 °C C1D1 DOD50 SOC75 case, that confirm this behaviour can be seen in Figure 7.10b. Slow increase in R_{SEI} for cells that attain a voltage level of 4.2 V can be noticed.

Another interesting behaviour seen for the DOD100 case is that even though the SEI resistance is quite stable, the linear capacity fade in DOD100 case has not slowed down correspondingly (Figure 7.1). The initial linear capacity fade of DOD100 is found to be similar in magnitude to the DOD100n and DOD50 cases. R_s is also seen to increase at similar rates as for DOD50 or DOD100n (Figure 7.13a) and evidently the slow growth of SEI resistance does not account for the loss of electrolyte.

Answer to this seemingly lies at the side of the positive electrode. Consider R_{CT} for the DOD50, DOD100 and DOD100n cases as shown in Figure 7.13b. Except for DOD100 cases, R_{CT} for all other cases (other values of DOD) show a similar trend: a slight initial decrease followed by a slow, non steady increase. This small initial decrease is attributed to a reduction in graphite's charge transfer resistance due to increased surface area during initial cycling [123, 163]. On the other hand, in the case of DOD100, a very fast and steady increase in R_{CT} is noticed as the cell cycles for a few hundred EFC followed by an equally steady decrease. This behaviour is also thermodynamically activated (not observed for DOD90, hence activated at very high positive electrode potential) and kinetically slow (not observed for DOD100n, which has no CV phase at 4.2 V). Further evidence of the involvement of the positive electrode in causing capacity fade in DOD100 cases

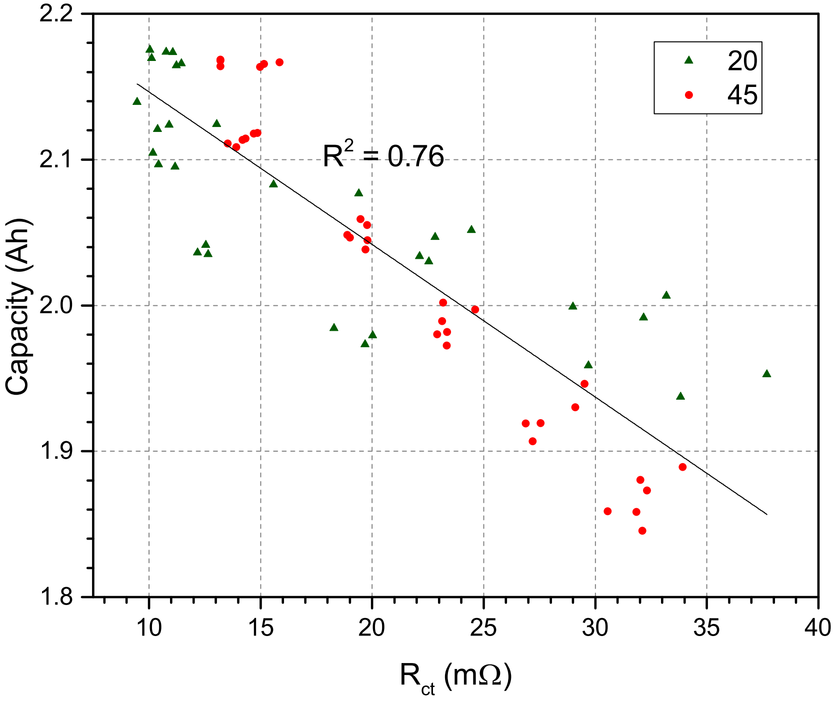

Figure 7.14. Correlation between charge transfer resistance and capacity fade for DOD100 cases

comes from Figure 7.14. Earlier in Figure 7.5c, it was seen that the correlation between charge transfer resistance and capacity fade is weak when all test cases are considered together. The involvement of positive electrode in causing capacity fade was ruled out. However for DOD100 cases, R-squared value for the correlation between charge transfer resistance and capacity fade is much higher.

In literature, different phenomenon have been reported at high potentials on NMC electrode:

(i) PF_6^- intercalation in the graphite added to positive electrode at >4.45 V Li/Li^+ [198].

(ii) Mn, Ni, Co dissociation from the positive electrode and migration to the negative electrode [136, 143].

(iii) Surface changes on the positive electrode, such as decomposition film growth due to unstable electrolyte [128, 136, 141, 199], reduced-reaction layer formation at potential >4.3 V Li/Li^+ [200], layered to spinal phase transition for NMC811 at >4.3 V [184], Li deficit cubic phase on surface for NMC111 cell cycled until 4.2 V [201].

(iv) Cracks caused in the positive electrode surface due to volume changes [142].

Transition metal dissolution in NMC is reported to be not significant [131, 143]. Bach et al. [186] and Schuster et al. [183] report that no major morphological changes take place in the bulk of the positive electrode even when cycled until 4.2 V (CCCV). However, deliberate surface treatment on NMC electrode surface is known to improve capacity retention and slow down impedance increase [202, 203]. Thus, the most plausible theory that can explain the decreasing capacity and increasing series resistance in the case of DOD100 is the change of the positive electrode particle surface due to local electrolyte oxidation at high positive electrode potential. Chen et al. [204] showed that NMC electrodes are responsible for capacity fade and impedance increase for cells cycled over 4.2 V.

Relatable results for R_{CT} are seen in the work of Stiaszny et al. [163]. They observe a burgeoning EIS spectra for the second loop for their cell cycled until 4.2 V (CCCV) that follows the same pattern as seen in this work, an increase for 400-500 cycles followed by a decrease. NMC impedance unlike graphite impedance is a strong function of voltage level (Figures 5.2b and 5.2c). As the reversible lithium content drops inside the cell due to aging, NMC electrode reaches higher potentials at 50 % SOC (EIS measurement were done at this SOC level). For the first few hundred cycles, increased impedance due to electrolyte oxidation on the surface of the positive electrode is dominant. But as the cell ages, the potential effect dominates and is manifested by the decrease in R_{CT} noticed after a few hundred cycles [163].

7.5 Calendar aging results in light of cycle aging behaviour

Periodic characterizations were observed to cause additional degradation during calendar aging studies (Section 6.4.3). Plotting the capacity and impedance data as a function of EFC instead of time provided a better estimate of the relative differences between the different storage conditions.

In the case of calendar aged cells, a counter-intuitive slow impedance increase for cells stored at 50 % SOC compared to 25 % is seen even after the effect of EFC is taken into account. From the dV/dQ curves of the cell and through the calculation of degradation parameters in Section 7.4.4, it is seen that the region around 50 % SOC is a plateau on the dV/dQ curve and has low degradation parameters associated to it. On the other hand, a graphite peak is located around 25 % SOC and the associated degradation parameter value is high. The slower increase in impedance for the 50 % storage SOC case might not only be due to less charge throughput but also charge throughput that causes less degradation. Further evidence of it is seen in [153], where the resistance of the cells stored at 50 % SOC is similar to the cells stored at 30 % SOC initially but with more storage time (>310 days), the resistance for cells stored at 30 % SOC becomes

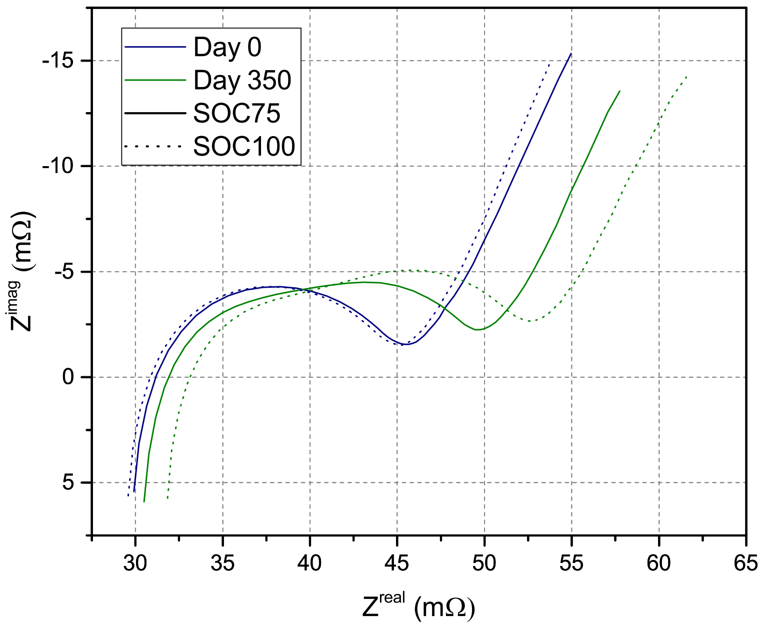

Figure 7.15. EIS spectra for calendar aging cases - SOC75 and SOC100

higher than those stored at 50 % SOC.

Also, even after accounting for the effect of characterization, it was seen that cells stored at 75 % SOC have a greater capacity fade than the cells stored at 100 % SOC (Section 6.4.3). This is further confirmed by the behaviour of reference cells. On the other hand, the resistance, measured through pulse tests, increases more for cells stored at 100 % SOC. Individual resistances, R_s and R_p for cells stored at 100 % SOC are also greater.

From the analysis of cycle aging data for cells whose cycling procedure consists of holding them for a substantial time at an SOC of 100 %, it is seen that they have a slower capacity fade and a longer life. These cells include the DOD50 SOC75 as well as DOD100 SOC50 cases. The reason is found to be a slow increase of R_{SEI} due to formation of a stable SEI layer because of low local potential at graphite electrode.

The calendar aged cells stored at an SOC of 100 % also experience the same favourable conditions for the formation of a stable SEI layer as the cycle aged cells discussed above but for an even longer time. Their slow capacity fade can thus be attributed to the formation of a stable SEI layer while the fast increase of series resistance can be attributed to electrolyte oxidation at the positive electrode surface causing an increase in charge transfer resistance.

Since the calendar aging tests were fitted with one ZARC element, only the total polarization resistance R_p is known. For cells stored at 100 % SOC, even though there is little increase in R_{SEI}, the greater increase in R_{CT} causes a faster increase in R_p than for the cells stored at 75 % SOC. The EIS spectra for these cells are seen in Figure 7.15. The initial spectrum for both cells is almost the same, however after 350 days of storage, the spectrum of the cell stored at 100 % storage SOC shows a much larger separation of the electrode processes and a much bigger second semicircle which corresponds to higher value of R_{CT}.

Part III

Optimal Operation

The essence of knowledge is, having it, to apply it.

Confucius

Chapter 8

Lithium-ion batteries in power systems

As discussed in chapter 1, research into large-scale integration of storage technology in power systems is rooted in conscious efforts across the world to de-carbonize the electricity sector. Concerns of global warming have led renewable energy to occupy a dominant position on the agenda of policy makers and governments throughout the world. As of 1 June 2018, 195 members of United Nations Framework Convention on Climate Change (UNFCCC) are signatories to the Paris Agreement [205]. The International Renewable Energy Agency (IRENA) predicts that by 2050 about 80 % of the electricity could derive from renewable sources, 52 % coming from just solar PV and wind power [8]. DNV-GL forecasts that by 2050, electricity will become the largest energy carrier and its consumption will have increased by 140 % from 2015 [206].

Demand for electricity is highly inelastic. Even today, without significant contribution from renewables, a range of ancillary services are needed to ensure a reliable and safe operation of the power systems. Apart from balancing supply and demand at all times, grid operators also need to ensure supply quality. As contribution of renewables in our electricity mix grows, even greater flexibility will be required. Flexibility currently comes from the generation side through adjusting the output of generators by regulating the flow of coal, oil, gas or water. Wind and sun are however inherently intermittent sources. Thus, wind and solar PV systems cannot contribute significantly to flexibility. The increasing need for flexibility needs to be met by other means such as electrical energy storage systems based on lithium-ion batteries. This chapter explores the role lithium-ion batteries can play in power systems from the point of view of technical and economical feasibility.

8.1 Possible applications in power systems

Lithium-ion technology based storage are a part of the solution to de-carbonize the electricity sector by enabling a greater contribution of renewable energy sources in power systems. The different applications where storage can play a part vary in terms of the how much is the power requirement of the application and for how long it needs to be sustained.

Some prominent applications are:

1. *Operating reserve:* additional capacity available within a short time duration to ensure reliability of supply in case of a peak in demand or failure of a generation unit.
2. *Power quality:* maintaining the voltage, frequency and waveform within prescribed ranges is important to ensure proper functioning of load.
3. *Black start:* initial power supply to restart a grid after blackout.
4. *Power fleet optimization:* service to maximize the share of low marginal cost power plants and minimize the need for peak-power plants, start-ups and shut-downs. Includes peak shaving, load levelling and load shifting applications.
5. *Transmission and distribution (T&D) deferral :* avoiding grid congestion and bottlenecks.
6. *Intermittent balancing:* avoiding curtailment or firming output of renewable power plants.

The power and duration requirements of these applications are plotted in Figure 8.1. Other applications of storage systems include Vehicle to Grid (V2G), Behind-the-Meter and Off-Grid applications. V2G entails using the vehicle battery as an energy storage option for different grid services, Behind-the-Meter applications include maximizing self-consumption of locally produced electricity, hiding demand profile, etc. Village electrification and island grid are examples of Off-Grid applications.

8.2 Technical feasibility of lithium-ion batteries in power systems

Lithium-ion battery technology has increased in popularity in recent years driven by its demand in electric vehicles. High efficiencies, low self discharge, fast response time, good specific energy and power densities have made this technology attractive for integration in power systems. The technical characteristics of these batteries are tabulated in Table 1.1. Based on their power rating and energy capacity, the service area of these batteries has been outlined in

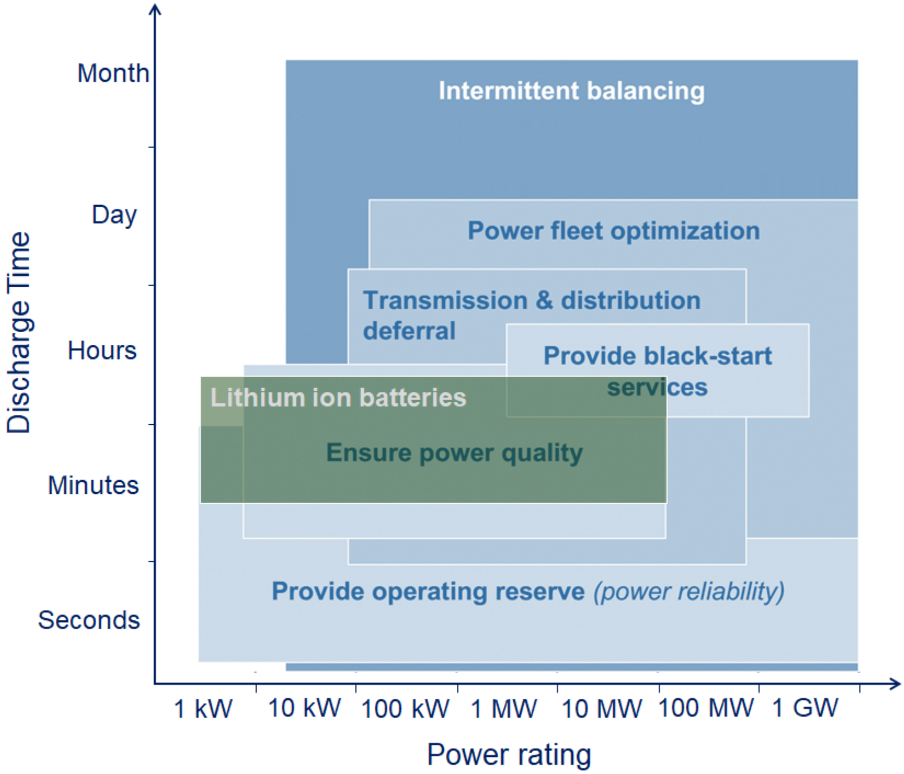

Figure 8.1. Electricity storage applications by power rating and discharge time [10]. Service zone of lithium-ion batteries is highlighted

Figure 8.1. As can be seen, they can be applied to most applications to varying degrees. This versatility of lithium-ion batteries is well recognized. The International Renewable Energy Agency finds them suitable for most grid services [207]. A.T. Kearney Energy Transition Institute believes that the main application areas for these batteries will be T&D deferral, black-start services and intermittent balancing [10]. According to [208], power quality will be the dominant play field for this technology. Hesse et al. [209] consider them suitable for a range of applications such as frequency regulation, black-start, emergency power supply, voltage support, as well as Behind-the-Meter applications on both the low voltage and medium voltage side of the grid.

Since lithium-ion technology has emerged as the most popular option for electric propulsion in vehicles, V2G application will largely be served by these batteries. Their favourable technical characteristics make them suitable for Behind-the-Meter home storage, emergency power supply, islands and Off-Grid villages [207].

8.3 Current structure of the power system

Until 1990s, power systems around the world were centralized where vertically integrated utilities were responsible for generation, transmission, distribution and retail of electricity. Liberalization of the electricity sector began in the 1990s in Europe. The power systems which were mostly state monopolies were unbundled with separation of generation, transmission, distribution and retail activities. In the current power systems in Europe (and some other countries), there is competition among producers and among retailers, pricing of electricity is according to the marginal cost of production and trading of energy and other related products takes place in markets.

These electricity markets have been implemented in many different ways in different geographical locations. However, there are certain common characteristics between these markets [210]. Generation and retail have been opened up for competition. Transmission remains a monopoly managed by non-commercial organizations. To enable trading, different exchanges are usually organized. The most common of them are:

1. *Day-ahead market:* also called as the spot market (or forward market in the USA) is the exchange for short-term transactions. Market participants can submit offers and bids for selling or buying electricity from the grid for the following day. Most countries in Europe have 24 auctions, one for each hour.
2. *Intra-day market:* also known as adjustment market, it allows later adjustments of day-ahead contracts by allowing participants to improve their position based on better information about their consumption or production.
3. *Balancing market:* also called regulation market or real-time market, they ensure that production and consumption are matched at any time through regulating power that is offered by market participants. The imbalances are usually settled ex-post by accounting for actual production and consumption.

These three markets are called energy markets as the remuneration scheme is directly proportional to the amount of energy throughput. Apart from the energy markets, there are ancillary service for which providers can compete. These services improve the reliability and quality of supply. Just like the energy markets, different products exist in different geographical markets for these ancillary services that include black-start capability, frequency response, provision of reactive power, etc.

As an example, in the Netherlands, the three main ancillary services are as follows [211]:

1. *Primary reserve:* also known as frequency containment reserve (FCR), it is the reserve power that acts first in case of an unexpected disturbance. Units providing primary reserve should be able to deliver their full primary reserve power within 30 s. The remuneration is both for the capacity and the energy.

2. *Secondary reserve:* also known as automatic frequency restoration reserve (aFRR) is the second set of reserve power to act in case of an unexpected disturbance and to free up primary reserve to react to a new disturbance. This reserve is activated automatically by the transmission system operator (TSO). The remuneration is both for the capacity and the energy.
3. *Tertiary reserve:* also known as manual frequency restoration reserve (mFRR) is the last set of reserve power for an unexpected disturbance used when the disturbance is very large. The remuneration is both for the capacity and the energy.

Apart from these three ancillary services, there are products for black-start capability and reactive power provision in the Netherlands.

8.4 Economic feasibility of lithium-ion batteries in power systems

While lithium-ion batteries may be technically suitable for a number of services, and may have other societal benefits such as greenhouse gas emission reduction, their implementation in a liberalized power system will depend on their competitiveness vis-à-vis other options. In other words, the extent to which this technology can provide a service at a cost that is attractive compared to alternatives will define its commercial success.

Revenue streams: the economic value that can be derived from lithium-ion battery based storage can be divided into two streams. The first is the revenue from the energy and ancillary markets. The second is based on avoided costs such as deferral of investment for distribution and transmission network.

Deregulation of electricity markets has led to an increased energy price volatility [212]. Since the price is now determined by stochastic demand and supply and set according to the marginal cost of production, it can change at any time. At times of low demand, only inexpensive plants run while during high demand periods, plants with high variable costs are put into operation. Thus the marginal cost of producing power can vary considerably. There are intra-day, intra-week as well as seasonal price patterns seen in energy markets. Lithium-ion batteries can exploit these differences (especially at the intra-day level given their technical limits) by the mechanism of arbitrage. By charging when prices are low and discharging when prices are high, revenues can be generated. Energy markets where there are large differences between prices are theoretically more profitable for storage systems.

In case of ancillary services such as frequency containment reserve, frequency restoration reserves, etc., their provision by traditional power generation assets is mandatory in some EU countries. However, increasing number of countries are moving towards bilateral or an organised market for different ancillary services [213]. Provision of these services by storage systems is thus possible in these markets provided they fulfil other pre-requisites for market participation. The market result may lead to a bilateral contract with the transmission system operator. Revenues in the ancillary markets can be from both energy and power capability.

Storage systems provide two related value propositions based on avoided costs for transmission and distribution upgrade deferral. One is by obviating the need to upgrade the equipment. The other is through the extension of life of existing equipment. They do this by alleviating traffic congestion along the power lines and other T&D equipment during peak times. The benefit can be compelling if the upgrade that is deferred is expensive relative to the cost of the battery storage required.

Business cases: business cases for lithium-ion batteries in isolated systems such as for islands have been shown to be feasible for a variety of services [214–216]. Recognizing this potential of lithium-ion batteries, there have been some large investments in installing these batteries for different applications. Some examples include combined solar or wind and storage units (multi MW h/MW scale) that have been installed in island communities such as Maui and Kaua'i in Hawaii [8, 217] and Ta'u in American Samao [218]. These displace the use of diesel and allow greater integration of renewables. The main reason for the success of lithium-ion batteries in these island systems is the lack or high cost of alternatives.

For mainland systems, the business cases are more difficult to evaluate. Generic studies on economic value of batteries such as the study by McKinsey & Company [219] cite frequency regulation, renewable energy technology firming and smoothing and T&D investment deferral as the most promising applications on the utility side. On the customer side, demand charge reduction, self-consumption, power reliability and backup are seen to be the most profitable. A study from Deloitte [9] sees economic viability of lithium-ion batteries in providing ancillary services. According to them, other applications such as T&D investment deferral, renewable integration and small scale behind-the-meter storage are also becoming increasingly interesting economically. The economic potential for arbitrage is deemed low and is not expected to improve much in the future.

From the analysis of area-specific and detailed scientific studies, it can be inferred that there is not a generic answer. Whether lithium-ion batteries are economically feasible in a specific geographical marketplace depends on the structure and the prices for the different products in the energy and ancillary markets and on the characteristics and costs of the lithium-ion battery. For instance, while frequency regulation is found to be feasible in the German [220], Dutch [221], Korean [222] and the PJM (USA) markets [223], it is insufficient in the Danish, Portuguese and British market [224]. In contradiction, the Danish primary frequency regulation market is found to be economically profitable in [225]. Price arbitrage in day ahead market is seen to not have enough economic potential in Germany [226], Portugal [224], Denmark [224], Great Britain [224] as well as the PJM market [227].

Evidence of business cases in main land systems is limited but increasing. Some real-life large-scale commercial lithium-ion battery based storage systems include Tesla's 129 MW h/100 MW project in Australia to mainly act as an operating reserve [228], multiple multi MW projects in California such as AES Energy Storage and SDG&E 120 MW h/30 MW project to ensure reliability and maximize renewable energy use [229].

There is a consensus building up among researchers that a single application may yield too little to make a valid business case for lithium-ion battery based storage in many different geographical markets. Simultaneous participation in multiple markets is often suggested as the way forward for energy storage systems [149, 230, 231]. Economic feasibility has been demonstrated by combined participation in Iberian day-ahead market and secondary reserve market [232]. In [233], investment deferral combined with reduction of curtailment is found to be a viable business case in Belgium.

Other studies demonstrate that even combining markets may not be adequate. Zakeri et al. [230] studied the Nordic Power market and concluded that combination of energy and ancillary markets are not profitable for lithium-ion batteries. Participation in multiple markets is found to be insufficient to surpass costs for lithium-ion battery systems in the British, Portuguese and Danish marketplace [224]. The target costs for the lithium-ion battery system to allow pay-back is calculated to be €364.6 /kWh. In [226] it is shown that in Germany, combining benefits from multiple markets may also not be sufficient. This study also suggests that in the scenario of joint participation in price arbitrage and reserve markets, a business case exists only if the annualized cost of lithium-ion battery system drops to €310 /kWh.

Another school of thought focuses on economic viability of second-life of batteries in power system applications. Retired electric vehicle batteries can be acquired for lower costs and re-adapted for use in stationary storage applications at a reduced performance level. In [234], it is shown that use of second-life EV batteries for intermittent balancing of wind power in Crete is profitable. In [235], economic assessment of second-life batteries for short term energy market in West Australia is deemed promising as it offsets the cost of electric vehicle battery ownership. A business case is also seen in reusing vehicle batteries in control energy market in Austria [236]. In [237], the second life batteries are analysed for different applications and primary reserve control at utility scale is seen to be profitable in most EU countries.

Costs, cost projections and cost reduction potential: there is little uncertainty about the technical feasibility of lithium-ion batteries in providing different services in the power system but their economic feasibility is debatable for many applications. While creation of new electricity markets and energy products and lifting of entry barriers to participation in existing markets will help the economics of battery based storage, a major factor for the commercial success is undeniably related to their costs.

Lithium-ion battery technology has benefited from large investments in recent years both in research and manufacturing, leading to improvements in cost competitiveness. Schmidt et al. [6] differentiated prices for lithium-ion battery technology by scope and application and derived experience curves using historic product prices and cumulative installed capacity. For stationary storage applications at the utility scale, the prices were found to decrease from about US$2000 /kWh in 2010 to about US$1300 /kWh in 2015. These prices include balance of plant. A price range from US$290 /kWh to US$520 /kWh for these systems by 2030 is predicted. The price of only lithium-ion cells were seen to be below US$300 /kWh in 2011. It is expected that the prices will be about US$130 /kWh in 2030. According to the International Renewable Energy Agency [207], cell costs are currently about 35 % of the total costs for large systems compared to 46 % for residential systems. They report an energy installation cost of Li-ion battery systems between US$200 /kWh and US$840 /kWh for large scale stationary applications in 2016. The utility-scale costs are expected to decline to between US$77 /kWh and US$340 /kWh by 2030 [1].

The cost reduction in lithium-ion battery technology is being driven through different routes. They can be classified into:

1. Technical factors: further scaling-up of production and streamlining of supply chain will lead to lowering of capital costs of these batteries.
2. Material research: currently 60 % of the cost of a lithium-ion cell is due to material costs [10]. Use of cheaper materials can thus substantially lower capital costs. Novel materials that lead to performance and life improvement can also lead to lower lifetime costs.
3. Field experience: improved utilization of these battery through smart operational strategies by understanding their behaviour under different operating regimes can lead to lower lifetime costs.

In line with the approach of this dissertation, it is this third route that is explored in the next chapter. Through the insights gained into the behaviour of lithium ion batteries by experimental testing and quantification of their aging, an accurate degradation model of lithium-ion batteries has been developed for optimization studies. The model is used to develop operational strategies for battery based storage that ensure control over the revenue from markets and cycle life of these batteries.

---

[1] not considering lithium titanate (LTO) technology

Chapter 9

Optimizing the operation of lithium-ion batteries

In chapter 8, the feasibility of lithium-ion batteries in power systems both from a technical and economic point of view is discussed. While technical characteristics of these batteries make them applicable for providing many different grid services, their high lifetime cost casts a doubt about their profitability in many of these applications.

To investigate accurately the business case of lithium-ion batteries in electricity markets, a battery model that correctly simulates their behaviour is required. Since these batteries have a limited life, accurate determination of degradation in this model is imperative in realistically evaluating their economic feasibility. Moreover, a model that incorporates degradation behaviour as a function of operating conditions can be used to develop intelligent strategies for the operation of the batteries. An optimal operation of the storage system that ensures that the application needs are fulfilled but not at the cost of excessive degradation and shortening of life of these batteries could be the difference between profitability or no profitability of these batteries in many applications.

This chapter develops a degradation model of the lithium-ion battery that can be implemented to optimize the operation of storage in power systems. The application of the model has been demonstrated through a case study. The model is based on the performance and aging characteristics of the commercial cell discussed in detail in chapters 5, 6 and 7. Degradation is used synonymously with capacity fade in this chapter. This is because capacity is one of the most important indicators of the health of the battery. Usually, when the capacity of a battery is about 70-80% of the original capacity, it is retired from its primary application.

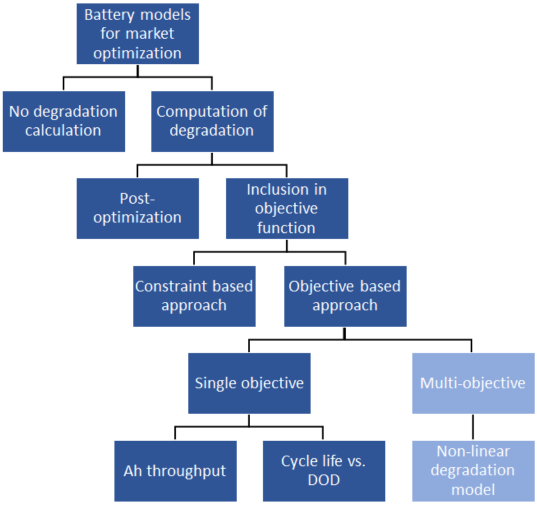

Figure 9.1. Summary of battery models used for market studies (the novelty of this work has been highlighted in a lighter shade)

9.1 Literature review of battery models applied to electricity markets

Some market studies on batteries focus on the economic viability of the storage options from a long-term perspective while others focus on optimizing their short-term operational strategy. The modus operandi of such studies is to jointly develop a model that simulates the market and battery behaviour. Modelling of the market mechanisms has been comprehensive, with studies considering single [238, 239], multiple [240, 241] or combination markets[149, 150, 242] assuming perfect price information [240, 241, 243, 244] or uncertainty in prices [242, 245].

Battery models in some studies often completely ignore the effect of degradation [243, 245, 246]. In some works degradation is calculated, but ex-post, such that the operation strategy is short-sighted and does not consider battery as a time-limited and costly resource [247–249].

Degradation conscious battery scheduling studies use either a constraint based approach [150, 242, 250] or an objective based approach [241, 251, 252]. In the constraint based approach, one or more of the following variables are constrained to extend battery life - power, number of cycles per day, depth of discharge (DOD), maximum and minimum state of charge (SOC). This approach is often based on rules-of-thumb and is non-optimal. In the objective based approach, the cost of battery operation is included as a marginal cost in the objective function. There have been two main methods here to estimate degradation - the Ah throughput method [252, 253] and the method of cycle life vs. DOD power function [150, 241, 251]. Some works combine the constraint based approach with the objective based approach [149].

From the point of view of objective function, most approaches are single objective, where degradation is assigned an economic cost. This cost is often based on the battery replacement cost [241, 247, 254, 255], sometimes on the economic utilization costs (investment + operating) [256] and other times on the marginal cost of operation [230]. The different ways to model batteries for market studies have been summarized in Figure 9.1.

9.2 Gaps in modelling degradation phenomena in lithium-ion batteries

While modelling of the market part of the scheduling models has been comprehensive, modelling of battery degradation phenomena is inadequate especially for lithium-ion batteries because of completely ignoring the effects of current and SOC on degradation. The reasons for this are partly due to paucity of data for developing detailed models and partly because of the requirement for such models to be simple and computationally effective. The former arises from the fact that aging in batteries is not completely understood and is a subject of ongoing research while the latter stems from the practical constraint of being able to optimize within the time horizons of market trading when using current computational power and algorithmic know-how.

The origins of the two most employed methods for quantifying degradation, cycle life vs. DOD and Ah throughput, can be traced to modelling lead-acid battery degradation behaviour [257–259]. In the former method, it is assumed that the number of cycles that a battery can perform is inversely proportional to the amplitude of DOD given by a simple power function. The latter method assumes that a certain amount of energy can be cycled through a battery before its end of life, irrespective of the DOD. Both methods do not consider any dependence on current or SOC. Degradation behaviour of lithium-ion batteries as seen in chapter 7 does not fit these models.

This has been reiterated in Figure 9.2. In Figure 9.2a, the cycle life of the cells is plotted for four test cases where the temperature, current and the average SOC are fixed and only DOD is varied. The cycle life does not follow an inversely proportional relationship with the DOD as is assumed in the cycle life vs. DOD method for accounting of degradation. In chapter 7, it is established that this happens because of superposition of the effect of traversing graphite peaks during cycling and the degradation caused because of voltage.

The invalidity of the cycle life vs. DOD method is further evident from Figure 9.2b. Here, the aging behaviour of the battery is plotted for two tests that are conducted at the same temperature, current and DOD. The only difference between the tests is the average SOC around which the cells are cycled. The number of equivalent full cycles (another way to measure charge throughput)

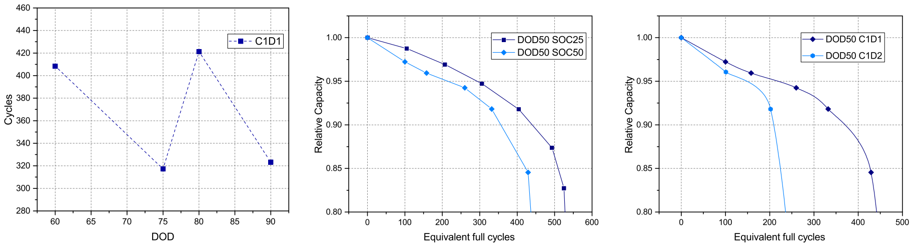

(a) Different DOD case

(b) Different average SOC case

(c) different current case, C refers to charging rate, D to discharging rate

Figure 9.2. Experimental aging behaviour in the NMC batteries

until the capacity of the battery reaches 80% of the original capacity is substantially lower in the test case where cells were cycled around SOC = 50% than around SOC = 25%. Similar results are reported in [153, 172, 260], where it is observed that depth of the cycle needs to be considered along with the mean SOC in order to analyse degradation. In [261] a physical model to explain the effect of mean SOC has also been developed. This effect of mean SOC is also not considered in the Ah throughput method.

From Figure 9.2c, the effect of current on capacity fade can be seen. The number of equivalent full cycles until the cell capacity is 80% of the original capacity decreases considerably as the magnitude of the discharge current doubles. As discussed in Section 7.4.1, higher current rates cause greater mechanical stress in the electrodes leading to higher capacity fades. Effect of current in the degradation models used in battery scheduling strategies cannot be ignored due to its substantial magnitude.

9.3 Scope of the chapter

This work is a study where the short-term operational strategy of a lithium-ion based storage is optimised. It demonstrates the working of the developed battery degradation model through its application in a day-ahead market. The work focuses on efficient scheduling of the storage system and not on evaluating the economics of lithium-ion batteries in this market or other markets or their combinations, even if this study is inspired by improving the cost competitiveness of these batteries. Through experience based learning of the degradation behaviour of batteries, strategies to use them more efficiently are investigated.

The main factors that cause decline in the capacity of a lithium-ion cell can be divided into:

(i) External factors: temperature, time

(ii) Internal factors: SOC, current, DOD

Internal factors are those that are directly affected by how the battery is operated, while external factors are independent of the operation of the battery. Considering that it is a short-term operational study, optimization is carried out only over the internal factors and the effect of calendar aging in causing degradation is not considered. Ignoring the effect of calendar aging in this work is expected to not cause significant error in a short term study as the effect of cycle aging is considerably more than calendar aging for the cell used in this work as seen in Chapters 6 and 7.

Temperature has been classified as an external factor, even though exothermic and endothermic processes inside the cell lead to heat being generated or absorbed by the cell causing its temperature to change. This is because most applications of battery based storage systems in the vehicle and the stationary storage sectors employ a thermal management system to keep the battery temperature regulated due to safety reasons (as discussed in chapter 4). Thus, temperature is assumed to be constant in this study. All values of degradation parameters used in this work are determined for 20 °C. It has also been assumed that the storage system is overall managed by a battery management system (BMS) that ensures that state and operation of the cells of the storage system are homogenized. Thus, the study of degradation of one cell of the storage system is representative of the storage system.

No artificial constraints are imposed in the model except for limiting the maximum input/output power. This upper limit on power is based on the availability of experimental data of the batteries under consideration.

9.4 Quantification and visualization of degradation

As discussed before, the study of cycle life of a battery as a function of DOD is incomplete without accounting for the effect of mean SOC. Degradation parameters that take into account the dependence of SOC and DOD on NMC battery degradation were calculated in Section 7.4.4. They are shown for 1 C current in Figure 9.3. The effect of current rate is found to be independent of the effect of SOC and DOD. Parameters for 2 C current were found to be about 30 % higher. Areas of high degradation are observed at high and low SOC. Low degradation is seen in the mid SOC range. As discussed before, this is a common observation in lithium-ion batteries [153, 172]. In chapter 7, the reasons for this nature of degradation in these cells have been discussed in detail. Concisely speaking, the values of degradation parameters reflect the combined effect of voltage and the staging behaviour in graphite. The plateau in cell's dV/dQ curve (see Figure 7.11) from 30 % to 50 % SOC is found to correspond to the low degradation in this SOC range. High SOC ($> 60\,\%$) causes higher degradation due to high voltage in the cell.

In Figure 9.4, capacity fade for every possible change of state of the battery

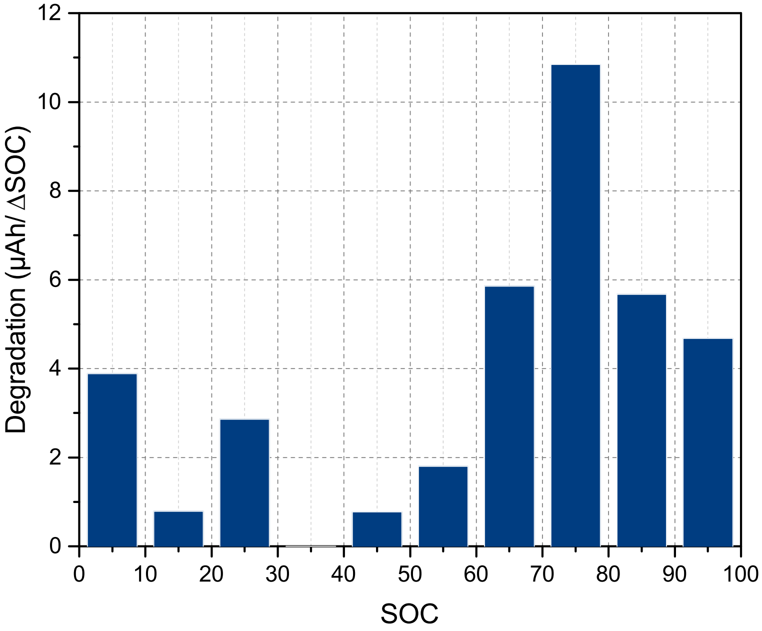

Figure 9.3. 1 C rate degradation parameters determined from experiments

is mapped for two currents to visualize the surface of degradation. The graph is symmetric along the x=y plane, which means that degradation is direction-independent. It is however path-dependent and non-linear. The actual degradation for any transition between states can be calculated by taking the difference of the degradation values read for the two states. This has been done in Figure 9.5 for 1 C current rate. Here, the actual degradation can be read directly for any transition. The low degradation cycles can also be traced out. As can be seen, even small cycles in the high SOC regions can cause a lot of degradation in the cell. Cycling in low SOC region is also considerably more detrimental to the cell than cycling in the mid SOC range.

9.5 Multi-objective scheduling model

The proposed model is distinguished from existing models on two main counts. First is how the degradation is handled given the non-linearity of degradation behaviour discussed before. Secondly, degradation is treated as a second objective along with revenue from market trading.

The multi-objective function to be maximized in given by Equation 9.1 where ζ is the fictitious composite objective.

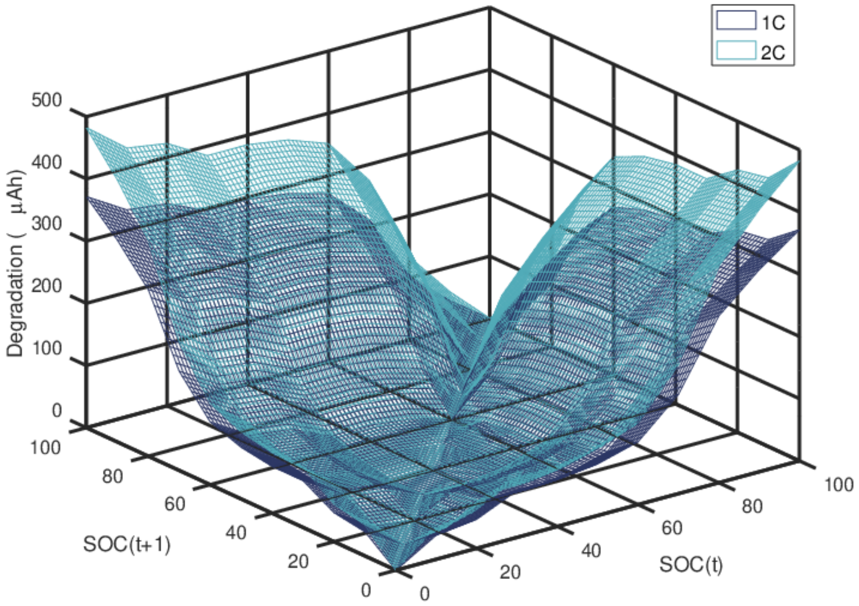

Figure 9.4. Mapped degradation surface for 1 C and 2 C rates

$$\zeta = \omega \cdot R - (1 - \omega) \cdot D \tag{9.1}$$

The values of revenue R (€) and degradation D (A h) are scaled to be of the same order of magnitude. The weight ω is varied between 0 and 1 in a parametric sweep to generate Pareto solutions of scheduling strategies. The two objective functions are detailed in Equation 9.2 and Equation 9.3.

$$R = \sum_t [\lambda_t \cdot (P_t^{dis,m} - P_t^{ch,m})] \cdot \Delta T \quad \forall t \tag{9.2}$$

where
λ is the market clearing price, assumed to be a known parameter for the optimization (€W^{-1} h)
ΔT is duration of a trading interval (h)
$P_t^{dis,m}$ is the power supplied to the market in trading interval t (W)
$P_t^{ch,m}$ is the power demanded from the market in one trading interval t (W)

In this study, a single energy market is considered. However, multiple markets can be considered in this equation such as in in [262]. The proposed model can be readily embedded in other applications by replacing the primary objective function with, for e.g., the maximization of privacy or self-consumption.

The overall battery degradation D (A h) during the entire duration of the

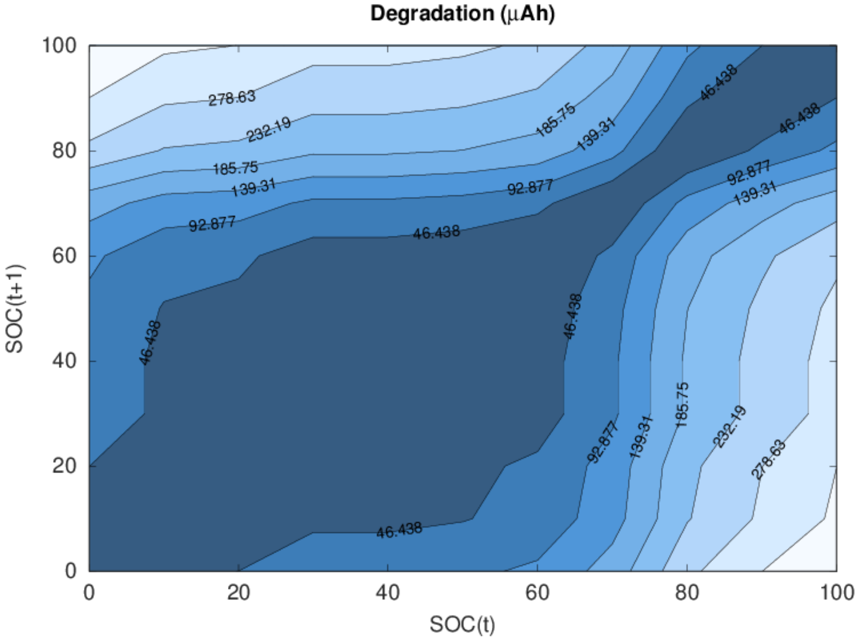

Figure 9.5. Contour map of degradation for 1 C rate

decision making horizon is given by the sum of individual degradation components d_t (A h) caused during each time interval as defined by Equation 9.3.

$$D = \sum_t d_t \quad \forall t \tag{9.3}$$

The SOC of the storage system is updated in Equation 9.4 depending on whether charging or discharging takes place during a market interval.

$$SOC_t = SOC_{t-1} + \frac{(P_t^{ch,b} - P_t^{dis,b}) \cdot \Delta T}{V_{nom} \cdot Q} \quad \forall t > 1 \tag{9.4}$$

where
$P_t^{dis,b}$ is the power supplied by the battery in trading interval t (W)
$P_t^{ch,b}$ is the power demanded by the battery in trading interval t (W)
V_{nom} is the nominal voltage of the battery equal to 3.7 V
Q is the capacity of the battery equal to 2.15 A h

The lower bound of zero and the upper bound on the power capability of the battery are set through Equation 9.5 and Equation 9.6. Using the binary variable u_t, it also ensures that during any trading interval, the storage system either charges ($u_t = 1$) or discharges ($u_t = 0$).

$$0 \leq P_t^{ch,b} \leq P^{ch,max} \cdot u_t \quad \forall t \tag{9.5}$$

$$0 \leq P_t^{dis,b} \leq P^{dis,max} \cdot (1 - u_t) \quad \forall t \tag{9.6}$$

where
$P^{ch,max}$ is the maximum input power to the battery (W)
$P^{dis,max}$ is the maximum output power of the battery (W)

The process of energy conversion in the storage system is not 100 % efficient, and it is taken into account in Equation 9.7 and Equation 9.8. These equations distinguish the battery input/output power (subscript b) from that exchanged in the market (subscript m). A constant efficiency ($\eta = 0.95$) is assigned to the conversion and transmission processes. In reality, η is not a constant but it is also a factor of operating and environmental conditions. If this is factored in, it will introduce additional non-linearity and complexity in the work. However, given the overall high efficiencies of lithium-ion batteries (Table 1.1), it has been assumed a constant in this work.

$$P_t^{ch,b} = P_t^{ch,m} \cdot \eta \quad \forall t \tag{9.7}$$

$$P_t^{dis,b} \cdot \eta = P_t^{dis,m} \quad \forall t \tag{9.8}$$

The SOC of the battery (given in percentage) is constrained through Equation 9.9 because of its definition.

$$0 \leq SOC_t \leq 100 \quad \forall t \tag{9.9}$$

Since higher currents lead to greater degradation in batteries, the degradation for every market time interval can be expressed in a bilinear form in Equation 9.10 with the degradation at 1 C as a basis. The equation relates the actual degradation caused in the battery in a time interval, d_t (A h), to the degradation that will be caused in the battery for the same change of state but at 1 C current rate, d_t^{1C} (A h). It introduces through the scaling factor Ψ the non-linearity caused by the effect of current on degradation. Ψ is a function of the current rate, i_t (h^{-1}), which is calculated in Equation 9.11. In this equation, the current rate has been determined using a constant value of voltage (nominal battery voltage, V_{nom}). In reality, however, the voltage of the battery is not constant but a function of the state of charge. Including this dependency is outside the scope of this work as it will lead to additional non-linearity and computational burden.

$$d_t = d_t^{1C} \cdot \Psi_t \quad \forall t \tag{9.10}$$

$$i_t = \frac{(P_t^{ch,b} + P_t^{dis,b})}{V_{nom} \cdot I_{1C}} \quad \forall t \tag{9.11}$$

where I_{1C} is the 1 C current equal to 2.15 A

The experimental tests on the cells under consideration have been conducted at two current values, at 1 C and 2 C. The values of Ψ are thus known for these two states. At no load conditions, no cycle aging takes place. Thus Ψ is equal to zero when the storage is idle. In this work, Ψ is assumed to scale linearly between these three currents in absence of more intermediate degradation values.

The scaling factor, Ψ, is equal to zero at no load conditions (0 C) as no cycle aging takes place when the battery is idle. Being based on 1 C current rate, it has the value of 1 at 1 C. From the data in Section 7.4.4, its value at 2 C is determined to be about 1.3. Since intermediate experiments at other current values were not carried out, it has been assumed that the parameters scale linearly between 0 C - 1 C and 1 C - 2 C. For example, if the current rate is 1.5 C, the scaling factor is the average of 1 and 1.3.

Assuming a linear scaling factor in the absence of more precise data for intermediate current values can be a reasonable assumption because increasing current causes increasing degradation in the battery. Thus the scaling factor will be a monotonically increasing function of current. Accuracy can be improved by adding the intermediate values of the scaling factor if experimental results for more current values are available. This can be achieved without any change in the structure of the developed model.

In order to determine d_t^{1C} for each change in battery state, the experimental data on degradation is first expressed in cumulative form as shown in Figure 9.6. The cumulative degradation function, δ_t^{1C} (A h), is made up of n segments (where n=10). This cumulative degradation function (δ_t^{1C}) does not have a physical significance unlike d_t^{1C}. It is a mathematical tool, conceived in order to implement the non-linear degradation behaviour represented in Figure 9.4, in the framework of MILP. Using the cumulative function facilitates modelling as degradation during a time interval (d_t^{1C}) can be simply determined as a difference of the cumulative degradation values before and after the trading interval. This is expressed in Equation 9.12.

$$d_t^{1C} = |\delta_t^{1C} - \delta_{t-1}^{1C}| \quad \forall t \tag{9.12}$$

The value of δ_t^{1C} at any time interval is determined using the incremental cost formulation [263, 264]. This formulation allows accessing a piecewise linear function such as the one of Figure 9.6 in a MILP. To implement the formulation at any trading interval t, the piecewise linear cumulative degradation function of Figure 9.4 is specified by the points $(s_{t,i}, \delta^{1C}(s_{t,i}))$ $\forall i \in \{0, ..., n\}$ where n is the total number of segments. Thus, $s_{t,i}$ is the x-coordinate and $\delta^{1C}(s_{t,i})$ is the y-coordinate of the points highlighted in Figure 9.6.

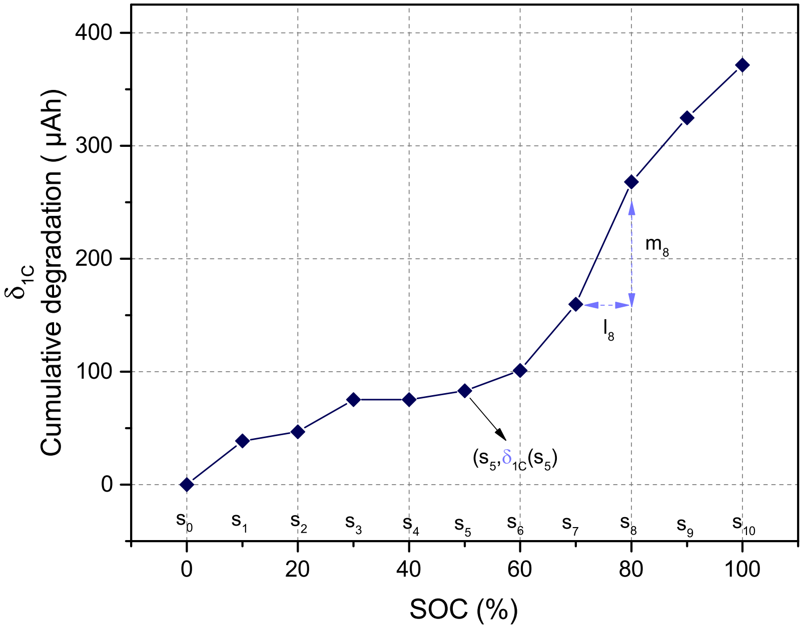

Figure 9.6. Cumulative degradation function. Annotations to clarify the implementation of the incremental cost formulation (Equations 9.13-9.17) are shown in a lighter shade of blue.

Next let,
$l_{t,i} = s_{t,i}$ - $s_{t,i-1}$ and $m_{t,i} = \delta^{1C}(s_{t,i})$ - $\delta^{1C}(s_{t,i-1})$ $\forall$ i.

Any value of the state of charge SOC_t such that $s_{t,0} \leq SOC_t \leq s_{t,n}$ can be written as in Equation 9.13.

$$SOC_t = s_{t,0} + \sum_{i=1}^{n} v_{t,i} \tag{9.13}$$

where the introduced variable $v_{t,i}$ is bounded $0 \leq v_{t,i} \leq l_{t,i}$ $\forall$ i.

Then the cumulative degradation function value for time interval t and SOC_t is given by Equation 9.14.

$$\delta_t^{1C} = \delta_t^{1C}(s_0) + \sum_{i=1}^{n} \frac{m_{t,i}}{l_{t,i}} \cdot v_{t,i} \tag{9.14}$$

if the following holds true:
$v_{t,i} < l_{t,i}$, $v_{t,i+1} = 0 \; \forall i \in \{1, ..., n-1\}$.

This can be forced in the MILP through the following constraints and introducing the binary variables $z_{t,i}$, $i \in \{1, ..., n-1\}$.

$$l_{t,1} \cdot z_{t,1} \leq v_{t,1} \leq l_{t,1} \tag{9.15}$$

$$l_{t,i} \cdot z_{t,i} \leq v_{t,i} \leq l_{t,i-1} \cdot z_{t,i-1} \quad \forall i \in \{2, ..., n-1\} \tag{9.16}$$

$$0 \leq v_{t,i} \leq l_{t,i} \cdot z_{t,n-1} \tag{9.17}$$

The product of d_t^{1C} and Ψ_t which gives the actual degradation d_t is calculated using following identity:

$$d_t^{1C}.\Psi_t = \left(\frac{d_t^{1C} + \Psi_t}{2}\right)^2 - \left(\frac{d_t^{1C} - \Psi_t}{2}\right)^2 \tag{9.18}$$

These two squared terms are approximated by piecewise linear formulations. To determine values of the squared terms as well as Ψ_t from their piecewise linear functions, incremental cost formulation is used, similar to the implementation in Equations 9.13 - 9.17. This method introduces n-1 binaries and 2n constraints where n is the number of segments of the piecewise linear function. The absolute value in Equation 9.12 is determined by adding the inequalities of Equation 9.19 and Equation 9.20 to the model:

$$|\delta_t^{1C} - \delta_{t-1}^{1C}| \geq \delta_t^{1C} - \delta_{t-1}^{1C} \tag{9.19}$$

$$|\delta_t^{1C} - \delta_{t-1}^{1C}| \geq \delta_{t-1}^{1C} - \delta_t^{1C} \tag{9.20}$$

Since maximizing the objective function penalizes degradation, this formulation using the two inequalities computes the absolute value of δ_t^{1C}-δ_{t-1}^{1C} which is equal to d_t^{1C}.

9.6 Case study and comparisons

The proposed model is implemented using GAMS 24.8.5 and the resulting MILP problem is solved using CPLEX 12. In order to demonstrate the functioning, results and advantages of the model compared to contemporary approaches, application of the storage in a day-ahead market is investigated in this case study. A 1 MW h/2 MW storage system is considered for the case study made of the basic unit of the commercial cell of Table 5.1. Individual variations among the cells upon prolonged operation are not considered in this case study. The one way efficiency of this system (η) is assumed to be 95 %. The day-ahead market prices on Monday, 22 January 2018 for the UK SEM were obtained from the ENTSO-E online platform [265]. This day-ahead market has half-hourly trading intervals (ΔT = 0.5 h). It is assumed that the storage system is a price-taker, which means

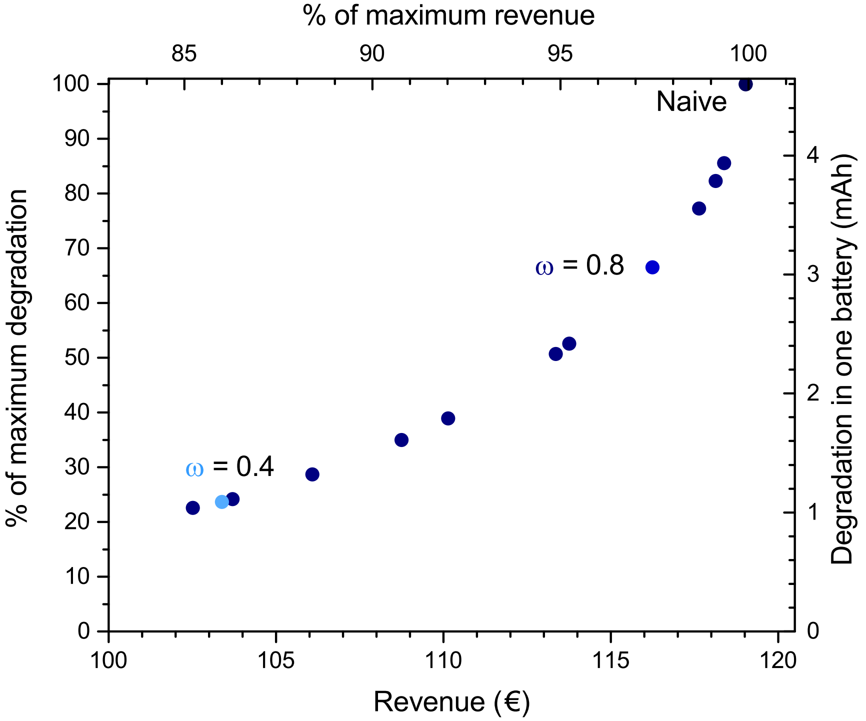

Figure 9.7. Pareto efficient scheduling strategies for the day-ahead market trading

that its presence does not affect the market prices. The choice of the market is not motivated from an economic perspective but because it fits the charge-discharge characteristics of the battery under study.

9.6.1 Single objective

The optimization is first carried out with the naive objective of maximizing only revenue. Degradation is computed but it does not affect the scheduling strategy, which is geared towards extracting the most financial gain from the market. This case is assumed as the base case against which multi-objective scheduling strategies can be compared. Note that this case corresponds to $\omega = 1.00$ in the multi-objective problem. The other extreme when $\omega = 0.00$, is the trivial case of minimization of degradation, which takes place when the storage is not operated, leading to zero degradation and zero revenue.

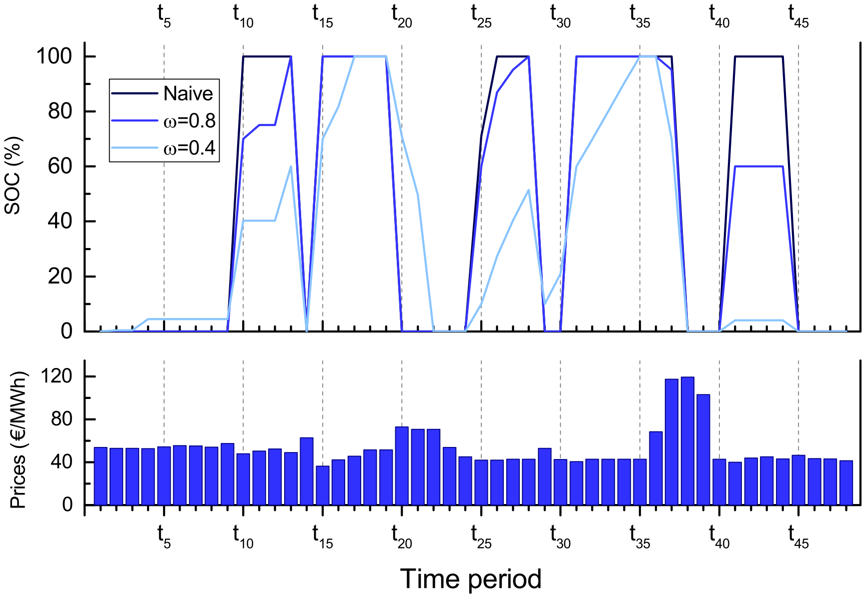

Figure 9.8. Dispatch strategy for 3 cases. The naive case does not take battery degradation into account. The other 2 cases increasingly penalize degradation

9.6.2 Multi objective

The parametric sweep is carried out next, starting with $\omega = 0.95$ and decreasing it by 0.05 with every iteration. The results for the naive objective and the multi-objective approaches are shown in Figure 9.7. The naive objective which only maximizes revenue, also maximizes the degradation in the battery. Results for 13 values of ω are compared with this as basis. As the weight is decreased, the revenue from the market decreases as well as the degradation. However, the proportions by which each objective decreases are not equal.

Each point in Figure 9.7 represents an optimal scheduling strategy. The algorithm finds intelligent scheduling strategies based on the input degradation data of the battery by modulating the charge and discharge states depending on the price signals. In order to understand better how the algorithm works, two such Pareto optimal scheduling strategies ($\omega = 0.8$ and $\omega = 0.4$) are compared against the base case in Figure 9.8.

In the naive case, every opportunity to generate revenue from the market is fully utilized. This results in steep changes in SOC which causes the most degradation in the storage system. When $\omega = 0.8$, the scheduling strategy is more biased towards revenue generation than preservation of the storage. Still, it is able to bring down the degradation by about 22.7 % while generating 98.8 % of the maximum revenue. This is made possible by charging and discharging at very

Table 9.1. Comparison of Errors Using Different Optimization and Degradation Models

Case	**Non-linear**	**MILP (6 segment)**		**Current independent**		**Ah Throughput**	
	Degradation (mAh)	**Degradation (mAh)**	**% error**	**Degradation (mAh)**	**% error**	**Degradation (mAh)**	**% error**
Naive	4.65	4.60	1.07	3.72	20.11	2.58	44.52
$\omega = 0.9$	3.99	3.94	1.26	4.77	-19.58	2.42	39.42
$\omega = 0.8$	3.56	3.56	0.13	3.89	-9.20	2.37	33.34
$\omega = 0.7$	2.45	2.42	1.38	3.29	-34.02	2.06	16.11
$\omega = 0.6$	1.81	1.79	1.18	2.18	-20.55	1.81	0.25
$\omega = 0.5$	1.34	1.32	1.08	2.40	-79.89	1.63	-21.94
$\omega = 0.4$	1.11	1.09	1.58	1.84	-66.43	1.58	-42.62

high currents only when the prices are relatively very low or very high, respectively. In other trading intervals, the current is reduced or cycling at high SOC is completely avoided ($t_{40} - t_{45}$). The scheduling strategy when $\omega = 0.4$ gives a lot more importance to the degradation in the cells. This is evident from Figure 9.7, where degradation is only 23.7 % of the maximum. However, 86.9 % of the maximum revenue is still possible. The way the storage is operated in this scheduling strategy is to spread out the charging and discharging over longer intervals. Also very high states of charge are discernibly avoided until price differences justify them. Even when 100 % state of charge is reached, it is done in stages with low currents applied at high states of charge (see $t_{15} - t_{18}$ and $t_{31} - t_{35}$ in Figure 9.8). This strategy is akin to the charging scheme currently adopted for electric vehicles and devices such as mobile phones and laptops where batteries are charged at a faster rate until they reach 80 % SOC followed by charging at a reduced current.

9.6.3 Comparison of the approaches

The actual battery degradation behaviour is non-linear. It was cast as a mixed integer linear problem with the addition of piecewise linear segments and binary variables. This approach approximates the actual non-linear behaviour. Six segments were used to linearise the square function in (Equation 9.18). The accuracy of this MILP is compared against the non-linear post-optimization computation in Table 9.1. It is seen that the MILP approach is quite accurate and represents the non-linear degradation behaviour with good accuracy.

The importance of inclusion of current dependence can be gauged by calculating the degradation that would be caused with the same scheduling strategy when no dependence of degradation on current is assumed. Thus, the degradation caused, for example, at 2 C rate is the same as 1 C rate. Algorithmically, this is determined post-optimization by setting the value of ψ to be always one, which means that the value of d_t is always equal to d_t^{1C}. The error of this assumption has also been quantified in Table 9.1.

The actual degradation can also be compared against the Ah throughput model, which assumes no influence of current rate and average state of charge on degradation. The degradation from this approach can be calculated post-optimization from the data available from the battery data sheet (Table 5.1). The degradation caused by one Ah of charge/discharge is equal to 120 µA h. The inadequacy of this approach to represent degradation for this battery can been seen in Table 9.1.

The aforementioned data indicate that a scheduling strategy for an energy storage system based on lithium-ion batteries that is derived using incorrect degradation models is likely to be far from the actual optimum.

9.7 Two-stage temporal decomposition technique

A scheduling algorithm is only useful when it can generate an optimal strategy (or at least a near optimal strategy) within time restrictions imposed by the market horizon. All optimal strategies discussed till now were generated in a few hundred seconds using the optimization model. For cases where greater accuracy is desired (e.g. by increasing the linear segments defining a non-linear function) or when optimizing for more trading intervals such as for multiple days in the day-ahead market or for a balancing market (with 15 min trading intervals), the optimization routine is unable to provide solutions with zero optimality gap within reasonable time. In this section, a decomposition technique is developed to enable computation for these cases while delivering near-optimal solutions much quicker than the original program.

The decomposition method works by breaking the problem in the time domain into smaller tractable sub-problems. By tractable, it is implied that each of these sub-problems can be solved with a zero optimality gap in a reasonable time-frame with the computing resources at hand.

In the model structure, variable d_t^{1C} is computed as the difference of two consecutive time interval values of δ^{1C} where δ^{1C} is only a function of SOC (Equation 9.12). Thus, fixing an intermediate SOC value, effectively divides the problem into two independent sub-problems. This forms the basis of the temporal decomposition technique.

As for the value of the fixed intermediate SOC, the midway value of 50 % is a good heuristic as it hedges equally on the possibility of both charging and discharging. However, an even better guess for setting the intermediate SOC is possible. This is achieved by solving the original non-decomposed optimization problem for the entire market period for a fixed period of computation time or optimality gap, whichever comes earlier. The best feasible solution at this stage is used for fixing the intermediate SOC value. Typically, the optimization algorithm (such as CPLEX) finds good feasible solutions in little time initially but then has difficulty closing the optimality gap. It is demonstrated later in this chapter that fixing the intermediate SOC value in this way can lead to better solutions than fixing the intermediate SOC state at 50 %.

Once the intermediate SOC value has been fixed, the decoupled sub-periods,

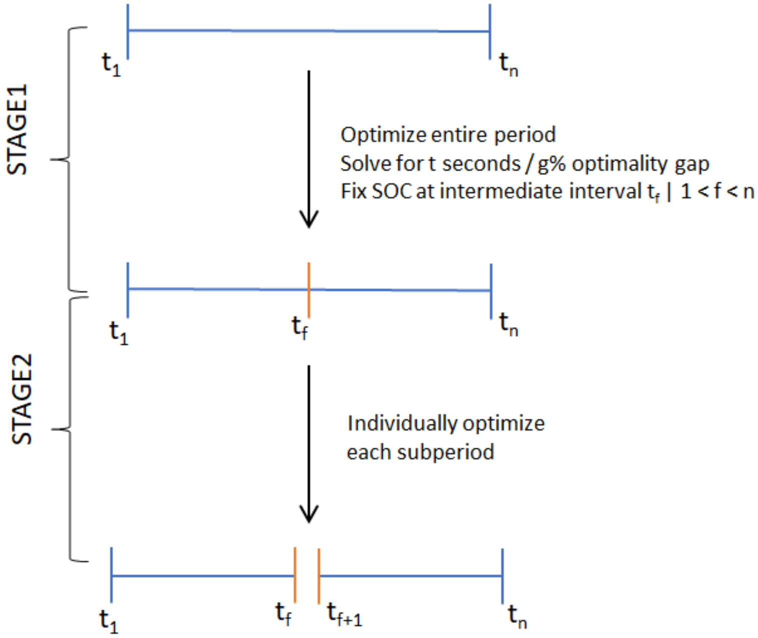

Figure 9.9. Two-stage temporal decomposition method

which are easier problems, are solved individually. The two-stage methodology is graphically shown in Figure 9.9. The method is not limited to fixing just one intermediate SOC. More intermediate SOC values can be fixed depending on the complexity of the problem.

Equivalence of the decomposition technique: the equivalence of the decomposition method to the original problem is first shown through the day-ahead market of the previous section of 48 trading intervals. The decomposition method works by fixing intermediate SOC values. For demonstration, the SOC at the end of the trading interval 24 is fixed at 50 %. Optimizing for scheduling for the entire duration of 48 intervals is now equivalent to separately optimizing for the first 24 intervals and the last 24 intervals. This equivalence can be seen for the case $\omega = 0.4$ in Table 9.2.

The solution obtained by fixing the intermediate SOC value to 50 % is sub-optimal compared to the full optimization over the 48-hour interval seen in Figure 9.7. This is because, the fixed SOC is not the optimal SOC state for that time interval. From Figure 9.8, the optimal SOC state after the 24th trading interval is seen to be zero. If the intermediate SOC at interval t_{24} had been fixed at 0, instead of 50, it would have resulted in the optimal solution also using the two-stage temporal decomposition technique.

Table 9.2. Decomposition equality

	48 interval SOC(t_{24})=50	**24 interval t_1 - t_{24}**	**24 interval t_{25} - t_{48}**	**Sum of two 24 intervals**
Revenue (€)	102.40	8.50	93.90	102.40
Degradation (mAh)	1.19	0.74	0.45	1.19
ζ	33.84	-1.01	34.85	33.84

Table 9.3. Progress of solving 336 interval as a whole

Time (s)	**Value of ζ**
1000	111.29
1500	113.69
3600	115.94
10000	116.25
15000	116.26
36000	116.36

Application of the decomposition technique: the application of the proposed decomposition technique for solving the optimization problem for more trading intervals is demonstrated by considering the day-ahead market prices for one week from 22 January 2018 to 29 January 2018 for the UK SEM. The number of trading intervals is 336. To make the problem even more difficult and highlight the utility of the two-stage temporal decomposition approach, $\omega = 0.3$ case is chosen for demonstration. For this value of ω, the 48 interval problem could not find an optimal solution even after 3600 s.

When optimizing for the entire 336 interval as a whole, the multi-objective function ζ progress with time is as shown in Table 9.3. The incremental progress is very slow after 1500 s. Using the two-stage decomposition approach, 336 trading intervals are subdivided into 14 periods of 24 intervals each. The intermediate SOC values are set using the best solution case at 1500 s. Each sub-period is then individually optimized. The value of ζ after adding the individual sub-periods is found to be 116.89. The entire two-stage optimization routine runs in less than 2000 s and outputs a better scheduling strategy than the original program even after 36 000 s. This strategy can be seen in Figure 9.9.

In terms of the two objectives, this scheduling strategy yields 79 % of the maximum revenue (€497.15 vs. €629.45) while reducing the degradation by 81.6 % (4.61 mA h vs. 25.12 mA h). Degradation measured as capacity fade in one battery unit forming the storage system is also plotted in Figure 9.10. Sharp changes of SOC at high SOC values cause the most capacity fade in the battery.

There is a scope of further improvement in the total time taken by the

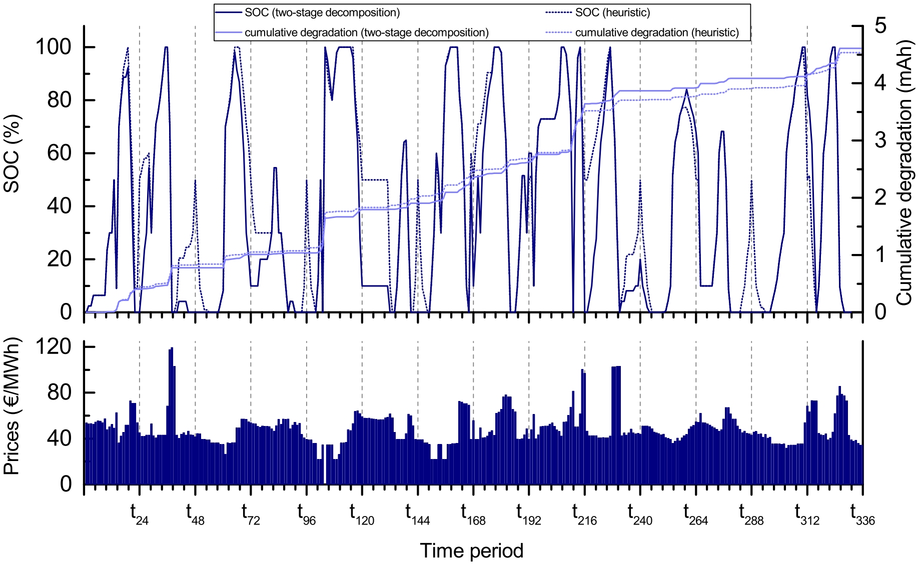

Figure 9.10. Scheduling strategy for the week-long multi-objective optimization problem for $\omega = 0.3$ plotted along with electricity prices for the two stage decomposition technique and the heuristic approach of fixing intermediate SOC at 50%

optimization by solving the decoupled 24 interval sub-periods in parallel rather than sequentially.

The effectiveness of the two-stage decomposition technique vs. the heuristic of fixing the intermediate SOC values to 50% can also be adjudged. To evaluate the dispatch strategy using the heuristic, only the second stage of the two-stage decomposition technique is run after fixing the intermediate states to the value of 50%. The 336-interval optimization problem yields the dispatch strategy which can be seen in Figure 9.10. In this case, the value of the composite objective function is 104.92. The simulation takes less than 1200 s. The value of the objective function is however considerably lower than the one obtained by the two-stage technique (116.89) demonstrating the effectiveness of this two-stage technique. In terms of the two objectives, revenues of €455.5 are generated and degradation of 4.53 mA h is caused for the case when $\omega = 0.3$ using the heuristic approach.

9.8 Outcome and advantages

In this chapter, a model that incorporates the non-linear degradation behaviour of the battery is developed. The model accounts for the effect of current, depth-of-discharge and state-of-charge on degradation of lithium-ion batteries. The utility of the model is demonstrated by optimizing the short term operation of lithium-ion batteries in an energy market. A multi-objective approach is introduced with revenue and degradation as the two objectives. Not assigning an economic cost to degradation in the objective function as in the single objective approach allows factoring in economic costs ex-post depending, for example, on the short-term or long-term financial goals or other exigencies or social benefits, etc. A decomposition technique is also proposed and demonstrated that allows the model to handle more trading intervals but obtains, for such cases, better scheduling strategies faster than the original optimization method.

Results of the case study show that it is possible to operate batteries in a smarter way in order to slow down degradation processes without compromising much on their primary goal. Markets, where the profitability of storage is marginal, can greatly benefit from such smarter scheduling strategies. Additionally, falling capital costs of battery systems combined with smarter scheduling could advance their suitability for other markets hastening their adoption.

Chapter 10

Conclusions, recommendations and future of batteries

Analysis, trends and forecasts all point towards greater need and greater deployment of lithium-ion batteries in the electric vehicle and stationary storage sectors in the coming decade. Concerted progress through all the three paths that were outlined in chapter 1, that of optimizing, scaling-up and breakthrough research, will lead to the overcoming of the challenges of safety, lifetime and price-performance ratio that currently limit their potential.

The research philosophy presented in this work is that of optimizing the technology. It aims to maximize the utilization of these batteries by understanding their behaviour and limits through modelling and experimental means.

10.1 Conclusions

Modelling: a fully parametrized pseudo 2D electrochemical model coupled with a 3D thermal model is developed for a lithium iron phosphate battery. The model accurately predicts the electrochemical and thermal behaviour of the battery over a wide range of operating conditions. Missing parameter values with good confidence level were determined by analysis of traditional charge discharge curves through mathematical means including analytical and graphical approaches. It is shown that thermal validation can resolve ambiguity in parameter values. The developed model is a powerful tool for optimizing the LFP battery for specific applications in terms of both electrochemical and thermal behaviour. Effect of electrode thickness, separator thickness, electrode loading, etc. on the electrochemical and thermal performance of the LFP battery can be studied using the developed model. Given the 3D nature of the thermal model, pinpointing of thermal hotspots is possible. Though the parametrized model is valid for the LFP battery under study, certain parametrization techniques used in this work can be applied for developing models for other lithium-ion batteries.

Physics based models have also been shown to be effective in improving understanding of lithium-ion batteries. The particle size distribution is found to be an important factor deciding the electrochemical and thermal performance of LFP batteries tested in this work. Small radius values seen at higher currents are evidence of mass diffusion being the dominating rate limiting factor. Fast kinetics of iron-phosphate material can be inferred from the determined parameter values. The heat generation differences during charge and discharge are also investigated using the developed model. The greater heat generation during charging at high current rate as compared to discharging is found to be due to greater reversible heat losses in the batteries. The contribution of graphite electrode dominates over the LiFePO4 electrode both for reversible and irreversible heats as well as for both charge and discharge.

The modular nature of the developed electrochemical-thermal model is capable of being scaled to large application scales such as that of battery packs. Though it is cumbersome for on-board battery management systems, it can be used for the design and analysis of thermal management systems for battery packs. In the battery packs, inter and intra module temperature differences should be kept at a minimum to ensure a safe and optimized performance level. Different designs of cooling systems are simulated for a fixed battery pack design. The flexibility of this model is also demonstrated by effecting lower level changes.

Aging: the degradation behaviour of commercial NMC cylindrical cells is extensively studied as a function of time (calendar aging) and operation (cycle aging) in different conditions.

Calendar aging is studied as a function of temperature and storage SOC. In general it is seen that storing the battery at a low temperature and at a low SOC leads to a slow decrease in capacity and slow increase in impedance with time. High temperature and high SOC cause faster decline of capacity and increase in impedance with time. EIS spectra were fitted by an equivalent circuit model representing ohmic resistance, polarization resistance, capacitive effects and diffusion processes in order to quantify changes of these parameters with aging. The ohmic and the polarization resistance were found to increase with storage time with the increase of polarization resistance being much greater. The time constant of the polarization and the depression of the polarization semi-circle were also found to increase with storage time. The values for the internal resistance determined after 1 s from pulse tests are in good agreement with the sum of ohmic and polarization resistance from the EIS analysis implying low current dependency of polarization resistance. It was observed that the results of the calendar aging study are significantly influenced by the characterizations and the resetting of SOC. This has so far been neglected in the literature. It can be assumed that the influence of aging processes occurring during storage is often overestimated and the real battery lifetime without any operation is longer than that inferred from calendar aging studies which include frequent electrochemical characterizations. The substantial influence of charge throughput on calendar aging also indicates the dominant effect of cycle aging.

Cycle aging is studied as a function of the state of charge, depth of discharge, temperature and discharge current rate. It is found that operating temperature has a strong impact on the lifetime of cells. Operation at low temperature (0 °C) is found to be very detrimental to the cell. Greater capacity fade is seen at higher current rate. The role of DOD and mean SOC in causing aging is intertwined and depends on the voltage and the crossing of voltage peaks. The capacity fade of all tested cells tends to decrease linearly initially. Gradual increase in ohmic resistance and SEI resistance is also seen in the linear capacity fade stage. These result from reduced transport properties of the electrolyte and the growth of the SEI at the negative electrode, respectively. The rapid capacity fade stage that is subsequently seen for most cells has been attributed to an increase of SEI resistance over a critical SEI resistance value causing a positive feedback loop of lithium deposition and a deposit layer growth. EDX analysis showed that the deposit layer contains a high amount of oxygen and phosphorous confirming the reduction of electrolyte. Critical SEI resistance value is reasoned and seen to be a function of the operating conditions of the cell. The cells cycled until 4.2 V show little increase in SEI resistance with cycling but a large increase in charge transfer resistance. This has been attributed to the formation of highly inorganic SEI at very low negative electrode potentials and surface modifications at positive electrode at very high potentials, respectively. A distillation of cycling data in terms of degradation parameters reveals a distinct effect of the staging behaviour in graphite on capacity fade superimposed upon the capacity fade caused due to high voltages.

Optimal Operation: A proof of concept of optimally using lithium-ion batteries applying the new found knowledge of battery behaviour is demonstrated. A more accurate way to quantify and account for non-linear degradation behaviour of lithium-ion batteries for storage scheduling models in electricity markets has been presented. A multi-objective approach that maximizes revenue in the market and minimizes degradation has been proposed. Evidently, multiple Pareto optimal operating strategies for storage systems are possible. The choice of the operating strategy requires active decision making and has the advantage that it allows ex-post factoring in of not only the economic costs of the batteries but other economic goals or social obligations of the storage operator. The developed mixed integer linear program is also shown to be applicable for more computationally intensive optimization studies through the proposed decomposition technique. Though, the exact degradation parameters used in this work are applicable only to the NMC battery under study, degradation parameters for other batteries can be quantified from aging experiments following the methodology shown in Part II of this work. It is expected that the degradation parameters for other lithium-ion batteries, especially NMC based ones, show similar trends as the battery of this study.

Therefore the linearisation techniques proposed can be successfully re-used. The important revenue versus degradation trade-off highlighted in this work can be easily replicated for other batteries, provided the experimental data on their specific degradation behaviour becomes available.

10.2 Recommendation

Several extensions and deepening of the research presented in this work are possible. A non-exhaustive list of possibilities is as follows:

- Analysis of geometry in influencing the electrochemical as well as the thermal behaviour at high current rates in large format cells can be studied using the P2D model. The possible outcome is optimized dimensioning of the cell.
- Inclusion of heat loss at cell tabs. Even though contact resistance at cell tabs is external to the cell, it is a phenomena that is commonly seen and becomes especially relevant at high current rates.
- Electrochemical impedance spectroscopy conducted on cell can also be used for calibration and validation of physics based model. This adds a further source for values of parameters and an additional check of their validity.
- Parametric study of different cooling system solutions to map out their effectiveness can be conducted. This can help choose an optimum technical solution for a particular application.
- Addition of the degradation model to the P2D model by inclusion of SEI formation and growth phenomena in the P2D model and the change of battery parameters with operation and time.
- Further experiments that quantitatively investigate the impact of the electrochemical characterization can be conducted to design and analyse future calendar aging studies. Such information can also help select the periodicity of the electrochemical characterizations to ensure minimum influence on calendar aging from them.
- Recalculation of calendar aging results by subtracting cycle aging.
- Investigation of the application of critical SEI resistance as a metric for health of second-life batteries and as a tool for designing homogeneous packs based on the value of critical SEI resistance.
- Investigation of the application of critical SEI resistance instead of degradation parameters to dynamically limit the SOC, DOD and currents in order to maximize utilization of battery.
- Accelerated degradation parameter calculation with better designed experimental testing conducted at multiple current values.

- Study of the change of open circuit voltage, dV/dQ curves, other EIS parameters (not analysed in this study) with aging can also reveal new insights into battery degradation behaviour.
- Calculating degradation parameters for other lithium-ion batteries can help reveal more information about the specific degradation pathways at different voltages (or SOC).
- Extension of the battery model developed for markets to multiple markets, for stochastic pricing, and when storage is a price maker.
- Identification of markets where profitability using a storage system is marginal and development of strategies using the developed degradation model for such markets to evaluate economic feasibility through optimized operation.
- Inclusion of temperature as a controlled parameter in the battery model applied to markets. Modulation of temperature of battery packs to boost instantaneous performance can have substantial economic gains.
- Inclusion of calendar aging in degradation model for long term market studies especially for applications where idle periods dominate.

10.3 Peek into the future

Though incremental improvements to the current technology through improved understanding and optimized use can help expand the user base of these batteries in the near future, the long term advancement of battery storage will need step changes and breakthroughs in battery technology. To conclude the thesis, the direction in which lithium-ion technology in particular and battery technology in general are headed is listed.

R&D efforts in materials for advancing lithium-ion technology are in the following directions:

- Developing electrolytes that are stable even at 5 V will lead to use of high potential positive electrodes such as $LiNi_{0.5}Mn_{1.5}O_4$, $LiNiPO_4$, etc. [266–268]. The benefit would be increased energy and power densities.
- Use of silicon instead of graphite as the negative electrode is being investigated. Silicon has more capacity than graphite but this comes at the cost of more volumetric expansion and degradation leading to poor cyclic stability [269, 270].

Much effort is being put into developing post lithium-ion technology. This consists of battery technology that do not fit into the traditional definition of lithium-ion batteries of consisting of two insertion electrode with the shuttling of lithium ions between them. Post lithium-ion batteries can be divided into two categories - lithium based batteries and non lithium based alternatives.

Lithium based batteries are those that use metallic lithium as negative electrodes instead of an insertion material. Charge conduction through the electrolyte is still through lithium ions. These include:

- Lithium-sulphur batteries: sulphur as positive electrode material has a high capacity and a low cost compared to conventional electrodes but problems include poor power capability, low conductivity, high self-discharge and short cycle lifetime [271, 272].
- Lithium-air batteries: they are attractive because one of the active materials oxygen is available directly from air. Thus theoretically they have the highest specific energy of any rechargeable battery. Moreover, they are inherently safe. Practically, much lower storage capabilities have been realized and vulnerability to environment conditions such as humidity is seen [273, 274].
- Solid state batteries: use of solid electrolyte enables use of metal lithium as the negative electrode. Advantages include safe packaging, improved energy density, etc. Currently the power capability is limited because of low conductivity of electrolyte and slow kinetics [275–277].

Several non-lithium based battery alternatives are also in the R&D pipeline. These include:

- Fluoride and chloride ion batteries: charge transport is enabled through negative ions in these batteries. The advantage lies in using easily available materials such as metal chlorides and fluorides. They are at a very early stage of research with the search for suitable active materials [278, 279].
- Sodium ion batteries: attractive option because sodium metal is more easily available than lithium, however at the same time it is less energy dense. Appropriate insertion materials are required that can handle the greater size of sodium ion [279, 280].
- Magnesium ion batteries: each magnesium ion transfers two times the charge as a lithium ion, hence theoretically these batteries have high energy densities. Compatibility of the positive electrode, finding a good electrolyte are still some challenges for this technology [281, 282].
- Aluminium ion batteries: each aluminium ion transfers three times the charge as a lithium ion, hence theoretically these batteries have high energy densities. Finding a suitable positive electrode to insert Al^{3+} is an issue [283].
- Liquid metal batteries: consist of three liquid layers separated due to difference in densities. Liquid phase permits high power capability and obviates problems associated with mechanical stresses in solids. High

temperature of operation to keep the materials in liquid phase poses multiple challenges [284].

- Metal-air batteries: similar conceptually to lithium-air batteries, they enable high theoretical energy densities. Different metal options being researched are aluminium[285], magnesium, potassium, zinc, etc. [286, 287].

The list above is not exhaustive as new concepts are being hypothesized, developed and tested in laboratories around the world.

Appendix A

Parameters of P2D electrochemical 3D Thermal model

Table A.1. Electrode properties

S. No.	Property	Other details	Units	Comments
1	Particle radius		m	
2	Thickness		m	
3	Volume fraction	Solid		
		Electrolyte		Any 2 of 3, s+e+o = 1
		Other		
4	Lithium Diffusivity	Coupled value	$m^2\,s^{-1}$	
5	Max concentration		$mol\,m^{-3}$	active material only
6	Initial concentration		$mol\,m^{-3}$	
7	Reaction rate constant	Coupled value	$m\,s^{-1}$	
8	Electrical conductivity		$S\,m^{-1}$	
9	Thermal conductivity		$W\,m^{-1}\,K^{-1}$	
10	Density		$kg\,m^{-3}$	
11	Heat Capacity		$J\,kg^{-1}\,K^{-1}$	
12	Electrode Potential	Coupled value	V	function of SOC
13	Entropy coefficient		$V\,K^{-1}$	function of SOC
14	Diffusion activation energy		$J\,mol^{-1}$	
14	Diffusion activation energy		$J\,mol^{-1}$	

Table A.2. Electrolyte/Separator properties

S. No.	Property	Other details	Units
1	Thickness		m
2	Initial electrolyte salt conc.		$\mathrm{mol\,m^{-3}}$
3	Electrical conductivity	Coupled value	$\mathrm{S\,m^{-1}}$
4	Thermal conductivity	Electrolyte Separator	$\mathrm{W\,m^{-1}\,K^{-1}}$
5	Diffusivity	Coupled value	$\mathrm{m^2\,s^{-1}}$
6	Density	Electrolyte Separator	$\mathrm{kg\,m^{-3}}$
7	Heat Capacity	Electrolyte Separator	$\mathrm{J\,kg^{-1}\,K^{-1}}$
8	Activity coefficient	Coupled value	
9	Transport number		

Table A.3. Others

S. No.	Property	Units
1	Thickness - current collector	m
2	1C current	$\mathrm{A\,m^{-2}}$
3	Capacity of cell	Ah
4	General dimensions of cell	m

Appendix B
Calendar aging fitted EIS data

The quantities have the following units:
R_s: Ω
R_p: Ω
τ: s
α_p: unit less quantity
K_d: $\mathrm{s}^{\beta}/\Omega$
β: unit less quantity
L: H

Table B.1. 0 °C 50 SOC

Initial	R_s	R_p	τ	α_p	K_d	β	L	error
Cell 1	0.027403	0.019444	0.001288	0.584519	0.002579	0.677684	6.45E-07	0.03451
Cell 2	0.027379	0.019702	0.001234	0.585177	0.002628	0.672607	6.17E-07	0.035677
Cell 3	0.027074	0.019455	0.001264	0.586794	0.002554	0.677038	6.12E-07	0.037817
40 days	R_s	R_p	τ	α_p	K_d	β	L	error
Cell 1	0.027376	0.018798	0.001292	0.566992	0.002256	0.703832	6.45E-07	0.06969
Cell 2	0.027352	0.019028	0.001262	0.568654	0.002351	0.69536	6.16E-07	0.078368
Cell 3	0.027078	0.018699	0.001277	0.573631	0.002351	0.693452	6.13E-07	0.056331
75 days	R_s	R_p	τ	α_p	K_d	β	L	error
Cell 1	0.027401	0.01705	0.001202	0.559958	0.0024	0.674174	6.45E-07	0.028176
Cell 2	0.027412	0.017297	0.001185	0.561797	0.002469	0.668666	6.17E-07	0.033787
Cell 3	0.027051	0.017223	0.001196	0.563085	0.002352	0.679148	6.12E-07	0.035862
109 days	R_s	R_p	τ	α_p	K_d	β	L	error
Cell 1	0.027437	0.020095	0.001663	0.539681	0.002166	0.708298	6.44E-07	0.033183
Cell 2	0.027384	0.020465	0.001629	0.54297	0.0022	0.70615	6.16E-07	0.054859
Cell 3	0.027038	0.020261	0.001607	0.546188	0.002175	0.705738	6.12E-07	0.045569
138 days	R_s	R_p	τ	α_p	K_d	β	L	error
Cell 1	0.027429	0.018039	0.001574	0.522215	0.002185	0.690532	6.45E-07	0.06563
Cell 2	0.027434	0.018151	0.001534	0.528945	0.002252	0.685838	6.17E-07	0.060599
Cell 3	0.027161	0.02088	0.00204	0.521587	0.001969	0.733782	6.12E-07	0.144495
169 days	R_s	R_p	τ	α_p	K_d	β	L	error
Cell 1	0.027402	0.018794	0.001745	0.511186	0.002158	0.696013	6.45E-07	0.052662
Cell 2	0.027406	0.019231	0.001769	0.513284	0.00218	0.696139	6.16E-07	0.065735
Cell 3	0.027258	0.018767	0.001741	0.530695	0.002078	0.708146	6.13E-07	0.060632
200 days	R_s	R_p	τ	α_p	K_d	β	L	error
Cell 1	0.027566	0.01894	0.001919	0.515226	0.002195	0.688437	6.46E-07	0.037388
Cell 2	0.027403	0.019875	0.001926	0.511358	0.002136	0.700258	6.17E-07	0.057875
Cell 3	0.027231	0.020175	0.002151	0.510719	0.00188	0.73634	6.12E-07	0.12243
231 days	R_s	R_p	τ	α_p	K_d	β	L	error
Cell 1	0.027562	0.019226	0.002033	0.511788	0.002218	0.686191	6.45E-07	0.040674
Cell 2	0.027612	0.019521	0.002073	0.514944	0.002271	0.684236	6.16E-07	0.043985
Cell 3	0.027203	0.019552	0.002114	0.505375	0.002068	0.707455	6.12E-07	0.053202
262 days	R_s	R_p	τ	α_p	K_d	β	L	error
Cell 1	0.027766	0.016761	0.001802	0.517407	0.002262	0.666834	6.45E-07	0.037048
Cell 2	0.027748	0.016991	0.001785	0.519245	0.00234	0.660821	6.17E-07	0.035983
Cell 3	0.027336	0.016663	0.001691	0.519821	0.002275	0.663039	6.11E-07	0.044576
298 days	R_s	R_p	τ	α_p	K_d	β	L	error
Cell 1	0.027739	0.0192	0.002276	0.508244	0.00203	0.70715	6.44E-07	0.062099
Cell 2	0.02772	0.019694	0.002255	0.509824	0.002068	0.706113	6.16E-07	0.089177
Cell 3	0.027356	0.019287	0.002252	0.50943	0.002081	0.701221	6.12E-07	0.049885
322 days	R_s	R_p	τ	α_p	K_d	β	L	error
Cell 1	0.027711	0.020154	0.002591	0.49956	0.001989	0.715432	6.43E-07	0.080008
Cell 2	0.027692	0.020533	0.002584	0.500489	0.002066	0.70819	6.15E-07	0.093805
Cell 3	0.027329	0.020359	0.00256	0.50129	0.002007	0.71402	6.11E-07	0.075046
358 days	R_s	R_p	τ	α_p	K_d	β	L	error
Cell 1	0.027859	0.017909	0.002252	0.507147	0.00216	0.686056	6.43E-07	0.054225
Cell 2	0.02773	0.018407	0.002215	0.504394	0.002225	0.681116	6.15E-07	0.063243
Cell 3								

Table B.2. 0 °C 100 SOC

Initial	R_s	R_p	τ	α_p	K_d	β	L	error
Cell 1	0.027265	0.02	0.00123	0.585954	0.002633	0.672964	6.27E-07	0.040084
Cell 2	0.026744	0.020273	0.001262	0.55529	0.00269	0.663357	6.64E-07	0.091279
Cell 3	0.026892	0.020384	0.001279	0.553222	0.002653	0.670023	6.44E-07	0.091327
40 days	R_s	R_p	τ	α_p	K_d	β	L	error
Cell 1	0.027238	0.019298	0.001267	0.56911	0.002438	0.694301	6.26E-07	0.088249
Cell 2	0.026806	0.018681	0.00115	0.558596	0.002491	0.681896	6.63E-07	0.039929
Cell 3	0.027296	0.018259	0.001183	0.567556	0.002515	0.680447	6.43E-07	0.041697
75 days	R_s	R_p	τ	α_p	K_d	β	L	error
Cell 1	0.02721	0.019834	0.001452	0.549286	0.002409	0.689746	6.26E-07	0.038836
Cell 2	0.026809	0.019616	0.001317	0.547862	0.002345	0.69255	6.63E-07	0.057489
Cell 3	0.027381	0.019378	0.001362	0.560913	0.002459	0.681334	6.42E-07	0.061178
115 days	R_s	R_p	τ	α_p	K_d	β	L	error
Cell 1	0.027632	0.020259	0.001776	0.542249	0.002369	0.694569	6.26E-07	0.04263
Cell 2	0.026805	0.020702	0.001562	0.520695	0.002219	0.709493	6.62E-07	0.075257
Cell 3	0.027445	0.020064	0.001641	0.533474	0.002241	0.705273	6.42E-07	0.052174
139 days	R_s	R_p	τ	α_p	K_d	β	L	error
Cell 1	0.027604	0.022848	0.002494	0.510599	0.001977	0.74871	6.26E-07	0.165039
Cell 2	0.026897	0.022159	0.002182	0.506373	0.001964	0.742285	6.61E-07	0.205178
Cell 3	0.027417	0.022107	0.002236	0.503568	0.001891	0.754753	6.41E-07	0.126443
169 days	R_s	R_p	τ	α_p	K_d	β	L	error
Cell 1	0.027577	0.020311	0.002206	0.513935	0.002065	0.720683	6.25E-07	0.077597
Cell 2	0.026913	0.021714	0.001965	0.491654	0.00206	0.725473	6.61E-07	0.119431
Cell 3	0.02739	0.020743	0.002028	0.5016	0.002026	0.728493	6.40E-07	0.100481
200 days	R_s	R_p	τ	α_p	K_d	β	L	error
Cell 1	0.027555	0.020556	0.00237	0.495915	0.002271	0.692367	6.24E-07	0.065227
Cell 2	0.026923	0.020871	0.002151	0.481355	0.00213	0.700624	6.60E-07	0.146394
Cell 3	0.027862	0.019728	0.002343	0.502891	0.002217	0.695777	6.40E-07	0.060297
235 days	R_s	R_p	τ	α_p	K_d	β	L	error
Cell 1	0.027819	0.019769	0.002435	0.503164	0.002404	0.675061	6.24E-07	0.066927
Cell 2	0.02693	0.020552	0.002122	0.479182	0.002224	0.694056	6.59E-07	0.134097
Cell 3	0.027834	0.019616	0.002405	0.497623	0.002195	0.701695	6.39E-07	0.070233
264 days	R_s	R_p	τ	α_p	K_d	β	L	error
Cell 1	0.027977	0.019858	0.002689	0.50159	0.002413	0.675423	6.23E-07	0.081447
Cell 2	0.027068	0.020676	0.002356	0.476053	0.002268	0.691147	6.59E-07	0.153781
Cell 3	0.027908	0.019879	0.002575	0.495009	0.002274	0.689218	6.38E-07	0.108738
298 days	R_s	R_p	τ	α_p	K_d	β	L	error
Cell 1	0.027949	0.021826	0.003266	0.487356	0.002174	0.707954	6.22E-07	0.152035
Cell 2	0.027262	0.022305	0.003013	0.470741	0.002028	0.720693	6.58E-07	0.206332
Cell 3	0.027886	0.021554	0.003118	0.482215	0.002089	0.714746	6.38E-07	0.141317
322 days	R_s	R_p	τ	α_p	K_d	β	L	error
Cell 1	0.027921	0.023243	0.003895	0.475132	0.002092	0.721665	6.22E-07	0.209092
Cell 2	0.027278	0.023734	0.003646	0.459745	0.001953	0.734623	6.57E-07	0.272134
Cell 3	0.027994	0.022703	0.003765	0.475235	0.002017	0.727997	6.37E-07	0.196292
358 days	R_s	R_p	τ	α_p	K_d	β	L	error
Cell 1	0.028065	0.020845	0.00341	0.480275	0.002297	0.689486	6.21E-07	0.156154
Cell 2	0.027486	0.021921	0.003435	0.463061	0.002149	0.706222	6.57E-07	0.206433
Cell 3	0.028091	0.021068	0.003446	0.47719	0.002187	0.701351	6.36E-07	0.181058

Table B.3. 20 °C 25 SOC

Initial	R_s	R_p	τ	α_p	K_d	β	L	error
Cell 1	0.026697	0.018804	0.001182	0.592648	0.002781	0.653355	5.88E-07	0.031762
Cell 2	0.027156	0.018263	0.001226	0.592126	0.002774	0.659149	5.94E-07	0.035901
Cell 3	0.027092	0.018263	0.00124	0.594168	0.002751	0.661679	6.12E-07	0.030835
30 days	R_s	R_p	τ	α_p	K_d	β	L	error
Cell 1	0.026219	0.01969	0.001358	0.534731	0.002464	0.677315	5.89E-07	0.095455
Cell 2	0.026888	0.018406	0.001353	0.545797	0.002424	0.679323	5.96E-07	0.065212
Cell 3	0.026956	0.018079	0.00135	0.55821	0.002393	0.681093	6.13E-07	0.038319
60 days	R_s	R_p	τ	α_p	K_d	β	L	error
Cell 1	0.027294	0.017936	0.00146	0.554411	0.002388	0.677396	5.90E-07	0.038181
Cell 2	0.02775	0.017643	0.001541	0.550623	0.002389	0.674854	5.97E-07	0.03643
Cell 3	0.027568	0.0176	0.001492	0.546784	0.002374	0.675422	6.15E-07	0.029775
126 days	R_s	R_p	τ	α_p	K_d	β	L	error
Cell 1	0.026725	0.021028	0.001863	0.502894	0.002336	0.681215	5.92E-07	0.106724
Cell 2	0.027383	0.020439	0.001963	0.512244	0.002267	0.688006	5.98E-07	0.093658
Cell 3	0.027188	0.020432	0.001917	0.506326	0.00227	0.687691	6.16E-07	0.081656
161 days	R_s	R_p	τ	α_p	K_d	β	L	error
Cell 1	0.027389	0.019917	0.002018	0.532475	0.00228	0.685909	5.93E-07	0.043967
Cell 2	0.027879	0.019813	0.002175	0.531596	0.002118	0.705361	5.99E-07	0.048191
Cell 3	0.02771	0.019813	0.00214	0.526725	0.002098	0.706813	6.17E-07	0.047332
186 days	R_s	R_p	τ	α_p	K_d	β	L	error
Cell 1	0.027278	0.018586	0.001949	0.515509	0.002309	0.675188	5.94E-07	0.039726
Cell 2	0.027981	0.017677	0.002059	0.526732	0.002327	0.669015	6.00E-07	0.047056
Cell 3	0.027748	0.017774	0.001963	0.519914	0.002284	0.673594	6.14E-07	0.039072
219 days	R_s	R_p	τ	α_p	K_d	β	L	error
Cell 1	0.027299	0.020219	0.002548	0.496774	0.00213	0.697594	5.95E-07	0.101615
Cell 2	0.027799	0.019867	0.002537	0.503026	0.002017	0.712485	6.02E-07	0.077059
Cell 3	0.027467	0.020703	0.002634	0.489332	0.001881	0.731699	6.14E-07	0.108178
248 days	R_s	R_p	τ	α_p	K_d	β	L	error
Cell 1	0.027299	0.020967	0.002624	0.498648	0.001878	0.739075	5.96E-07	0.141395
Cell 2								
Cell 3								
281 days	R_s	R_p	τ	α_p	K_d	β	L	error
Cell 1	0.027561	0.0216	0.00326	0.496158	0.002015	0.718974	5.98E-07	0.119143
Cell 2	0.02803	0.021015	0.00321	0.50092	0.001978	0.722247	5.99E-07	0.110206
Cell 3	0.027838	0.021432	0.003341	0.492118	0.001928	0.726615	6.11E-07	0.137836
317 days	R_s	R_p	τ	α_p	K_d	β	L	error
Cell 1	0.027669	0.020561	0.003122	0.49952	0.002127	0.699603	5.99E-07	0.105126
Cell 2	0.028128	0.020105	0.003135	0.502245	0.002032	0.707246	5.96E-07	0.112371
Cell 3	0.028083	0.020302	0.003369	0.498008	0.002043	0.707755	6.12E-07	0.104232
347 days	R_s	R_p	τ	α_p	K_d	β	L	error
Cell 1	0.02766	0.020698	0.003373	0.491643	0.002136	0.696743	5.99E-07	0.111861
Cell 2	0.028261	0.020017	0.003373	0.501332	0.002075	0.703211	5.97E-07	0.107533
Cell 3	0.028012	0.020519	0.003484	0.489451	0.002037	0.70859	6.09E-07	0.135682
374 days	R_s	R_p	τ	α_p	K_d	β	L	error
Cell 1	0.027733	0.021237	0.003744	0.487933	0.002091	0.704133	5.96E-07	0.136946
Cell 2	0.02824	0.020518	0.003645	0.494618	0.00205	0.707551	5.94E-07	0.128189
Cell 3	0.028126	0.020872	0.003823	0.488846	0.002051	0.704651	6.06E-07	0.168925

Table B.4. 20 °C 50 SOC

Initial	R_s	R_p	τ	α_p	K_d	β	L	error
Cell 1	0.0274	0.018041	0.001195	0.59574	0.002712	0.66634	6.35E-07	0.032193
Cell 2	0.027209	0.018292	0.001188	0.594227	0.002735	0.66381	6.59E-07	0.031691
Cell 3	0.027641	0.018087	0.001182	0.597213	0.002762	0.662528	6.30E-07	0.033993
41 days	R_s	R_p	τ	α_p	K_d	β	L	error
Cell 1								
Cell 2								
Cell 3	0.027744	0.016349	0.001113	0.585733	0.00291	0.636304	6.31E-07	0.059844
84 days	R_s	R_p	τ	α_p	K_d	β	L	error
Cell 1	0.027489	0.019545	0.001531	0.565555	0.00252	0.675579	6.34E-07	0.020469
Cell 2	0.027418	0.02195	0.001732	0.563066	0.002395	0.635812	6.57E-07	0.04338
Cell 3	0.027716	0.019619	0.001514	0.567026	0.00251	0.676583	6.30E-07	0.023622
131 days	R_s	R_p	τ	α_p	K_d	β	L	error
Cell 1	0.027579	0.017339	0.001377	0.559996	0.002332	0.675807	6.33E-07	0.02592
Cell 2	0.027397	0.018249	0.001559	0.546531	0.002089	0.71667	6.56E-07	0.161885
Cell 3	0.027688	0.017479	0.001363	0.552474	0.002283	0.684791	6.29E-07	0.062126
161 days	R_s	R_p	τ	α_p	K_d	β	L	error
Cell 1	0.027551	0.017888	0.001464	0.548863	0.002282	0.681995	6.32E-07	0.028172
Cell 2								
Cell 3	0.027696	0.018506	0.001489	0.541092	0.002234	0.692968	6.27E-07	0.030208
227 days	R_s	R_p	τ	α_p	K_d	β	L	error
Cell 1	0.027524	0.020249	0.001919	0.527985	0.002248	0.687721	6.30E-07	0.04605
Cell 2	0.02737	0.020576	0.001824	0.52543	0.002229	0.692418	6.55E-07	0.049343
Cell 3	0.027668	0.020276	0.001836	0.520552	0.002458	0.663307	6.29E-07	0.083999
257 days	R_s	R_p	τ	α_p	K_d	β	L	error
Cell 1	0.027806	0.017994	0.001727	0.541287	0.002374	0.663666	6.29E-07	0.037345
Cell 2	0.027595	0.018497	0.001642	0.532509	0.002296	0.676174	6.53E-07	0.063443
Cell 3	0.027641	0.019094	0.001652	0.519026	0.002201	0.689491	6.27E-07	0.034901
287 days	R_s	R_p	τ	α_p	K_d	β	L	error
Cell 1	0.027778	0.018633	0.001963	0.524999	0.002219	0.68181	6.28E-07	0.044977
Cell 2	0.027567	0.018898	0.001805	0.522158	0.00224	0.682341	6.52E-07	0.039038
Cell 3	0.027826	0.019088	0.001901	0.515381	0.002169	0.69076	6.26E-07	0.039303
320 days	R_s	R_p	τ	α_p	K_d	β	L	error
Cell 1	0.02775	0.020742	0.002492	0.506783	0.001892	0.733971	6.27E-07	0.103216
Cell 2	0.02754	0.021027	0.002373	0.499667	0.00189	0.736387	6.51E-07	0.183727
Cell 3	0.027798	0.021309	0.00245	0.498323	0.001904	0.73459	6.27E-07	0.112051
349 days	R_s	R_p	τ	α_p	K_d	β	L	error
Cell 1	0.027723	0.02104	0.00247	0.513055	0.001678	0.764004	6.25E-07	0.214184
Cell 2	0.027512	0.02108	0.002233	0.508415	0.00174	0.760023	6.49E-07	0.198597
Cell 3	0.027787	0.021153	0.002242	0.508375	0.001682	0.76943	6.26E-07	0.230437
381 days	R_s	R_p	τ	α_p	K_d	β	L	error
Cell 1	0.027695	0.02349	0.003384	0.491661	0.00154	0.8	6.27E-07	0.30636
Cell 2	0.027485	0.022328	0.00282	0.485925	0.001914	0.731993	6.48E-07	0.118424
Cell 3	0.027759	0.022409	0.002921	0.482836	0.00184	0.743891	6.25E-07	0.13499
416 days	R_s	R_p	τ	α_p	K_d	β	L	error
Cell 1	0.027667	0.022273	0.003252	0.474692	0.001694	0.764081	6.25E-07	0.181939
Cell 2	0.02819	0.020158	0.002538	0.532304	0.001973	0.71138	6.47E-07	0.419708
Cell 3	0.028685	0.019765	0.002629	0.538881	0.002024	0.706429	6.24E-07	0.375112

Table B.5. 20 °C 75 SOC

Initial	R_s	R_p	τ	α_p	K_d	β	L	error
Cell 1	0.027327	0.018706	0.001181	0.589205	0.00284	0.656934	6.17E-07	0.037443
Cell 2								
Cell 3								
30 days	R_s	R_p	τ	α_p	K_d	β	L	error
Cell 1	0.027138	0.018479	0.001278	0.553626	0.002381	0.681339	6.18E-07	0.044555
Cell 2								
Cell 3								
63 days	R_s	R_p	τ	α_p	K_d	β	L	error
Cell 1	0.027197	0.019308	0.001546	0.542053	0.002366	0.68625	6.19E-07	0.029041
Cell 2								
Cell 3								
126 days	R_s	R_p	τ	α_p	K_d	β	L	error
Cell 1	0.027328	0.02102	0.001988	0.527248	0.002049	0.72683	6.20E-07	0.074193
Cell 2								
Cell 3	0.027336	0.021325	0.001957	0.518	0.002059	0.724253	6.21E-07	0.065352
161 days	R_s	R_p	τ	α_p	K_d	β	L	error
Cell 1	0.027472	0.020319	0.002049	0.524985	0.00233	0.686585	6.20E-07	0.041704
Cell 2	0.028208	0.019642	0.002189	0.533823	0.002196	0.694513	6.21E-07	0.041635
Cell 3	0.027742	0.020455	0.002123	0.524747	0.002291	0.690884	6.22E-07	0.04479
190 days	R_s	R_p	τ	α_p	K_d	β	L	error
Cell 1								
Cell 2	0.028162	0.020146	0.00239	0.520995	0.002085	0.707379	6.18E-07	0.0604
Cell 3	0.027567	0.021613	0.002481	0.499735	0.002027	0.722775	6.24E-07	0.074754
219 days	R_s	R_p	τ	α_p	K_d	β	L	error
Cell 1	0.027414	0.022953	0.002796	0.494676	0.001747	0.766915	6.17E-07	0.229188
Cell 2	0.027865	0.022389	0.002826	0.492119	0.001616	0.784487	6.18E-07	0.207007
Cell 3	0.027287	0.02375	0.002904	0.474362	0.001632	0.790829	6.25E-07	0.239672
282 days	R_s	R_p	τ	α_p	K_d	β	L	error
Cell 1	0.027794	0.0215	0.003123	0.487622	0.002056	0.713718	6.14E-07	0.117658
Cell 2	0.028463	0.0204	0.003164	0.499662	0.002046	0.70903	6.15E-07	0.100845
Cell 3	0.0279	0.02177	0.003105	0.485179	0.002029	0.719648	6.22E-07	0.134194
322 days	R_s	R_p	τ	α_p	K_d	β	L	error
Cell 1	0.028177	0.022422	0.003884	0.489236	0.002183	0.698338	6.11E-07	0.187684
Cell 2	0.028714	0.021422	0.003723	0.497367	0.002133	0.699935	6.12E-07	0.173545
Cell 3	0.028158	0.022801	0.003802	0.480292	0.002139	0.703819	6.19E-07	0.229676
350 days	R_s	R_p	τ	α_p	K_d	β	L	error
Cell 1	0.028194	0.023346	0.004529	0.475752	0.002029	0.717999	6.08E-07	0.196194
Cell 2	0.028591	0.022567	0.004294	0.47763	0.001892	0.733216	6.09E-07	0.182788
Cell 3	0.028379	0.0233	0.004489	0.474944	0.002061	0.714255	6.16E-07	0.209077
378 days	R_s	R_p	τ	α_p	K_d	β	L	error
Cell 1	0.028365	0.024079	0.00506	0.474212	0.00192	0.737943	6.04E-07	0.261797
Cell 2	0.028799	0.023164	0.004719	0.480636	0.001869	0.741042	6.06E-07	0.263344
Cell 3	0.028397	0.024559	0.005036	0.466863	0.001853	0.748389	6.13E-07	0.317434

Table B.6. 20 °C 100 SOC

Initial	R_s	R_p	τ	α_p	K_d	β	L	error
Cell 1	0.027092	0.018582	0.001237	0.591441	0.002643	0.671945	6.28E-07	0.0304
Cell 2	0.027384	0.018978	0.001211	0.589809	0.002736	0.663211	6.03E-07	0.032147
Cell 3	0.027385	0.018741	0.001216	0.588366	0.00282	0.660094	6.11E-07	0.034181
30 days	R_s	R_p	τ	α_p	K_d	β	L	error
Cell 1	0.027104	0.018712	0.001317	0.571906	0.002443	0.686252	6.26E-07	0.033954
Cell 2	0.027357	0.019534	0.001402	0.555784	0.002454	0.688407	6.05E-07	0.049507
Cell 3	0.027358	0.019411	0.001416	0.553876	0.002497	0.688079	6.12E-07	0.048613
125 days	R_s	R_p	τ	α_p	K_d	β	L	error
Cell 1	0.027742	0.022394	0.002254	0.519994	0.002095	0.729534	6.25E-07	0.072688
Cell 2	0.027507	0.023214	0.002331	0.502397	0.002119	0.727941	6.06E-07	0.102897
Cell 3	0.027366	0.02274	0.00216	0.500002	0.002248	0.713247	6.11E-07	0.074945
160 days	R_s	R_p	τ	α_p	K_d	β	L	error
Cell 1	0.027714	0.023478	0.003193	0.461054	0.002304	0.740301	6.24E-07	0.240925
Cell 2	0.028039	0.022053	0.002377	0.516475	0.002318	0.702479	6.05E-07	0.074703
Cell 3	0.027975	0.022248	0.002396	0.513624	0.002272	0.709022	6.10E-07	0.086
189 days	R_s	R_p	τ	α_p	K_d	β	L	error
Cell 1	0.028105	0.023204	0.00322	0.489296	0.002011	0.734942	6.25E-07	0.125735
Cell 2	0.028319	0.022638	0.002865	0.509042	0.002163	0.717241	6.07E-07	0.130458
Cell 3	0.028153	0.022907	0.002873	0.50066	0.002237	0.709617	6.09E-07	0.120915
218 days	R_s	R_p	τ	α_p	K_d	β	L	error
Cell 1	0.028077	0.024929	0.003789	0.472589	0.001779	0.773538	6.25E-07	0.203111
Cell 2	0.028291	0.024913	0.003703	0.479651	0.001839	0.763933	6.05E-07	0.238988
Cell 3	0.028125	0.024507	0.003623	0.473035	0.001958	0.74826	6.08E-07	0.178216
247 days	R_s	R_p	τ	α_p	K_d	β	L	error
Cell 1	0.028049	0.024964	0.004293	0.439564	0.001957	0.738355	6.23E-07	0.395354
Cell 2	0.028263	0.025326	0.004419	0.443702	0.002023	0.731309	6.04E-07	0.491545
Cell 3	0.028097	0.024588	0.004177	0.436925	0.002154	0.714754	6.06E-07	0.432353
281 days	R_s	R_p	τ	α_p	K_d	β	L	error
Cell 1	0.028461	0.023577	0.004095	0.459532	0.002152	0.710238	6.25E-07	0.29719
Cell 2	0.028461	0.024064	0.003977	0.456836	0.002225	0.704911	6.03E-07	0.300186
Cell 3	0.028618	0.022891	0.003759	0.465672	0.002369	0.688273	6.05E-07	0.385811
324 days	R_s	R_p	τ	α_p	K_d	β	L	error
Cell 1	0.02945	0.023045	0.00464	0.487685	0.002267	0.696933	6.23E-07	0.3005
Cell 2	0.029676	0.022018	0.003819	0.508682	0.002274	0.692787	6.02E-07	0.701204
Cell 3								
349 days	R_s	R_p	τ	α_p	K_d	β	L	error
Cell 1	0.029421	0.025614	0.006303	0.459926	0.002084	0.722358	6.22E-07	0.36709
Cell 2	0.029647	0.025901	0.006285	0.464372	0.002152	0.717804	6.01E-07	0.376851
Cell 3	0.029605	0.024618	0.005317	0.475237	0.00215	0.71239	6.04E-07	0.681358
377 days	R_s	R_p	τ	α_p	K_d	β	L	error
Cell 1	0.029762	0.026958	0.00772	0.455274	0.001894	0.755088	6.21E-07	0.425855
Cell 2	0.029653	0.027738	0.007316	0.448552	0.001981	0.746645	5.99E-07	0.458765
Cell 3	0.029664	0.0277	0.007503	0.448349	0.002011	0.741904	6.03E-07	0.517379

Table B.7. 45 °C 50 SOC

Initial	R_s	R_p	τ	α_p	K_d	β	L	error
Cell 1	0.027892	0.01832	0.001256	0.609543	0.002882	0.613709	6.34E-07	0.018903
Cell 2	0.027449	0.019375	0.001231	0.583829	0.002592	0.675003	6.27E-07	0.039081
Cell 3	0.027263	0.019485	0.001217	0.582497	0.002618	0.674592	6.28E-07	0.050588
35 days	R_s	R_p	τ	α_p	K_d	β	L	error
Cell 1	0.027864	0.018356	0.00126	0.584212	0.002383	0.679397	6.33E-07	0.041414
Cell 2	0.027826	0.018611	0.00125	0.580418	0.002467	0.667566	6.26E-07	0.05782
Cell 3	0.0279	0.017841	0.001267	0.598102	0.00264	0.655765	6.29E-07	0.108432
74 days	R_s	R_p	τ	α_p	K_d	β	L	error
Cell 1	0.027836	0.019244	0.001389	0.560417	0.002621	0.650634	6.32E-07	0.255131
Cell 2	0.02806	0.019622	0.001439	0.567388	0.002714	0.649541	6.27E-07	0.221018
Cell 3	0.028455	0.017297	0.001287	0.632314	0.002904	0.618109	6.28E-07	0.377277
101 days	R_s	R_p	τ	α_p	K_d	β	L	error
Cell 1	0.028437	0.018755	0.001524	0.581459	0.002848	0.621516	6.31E-07	0.262024
Cell 2	0.028213	0.020582	0.001654	0.554507	0.002259	0.688126	6.28E-07	0.029252
Cell 3	0.028427	0.019913	0.00169	0.575628	0.002276	0.685821	6.27E-07	0.074961
133 days	R_s	R_p	τ	α_p	K_d	β	L	error
Cell 1	0.028408	0.022358	0.002067	0.542858	0.002136	0.702175	6.29E-07	0.045332
Cell 2	0.028185	0.023873	0.002067	0.536672	0.001881	0.746787	6.27E-07	0.138286
Cell 3	0.028398	0.022525	0.002059	0.552197	0.001914	0.739449	6.26E-07	0.172292
161 days	R_s	R_p	τ	α_p	K_d	β	L	error
Cell 1	0.02838	0.022028	0.001861	0.545148	0.002073	0.710562	6.28E-07	0.10036
Cell 2	0.028156	0.023993	0.002208	0.519697	0.001829	0.753945	6.28E-07	0.135869
Cell 3	0.02837	0.023594	0.002296	0.534575	0.001886	0.746874	6.24E-07	0.155141
196 days	R_s	R_p	τ	α_p	K_d	β	L	error
Cell 1	0.028351	0.022451	0.002108	0.517146	0.002281	0.680121	6.29E-07	0.090658
Cell 2	0.028128	0.023379	0.002584	0.470478	0.002011	0.718076	6.30E-07	0.404437
Cell 3	0.028342	0.023907	0.002724	0.497733	0.002075	0.71337	6.23E-07	0.269531
226 days	R_s	R_p	τ	α_p	K_d	β	L	error
Cell 1	0.028459	0.023057	0.002179	0.51744	0.002021	0.712285	6.28E-07	0.098787
Cell 2	0.028762	0.022824	0.002325	0.520825	0.002145	0.699812	6.31E-07	0.072239
Cell 3	0.028767	0.022888	0.002451	0.52601	0.002114	0.706626	6.22E-07	0.120882
259 days	R_s	R_p	τ	α_p	K_d	β	L	error
Cell 1	0.028793	0.023473	0.002494	0.515075	0.002204	0.69041	6.29E-07	0.099603
Cell 2	0.028733	0.024049	0.002464	0.511058	0.002147	0.701307	6.30E-07	0.100941
Cell 3	0.028739	0.023931	0.002504	0.520577	0.002212	0.692801	6.21E-07	0.125252
287 days	R_s	R_p	τ	α_p	K_d	β	L	error
Cell 1	0.028801	0.022764	0.002326	0.510204	0.001709	0.760386	6.31E-07	0.171894
Cell 2	0.028705	0.023405	0.0023	0.506709	0.002092	0.70491	6.28E-07	0.093785
Cell 3	0.02871	0.023456	0.002366	0.514812	0.002134	0.699958	6.19E-07	0.111886
318 days	R_s	R_p	τ	α_p	K_d	β	L	error
Cell 1	0.028772	0.024718	0.002631	0.496557	0.00188	0.735143	6.29E-07	0.125573
Cell 2	0.028676	0.0249	0.002512	0.495526	0.002001	0.720291	6.27E-07	0.138716
Cell 3	0.028681	0.024329	0.002537	0.504463	0.0021	0.707054	6.21E-07	0.121709
358 days	R_s	R_p	τ	α_p	K_d	β	L	error
Cell 1	0.028862	0.026527	0.003025	0.492332	0.002068	0.713991	6.31E-07	0.314737
Cell 2	0.028647	0.027391	0.003052	0.477521	0.002201	0.698834	6.26E-07	0.348879
Cell 3	0.028652	0.026521	0.002784	0.497215	0.00231	0.686766	6.19E-07	0.325644

Table B.8. 45 °C 100 SOC

Initial	R_s	R_p	τ	α_p	K_d	β	L	error
Cell 1	0.027504	0.019415	0.001189	0.597585	0.002407	0.715992	6.22E-07	0.172291
Cell 2	0.027523	0.019169	0.001183	0.601115	0.002444	0.710532	6.08E-07	0.158088
Cell 3	0.027779	0.019752	0.001248	0.586746	0.002439	0.701132	6.32E-07	0.082023
33 days	R_s	R_p	τ	α_p	K_d	β	L	error
Cell 1	0.027934	0.017872	0.001216	0.595355	0.002638	0.656314	6.20E-07	0.086695
Cell 2	0.027992	0.017898	0.001242	0.601775	0.002689	0.648887	6.07E-07	0.079679
Cell 3	0.027936	0.018706	0.001259	0.564935	0.002552	0.658638	6.33E-07	0.036677
72 days	R_s	R_p	τ	α_p	K_d	β	L	error
Cell 1	0.028782	0.018727	0.001345	0.586166	0.002902	0.630311	6.19E-07	0.170455
Cell 2	0.028534	0.020783	0.001644	0.553575	0.002476	0.673132	6.08E-07	0.029841
Cell 3	0.028964	0.020674	0.001637	0.554731	0.002448	0.673027	6.32E-07	0.024689
99 days	R_s	R_p	τ	α_p	K_d	β	L	error
Cell 1	0.028958	0.021506	0.001911	0.528069	0.002394	0.681722	6.20E-07	0.042744
Cell 2	0.028765	0.021843	0.001881	0.520991	0.002332	0.686494	6.07E-07	0.04894
Cell 3	0.029482	0.02106	0.001923	0.530364	0.002312	0.682829	6.33E-07	0.049834
131 days	R_s	R_p	τ	α_p	K_d	β	L	error
Cell 1	0.029243	0.024244	0.002324	0.506577	0.002188	0.712295	6.19E-07	0.103801
Cell 2	0.029206	0.024333	0.002309	0.506558	0.00213	0.71799	6.06E-07	0.132523
Cell 3	0.030087	0.023521	0.0024	0.51245	0.002215	0.703956	6.32E-07	0.099971
159 days	R_s	R_p	τ	α_p	K_d	β	L	error
Cell 1	0.029608	0.024344	0.002557	0.495065	0.002125	0.718573	6.20E-07	0.124468
Cell 2	0.029407	0.024575	0.002473	0.488907	0.0021	0.720817	6.05E-07	0.151005
Cell 3	0.030832	0.02385	0.002552	0.49966	0.002116	0.71359	6.31E-07	0.180584
197 days	R_s	R_p	τ	α_p	K_d	β	L	error
Cell 1	0.029866	0.024784	0.002916	0.473405	0.002245	0.699851	6.21E-07	0.126209
Cell 2	0.029725	0.025103	0.00288	0.468438	0.002176	0.707405	6.03E-07	0.136327
Cell 3	0.031376	0.023799	0.002834	0.488884	0.002254	0.696161	6.32E-07	0.127606
229 days	R_s	R_p	τ	α_p	K_d	β	L	error
Cell 1	0.030473	0.024911	0.002913	0.492221	0.002075	0.725887	6.20E-07	0.577188
Cell 2	0.029902	0.02706	0.003315	0.457353	0.002084	0.725715	6.02E-07	0.232352
Cell 3	0.031839	0.024184	0.002892	0.498778	0.002067	0.724355	6.31E-07	0.678039
257 days	R_s	R_p	τ	α_p	K_d	β	L	error
Cell 1	0.030443	0.026277	0.003693	0.459641	0.002282	0.698616	6.19E-07	0.207935
Cell 2	0.030268	0.0265	0.003606	0.454096	0.002235	0.704049	6.01E-07	0.222222
Cell 3	0.031807	0.026044	0.003713	0.465532	0.002208	0.705345	6.29E-07	0.225639
285 days	R_s	R_p	τ	α_p	K_d	β	L	error
Cell 1	0.030412	0.025511	0.003323	0.448266	0.002334	0.689062	6.18E-07	0.198451
Cell 2	0.030612	0.024922	0.003496	0.455399	0.002372	0.683395	6.02E-07	0.193266
Cell 3	0.03199	0.023963	0.003342	0.462195	0.00229	0.691114	6.28E-07	0.164288
316 days	R_s	R_p	τ	α_p	K_d	β	L	error
Cell 1	0.030382	0.026915	0.003789	0.431992	0.001835	0.8	6.16E-07	0.494895
Cell 2	0.030585	0.027683	0.004143	0.437451	0.002225	0.706344	6.01E-07	0.277369
Cell 3	0.032122	0.025359	0.003581	0.452653	0.002186	0.707882	6.28E-07	0.18351
356 days	R_s	R_p	τ	α_p	K_d	β	L	error
Cell 1	0.030765	0.03154	0.006154	0.419735	0.001942	0.749438	6.18E-07	0.362836
Cell 2	0.030554	0.032234	0.006153	0.412318	0.001801	0.771925	6.00E-07	0.378516
Cell 3	0.032786	0.030431	0.006397	0.441904	0.001817	0.770003	6.26E-07	0.397152

Appendix C
Cycle aging fitted EIS data

The quantities have the following units:
R_s: Ω
R_{SEI}: Ω
τ_a: s
α_p: unit less quantity
R_{CT}: Ω
τ_c: s
α_c: unit less quantity
K_d: s^{β}/Ω
β: unit less quantity
L: H

Table C.1. 0 °C DOD50 C1D1

	EFC	R_s	R_{SEI}	τ_a	α_a	R_{ct}	τ_c	α_c	K_d	β	L	error
Cell 1	0	0.028402	0.00648	0.000744	0.790833	0.011682	0.0027	0.565036	0.002529	0.690393	6.06E-07	0.041314
Cell 2	0	0.028438	0.00648	0.000718	0.799434	0.011815	0.0027	0.569396	0.002565	0.688478	5.70E-07	0.046527
Cell 3	0	0.028558	0.00648	0.000748	0.781593	0.011433	0.0027	0.569232	0.002482	0.693077	5.87E-07	0.045892
	EFC	R_s	R_{SEI}	τ_a	α_a	R_{ct}	τ_c	α_c	K_d	β	L	error
Cell 1	84	0.035757	0.01944	0.00103	0.733814	0.012102	0.005533	0.894839	0.00956	0.546142	6.04E-07	0.053298
Cell 2	73	0.035818	0.019423	0.001054	0.745338	0.012126	0.005831	0.909518	0.009807	0.539471	5.69E-07	0.057123
Cell 3	84	0.035757	0.01838	0.000963	0.74665	0.012671	0.005495	0.898134	0.009654	0.540841	5.85E-07	0.042107

Table C.2. 0 °C DOD100 C1D1

	EFC	R_s	R_{SEI}	τ_a	α_a	R_{ct}	τ_c	α_c	K_d	β	L	error
Cell 1	0	0.028373	0.00648	0.000722	0.78539	0.011576	0.0027	0.574165	0.002556	0.686095	5.77E-07	0.040488
Cell 2	0	0.028157	0.00648	0.000781	0.786839	0.012267	0.0027	0.548072	0.002479	0.69433	5.96E-07	0.045878
Cell 3	0	0.028184	0.00648	0.000769	0.788891	0.012101	0.0027	0.554886	0.002512	0.691772	5.91E-07	0.046064
	EFC	R_s	R_{SEI}	τ_a	α_a	R_{ct}	τ_c	α_c	K_d	β	L	error
Cell 1	87	0.035853	0.018255	0.001128	0.72186	0.015302	0.0081	0.837273	0.006086	0.596049	5.75E-07	0.052857
Cell 2	87	0.035624	0.019104	0.001149	0.722329	0.013531	0.0081	0.8776	0.007211	0.540971	5.94E-07	0.087628
Cell 3	89	0.033247	0.013485	0.001039	0.766453	0.014462	0.0081	0.842549	0.006396	0.547514	5.90E-07	0.069188

Table C.3. 0 °C DOD50 C1D2

	EFC	R_s	R_{SEI}	τ_a	α_a	R_{ct}	τ_c	α_c	K_d	β	L	error
Cell 1	0	0.028646	0.00648	0.000768	0.782509	0.012003	0.0027	0.557626	0.00247	0.693375	5.78E-07	0.046428
Cell 2	0	0.028232	0.00648	0.000781	0.78891	0.0121	0.0027	0.558285	0.002453	0.691989	5.89E-07	0.043898
Cell 3	0	0.027824	0.00648	0.000802	0.786426	0.012252	0.0027	0.539726	0.00243	0.692332	6.08E-07	0.046249
	EFC	R_s	R_{SEI}	τ_a	α_a	R_{ct}	τ_c	α_c	K_d	β	L	error
Cell 1	66	0.033364	0.009413	0.000776	0.774684	0.012766	0.004483	0.836439	0.008208	0.555291	5.79E-07	0.04747
Cell 2	69	0.032966	0.010175	0.000789	0.749482	0.012748	0.004501	0.837428	0.008674	0.547927	5.87E-07	0.042634
Cell 3	64	0.031659	0.013052	0.001203	0.630024	0.012939	0.004912	0.781149	0.006782	0.601785	6.10E-07	0.140709

Table C.4. 0 °C DOD100 C1D2

	EFC	R_s	R_{SEI}	τ_a	α_a	R_{ct}	τ_c	α_c	K_d	β	L	error
Cell 1	0	0.028683	0.00648	0.000792	0.791439	0.012391	0.0027	0.551519	0.002452	0.696894	5.93E-07	0.047352
Cell 2	0	0.028422	0.00648	0.000815	0.781782	0.012158	0.0027	0.546665	0.002456	0.695819	6.00E-07	0.041238
Cell 3	0	0.02834	0.00648	0.000744	0.80112	0.012676	0.0027	0.557258	0.002536	0.686136	5.98E-07	0.047418
	EFC	R_s	R_{SEI}	τ_a	α_a	R_{ct}	τ_c	α_c	K_d	β	L	error
Cell 1	66	0.034078	0.01906	0.001584	0.692547	0.012867	0.008448	0.818267	0.00511	0.63542	5.94E-07	0.110802
Cell 2	82	0.034479	0.017755	0.001382	0.711091	0.013882	0.00945	0.828405	0.005384	0.619698	6.02E-07	0.096159
Cell 3	64	0.034314	0.018748	0.001488	0.697582	0.014055	0.008838	0.807552	0.005278	0.629054	6.00E-07	0.103189

Table C.5. 20 °C DOD25 C1D1

	EFC	R_s	R_{SEI}	τ_a	α_a	R_{ct}	τ_c	α_c	K_d	β	L	error
Cell 1	0	0.02948	0.00648	0.000712	0.782963	0.01066	0.00225	0.561456	0.002788	0.659967	5.90E-07	0.035998
Cell 2	0	0.029173	0.00648	0.000744	0.78026	0.010699	0.00225	0.549671	0.002753	0.662834	6.11E-07	0.035338
Cell 3	0	0.029233	0.00648	0.000745	0.785118	0.010852	0.00225	0.54933	0.002781	0.663956	5.91E-07	0.03338
	EFC	R_s	R_{SEI}	τ_a	α_a	R_{ct}	τ_c	α_c	K_d	β	L	error
Cell 1	161	0.029391	0.008282	0.000795	0.653786	0.006303	0.008039	0.734776	0.002633	0.651224	5.92E-07	0.021081
Cell 2	161	0.028502	0.013434	0.001476	0.551273	0.002019	0.009565	0.936433	0.002526	0.660404	6.11E-07	0.011914
Cell 3												
	EFC	R_s	R_{SEI}	τ_a	α_a	R_{ct}	τ_c	α_c	K_d	β	L	error
Cell 1	264	0.027354	0.008612	0.000791	0.61609	0.00525	0.008585	0.764656	0.00264	0.645082	5.93E-07	0.017655
Cell 2	264	0.026489	0.0133	0.001469	0.524644	0.001529	0.009373	1	0.002429	0.664767	6.10E-07	0.01744
Cell 3												
	EFC	R_s	R_{SEI}	τ_a	α_a	R_{ct}	τ_c	α_c	K_d	β	L	error
Cell 1	350	0.027471	0.008526	0.000822	0.622251	0.006805	0.011246	0.763275	0.002628	0.652996	5.95E-07	0.024185
Cell 2	347	0.026459	0.014391	0.001764	0.510309	0.002244	0.012568	1	0.002399	0.674601	6.09E-07	0.021073
Cell 3	326	0.028876	0.015201	0.002706	0.520485	0.002114	0.018017	1	0.002563	0.659231	5.93E-07	0.045224
	EFC	R_s	R_{SEI}	τ_a	α_a	R_{ct}	τ_c	α_c	K_d	β	L	error
Cell 1												
Cell 2												
Cell 3	411	0.028793	0.015455	0.002692	0.515991	0.003096	0.021213	1	0.00251	0.707132	5.94E-07	0.033336
	EFC	R_s	R_{SEI}	τ_a	α_a	R_{ct}	τ_c	α_c	K_d	β	L	error
Cell 1												
Cell 2												
Cell 3	493	0.0288	0.015506	0.002805	0.506646	0.003664	0.023297	1	0.002655	0.657994	5.95E-07	0.024222
	EFC	R_s	R_{SEI}	τ_a	α_a	R_{ct}	τ_c	α_c	K_d	β	L	error
Cell 1												
Cell 2												
Cell 3	579	0.028963	0.015351	0.003046	0.511712	0.003868	0.023521	1	0.002908	0.640007	5.97E-07	0.022828
	EFC	R_s	R_{SEI}	τ_a	α_a	R_{ct}	τ_c	α_c	K_d	β	L	error
Cell 1												
Cell 2												
Cell 3	674	0.029003	0.015807	0.003031	0.516829	0.005458	0.028972	1	0.003053	0.635665	5.98E-07	0.011927
	EFC	R_s	R_{SEI}	τ_a	α_a	R_{ct}	τ_c	α_c	K_d	β	L	error
Cell 1												
Cell 2												
Cell 3	769	0.029015	0.015692	0.003016	0.521998	0.004319	0.028393	1	0.003	0.641562	5.99E-07	0.050725
	EFC	R_s	R_{SEI}	τ_a	α_a	R_{ct}	τ_c	α_c	K_d	β	L	error
Cell 1												
Cell 2												
Cell 3	849	0.02906	0.016488	0.003001	0.527218	0.007256	0.033897	0.987789	0.003388	0.62473	6.00E-07	0.011939
	EFC	R_s	R_{SEI}	τ_a	α_a	R_{ct}	τ_c	α_c	K_d	β	L	error
Cell 1												
Cell 2												
Cell 3	928	0.029111	0.016389	0.002986	0.53249	0.00746	0.033965	0.992469	0.003839	0.598753	6.01E-07	0.016895
	EFC	R_s	R_{SEI}	τ_a	α_a	R_{ct}	τ_c	α_c	K_d	β	L	error
Cell 1												
Cell 2												
Cell 3	1019	0.029254	0.016529	0.003059	0.537815	0.008243	0.035563	0.980783	0.003951	0.60155	6.03E-07	0.011991
	EFC	R_s	R_{SEI}	τ_a	α_a	R_{ct}	τ_c	α_c	K_d	β	L	error
Cell 1												
Cell 2												
Cell 3	1109	0.029452	0.016443	0.003043	0.53967	0.008365	0.035196	0.96294	0.004099	0.601537	6.04E-07	0.007888
	EFC	R_s	R_{SEI}	τ_a	α_a	R_{ct}	τ_c	α_c	K_d	β	L	error
Cell 1												
Cell 2												
Cell 3	1194	0.030039	0.017242	0.003138	0.545066	0.009422	0.036939	0.962907	0.004573	0.597152	6.05E-07	0.011178
	EFC	R_s	R_{SEI}	τ_a	α_a	R_{ct}	τ_c	α_c	K_d	β	L	error
Cell 1												
Cell 2												
Cell 3	1266	0.032752	0.022862	0.003207	0.550517	0.00881	0.0362	1	0.006137	0.589159	6.06E-07	0.030357
	EFC	R_s	R_{SEI}	τ_a	α_a	R_{ct}	τ_c	α_c	K_d	β	L	error
Cell 1												
Cell 2												
Cell 3	1293	0.043283	0.03016	0.001541	0.5723	0.012755	0.020663	0.961299	0.017655	0.443508	5.70E-07	0.016417

Table C.6. 20 °C DOD50 C1D1

	EFC	R_s	R_{SEI}	τ_a	α_a	R_{ct}	τ_c	α_c	K_d	β	L	error
Cell 1	0	0.029179	0.007776	0.000893	0.748367	0.00964	0.0021	0.501826	0.002732	0.665735	6.24E-07	0.031752
Cell 2	0	0.028966	0.007776	0.000918	0.755866	0.009685	0.0021	0.492883	0.00275	0.670383	5.96E-07	0.033522
Cell 3	0	0.029058	0.007776	0.00091	0.743626	0.00911	0.0021	0.500991	0.002776	0.66376	6.36E-07	0.037063
	EFC	R_s	R_{SEI}	τ_a	α_a	R_{ct}	τ_c	α_c	K_d	β	L	error
Cell 1	100	0.029313	0.009447	0.001079	0.594061	0.000964	0.005171	0.945163	0.002924	0.598447	6.26E-07	0.127003
Cell 2												
Cell 3	99	0.028908	0.012368	0.001349	0.57573	0.00108	0.00673	1	0.002498	0.650461	6.36E-07	0.022235
	EFC	R_s	R_{SEI}	τ_a	α_a	R_{ct}	τ_c	α_c	K_d	β	L	error
Cell 1												
Cell 2	167	0.029562	0.008959	0.000872	0.66662	0.006593	0.010639	0.81431	0.002658	0.638602	5.98E-07	0.015045
Cell 3	170	0.028738	0.012883	0.001282	0.559147	0.003554	0.011513	0.934042	0.002574	0.64467	6.34E-07	0.011727
	EFC	R_s	R_{SEI}	τ_a	α_a	R_{ct}	τ_c	α_c	K_d	β	L	error
Cell 1	242	0.029625	0.012936	0.001525	0.586736	0.00482	0.01834	0.936748	0.002631	0.646279	6.24E-07	0.019316
Cell 2												
Cell 3												
	EFC	R_s	R_{SEI}	τ_a	α_a	R_{ct}	τ_c	α_c	K_d	β	L	error
Cell 1	341	0.029709	0.013487	0.001449	0.603823	0.007474	0.020424	0.892199	0.003015	0.636818	6.26E-07	0.004831
Cell 2	327	0.029951	0.009548	0.000996	0.675903	0.008837	0.014923	0.830565	0.002977	0.632736	5.99E-07	0.005768
Cell 3	329	0.028944	0.014954	0.001744	0.54452	0.005105	0.017305	0.93195	0.002668	0.66003	6.33E-07	0.009514
	EFC	R_s	R_{SEI}	τ_a	α_a	R_{ct}	τ_c	α_c	K_d	β	L	error
Cell 1												
Cell 2	423	0.030221	0.012342	0.001343	0.66978	0.011261	0.021001	0.845332	0.003388	0.636144	6.01E-07	0.018209
Cell 3	425	0.029291	0.018265	0.002484	0.556068	0.006458	0.024581	0.957004	0.003067	0.655283	6.31E-07	0.020925
	EFC	R_s	R_{SEI}	τ_a	α_a	R_{ct}	τ_c	α_c	K_d	β	L	error
Cell 1	467	0.039713	0.03545	0.003	0.496623	0.007098	0.020612	1	0.013826	0.488798	6.28E-07	0.041525
Cell 2	483	0.039722	0.029211	0.002589	0.517438	0.007615	0.022791	1	0.013387	0.477503	6.03E-07	0.022848
Cell 3	496	0.039168	0.030006	0.00236	0.506154	0.00703	0.025236	1	0.014665	0.461045	6.29E-07	0.013234

Table C.7. 20 °C DOD60 C1D1

	EFC	R_s	R_{SEI}	τ_a	α_a	R_{ct}	τ_c	α_c	K_d	β	L	error
Cell 1	0	0.027669	0.007776	0.000875	0.804244	0.009346	0.0021	0.434951	0.0026	0.674641	6.00E-07	0.031175
Cell 2	0	0.027774	0.007776	0.000887	0.807935	0.009174	0.0021	0.448405	0.002544	0.680366	5.99E-07	0.028014
	EFC	R_s	R_{SEI}	τ_a	α_a	R_{ct}	τ_c	α_c	K_d	β	L	error
Cell 1	99	0.027462	0.011345	0.001313	0.648717	0.003075	0.002695	0.3	0.00234	0.668731	6.02E-07	0.038375
Cell 2	99	0.027752	0.011937	0.001331	0.640901	0.001835	0.003389	0.386284	0.00229	0.674215	5.98E-07	0.05053
	EFC	R_s	R_{SEI}	τ_a	α_a	R_{ct}	τ_c	α_c	K_d	β	L	error
Cell 1	197	0.028137	0.014785	0.001619	0.613732	0.001565	0.007153	1	0.002733	0.649377	6.04E-07	0.008343
Cell 2	197	0.027982	0.014563	0.001547	0.606442	0.001708	0.006643	1	0.002633	0.658651	5.96E-07	0.020141
	EFC	R_s	R_{SEI}	τ_a	α_a	R_{ct}	τ_c	α_c	K_d	β	L	error
Cell 1	292	0.029946	0.018568	0.002038	0.619869	0.003131	0.011653	0.972909	0.003719	0.638011	6.02E-07	0.015879
Cell 2	293	0.030254	0.019303	0.0021	0.612507	0.002653	0.010793	1	0.003793	0.641888	5.94E-07	0.033523
	EFC	R_s	R_{SEI}	τ_a	α_a	R_{ct}	τ_c	α_c	K_d	β	L	error
Cell 1	335	0.04046	0.026886	0.002164	0.524814	0.00611	0.016859	1	0.012129	0.486394	6.00E-07	0.025254
Cell 2												
	EFC	R_s	R_{SEI}	τ_a	α_a	R_{ct}	τ_c	α_c	K_d	β	L	error
Cell 1	346	0.040927	0.026263	0.002055	0.507092	0.007029	0.019437	0.980658	0.013762	0.474582	5.99E-07	0.013354
Cell 2	340	0.040131	0.031424	0.00315	0.45938	0.004634	0.01665	1	0.012999	0.48298	5.96E-07	0.061844

Table C.8. 20 °C DOD75 C1D1

	EFC	R_s	R_{SEI}	τ_a	α_a	R_{ct}	τ_c	α_c	K_d	β	L	error
Cell 1	0	0.029017	0.0072	0.000838	0.757409	0.009841	0.002025	0.512419	0.002848	0.658412	5.99E-07	0.03709
Cell 2	0	0.028001	0.0072	0.00091	0.760885	0.0102	0.002025	0.501425	0.002682	0.671253	6.11E-07	0.0295
Cell 3												
	EFC	R_s	R_{SEI}	τ_a	α_a	R_{ct}	τ_c	α_c	K_d	β	L	error
Cell 1	101	0.029619	0.008046	0.00067	0.712855	0.006085	0.007627	0.808855	0.002706	0.621714	6.00E-07	0.059667
Cell 2	101	0.028435	0.008765	0.000728	0.649602	0.005719	0.007304	0.766057	0.002548	0.63772	6.09E-07	0.017921
Cell 3												
	EFC	R_s	R_{SEI}	τ_a	α_a	R_{ct}	τ_c	α_c	K_d	β	L	error
Cell 1	189	0.029673	0.010957	0.001065	0.668679	0.008774	0.017582	0.859293	0.002972	0.618965	6.02E-07	0.015658
Cell 2	168	0.028685	0.011546	0.001112	0.646965	0.008482	0.016574	0.847547	0.002724	0.641953	6.11E-07	0.004467
Cell 3	188	0.028161	0.015434	0.001652	0.578403	0.005606	0.017986	0.923009	0.00271	0.646755	6.10E-07	0.003269
	EFC	R_s	R_{SEI}	τ_a	α_a	R_{ct}	τ_c	α_c	K_d	β	L	error
Cell 1	289	0.030079	0.013766	0.001346	0.622627	0.009508	0.021859	0.869754	0.003347	0.62693	6.04E-07	0.012491
Cell 2	268	0.029281	0.013365	0.001437	0.634611	0.007616	0.019001	0.926547	0.004696	0.502427	6.13E-07	0.18269
Cell 3	287	0.029485	0.015126	0.001591	0.637246	0.00765	0.019993	0.930213	0.00561	0.486272	6.12E-07	0.238553

Table C.9. 20 °C DOD80 C1D1

	EFC	R_s	R_{SEI}	τ_a	α_a	R_{ct}	τ_c	α_c	K_d	β	L	error
Cell 1	0	0.027689	0.0072	0.000852	0.804384	0.009249	0.002025	0.477488	0.002565	0.674166	5.77E-07	0.028348
Cell 2	0	0.027891	0.0072	0.000894	0.824281	0.009924	0.002025	0.459432	0.002526	0.683152	5.88E-07	0.034846
	EFC	R_s	R_{SEI}	τ_a	α_a	R_{ct}	τ_c	α_c	K_d	β	L	error
Cell 1	99	0.028238	0.010004	0.001436	0.640027	0.003699	0.002025	0.549112	0.002437	0.65139	5.78E-07	0.041925
Cell 2	99	0.028277	0.010104	0.001441	0.664841	0.00397	0.002371	0.450244	0.0024	0.657821	5.90E-07	0.036038
	EFC	R_s	R_{SEI}	τ_a	α_a	R_{ct}	τ_c	α_c	K_d	β	L	error
Cell 1	197	0.028535	0.009803	0.001408	0.61272	0.006964	0.004613	0.631479	0.002475	0.664417	5.77E-07	0.042169
Cell 2	198	0.028642	0.01571	0.002394	0.607879	0.001588	0.002371	0.544795	0.002456	0.670977	5.88E-07	0.057055
	EFC	R_s	R_{SEI}	τ_a	α_a	R_{ct}	τ_c	α_c	K_d	β	L	error
Cell 1	293	0.028904	0.012021	0.001379	0.618711	0.009204	0.011624	0.7262	0.002748	0.668297	5.78E-07	0.045335
Cell 2	294	0.029047	0.017575	0.002652	0.586325	0.004763	0.012053	0.659202	0.002656	0.684397	5.87E-07	0.118442
	EFC	R_s	R_{SEI}	τ_a	α_a	R_{ct}	τ_c	α_c	K_d	β	L	error
Cell 1	384	0.03353	0.01717	0.001352	0.631086	0.010431	0.017027	0.83513	0.005401	0.60206	5.80E-07	0.010646
Cell 2	378	0.042404	0.031976	0.002599	0.565209	0.005074	0.012053	0.797634	0.007577	0.583229	5.85E-07	0.086942
	EFC	R_s	R_{SEI}	τ_a	α_a	R_{ct}	τ_c	α_c	K_d	β	L	error
Cell 1	414	0.039545	0.033589	0.002638	0.479843	0.007408	0.02243	0.9604	0.013654	0.485444	5.82E-07	0.033771
Cell 2	392	0.040753	0.034428	0.002547	0.498368	0.007282	0.022036	0.965137	0.012401	0.500275	5.84E-07	0.022756

Table C.10. 20 °C DOD90 C1D1

	EFC	R_s	R_{SEI}	τ_a	α_a	R_{ct}	τ_c	α_c	K_d	β	L	error
Cell 1	0	0.027855	0.0072	0.000862	0.819237	0.009605	0.002025	0.481312	0.002545	0.680038	5.82E-07	0.032697
Cell 2	0	0.027931	0.0072	0.000847	0.824119	0.010007	0.002025	0.477182	0.002621	0.678508	5.88E-07	0.03391
	EFC	R_s	R_{SEI}	τ_a	α_a	R_{ct}	τ_c	α_c	K_d	β	L	error
Cell 1	99	0.028003	0.010641	0.001547	0.614428	0.003842	0.002025	0.536611	0.002444	0.653343	5.84E-07	0.030533
Cell 2	99	0.028198	0.009997	0.001671	0.618089	0.005559	0.002025	0.553531	0.002503	0.652644	5.89E-07	0.031606
	EFC	R_s	R_{SEI}	τ_a	α_a	R_{ct}	τ_c	α_c	K_d	β	L	error
Cell 1	198	0.028176	0.015691	0.002223	0.574759	0.002494	0.006382	0.622469	0.00261	0.652696	5.86E-07	0.088937
Cell 2	195	0.028508	0.011531	0.001638	0.583595	0.008255	0.006101	0.642096	0.002702	0.659392	5.88E-07	0.060306
	EFC	R_s	R_{SEI}	τ_a	α_a	R_{ct}	τ_c	α_c	K_d	β	L	error
Cell 1	294	0.028571	0.015611	0.002179	0.560738	0.007483	0.014978	0.722064	0.002758	0.66575	5.85E-07	0.077491
Cell 2	289	0.030576	0.016426	0.001605	0.595267	0.0123	0.016535	0.744832	0.003996	0.649736	5.89E-07	0.126772
	EFC	R_s	R_{SEI}	τ_a	α_a	R_{ct}	τ_c	α_c	K_d	β	L	error
Cell 1	384	0.03309	0.020537	0.002135	0.571953	0.009261	0.023213	0.837595	0.005498	0.599022	5.87E-07	0.030129
Cell 2	325	0.039707	0.027932	0.001919	0.510145	0.010797	0.022141	0.864005	0.011568	0.498001	5.91E-07	0.033383
	EFC	R_s	R_{SEI}	τ_a	α_a	R_{ct}	τ_c	α_c	K_d	β	L	error
Cell 1	411	0.039555	0.033576	0.002416	0.479081	0.008188	0.02543	0.97161	0.013447	0.47771	5.89E-07	0.024568
Cell 2	335	0.040889	0.032965	0.002617	0.478761	0.00763	0.024013	1.002246	0.014215	0.470381	5.89E-07	0.015054

Table C.11. 20 °C DOD100 C1D1

	EFC	R_s	R_{SEI}	τ_a	α_a	R_{ct}	τ_c	α_c	K_d	β	L	error
Cell 1	0	0.027804	0.0072	0.000889	0.752176	0.010119	0.00192	0.509774	0.002769	0.662308	6.27E-07	0.035322
Cell 2	0	0.027931	0.007137	0.000771	0.703177	0.010052	0.00192	0.558012	0.002858	0.651664	5.96E-07	0.154873
Cell 3	0	0.027745	0.0072	0.00093	0.746653	0.010771	0.00192	0.520033	0.002662	0.673933	6.29E-07	0.026576
	EFC	R_s	R_{SEI}	τ_a	α_a	R_{ct}	τ_c	α_c	K_d	β	L	error
Cell 1	100	0.02831	0.010514	0.000786	0.598914	0.01038	0.028114	0.768376	0.00302	0.609624	6.25E-07	0.018118
Cell 2	101	0.029019	0.009044	0.000735	0.674016	0.010905	0.025157	0.76317	0.003024	0.608775	5.98E-07	0.034227
Cell 3	76	0.028191	0.0126	0.001011	0.575054	0.013041	0.045471	0.839654	0.003088	0.590977	6.25E-07	0.034212
	EFC	R_s	R_{SEI}	τ_a	α_a	R_{ct}	τ_c	α_c	K_d	β	L	error
Cell 1	168	0.028497	0.012118	0.000915	0.561259	0.019399	0.071239	0.810165	0.004675	0.534957	6.23E-07	0.02844
Cell 2	170	0.029345	0.009823	0.000933	0.61749	0.015578	0.054053	0.804603	0.004559	0.528867	6.00E-07	0.057213
Cell 3												
	EFC	R_s	R_{SEI}	τ_a	α_a	R_{ct}	τ_c	α_c	K_d	β	L	error
Cell 1	268	0.028469	0.012106	0.001317	0.452666	0.022829	0.108491	0.734959	0.005217	0.515739	6.25E-07	0.162132
Cell 2	265	0.029697	0.009813	0.000902	0.602665	0.02446	0.097805	0.779133	0.005606	0.506434	6.02E-07	0.028577
Cell 3	280	0.028134	0.012575	0.001111	0.464919	0.022133	0.112217	0.799239	0.007308	0.452686	6.27E-07	0.036612
	EFC	R_s	R_{SEI}	τ_a	α_a	R_{ct}	τ_c	α_c	K_d	β	L	error
Cell 1	370	0.028671	0.012081	0.000947	0.477768	0.029006	0.151604	0.800721	0.00954	0.425316	6.29E-07	0.064167
Cell 2	359	0.030066	0.009803	0.000775	0.624054	0.033196	0.149643	0.791207	0.008685	0.447238	6.04E-07	0.105553
Cell 3	376	0.028106	0.012562	0.000824	0.455725	0.03217	0.178366	0.779884	0.00974	0.432021	6.29E-07	0.13466
	EFC	R_s	R_{SEI}	τ_a	α_a	R_{ct}	τ_c	α_c	K_d	β	L	error
Cell 1	474	0.028642	0.012069	0.000888	0.400426	0.033819	0.211865	0.730618	0.012674	0.396167	6.27E-07	0.254443
Cell 2	464	0.030036	0.009793	0.001428	0.480822	0.029691	0.190111	0.843634	0.017913	0.338574	6.02E-07	0.093381
Cell 3	439	0.028078	0.01255	0.000668	0.434713	0.037692	0.218793	0.751477	0.009819	0.436341	6.31E-07	0.273287
	EFC	R_s	R_{SEI}	τ_a	α_a	R_{ct}	τ_c	α_c	K_d	β	L	error
Cell 1	570	0.028613	0.012057	0.001776	0.314064	0.024029	0.201271	0.827633	0.021326	0.319448	6.29E-07	0.080946
Cell 2	558	0.030006	0.009784	0.002856	0.352567	0.029852	0.239364	0.813857	0.022198	0.319321	6.00E-07	0.129531
Cell 3	542	0.02805	0.012537	0.001337	0.3	0.033257	0.266069	0.798312	0.022594	0.331698	6.29E-07	0.175568
	EFC	R_s	R_{SEI}	τ_a	α_a	R_{ct}	τ_c	α_c	K_d	β	L	error
Cell 1	662	0.029073	0.012045	0.003552	0.3	0.028029	0.287883	0.788998	0.024915	0.320254	6.27E-07	0.169299
Cell 2	649	0.029976	0.009774	0.00156	0.308868	0.033914	0.295721	0.763948	0.024495	0.322514	5.98E-07	0.193719
Cell 3	634	0.028022	0.012525	0.001034	0.3	0.034409	0.34844	0.736699	0.023778	0.335015	6.31E-07	0.238907
	EFC	R_s	R_{SEI}	τ_a	α_a	R_{ct}	τ_c	α_c	K_d	β	L	error
Cell 1	751	0.030324	0.012033	0.007104	0.3	0.023325	0.273489	0.832998	0.03317	0.323059	6.25E-07	0.212949
Cell 2	734	0.032952	0.010063	0.00312	0.477914	0.020348	0.280935	0.732333	0.033243	0.325739	6.00E-07	0.712933
Cell 3	722	0.028989	0.012512	0.000517	0.3	0.028575	0.331018	0.643502	0.027975	0.338365	6.29E-07	0.296365
	EFC	R_s	R_{SEI}	τ_a	α_a	R_{ct}	τ_c	α_c	K_d	β	L	error
Cell 1	824	0.032219	0.046114	0.017327	0.31953	0.01234	0.063987	1	0.006296	0.67031	6.38E-07	0.025373
Cell 2												
Cell 3	788	0.03923	0.029153	0.0024	0.454406	0.0167	0.04343	0.888557	0.009031	0.580763	6.28E-07	0.004697

Table C.12. 20 °C DOD100n C1D1

	EFC	R_s	R_{SEI}	τ_a	α_a	R_{ct}	τ_c	α_c	K_d	β	L	error
Cell 1	0	0.027895	0.0072	0.000833	0.813982	0.00915	0.00192	0.4934	0.002652	0.666182	5.95E-07	0.041842
Cell 2	0	0.02791	0.0072	0.00086	0.817436	0.009379	0.00192	0.471312	0.002488	0.687812	5.92E-07	0.060706
Cell 3	0	0.027884	0.0072	0.000808	0.818624	0.008837	0.00192	0.486556	0.002627	0.666743	5.91E-07	0.054892
	EFC	R_s	R_{SEI}	τ_a	α_a	R_{ct}	τ_c	α_c	K_d	β	L	error
Cell 1	82	0.028289	0.007128	0.000753	0.673712	0.004735	0.00578	0.636923	0.003265	0.569635	5.97E-07	0.155543
Cell 2	82	0.028356	0.007323	0.000774	0.653949	0.005241	0.005327	0.605854	0.002991	0.597961	5.94E-07	0.079223
Cell 3	82	0.028168	0.007128	0.000817	0.654899	0.005343	0.005636	0.601072	0.003073	0.590497	5.93E-07	0.127418
	EFC	R_s	R_{SEI}	τ_a	α_a	R_{ct}	τ_c	α_c	K_d	β	L	error
Cell 1	164	0.028365	0.007057	0.000689	0.67613	0.007769	0.008284	0.662676	0.002429	0.665812	5.99E-07	0.03923
Cell 2	164	0.028352	0.007876	0.000697	0.636729	0.006649	0.008937	0.674761	0.00256	0.646786	5.96E-07	0.018561
Cell 3	164	0.028192	0.008083	0.000735	0.660522	0.006413	0.008752	0.710006	0.002665	0.636822	5.95E-07	0.013173
	EFC	R_s	R_{SEI}	τ_a	α_a	R_{ct}	τ_c	α_c	K_d	β	L	error
Cell 1	244	0.028616	0.006986	0.000689	0.689652	0.00979	0.009852	0.659295	0.002396	0.67992	6.01E-07	0.081692
Cell 2	244	0.02833	0.007914	0.000627	0.633809	0.009189	0.010668	0.657986	0.002357	0.683014	5.94E-07	0.076364
Cell 3	244	0.02854	0.008626	0.000805	0.673732	0.007644	0.011323	0.73872	0.002865	0.626037	5.96E-07	0.006225
	EFC	R_s	R_{SEI}	τ_a	α_a	R_{ct}	τ_c	α_c	K_d	β	L	error
Cell 1	321	0.028644	0.011202	0.001072	0.641023	0.007468	0.016544	0.802692	0.003409	0.592218	6.02E-07	0.029229
Cell 2	322	0.028834	0.010663	0.000985	0.646485	0.00857	0.01863	0.77119	0.003137	0.61194	5.95E-07	0.019439
Cell 3	321	0.02863	0.010481	0.000961	0.652554	0.009063	0.015602	0.762441	0.003268	0.610052	5.98E-07	0.013363
	EFC	R_s	R_{SEI}	τ_a	α_a	R_{ct}	τ_c	α_c	K_d	β	L	error
Cell 1	500	0.028922	0.011141	0.001087	0.653844	0.008097	0.017584	0.77538	0.004495	0.533035	6.04E-07	0.26353
Cell 2	500	0.028844	0.012482	0.001164	0.624218	0.006768	0.020596	0.844432	0.004125	0.548747	5.94E-07	0.126246
Cell 3	500	0.028615	0.013591	0.00135	0.612797	0.00601	0.018646	0.861219	0.004242	0.556799	5.96E-07	0.108928
	EFC	R_s	R_{SEI}	τ_a	α_a	R_{ct}	τ_c	α_c	K_d	β	L	error
Cell 1	600	0.031534	0.01429	0.001267	0.666921	0.011477	0.021046	0.780707	0.004655	0.610689	6.06E-07	0.024222
Cell 2	600	0.029623	0.013413	0.00128	0.636703	0.011369	0.025707	0.768203	0.003316	0.658496	5.95E-07	0.084795
Cell 3	600	0.032844	0.018524	0.001537	0.625052	0.00918	0.021387	0.834021	0.0054	0.602159	5.98E-07	0.025391
	EFC	R_s	R_{SEI}	τ_a	α_a	R_{ct}	τ_c	α_c	K_d	β	L	error
Cell 1	700	0.042427	0.028695	0.001593	0.606004	0.006956	0.019994	1	0.016213	0.456321	6.04E-07	0.127558
Cell 2	700	0.035755	0.022424	0.001824	0.595858	0.007067	0.024422	0.956787	0.007563	0.539312	5.97E-07	0.157849
Cell 3	700	0.043702	0.03221	0.001562	0.584519	0.007381	0.020318	1	0.016566	0.460841	5.96E-07	0.129827

Table C.13. 20 °C DOD25 C1D2

	EFC	R_s	R_{SEI}	τ_a	α_a	R_{ct}	τ_c	α_c	K_d	β	L	error
Cell 1	89	0.028514	0.007499	0.000834	0.694892	0.003316	0.006021	0.85555	0.003295	0.569379	5.91E-07	0.036564
Cell 2	90	0.028354	0.00797	0.00081	0.657285	0.003083	0.005751	0.855097	0.003161	0.579557	5.91E-07	0.027915
Cell 3	90	0.028135	0.008072	0.00081	0.642368	0.003083	0.005277	0.821028	0.00305	0.5914	5.91E-07	0.03639
	EFC	R_s	R_{SEI}	τ_a	α_a	R_{ct}	τ_c	α_c	K_d	β	L	error
Cell 1	179	0.028511	0.008103	0.000987	0.659916	0.003983	0.007685	0.820553	0.002954	0.613901	5.92E-07	0.020843
Cell 2	179	0.028352	0.007969	0.000817	0.639771	0.004516	0.006899	0.795844	0.002846	0.621072	5.90E-07	0.026278
Cell 3	179	0.028133	0.011261	0.001479	0.600163	0.001455	0.008889	1	0.002769	0.629219	5.91E-07	0.015609
	EFC	R_s	R_{SEI}	τ_a	α_a	R_{ct}	τ_c	α_c	K_d	β	L	error
Cell 1	279	0.028509	0.011751	0.001826	0.611282	0.003054	0.013439	0.942709	0.002835	0.642239	5.92E-07	0.010412
Cell 2	280	0.028349	0.011199	0.001512	0.592689	0.00358	0.012273	0.900653	0.002727	0.647473	5.90E-07	0.011237
Cell 3	279	0.02813	0.012301	0.001753	0.58516	0.002635	0.012812	0.977886	0.002746	0.643859	5.90E-07	0.00787
	EFC	R_s	R_{SEI}	τ_a	α_a	R_{ct}	τ_c	α_c	K_d	β	L	error
Cell 1	376	0.028523	0.013594	0.002251	0.57171	0.002861	0.016411	1	0.002991	0.634443	5.93E-07	0.006334
Cell 2	378	0.028346	0.013244	0.001955	0.55875	0.002939	0.015121	0.982537	0.002854	0.639813	5.90E-07	0.003057
Cell 3	377	0.028199	0.012924	0.001807	0.566407	0.003326	0.015004	0.956663	0.00288	0.637434	5.91E-07	0.008918
	EFC	R_s	R_{SEI}	τ_a	α_a	R_{ct}	τ_c	α_c	K_d	β	L	error
Cell 1	475	0.028637	0.013592	0.002059	0.587335	0.003887	0.017187	0.967258	0.003213	0.629454	5.93E-07	0.004465
Cell 2	477	0.028354	0.013289	0.001759	0.568378	0.004006	0.01587	0.945732	0.003006	0.636681	5.91E-07	0.004096
Cell 3	476	0.028364	0.012923	0.001726	0.584952	0.004081	0.015806	0.94948	0.003121	0.62702	5.91E-07	0.009058
	EFC	R_s	R_{SEI}	τ_a	α_a	R_{ct}	τ_c	α_c	K_d	β	L	error
Cell 1	571	0.028635	0.017958	0.003468	0.551476	0.003398	0.020881	1	0.003184	0.652818	5.94E-07	0.063711
Cell 2	575	0.028351	0.017345	0.003026	0.536384	0.003349	0.019553	1	0.002953	0.658519	5.90E-07	0.043781
Cell 3	573	0.028361	0.017337	0.00306	0.54964	0.003494	0.020372	1	0.003001	0.65546	5.91E-07	0.088775
	EFC	R_s	R_{SEI}	τ_a	α_a	R_{ct}	τ_c	α_c	K_d	β	L	error
Cell 1	665	0.029112	0.018024	0.003121	0.575072	0.004792	0.022627	1	0.004125	0.612485	5.93E-07	0.018166
Cell 2	670	0.028373	0.017343	0.002723	0.551783	0.004575	0.021244	1	0.003513	0.628695	5.91E-07	0.010194
Cell 3	668	0.028428	0.017335	0.002885	0.561553	0.004495	0.021388	1	0.00359	0.625867	5.91E-07	0.012441
	EFC	R_s	R_{SEI}	τ_a	α_a	R_{ct}	τ_c	α_c	K_d	β	L	error
Cell 1	724	0.037053	0.0304	0.003312	0.57408	0.00407	0.019575	1	0.012965	0.498798	5.69E-07	0.060898
Cell 2	763	0.028976	0.017342	0.002536	0.577613	0.006684	0.024147	0.972468	0.004045	0.617871	5.92E-07	0.012474
Cell 3	761	0.029196	0.017734	0.002597	0.591327	0.006465	0.024012	0.990857	0.004293	0.612595	5.91E-07	0.014516
	EFC	R_s	R_{SEI}	τ_a	α_a	R_{ct}	τ_c	α_c	K_d	β	L	error
Cell 1												
Cell 2	818	0.039874	0.031454	0.003312	0.616772	0.004	0.019575	1	0.012732	0.515233	5.69E-07	0.082301
Cell 3	800	0.038843	0.032916	0.003312	0.594972	0.004144	0.019575	1	0.012881	0.507929	5.69E-07	0.065761

Table C.14. 20 °C DOD50 C1D2

	EFC	R_s	R_{SEI}	τ_a	α_a	R_{ct}	τ_c	α_c	K_d	β	L	error
Cell 1	102	0.028064	0.009264	0.00102	0.624194	0.004909	0.006808	0.764858	0.002507	0.657426	5.64E-07	0.020134
Cell 2	101	0.028443	0.008883	0.00106	0.624194	0.005138	0.006752	0.748314	0.002464	0.662459	5.64E-07	0.025056
Cell 3	101	0.028064	0.008597	0.000846	0.64001	0.006005	0.006245	0.75594	0.002511	0.660249	5.61E-07	0.016415
	EFC	R_s	R_{SEI}	τ_a	α_a	R_{ct}	τ_c	α_c	K_d	β	L	error
Cell 1	202	0.028328	0.012363	0.00158	0.625935	0.004185	0.011141	0.891276	0.002799	0.645279	5.66E-07	0.007948
Cell 2	202	0.028595	0.012348	0.001642	0.620243	0.003342	0.010746	0.920403	0.002809	0.639791	5.66E-07	0.011573
Cell 3												
	EFC	R_s	R_{SEI}	τ_a	α_a	R_{ct}	τ_c	α_c	K_d	β	L	error
Cell 1	298	0.038335	0.01666	0.001565	0.638454	0.008448	0.016237	0.967847	0.009992	0.501778	5.64E-07	0.033943
Cell 2	282	0.038576	0.017002	0.001626	0.629006	0.007674	0.016256	0.978808	0.009347	0.510466	5.64E-07	0.042654
Cell 3	287	0.037527	0.014962	0.001209	0.65281	0.009359	0.014322	0.947185	0.010112	0.494172	5.59E-07	0.033034

Table C.15. 20 °C DOD75 C1D2

	EFC	R_s	R_{SEI}	τ_a	α_a	R_{ct}	τ_c	α_c	K_d	β	L	error
Cell 1	103	0.028459	0.012	0.001272	0.638824	0.003862	0.014304	1	0.002586	0.64727	5.64E-07	0.888577
Cell 2	103	0.029074	0.007764	0.000838	0.726514	0.00805	0.008581	0.769844	0.002747	0.635887	5.64E-07	0.021775
Cell 3	103	0.028359	0.009105	0.000838	0.648638	0.007025	0.008769	0.769953	0.002625	0.644101	5.64E-07	0.017859
	EFC	R_s	R_{SEI}	τ_a	α_a	R_{ct}	τ_c	α_c	K_d	β	L	error
Cell 1												
Cell 2	204	0.029745	0.012544	0.00123	0.6769	0.009345	0.014729	0.848844	0.003949	0.61184	5.66E-07	0.020964
Cell 3	205	0.028525	0.013758	0.001508	0.598755	0.006315	0.015725	0.887132	0.0031	0.632134	5.66E-07	0.013665
	EFC	R_s	R_{SEI}	τ_a	α_a	R_{ct}	τ_c	α_c	K_d	β	L	error
Cell 1	249	0.038239	0.022074	0.002539	0.578459	0.006642	0.02296	1	0.009901	0.509974	5.64E-07	0.00818
Cell 2	240	0.0382	0.019344	0.001547	0.588707	0.009892	0.017235	0.920559	0.00971	0.514555	5.67E-07	0.007859
Cell 3	254	0.038028	0.01991	0.001478	0.578598	0.010558	0.018632	0.907689	0.009182	0.522055	5.67E-07	0.008729

Table C.16. 20 °C DOD100 C1D2

	EFC	R_s	R_{SEI}	τ_a	α_a	R_{ct}	τ_c	α_c	K_d	β	L	error
Cell 1	0	0.028067	0.006	0.000855	0.832259	0.011073	0.00225	0.514349	0.002405	0.692176	5.62E-07	0.090666
Cell 2	0	0.028359	0.006	0.000839	0.812301	0.011229	0.00225	0.53208	0.002506	0.68543	5.52E-07	0.064907
Cell 3	0	0.028114	0.006	0.000838	0.816776	0.01146	0.00225	0.523801	0.002488	0.687638	5.49E-07	0.063675
	EFC	R_s	R_{SEI}	τ_a	α_a	R_{ct}	τ_c	α_c	K_d	β	L	error
Cell 1	103	0.028602	0.009158	0.000847	0.684116	0.010179	0.020147	0.790063	0.003043	0.61138	5.64E-07	0.047569
Cell 2	102	0.028777	0.008924	0.000785	0.684031	0.011175	0.02081	0.769319	0.002895	0.627748	5.53E-07	0.017855
Cell 3	102	0.028722	0.009369	0.00087	0.676694	0.010431	0.021054	0.791499	0.002974	0.618894	5.50E-07	0.031022
	EFC	R_s	R_{SEI}	τ_a	α_a	R_{ct}	τ_c	α_c	K_d	β	L	error
Cell 1	203	0.028858	0.009059	0.001	0.669902	0.012555	0.030674	0.796343	0.003198	0.616296	5.66E-07	0.00873
Cell 2	202	0.029134	0.009667	0.001089	0.652488	0.012184	0.03275	0.816129	0.003248	0.614579	5.55E-07	0.006901
Cell 3	202	0.029111	0.009416	0.001071	0.667314	0.012655	0.032371	0.808532	0.003168	0.621832	5.52E-07	0.011735
	EFC	R_s	R_{SEI}	τ_a	α_a	R_{ct}	τ_c	α_c	K_d	β	L	error
Cell 1	301	0.028973	0.010333	0.001171	0.651549	0.018292	0.054788	0.830421	0.004311	0.569104	5.67E-07	0.011455
Cell 2	299	0.02931	0.010144	0.00108	0.660335	0.020032	0.05843	0.814599	0.00392	0.597825	5.57E-07	0.054631
Cell 3	300	0.029313	0.010424	0.001168	0.662592	0.019689	0.057605	0.824944	0.004069	0.589987	5.53E-07	0.044793
	EFC	R_s	R_{SEI}	τ_a	α_a	R_{ct}	τ_c	α_c	K_d	β	L	error
Cell 1	397	0.029158	0.012006	0.00159	0.586307	0.016683	0.065192	0.906284	0.00714	0.478101	5.69E-07	0.107431
Cell 2	393	0.029748	0.012685	0.001681	0.582053	0.016649	0.06609	0.926983	0.007721	0.470632	5.58E-07	0.132615
Cell 3	391	0.030068	0.015011	0.00178	0.5924	0.015129	0.055584	0.952883	0.008624	0.47984	5.55E-07	0.106999
	EFC	R_s	R_{SEI}	τ_a	α_a	R_{ct}	τ_c	α_c	K_d	β	L	error
Cell 1	481	0.032048	0.013057	0.001146	0.690445	0.02644	0.064185	0.812924	0.009204	0.516816	5.71E-07	0.152234
Cell 2	471	0.036542	0.017399	0.001106	0.637147	0.023698	0.03962	0.796348	0.007029	0.603214	5.60E-07	0.134721
Cell 3	431	0.038981	0.019092	0.001397	0.608792	0.012195	0.022563	0.907027	0.011258	0.508167	5.53E-07	0.011245

Table C.17. 45 °C DOD50 C1D1

	EFC	R_s	R_{SEI}	τ_a	α_a	R_{ct}	τ_c	α_c	K_d	β	L	error
Cell 1	0	0.027609	0.00275	0.00045	0.75	0.016761	0.001604	0.584205	0.002465	0.691646	6.41E-07	0.066587
Cell 2	0	0.028178	0.004291	0.001045	0.858903	0.01493	0.001714	0.531028	0.002312	0.705159	5.61E-07	0.080151
Cell 3	0	0.028121	0.004291	0.001047	0.885784	0.01549	0.001714	0.513852	0.002312	0.712626	5.32E-07	0.088637
	EFC	R_s	R_{SEI}	τ_a	α_a	R_{ct}	τ_c	α_c	K_d	β	L	error
Cell 1	107	0.028705	0.004125	0.000301	0.825	0.015194	0.005524	0.620695	0.001972	0.718114	6.39E-07	0.095373
Cell 2	107	0.029638	0.003597	0.000438	0.93014	0.014145	0.005999	0.63389	0.002019	0.708925	5.62E-07	0.083414
Cell 3	107	0.029909	0.003247	0.000455	0.974362	0.015023	0.005999	0.62923	0.002001	0.715147	5.33E-07	0.081598
	EFC	R_s	R_{SEI}	τ_a	α_a	R_{ct}	τ_c	α_c	K_d	β	L	error
Cell 1	212	0.029413	0.006188	0.000427	0.824365	0.01304	0.011423	0.696375	0.002248	0.681451	6.37E-07	0.039407
Cell 2	214	0.030223	0.005938	0.000586	0.860194	0.011316	0.011868	0.736757	0.002358	0.665676	5.61E-07	0.017898
Cell 3	213	0.030538	0.006352	0.000633	0.876926	0.012019	0.01384	0.745996	0.002446	0.660714	5.32E-07	0.020013
	EFC	R_s	R_{SEI}	τ_a	α_a	R_{ct}	τ_c	α_c	K_d	β	L	error
Cell 1	313	0.029613	0.008726	0.000616	0.741928	0.011605	0.020361	0.785008	0.002638	0.64335	6.35E-07	0.031736
Cell 2	315	0.030326	0.008083	0.000772	0.774174	0.01149	0.02135	0.793652	0.00259	0.648124	5.59E-07	0.016995
Cell 3	314	0.030654	0.008155	0.000785	0.789233	0.012106	0.022509	0.792492	0.002571	0.653591	5.30E-07	0.022599
	EFC	R_s	R_{SEI}	τ_a	α_a	R_{ct}	τ_c	α_c	K_d	β	L	error
Cell 1	412	0.030763	0.01053	0.000751	0.667735	0.01135	0.027978	0.83673	0.002719	0.660072	6.33E-07	0.054604
Cell 2	414	0.031368	0.009808	0.0009	0.696757	0.011427	0.029175	0.846263	0.002903	0.68053	5.57E-07	0.041542
Cell 3	413	0.03205	0.009923	0.000944	0.71031	0.0119	0.030516	0.845919	0.002908	0.68627	5.32E-07	0.030854
	EFC	R_s	R_{SEI}	τ_a	α_a	R_{ct}	τ_c	α_c	K_d	β	L	error
Cell 1	507	0.030983	0.013351	0.00095	0.600962	0.01581	0.047512	0.836833	0.002624	0.67979	6.34E-07	0.085338
Cell 2	509	0.031422	0.01228	0.001016	0.627081	0.014987	0.044632	0.843366	0.002881	0.650036	5.59E-07	0.037015
Cell 3	508	0.032112	0.012619	0.001083	0.639279	0.015065	0.045522	0.857753	0.003157	0.633868	5.33E-07	0.044357
	EFC	R_s	R_{SEI}	τ_a	α_a	R_{ct}	τ_c	α_c	K_d	β	L	error
Cell 1	600	0.030873	0.015999	0.001109	0.540866	0.014644	0.050722	0.880556	0.003312	0.6276	6.36E-07	0.014944
Cell 2	601	0.032116	0.013104	0.001103	0.620943	0.015894	0.048899	0.860608	0.003203	0.635992	5.61E-07	0.065669
Cell 3	599	0.032481	0.013718	0.001095	0.622582	0.015876	0.048869	0.863879	0.003446	0.625407	5.35E-07	0.031588
	EFC	R_s	R_{SEI}	τ_a	α_a	R_{ct}	τ_c	α_c	K_d	β	L	error
Cell 1	689	0.030564	0.018368	0.001232	0.498662	0.012895	0.050215	0.922288	0.003728	0.607331	6.34E-07	0.007807
Cell 2	690	0.03206	0.015212	0.001332	0.564218	0.013425	0.04841	0.906296	0.003869	0.595627	5.62E-07	0.005603
Cell 3	687	0.032381	0.01632	0.001327	0.560324	0.013178	0.04838	0.914035	0.004113	0.591663	5.36E-07	0.00672
	EFC	R_s	R_{SEI}	τ_a	α_a	R_{ct}	τ_c	α_c	K_d	β	L	error
Cell 1	775	0.03065	0.019876	0.001257	0.481999	0.012545	0.049712	0.938079	0.004015	0.602261	6.32E-07	0.009129
Cell 2	775	0.032382	0.016484	0.001352	0.547737	0.013105	0.047926	0.919065	0.004117	0.594304	5.64E-07	0.007094
Cell 3	770	0.032611	0.018533	0.001414	0.532898	0.01255	0.047896	0.933793	0.004474	0.589733	5.38E-07	0.009786
	EFC	R_s	R_{SEI}	τ_a	α_a	R_{ct}	τ_c	α_c	K_d	β	L	error
Cell 1	856	0.031495	0.022582	0.001485	0.473865	0.011816	0.049215	0.953683	0.004592	0.599398	6.34E-07	0.012794
Cell 2	855	0.032061	0.020473	0.001513	0.492963	0.011624	0.047447	0.946502	0.004592	0.592552	5.66E-07	0.010663
Cell 3	846	0.038644	0.032018	0.001819	0.502606	0.011415	0.047417	0.998984	0.006296	0.607411	5.36E-07	0.074078
	EFC	R_s	R_{SEI}	τ_a	α_a	R_{ct}	τ_c	α_c	K_d	β	L	error
Cell 1	920	0.041499	0.036792	0.00203	0.492821	0.010352	0.019837	0.960984	0.016337	0.464842	6.08E-07	0.030845
Cell 2	932	0.060472	0.037459	0.000558	0.577855	0.028528	0.025378	0.771075	0.016516	0.515475	4.93E-07	0.016581
Cell 3												

Table C.18. 45 °C DOD100 C1D1

	EFC	R_s	R_{SEI}	τ_a	α_a	R_{ct}	τ_c	α_c	K_d	β	L	error
Cell 1	0	0.027908	0.004291	0.0009	0.830476	0.015153	0.001714	0.53954	0.002312	0.712298	5.91E-07	0.077358
Cell 2	0	0.027611	0.004291	0.000937	0.886814	0.015856	0.001714	0.496103	0.002312	0.707614	6.05E-07	0.064515
Cell 3	0	0.028105	0.004291	0.000966	0.864874	0.014979	0.001714	0.510686	0.002312	0.706622	6.07E-07	0.050665
	EFC	R_s	R_{SEI}	τ_a	α_a	R_{ct}	τ_c	α_c	K_d	β	L	error
Cell 1	106	0.029707	0.011506	0.000828	0.675028	0.01469	0.041614	0.799224	0.002764	0.641236	5.93E-07	0.017047
Cell 2	106	0.029164	0.012485	0.000778	0.640155	0.014853	0.042847	0.796028	0.00258	0.662894	6.04E-07	0.021551
Cell 3	106	0.029577	0.012661	0.000859	0.629947	0.013521	0.041699	0.815087	0.002645	0.651474	6.09E-07	0.009462
	EFC	R_s	R_{SEI}	τ_a	α_a	R_{ct}	τ_c	α_c	K_d	β	L	error
Cell 1	214	0.029973	0.012336	0.000892	0.63672	0.019773	0.074847	0.819829	0.003305	0.606071	5.94E-07	0.019515
Cell 2	214	0.029685	0.0127	0.000885	0.62238	0.019481	0.074121	0.824088	0.003383	0.600842	6.05E-07	0.015042
Cell 3	213	0.030282	0.012165	0.000893	0.634926	0.018889	0.07086	0.822312	0.003264	0.607074	6.11E-07	0.016404
	EFC	R_s	R_{SEI}	τ_a	α_a	R_{ct}	τ_c	α_c	K_d	β	L	error
Cell 1	314	0.030157	0.012934	0.000898	0.608927	0.024619	0.105058	0.811631	0.003697	0.592293	5.96E-07	0.042276
Cell 2	314	0.030088	0.012376	0.000851	0.618937	0.023187	0.096344	0.815847	0.004287	0.553886	6.07E-07	0.018938
Cell 3	313	0.030615	0.01232	0.000852	0.621651	0.023128	0.095556	0.814089	0.004065	0.56563	6.09E-07	0.021429
	EFC	R_s	R_{SEI}	τ_a	α_a	R_{ct}	τ_c	α_c	K_d	β	L	error
Cell 1												
Cell 2	414	0.030665	0.012278	0.00083	0.634165	0.02952	0.130003	0.812906	0.005903	0.501519	6.05E-07	0.033812
Cell 3	413	0.031353	0.012147	0.000841	0.641122	0.029101	0.126883	0.811532	0.005695	0.509103	6.07E-07	0.038921
	EFC	R_s	R_{SEI}	τ_a	α_a	R_{ct}	τ_c	α_c	K_d	β	L	error
Cell 1	509	0.031368	0.012419	0.000835	0.628138	0.032019	0.153906	0.803514	0.0072	0.474927	5.98E-07	0.04889
Cell 2	510	0.03108	0.013179	0.000871	0.607503	0.033919	0.162167	0.804777	0.006101	0.515608	6.07E-07	0.125457
Cell 3	507	0.031819	0.012517	0.00084	0.623588	0.032313	0.152981	0.803416	0.006734	0.489696	6.05E-07	0.066468
	EFC	R_s	R_{SEI}	τ_a	α_a	R_{ct}	τ_c	α_c	K_d	β	L	error
Cell 1	601	0.031976	0.012058	0.000773	0.638277	0.033495	0.16802	0.795479	0.009078	0.444277	5.96E-07	0.069165
Cell 2	602	0.032069	0.011629	0.000761	0.653787	0.032857	0.163439	0.796729	0.009619	0.432123	6.05E-07	0.049751
Cell 3	599	0.032646	0.011641	0.000752	0.650654	0.031772	0.159316	0.800964	0.009896	0.423939	6.04E-07	0.045022
	EFC	R_s	R_{SEI}	τ_a	α_a	R_{ct}	τ_c	α_c	K_d	β	L	error
Cell 1	691	0.032579	0.010824	0.000738	0.662207	0.028261	0.163499	0.827655	0.015205	0.35969	5.98E-07	0.022443
Cell 2	692	0.032016	0.011274	0.000676	0.625852	0.026938	0.160344	0.837475	0.015838	0.35229	6.04E-07	0.023851
Cell 3	688	0.033194	0.010502	0.000748	0.668745	0.02758	0.158919	0.828757	0.015115	0.358185	6.05E-07	0.020318
	EFC	R_s	R_{SEI}	τ_a	α_a	R_{ct}	τ_c	α_c	K_d	β	L	error
Cell 1	778	0.032986	0.010369	0.00072	0.664613	0.024676	0.161552	0.866797	0.020261	0.332825	6.00E-07	0.01708
Cell 2	779	0.032551	0.010522	0.000641	0.632185	0.022765	0.156432	0.889211	0.022139	0.320183	6.02E-07	0.016716
Cell 3	775	0.03355	0.009748	0.000707	0.676883	0.023909	0.159837	0.869753	0.021	0.324133	6.07E-07	0.016454
	EFC	R_s	R_{SEI}	τ_a	α_a	R_{ct}	τ_c	α_c	K_d	β	L	error
Cell 1	862	0.033142	0.011806	0.000671	0.613349	0.022369	0.155924	0.903347	0.023016	0.339554	5.98E-07	0.017018
Cell 2	861	0.033657	0.012979	0.000723	0.599111	0.023029	0.148611	0.896	0.021756	0.363243	6.04E-07	0.018091
Cell 3	859	0.033705	0.011477	0.000661	0.615372	0.021524	0.151961	0.904471	0.023287	0.339132	6.05E-07	0.016682
	EFC	R_s	R_{SEI}	τ_a	α_a	R_{ct}	τ_c	α_c	K_d	β	L	error
Cell 1	941	0.034409	0.014464	0.000762	0.582779	0.023126	0.149941	0.894314	0.021243	0.383916	6.00E-07	0.024597
Cell 2	936	0.034661	0.019078	0.000729	0.52126	0.024787	0.14118	0.892151	0.020041	0.422504	6.02E-07	0.023352
Cell 3	938	0.034602	0.014727	0.000741	0.567144	0.022009	0.144363	0.904071	0.021097	0.386041	6.07E-07	0.044692
	EFC	R_s	R_{SEI}	τ_a	α_a	R_{ct}	τ_c	α_c	K_d	β	L	error
Cell 1	1011	0.035365	0.023264	0.000944	0.488639	0.026246	0.142444	0.896949	0.016133	0.486716	6.02E-07	0.030313
Cell 2	994	0.038183	0.038781	0.001595	0.419391	0.026064	0.134121	0.948186	0.014028	0.549338	6.00E-07	0.067055
Cell 3	1008	0.034857	0.023865	0.000897	0.460699	0.023782	0.137145	0.917149	0.017471	0.470042	6.09E-07	0.017551
	EFC	R_s	R_{SEI}	τ_a	α_a	R_{ct}	τ_c	α_c	K_d	β	L	error
Cell 1	1066	0.039032	0.031931	0.000482	0.511926	0.035069	0.103563	0.817304	0.01177	0.592227	6.94E-07	0.018753
Cell 2	1027	0.04581	0.066288	0.000434	0.405242	0.037978	0.065465	0.840349	0.019456	0.577226	7.57E-07	0.011089
Cell 3	1064	0.038949	0.033996	0.000767	0.455029	0.03	0.111787	0.89486	0.015116	0.543654	6.60E-07	0.014376

Table C.19. 45 °C DOD50 C1D2

	EFC	R_s	R_{SEI}	τ_a	α_a	R_{ct}	τ_c	α_c	K_d	β	L	error
Cell 1	0	0.028711	0.005148	0.000849	0.835924	0.0132	0.002257	0.54767	0.002415	0.696137	5.65E-07	0.045185
Cell 2	0	0.028778	0.005148	0.000829	0.846776	0.0132	0.002324	0.556062	0.002415	0.695567	5.72E-07	0.054788
Cell 3	0	0.028789	0.005148	0.000787	0.868351	0.0132	0.002484	0.545949	0.002415	0.696919	5.84E-07	0.062341
	EFC	R_s	R_{SEI}	τ_a	α_a	R_{ct}	τ_c	α_c	K_d	β	L	error
Cell 1	107	0.029847	0.007208	0.000679	0.802816	0.009302	0.009601	0.730923	0.002348	0.665271	5.67E-07	0.031948
Cell 2	107	0.029721	0.007492	0.000663	0.78795	0.009162	0.00967	0.734519	0.002367	0.664288	5.74E-07	0.022628
Cell 3	107	0.029438	0.007889	0.00063	0.760309	0.009453	0.009493	0.720535	0.002241	0.681513	5.86E-07	0.023628
	EFC	R_s	R_{SEI}	τ_a	α_a	R_{ct}	τ_c	α_c	K_d	β	L	error
Cell 1	239	0.030045	0.008043	0.000727	0.780791	0.010505	0.017206	0.784045	0.002421	0.663027	5.69E-07	0.017738
Cell 2	241	0.030166	0.008059	0.000738	0.790108	0.010641	0.017743	0.788675	0.002472	0.660689	5.76E-07	0.022664
Cell 3	241	0.029749	0.008788	0.000724	0.745956	0.009951	0.017175	0.791933	0.002504	0.65777	5.87E-07	0.010401
	EFC	R_s	R_{SEI}	τ_a	α_a	R_{ct}	τ_c	α_c	K_d	β	L	error
Cell 1	340	0.030152	0.009918	0.000882	0.714079	0.010828	0.025876	0.832234	0.002531	0.65596	5.70E-07	0.020771
Cell 2	341	0.030387	0.009658	0.000864	0.733389	0.011412	0.026216	0.82461	0.002574	0.658037	5.78E-07	0.018461
Cell 3	342	0.030052	0.009845	0.000829	0.715617	0.010779	0.024111	0.82306	0.002653	0.650007	5.89E-07	0.010305
	EFC	R_s	R_{SEI}	τ_a	α_a	R_{ct}	τ_c	α_c	K_d	β	L	error
Cell 1	446	0.031407	0.012005	0.001068	0.657971	0.013515	0.041421	0.867213	0.00292	0.638044	5.72E-07	0.018084
Cell 2	438	0.031688	0.012094	0.001034	0.661302	0.013617	0.041305	0.863834	0.003059	0.630028	5.79E-07	0.012853
Cell 3	447	0.0316	0.010971	0.000962	0.691736	0.012883	0.035272	0.855696	0.003099	0.625483	5.91E-07	0.015922
	EFC	R_s	R_{SEI}	τ_a	α_a	R_{ct}	τ_c	α_c	K_d	β	L	error
Cell 1	540	0.031999	0.012264	0.001014	0.655131	0.017174	0.051373	0.850724	0.003084	0.636506	5.74E-07	0.043049
Cell 2	532	0.032154	0.012566	0.001012	0.654855	0.017059	0.051455	0.854298	0.00317	0.636329	5.81E-07	0.030697
Cell 3	541	0.031754	0.012896	0.001008	0.645726	0.015667	0.047182	0.868358	0.003217	0.631738	5.93E-07	0.033772
	EFC	R_s	R_{SEI}	τ_a	α_a	R_{ct}	τ_c	α_c	K_d	β	L	error
Cell 1	631	0.032622	0.01278	0.001005	0.648709	0.017204	0.051699	0.86172	0.003562	0.612418	5.75E-07	0.02711
Cell 2												
Cell 3	632	0.032074	0.013578	0.00097	0.628537	0.015572	0.047182	0.87632	0.003863	0.598967	5.94E-07	0.006696
	EFC	R_s	R_{SEI}	τ_a	α_a	R_{ct}	τ_c	α_c	K_d	β	L	error
Cell 1	719	0.03292	0.013681	0.001043	0.624792	0.016182	0.051182	0.883281	0.004058	0.590517	5.77E-07	0.011055
Cell 2	709	0.033029	0.01402	0.001061	0.627453	0.015957	0.050941	0.886727	0.004316	0.582845	5.83E-07	0.013347
Cell 3	719	0.031928	0.015697	0.001041	0.571315	0.013866	0.046711	0.905078	0.004284	0.586405	5.96E-07	0.005829
	EFC	R_s	R_{SEI}	τ_a	α_a	R_{ct}	τ_c	α_c	K_d	β	L	error
Cell 1	803	0.033382	0.014633	0.001016	0.613419	0.016273	0.05067	0.891331	0.004459	0.582119	5.79E-07	0.01019
Cell 2	792	0.033394	0.015144	0.001036	0.61661	0.016039	0.050431	0.896836	0.004759	0.575614	5.84E-07	0.01247
Cell 3	802	0.032866	0.016468	0.00097	0.57909	0.014807	0.046244	0.904465	0.004803	0.578168	5.98E-07	0.008595
	EFC	R_s	R_{SEI}	τ_a	α_a	R_{ct}	τ_c	α_c	K_d	β	L	error
Cell 1	882	0.03414	0.017325	0.001033	0.578135	0.016085	0.050164	0.909129	0.005045	0.576488	5.81E-07	0.012201
Cell 2	868	0.034652	0.020331	0.001048	0.565543	0.016314	0.049927	0.91958	0.005627	0.58137	5.86E-07	0.020803
Cell 3	873	0.041166	0.05315	0.001459	0.37395	0.011605	0.033307	1	0.010832	0.582468	6.38E-07	0.011206
	EFC	R_s	R_{SEI}	τ_a	α_a	R_{ct}	τ_c	α_c	K_d	β	L	error
Cell 1	940	0.044958	0.052202	0.001302	0.384496	0.009751	0.029564	0.993089	0.0136	0.535322	6.26E-07	0.009462
Cell 2	901	0.044388	0.05747	0.001829	0.363362	0.008109	0.030676	1	0.016267	0.506981	6.38E-07	0.010907
Cell 3												

Table C.20. 45 °C DOD100 C1D2

	EFC	R_s	R_{SEI}	τ_a	α_a	R_{ct}	τ_c	α_c	K_d	β	L	error
Cell 1	0	0.028755	0.005148	0.000774	0.877973	0.0132	0.002501	0.548039	0.002415	0.696561	5.68E-07	0.069518
Cell 2	0	0.028517	0.005148	0.000775	0.845196	0.0132	0.002369	0.550832	0.002415	0.694293	5.74E-07	0.051975
Cell 3	0	0.029132	0.005148	0.000785	0.87347	0.0132	0.002557	0.550266	0.002415	0.699147	5.63E-07	0.066621
	EFC	R_s	R_{SEI}	τ_a	α_a	R_{ct}	τ_c	α_c	K_d	β	L	error
Cell 1	106	0.03003	0.01129	0.0008	0.698662	0.014329	0.038806	0.796895	0.002715	0.645484	5.69E-07	0.019021
Cell 2	106	0.029878	0.011531	0.000818	0.681918	0.014191	0.040113	0.804089	0.002673	0.647954	5.75E-07	0.016781
Cell 3	106	0.030337	0.011374	0.000837	0.691542	0.01391	0.039152	0.809212	0.002716	0.643977	5.64E-07	0.018756
	EFC	R_s	R_{SEI}	τ_a	α_a	R_{ct}	τ_c	α_c	K_d	β	L	error
Cell 1	211	0.030527	0.011832	0.000873	0.678494	0.019012	0.066907	0.817383	0.003304	0.606151	5.70E-07	0.024399
Cell 2	213	0.030464	0.011853	0.000885	0.672574	0.019787	0.070977	0.818066	0.003317	0.604741	5.76E-07	0.022495
Cell 3	212	0.030941	0.011681	0.000901	0.685161	0.019706	0.069862	0.817003	0.003348	0.604568	5.65E-07	0.028312
	EFC	R_s	R_{SEI}	τ_a	α_a	R_{ct}	τ_c	α_c	K_d	β	L	error
Cell 1	310	0.030951	0.011869	0.000848	0.670215	0.023354	0.091012	0.808636	0.004069	0.568652	5.71E-07	0.023376
Cell 2	312	0.030626	0.012336	0.000857	0.645321	0.022919	0.092603	0.820034	0.004147	0.559735	5.78E-07	0.024364
Cell 3	312	0.03135	0.011669	0.000885	0.673006	0.023339	0.091873	0.807997	0.003973	0.575435	5.66E-07	0.02828
	EFC	R_s	R_{SEI}	τ_a	α_a	R_{ct}	τ_c	α_c	K_d	β	L	error
Cell 1	409	0.031307	0.012276	0.00082	0.659762	0.027547	0.119112	0.816637	0.006136	0.494458	5.72E-07	0.033931
Cell 2	411	0.031053	0.012352	0.000826	0.646113	0.026883	0.118344	0.825017	0.006274	0.484037	5.79E-07	0.025818
Cell 3	410	0.031873	0.011657	0.000852	0.676282	0.027197	0.11682	0.814353	0.006257	0.48912	5.67E-07	0.026967
	EFC	R_s	R_{SEI}	τ_a	α_a	R_{ct}	τ_c	α_c	K_d	β	L	error
Cell 1	502	0.031697	0.012263	0.000737	0.648934	0.03184	0.147518	0.782866	0.006668	0.494467	5.74E-07	0.06652
Cell 2	504	0.031594	0.01234	0.000796	0.641102	0.030551	0.145189	0.803361	0.007387	0.465116	5.80E-07	0.062775
Cell 3	503	0.032447	0.011646	0.000792	0.677989	0.032108	0.146669	0.781469	0.006768	0.493105	5.68E-07	0.065225
	EFC	R_s	R_{SEI}	τ_a	α_a	R_{ct}	τ_c	α_c	K_d	β	L	error
Cell 1	592	0.032321	0.012251	0.000712	0.642847	0.030796	0.160933	0.7958	0.010408	0.420297	5.75E-07	0.043493
Cell 2	594	0.031848	0.012328	0.000709	0.62804	0.029133	0.15631	0.81512	0.011033	0.399939	5.81E-07	0.048529
Cell 3	592	0.032992	0.011634	0.000778	0.665458	0.030028	0.157385	0.796368	0.010536	0.419139	5.69E-07	0.04314
	EFC	R_s	R_{SEI}	τ_a	α_a	R_{ct}	τ_c	α_c	K_d	β	L	error
Cell 1	679	0.032289	0.012239	0.000682	0.603391	0.026111	0.169903	0.827302	0.015764	0.357253	5.76E-07	0.030271
Cell 2	682	0.03204	0.012315	0.000652	0.609691	0.028053	0.17309	0.813328	0.013847	0.373318	5.82E-07	0.036588
Cell 3	679	0.0331	0.011623	0.00072	0.641141	0.028084	0.175278	0.806145	0.014487	0.372487	5.71E-07	0.047703
	EFC	R_s	R_{SEI}	τ_a	α_a	R_{ct}	τ_c	α_c	K_d	β	L	error
Cell 1	762	0.032257	0.012227	0.0006	0.569841	0.021264	0.169683	0.890397	0.023118	0.322455	5.77E-07	0.032247
Cell 2	766	0.032008	0.012303	0.000702	0.539331	0.024219	0.197001	0.83514	0.020814	0.331822	5.83E-07	0.084069
Cell 3	762	0.033067	0.011611	0.000764	0.575217	0.023872	0.194313	0.828081	0.021621	0.336719	5.72E-07	0.100568
	EFC	R_s	R_{SEI}	τ_a	α_a	R_{ct}	τ_c	α_c	K_d	β	L	error
Cell 1	841	0.033464	0.012994	0.000643	0.594058	0.020268	0.161199	0.9184	0.025067	0.342419	5.78E-07	0.026627
Cell 2	847	0.032498	0.01364	0.000689	0.539147	0.021601	0.187151	0.886283	0.022839	0.346749	5.85E-07	0.053695
Cell 3	842	0.033385	0.014508	0.000875	0.532272	0.020775	0.184597	0.893526	0.022374	0.363489	5.73E-07	0.067247
	EFC	R_s	R_{SEI}	τ_a	α_a	R_{ct}	τ_c	α_c	K_d	β	L	error
Cell 1	914	0.034451	0.015158	0.00071	0.550962	0.018168	0.153139	0.948534	0.026885	0.358664	5.79E-07	0.03259
Cell 2	923	0.032466	0.01479	0.000661	0.489076	0.016946	0.177793	0.951579	0.027082	0.33862	5.86E-07	0.057492
Cell 3	916	0.033352	0.017091	0.000918	0.469629	0.017451	0.175367	0.936635	0.024617	0.370763	5.74E-07	0.053664
	EFC	R_s	R_{SEI}	τ_a	α_a	R_{ct}	τ_c	α_c	K_d	β	L	error
Cell 1	977	0.034608	0.027467	0.000905	0.448026	0.022812	0.145482	0.936937	0.018871	0.466263	5.80E-07	0.037842
Cell 2	994	0.034524	0.016264	0.00061	0.550242	0.018223	0.13808	0.952048	0.024995	0.382332	6.16E-07	0.025697
Cell 3	984	0.033319	0.026688	0.001298	0.412617	0.02029	0.166599	0.933677	0.017397	0.47131	5.75E-07	0.063893
	EFC	R_s	R_{SEI}	τ_a	α_a	R_{ct}	τ_c	α_c	K_d	β	L	error
Cell 1	1022	0.045142	0.031127	0.000652	0.553776	0.036091	0.092619	0.829132	0.011446	0.587599	5.80E-07	0.009495
Cell 2												
Cell 3	1039	0.038457	0.027112	0.000712	0.525645	0.028501	0.109959	0.862454	0.013617	0.54882	6.24E-07	0.011832

Bibliography

[1] OCDE & IEA. *Market Report Series: Renewables 2017, analysis and forecats to 2022*. Tech. rep. 42. 2017, pp. 20142–20142.

[2] European Commission. *Proposal for a directive of the European Parliament and of the council on the promotion of the use of energy from renewable sources (recast)*. Tech. rep. 2016. 2017.

[3] *European Commission - Europe leads the global clean energy transition: Commission welcomes ambitious agreement on further renewable energy development in the EU.* URL: `http://europa.eu/rapid/press-release{\_}STATEMENT-18-4155{\_}en.htm` (visited on 06/14/2018).

[4] X. Luo, J. Wang, M. Dooner, and J. Clarke. "Overview of current development in electrical energy storage technologies and the application potential in power system operation". In: *Applied Energy* 137 (2015), pp. 511–536.

[5] M. Yoshio, R. J. Brodd, and A. Kozawa. *Lithium-Ion Batteries.* 2009. ISBN: 9780387344447.

[6] O. Schmidt, A. Hawkes, A. Gambhir, and I. Staffell. "The future cost of electrical energy storage based on experience rates". In: *Nature Energy* 6.July (2017), p. 17110.

[7] The Boston Consulting Group. "Focus Batteries for Electric Cars". In: *Outlook* 1 (2010), pp. 1–18.

[8] International Renewable Energy Agency (IRENA). *REthinking Energy.* Tech. rep. July. 2017, p. 96.

[9] T. Diaz de la Rubia, F. Klein, B. Shaffer, N. Kim, and G. Lovric. "Energy storage: Tracking the technologies that will transform the power sector". In: *Deloitte* (2015), pp. 1–21.

[10] *Electricity Storage Gaining Momentum.* Tech. rep. A.T. Kearney Energy Transition Institute, 2018.

[11] A. W. Paper. *201 6 Annual Update on Lithium-Ion Battery Technology.* Tech. rep. Inventus Power, 2017.

[12] *Lithium Ion Batteries (Li-Ion): Cylindrical Series — Panasonic Industrial.* URL: `https://na.industrial.panasonic.com/products/batteries` (visited on 06/11/2018).

[13] International Air Transport Association. "2017 Lithium Battery Guidance Document". In: (2017), pp. 1–20.

[14] C. Curry. "Lithium-ion Battery Costs and Market". In: *Bloomberg New Energy Finance* (2017), p. 14.

[15] A. Maheshwari, M. A. Dumitrescu, M. Destro, and M. Santarelli. "Inverse parameter determination in the development of an optimized lithium iron phosphate Graphite battery discharge model". In: *Journal of Power Sources* 307 (2016), pp. 160–172.

[16] A. Maheshwari, M. A. Dumitrescu, M. Destro, and M. Santarelli. "A modelling approach to understand charge discharge differences in thermal behaviour in lithium iron phosphate - graphite battery". In: *Electrochimica Acta* 243 (2017), pp. 129–141.

[17] W. A. van Schalkwijk and B. Scrosati, eds. *Advances in Lithium-Ion Batteries.* Boston, MA: Springer US, 2002. ISBN: 978-0-306-47356-2.

[18] C. Julien, A. Mauger, A. Vijh, and K. Zaghib. *Lithium Batteries.* 2016, p. 626. ISBN: 978-3-319-19107-2.

[19] N. Lebedeva, F. Di Persio, and L. Boon-Brett. *Lithium ion battery value chain and related opportunities for Europe Title: Lithium ion battery value chain and related opportunities for Europe.* Tech. rep. 2016.

[20] A. K. Padhi, K. Nanjundaswamy, and J. Goodenough. "Phospho-olivines as Positive-Electrode Materials for Rechargeable Lithium Batteries". In: *Journal of The Electrochemical Society* 144.4 (1997), p. 1188.

[21] R. Jung, M. Metzger, F. Maglia, C. Stinner, and H. A. Gasteiger. "Oxygen Release and Its Effect on the Cycling Stability of LiNi _x Mn _y Co _z O ₂ (NMC) Cathode Materials for Li-Ion Batteries". In: *Journal of The Electrochemical Society* 164.7 (2017), A1361–A1377.

[22] A. A. H. Hussein and I. Batarseh. "An overview of generic battery models". In: *IEEE Power and Energy Society General Meeting* 4 (2011), pp. 4–9.

[23] A. Farmann, W. Waag, and D. U. Sauer. "Adaptive approach for on-board impedance parameters and voltage estimation of lithium-ion batteries in electric vehicles". In: *Journal of Power Sources* 299 (2015), pp. 176–188.

[24] P. W. C. Northrop, B. Suthar, V. Ramadesigan, S. Santhanagopalan, R. D. Braatz, and V. R. Subramanian. "Efficient Simulation and Reformulation of Lithium-Ion Battery Models for Enabling Electric Transportation". In: *Journal of the Electrochemical Society* 161.8 (2014), E3149–E3157.

[25] B. Rajabloo, A. Jokar, M. Désilets, and M. Lacroix. “An Inverse Method for Estimating the Electrochemical Parameters of Lithium-Ion Batteries”. In: *Journal of The Electrochemical Society* 164.2 (2017), A99–A105.

[26] L. Cai and R. E. White. “Mathematical modeling of a lithium ion battery with thermal effects in COMSOL Inc. Multiphysics (MP) software”. In: *Journal of Power Sources* 196.14 (2011), pp. 5985–5989.

[27] E. Prada, D. Di Domenico, Y. Creff, J. Bernard, V. Sauvant-Moynot, and F. Huet. “Simplified Electrochemical and Thermal Model of LiFePO4-Graphite Li-Ion Batteries for Fast Charge Applications”. In: *Journal of the Electrochemical Society* 159.9 (2012), A1508–A1519.

[28] J. Bhattacharya and A. Van Der Ven. “Phase stability and nondilute Li diffusion in spinel Li 1+xTi2O4”. In: *Physical Review B - Condensed Matter and Materials Physics* 81.10 (2010), pp. 27–30.

[29] a Van Der Ven and G Ceder. “Lithium Diffusion in Layered Li x CoO 2”. In: *Electrochemical and Solid-State Letters* 3.7 (2000), pp. 301–304.

[30] K. Leung and J. Budzien. “Ab initio Molecular Dynamics Simulations of the Initial Stages of Solid-electrolyte Interphase Formation on Lithium Ion Battery Graphitic Anodes”. In: d (2010), pp. 6583–6586.

[31] S. H. Garofalini. “Molecular dynamics simulations of Li transport between cathode crystals”. In: *Journal of Power Sources* 110.2 (2002), pp. 412–415.

[32] J. Newman and W. Tiedemann. “Porous-electrode theory with battery applications”. In: *AIChE Journal* 21.1 (1975), pp. 25–41.

[33] M. Doyle, T. F. Fuller, and J. Newman. “Modeling of Galvanostatic Charge and Discharge of the Lithium/Polymer/Insertion Cell”. In: *Journal of The Electrochemical Society* 140.6 (1993), p. 1526.

[34] M. Doyle and J. Newman. “The use of mathematical modeling in the design of lithium/polymer battery systems”. In: *Electrochimica Acta* 40.13-14 (1995), pp. 2191–2196.

[35] J. Newman. “Potential and Current Distribution in Electrochemical Cells”. In: *Journal of The Electrochemical Society* 140.7 (1993), p. 1961.

[36] L. O. Valoen and J. N. Reimers. “Transport Properties of LiPF[sub 6]-Based Li-Ion Battery Electrolytes”. In: *Journal of The Electrochemical Society* 152 (2005), A882.

[37] B. Tjaden, S. J. Cooper, D. J. Brett, D. Kramer, and P. R. Shearing. “On the origin and application of the Bruggeman correlation for analysing transport phenomena in electrochemical systems”. In: *Current Opinion in Chemical Engineering* 12 (2016), pp. 44–51.

[38] L. Rao and J. Newman. “Heat-Generation Rate and General Energy Balance for Insertion Battery Systems”. In: *Journal of The Electrochemical Society* 144.8 (1997), pp. 2697–2704.

[39] K. E. Thomas and J. Newman. “Thermal Modeling of Porous Insertion Electrodes”. In: *Journal of The Electrochemical Society* 150.2 (2003), A176.

[40] W. B. Gu and C.-y. Wang. “Thermal-Electrochemical Coupled Modeling of a Lithium-ion Cell”. In: *Electrochemical Society Proceedings* (1999).

[41] V. Srinivasan and J. Newman. “Discharge Model for the Lithium Iron-Phosphate Electrode”. In: *Journal of The Electrochemical Society* 151 (2004), A1517.

[42] C. Wang, U. S. Kasavajjula, and P. E. Arce. “A discharge model for phase transformation electrodes: Formulation, experimental validation, and analysis”. In: *Journal of Physical Chemistry C* 111.44 (2007), pp. 16656–16663.

[43] U. S. Kasavajjula, C. Wang, and P. E. Arce. “Discharge Model for LiFePO[sub 4] Accounting for the Solid Solution Range”. In: *Journal of The Electrochemical Society* 155 (2008), A866.

[44] S. Dargaville and T. W. Farrell. “Predicting Active Material Utilization in LiFePO[sub 4] Electrodes Using a Multiscale Mathematical Model”. In: *Journal of The Electrochemical Society* 157.7 (2010), A830.

[45] G. K. Singh, G. Ceder, and M. Z. Bazant. “Intercalation dynamics in rechargeable battery materials: General theory and phase-transformation waves in LiFePO4”. In: *Electrochimica Acta* 53.26 (2008), pp. 7599–7613.

[46] R. Malik, F. Zhou, and G Ceder. “Kinetics of non-equilibrium lithium incorporation in LiFePO4.” In: *Nature materials* 10.8 (2011), pp. 587–590.

[47] M. Z. Bazant. “Theory of Electrochemical Kinetics based on Nonequilibrium Thermodynamics”. In: ().

[48] B. Orvananos, H.-C. Yu, R. Malik, a. Abdellahi, C. P. Grey, G. Ceder, and K. Thornton. “Effect of a Size-Dependent Equilibrium Potential on Nano-LiFePO4 Particle Interactions”. In: *Journal of the Electrochemical Society* 162.9 (2015), A1718–A1724.

[49] V. Srinivasan and J. Newman. “Existence of Path-Dependence in the LiFePO[sub 4] Electrode”. In: *Electrochemical and Solid-State Letters* 9.3 (2006), A110.

[50] Y. Zhu and C. Wang. “Strain accommodation and potential hysteresis of LiFePO4 cathodes during lithium ion insertion/extraction”. In: *Journal of Power Sources* 196.3 (2011), pp. 1442–1448.

[51] W. Dreyer, J. Jamnik, C. Guhlke, R. Huth, J. Moskon, and M. Gaberscek. “The thermodynamic origin of hysteresis in insertion batteries.” In: *Nature materials* 9.5 (2010), pp. 448–453.

[52] Y. Honda, S. Muto, K. Tatsumi, H. Kondo, K. Horibuchi, T. Kobayashi, and T. Sasaki. “Microscopic mechanism of path-dependence on chargedischarge history in lithium iron phosphate cathode analysis using scanning transmission electron microscopy and electron energy-loss spectroscopy spectral imaging”. In: *Journal of Power Sources* 291 (2015), pp. 85–94.

[53] A. Barai, W. D. Widanage, J. Marco, A. McGordon, and P. Jennings. “A study of the open circuit voltage characterization technique and hysteresis assessment of lithium-ion cells”. In: *Journal of Power Sources* 295 (2015), pp. 99–107.

[54] M. a. Roscher, J. Vetter, and D. U. Sauer. “Characterisation of charge and discharge behaviour of lithium ion batteries with olivine based cathode active material”. In: *Journal of Power Sources* 191.2 (2009), pp. 582–590.

[55] W. C. Chueh, F. El Gabaly, J. D. Sugar, N. C. Bartelt, A. H. McDaniel, K. R. Fenton, K. R. Zavadil, T. Tyliszczak, W. Lai, and K. F. McCarty. “Intercalation pathway in many-particle LiFePO4 electrode revealed by nanoscale state-of-charge mapping”. In: *Nano Letters* 13.3 (2013), pp. 866–872.

[56] M. Safari and C. Delacourt. “Mathematical Modeling of Lithium Iron Phosphate Electrode: Galvanostatic Charge/Discharge and Path Dependence”. In: *Journal of The Electrochemical Society* 158 (2011), A63.

[57] M. Safari and C. Delacourt. “Modeling of a Commercial Graphite/LiFePO[sub 4] Cell”. In: *Journal of The Electrochemical Society* 158.5 (2011), A562–A571.

[58] P. Ramadass, B. Haran, P. M. Gomadam, R. White, and B. N. Popov. “Development of First Principles Capacity Fade Model for Li-Ion Cells”. In: *Journal of The Electrochemical Society* 151.2 (2004), A196.

[59] O. Y. Egorkina and a. M. Skundin. “The effect of temperature on lithium intercalation into carbon materials”. In: *Journal of Solid State Electrochemistry* 2.4 (1998), pp. 216–220.

[60] T. L. Kulova, a. M. Skundin, E. a. Nizhnikovskii, and a. V. Fesenko. “Temperature effect on the lithium diffusion rate in graphite”. In: *Russian Journal of Electrochemistry* 42.3 (2006), pp. 259–262.

[61] D. Y. W. Yu, C. Fietzek, W. Weydanz, K. Donoue, T. Inoue, H. Kurokawa, and S. Fujitani. “Study of LiFePO[sub 4] by Cyclic Voltammetry”. In: *Journal of The Electrochemical Society* 154.4 (2007), A253.

[62] D. Lepage, F. Sobh, C. Kuss, G. Liang, and S. B. Schougaard. “Delithiation kinetics study of carbon coated and carbon free LiFePO4”. In: *Journal of Power Sources* 256 (2014), pp. 61–65.

[63] J. L. Dodd. “Phase Composition and Dynamical Studies of Lithium Iron Phosphate Thesis by”. In: *Discovery* 2007 (2007).

[64] K. E. Thomas and J. Newman. “Heats of mixing and of entropy in porous insertion electrodes”. In: *Journal of Power Sources* 119-121 (2003), pp. 844–849.

[65] S. Al Hallaj, R. Venkatachalapathy, J. Prakash, and J. R. Selman. “Entropy Changes Due to Structural Transformation in the Graphite Anode and Phase Change of the LiCoO[sub 2] Cathode”. In: *Journal of The Electrochemical Society* 147.7 (2000), p. 2432.

[66] V. Srinivasan and C. Y. Wang. “Analysis of Electrochemical and Thermal Behavior of Li-Ion Cells”. In: *Journal of The Electrochemical Society* 150.1 (2003), A98.

[67] R. E. Gerver and J. P. Meyers. “Three-Dimensional Modeling of Electrochemical Performance and Heat Generation of Lithium-Ion Batteries in Tabbed Planar Configurations”. In: *Journal of The Electrochemical Society* 158.7 (2011), A835.

[68] A. Tourani, P. White, and P. Ivey. “A multi scale multi-dimensional thermo electrochemical modelling of high capacity lithium-ion cells”. In: *Journal of Power Sources* 255 (2014), pp. 360–367.

[69] J. Li, Y. Cheng, M. Jia, Y. Tang, Y. Lin, Z. Zhang, and Y. Liu. “An electrochemical-thermal model based on dynamic responses for lithium iron phosphate battery”. In: *Journal of Power Sources* 255 (2014), pp. 130–143.

[70] V. V. Viswanathan, D. Choi, D. Wang, W. Xu, S. Towne, R. E. Williford, J. G. Zhang, J. Liu, and Z. Yang. “Effect of entropy change of lithium intercalation in cathodes and anodes on Li-ion battery thermal management”. In: *Journal of Power Sources* 195.11 (2010), pp. 3720–3729.

[71] A. Yamada, H. Koizumi, S.-I. Nishimura, N. Sonoyama, R. Kanno, M. Yonemura, T. Nakamura, and Y. Kobayashi. “Room-temperaturemiscibility gap in LixFePO4”. In: *Nature materials* 5.5 (2006), pp. 357–60.

[72] D. Dees, E. Gunen, D. Abraham, A. Jansen, and J. Prakash. “Electrochemical Modeling of Lithium-Ion Positive Electrodes during Hybrid Pulse Power Characterization Tests”. In: *Journal of The Electrochemical Society* 155.8 (2008), A603.

[73] M. Doyle, J. Newman, A. S. Gozdz, C. N. Schmutz, and J.-M. Tarascon. “Comparison of Modeling Predictions with Experimental Data from Plastic Lithium Ion Cells”. In: *Journal of The Electrochemical Society* 143.6 (1996), p. 1890.

[74] T. F. Fuller, M. Doyle, and J. Newman. “Simulation and Optimization of the Dual Lithium Ion Insertion Cell”. In: *Journal of The Electrochemical Society* 141.1 (1994), p. 1.

[75] V. Srinivasan and J. Newman. “Design and Optimization of a Natural Graphite/Iron Phosphate Lithium-Ion Cell”. In: *Journal of The Electrochemical Society* 151 (2004), A1530.

[76] P. Arora, M. Doyle, A. S. Gozdz, R. E. White, and J. Newman. “Comparison between computer simulations and experimental data for high-rate discharges of plastic lithium-ion batteries”. In: *Journal of Power Sources* 88.2 (2000), pp. 219–231.

[77] C. Delacourt, L. Laffont, R. Bouchet, C. Wurm, J.-B. Leriche, M. Morcrette, J.-M. Tarascon, and C. Masquelier. “Toward Understanding of Electrical Limitations (Electronic, Ionic) in LiMPO[sub 4] (M=Fe, Mn) Electrode Materials”. In: *Journal of The Electrochemical Society* 152.5 (2005), A913.

[78] I. V. Thorat, T. Joshi, K. Zaghib, J. N. Harb, and D. R. Wheeler. “Understanding Rate-Limiting Mechanisms in LiFePO4 Cathodes for Li-Ion Batteries”. In: *Journal of The Electrochemical Society* 158.11 (2011), A1185.

[79] S. Yu, S Kim, and T. Kim. “Model Prediction and Experiments for the Electrode Design Optimization of LiFePO 4/Graphite Electrodes in High Capacity Lithium-ion Batteries”. In: *Bulletin of the Korean Chemical Society* 34.1 (2013).

[80] W. Wu, X. Xiao, and X. Huang. “The effect of battery design parameters on heat generation and utilization in a Li-ion cell”. In: *Electrochimica Acta* 83 (2012), pp. 227–240.

[81] S. C. Chen, C. C. Wan, and Y. Y. Wang. “Thermal analysis of lithium-ion batteries”. In: *Journal of Power Sources* 140.1 (2005), pp. 111–124.

[82] J. Nanda, S. K. Martha, W. D. Porter, H. Wang, N. J. Dudney, M. D. Radin, and D. J. Siegel. “Thermophysical properties of LiFePO4 cathodes with carbonized pitch coatings and organic binders: Experiments and first-principles modeling”. In: *Journal of Power Sources* 251 (2014), pp. 8–13.

[83] N. Takami, A. Satoh, M. Hara, and T. Ohsaki. “Structural and Kinetic Characterization of Lithium Intercalation into Carbon Anodes for Secondary Lithium Batteries”. In: *Journal of The Electrochemical Society* 142.2 (1995), p. 371.

[84] M. W. Verbrugge and B. J. Koch. “Electrochemical Analysis of Lithiated Graphite Anodes”. In: *Journal of The Electrochemical Society* 150.3 (2003), A374.

[85] M. Doyle and Y. Fuentes. “Computer Simulations of a Lithium-Ion Polymer Battery and Implications for Higher Capacity Next-Generation Battery Designs”. In: *Journal of The Electrochemical Society* 150.6 (2003), A706.

[86] C. Delacourt and M. Safari. “Analysis of lithium deinsertion/insertion in LiyFePO4 with a simple mathematical model”. In: *Electrochimica Acta* 56.14 (2011), pp. 5222–5229.

[87] a. S. Andersson and J. O. Thomas. “The source of first-cycle capacity loss in LiFePO4”. In: *Journal of Power Sources* 97-98 (2001), pp. 498–502.

[88] R. Darling and J. Newman. “Modeling a Porous Intercalation Electrode with Two Characteristic Particle Sizes”. In: *Journal of the Electrochemical Society* 144.12 (1997), pp. 4201–4208.

[89] D. P. DiVincenzo, C. D. Fuerst, and J. E. Fischer. “(P,T) phase boundary in Li-intercalated graphite: Theory and experiment”. In: *Physical Review B* 29.2 (1984), pp. 1115–1117.

[90] D. a. Stevens and J. R. Dahn. “The Mechanisms of Lithium and Sodium Insertion in Carbon Materials”. In: *Journal of The Electrochemical Society* 148.8 (2001), A803.

[91] P. Bai and M. Z. Bazant. “Charge transfer kinetics at the solidsolid interface in porous electrodes”. In: *Nature Communications* 5 (2014), p. 3585.

[92] T. Ohzuku, Y. Iwakoshi, and K. Sawai. “Formation of Lithium-Graphite Intercalation Compounds in Nonaqueous Electrolytes and Their Application as a Negative Electrode for a Lithium Ion (Shuttlecock) Cell”. In: *Journal of The Electrochemical Society* 140.9 (1993), p. 2490.

[93] R. Yazami and Y. Reynier. “Thermodynamics and crystal structure anomalies in lithium-intercalated graphite”. In: *Journal of Power Sources* 153.2 (2006), pp. 312–318.

[94] S.-I. Lee, U.-H. Jung, Y.-S. Kim, M.-H. Kim, D.-J. Ahn, and H.-S. Chun. “A study of electrochemical kinetics of lithium ion in organic electrolytes”. In: *Korean Journal of Chemical Engineering* 19.4 (2002), pp. 638–644.

[95] J. Song and M. Z. Bazant. “Effects of Nanoparticle Geometry and Size Distribution on Diffusion Impedance of Battery Electrodes”. In: *Journal of the Electrochemical Society* 160.1 (2013), A15–A24.

[96] P. P. Prosini, M. Lisi, D. Zane, and M. Pasquali. “Determination of the chemical diffusion coefficient of lithium in LiFePO4”. In: *Solid State Ionics* 148.1-2 (2002), pp. 45–51.

[97] D. Choi and P. N. Kumta. “Surfactant based sol-gel approach to nanostructured LiFePO4 for high rate Li-ion batteries”. In: *Journal of Power Sources* 163.2 (2007), pp. 1064–1069.

[98] N. Ravet, Y. Chouinard, J. F. Magnan, S. Besner, M. Gauthier, and M. Armand. “Electroactivity of natural and synthetic triphylite”. In: *Journal of Power Sources* 97-98 (2001), pp. 503–507.

[99] Y. Ji, Y. Zhang, and C.-Y. Wang. “Li-Ion Cell Operation at Low Temperatures”. In: *Journal of the Electrochemical Society* 160.4 (2013), A636–A649.

[100] T. Waldmann, M. Wilka, M. Kasper, M. Fleischhammer, and M. Wohlfahrt-Mehrens. “Temperature dependent ageing mechanisms in Lithium-ion batteries - A Post-Mortem study”. In: *Journal of Power Sources* 262 (2014), pp. 129–135.

[101] J. Fan and S. Tan. “Studies on Charging Lithium-Ion Cells at Low Temperatures”. In: *Journal of The Electrochemical Society* 153.6 (2006), A1081.

[102] K. Amine, J. Liu, and I. Belharouak. “High-temperature storage and cycling of C-LiFePO4/graphite Li-ion cells”. In: *Electrochemistry Communications* 7.7 (2005), pp. 669–673.

[103] P Ramadass, B. Haran, R. White, and B. N. Popov. “Capacity fade of Sony 18650 cells cycled at elevated temperatures”. In: *Journal of Power Sources* 112.2 (2002), pp. 606–613.

[104] F. Leng, C. M. Tan, and M. Pecht. “Effect of Temperature on the Aging rate of Li Ion Battery Operating above Room Temperature”. In: *Scientific Reports, Nature* 5 (2015), p. 12967.

[105] R. Spotnitz and J. Franklin. “Abuse behavior of high-power, lithium-ion cells”. In: *Journal of Power Sources* 113.1 (2003), pp. 81–100.

[106] T. M. Bandhauer, S. Garimella, and T. F. Fuller. “A Critical Review of Thermal Issues in Lithium-Ion Batteries”. In: *Journal of The Electrochemical Society* 158.3 (2011), R1.

[107] A. A. Pesaran, A. Vlahinos, S. D. Burch, and NREL. “Thermal Performance of EV and HEV Battery Modules and Packs”. In: *Fourteenth International Electric Vehicle Symposium* September (1997).

[108] K Yeow and H Teng. “Thermal Analysis of a Li-ion Battery System with Indirect Liquid Cooling Using Finite Element Analysis Approach”. In: *SAE Int. J. Alt. Power* 1.1 (2012), pp. 65–78.

[109] H. Teng and K. Yeow. “Design of Direct and Indirect Liquid Cooling Systems for High- Capacity, High-Power Lithium-Ion Battery Packs”. In: *SAE Technical Paper 2012-01-2017, doi:10.4271/2012-01-2017* (2012).

[110] Z. Rao and S. Wang. “A review of power battery thermal energy management”. In: *Renewable and Sustainable Energy Reviews* 15.9 (2011), pp. 4554–4571.

[111] S. Al-Hallaj and J. Selman. “Thermal modeling of secondary lithium batteries for electric vehicle/hybrid electric vehicle applications”. In: *Journal of Power Sources* 110.2 (2002), pp. 341–348.

[112] H. Bang, H. Yang, Y. K. Sun, and J. Prakash. “In Situ Studies of Li[sub x]Mn[sub 2]O[sub 4] and Li[sub x]Al[sub 0.17]Mn[sub 1.83]O[sub 3.97]S[sub 0.03] Cathode by IMC”. In: *Journal of The Electrochemical Society* 152.2 (2005), A421.

[113] D Bernardi, E Pawlikowski, and J. Newman. “A General Energy Balance for Battery Systems”. In: *Journal of The Electrochemical Society* 132.1 (1985), p. 5.

[114] Y. Chen and J. W. Evans. “Heat Transfer Phenomena in Lithium/Polymer-Electrolyte Batteries for Electric Vehicle Application”. In: *Journal of The Electrochemical Society* 140.7 (1993), p. 1833.

[115] C. R. Pals and J. Newman. “Thermal Modeling of the Lithium / Polymer Battery - II. Temperature profiles in cell stack”. In: *Journal of The Electrochemical Society* 142.10 (1995), pp. 3282–3288.

[116] M. W. Verbrugge. “3-Dimensional Temperature and Current Distribution in a Battery Module”. In: *AIChE Journal* 41.6 (1995), pp. 1550–1562.

[117] W. Gu, C. Wang, S. Li, M. Geng, and B. Liaw. “Modeling discharge and charge characteristics of nickelmetal hydride batteries”. In: *Electrochimica Acta* 44.November (1999), pp. 4525–4541.

[118] G.-H. Kim, K. Smith, K.-J. Lee, S. Santhanagopalan, and A. Pesaran. “Multi-Domain Modeling of Lithium-Ion Batteries Encompassing Multi-Physics in Varied Length Scales”. In: *Journal of The Electrochemical Society* 158.8 (2011), A955.

[119] C. Y. Wang, C. Y. Wang, V. Srinivasan, and V. Srinivasan. “Computational battery dynamics (CBD) electrochemical thermal coupled modeling and multi scale modeling”. In: *Journal of Power Sources* 110 (2002), pp. 364–376.

[120] K. Smith and C.-Y. Wang. “Power and thermal characterization of a lithium-ion battery pack for hybrid-electric vehicles”. In: *Journal of Power Sources* 160.1 (2006), pp. 662–673.

[121] R. Stella. “Development of an Electrochemical-Thermal Model for the Analysis of Lithium-Ion Batteries and Application to a FEV Battery Pack”. PhD thesis. Politecnico di Torino, 2015.

[122] G. H. Kim and A Pesaran. “Battery Thermal Management System Design Modeling”. In: *22nd International Battery, Hybrid and Fuel Cell Electric Vehicle Conference and Exhibition, Yokohama, Japan.* November. 2006.

[123] J. Schmitt, A. Maheshwari, M. Heck, S. Lux, and M. Vetter. “Impedance change and capacity fade of lithium nickel manganese cobalt oxide-based batteries during calendar aging”. In: *Journal of Power Sources* 353 (2017), pp. 183–194.

[124] A. Maheshwari, M. Heck, and M. Santarelli. “Cycle aging studies of lithium nickel manganese cobalt oxide-based batteries using electrochemical impedance spectroscopy”. In: *Electrochimica Acta* 273 (2018), pp. 335–348.

[125] R. Spotnitz. “Simulation of capacity fade in lithium-ion batteries”. In: *Journal of Power Sources* 113.August 2002 (2003), pp. 72–80.

[126] K. Uddin, S. Perera, W. Widanage, L. Somerville, and J. Marco. "Characterising Lithium-Ion Battery Degradation through the Identification and Tracking of Electrochemical Battery Model Parameters". In: *Batteries* 2.2 (2016), p. 13.

[127] H. J. Ploehn, P. Ramadass, and R. E. White. "Solvent Diffusion Model for Aging of Lithium-Ion Battery Cells". In: *J. Electrochem. Soc.* 151.3 (2004), A456.

[128] M. Broussely, P. Biensan, F. Bonhomme, P. Blanchard, S. Herreyre, K. Nechev, and R. J. Staniewicz. "Main aging mechanisms in Li ion batteries". In: *Journal of Power Sources* 146.1-2 (2005), pp. 90–96.

[129] S. Käbitz, J. B. Gerschler, M. Ecker, Y. Yurdagel, B. Emmermacher, D. André, T. Mitsch, and D. U. Sauer. "Cycle and calendar life study of a graphite—LiNi1/3Mn 1/3Co1/3O2 Li-ion high energy system. Part A: Full cell characterization". In: *Journal of Power Sources* 239 (2013), pp. 572–583.

[130] J. Wang, J. Purewal, J. Graetz, S. Soukiazian, H. Tataria, and M. W. Verbrugge. "Degradation of lithium ion batteries employing graphite negatives and nickelcobaltmanganese oxide + spinel manganese oxide positives: Part 2, chemicalmechanical degradation model". In: *Journal of Power Sources* 272 (2014), pp. 1154–1161.

[131] K. Jalkanen, J. Karppinen, L. Skogström, T. Laurila, M. Nisula, and K. Vuorilehto. "Cycle aging of commercial NMC/graphite pouch cells at different temperatures". In: *Applied Energy* 154 (2015), pp. 160–172.

[132] D. Li, D. L. Danilov, J. Xie, L. Raijmakers, L. Gao, Y. Yang, and P. H. L. Notten. "Degradation Mechanisms of C6/LiFePO4 Batteries: Experimental Analyses of Calendar Aging". In: *Electrochimica Acta* 190 (2016), pp. 1124–1133.

[133] P. Keil, S. F. Schuster, J. Wilhelm, J. Travi, A. Hauser, R. C. Karl, and A. Jossen. "Calendar Aging of Lithium-Ion Batteries". In: *Journal of The Electrochemical Society* 163.9 (2016), A1872–A1880.

[134] M. Ecker, J. B. Gerschler, J. Vogel, S. Käbitz, F. Hust, P. Dechent, and D. U. Sauer. "Development of a lifetime prediction model for lithium-ion batteries based on extended accelerated aging test data". In: *Journal of Power Sources* 215 (2012), pp. 248–257.

[135] V. Agubra and J. Fergus. "Lithium ion battery anode aging mechanisms". In: *Materials* 6.4 (2013), pp. 1310–1325.

[136] S. J. An, J. Li, C. Daniel, D. Mohanty, S. Nagpure, and D. L. Wood. "The state of understanding of the lithium-ion-battery graphite solid electrolyte interphase (SEI) and its relationship to formation cycling". In: *Carbon* 105 (2016), pp. 52–76.

[137] P. Lu, C. Li, E. W. Schneider, and S. J. Harris. “Chemistry, impedance, and morphology evolution in solid electrolyte interphase films during formation in lithium ion batteries”. In: *Journal of Physical Chemistry C* 118.2 (2014), pp. 896–903.

[138] H. Buqa, D. Goers, M. Holzapfel, M. E. Spahr, and P. Novak. “High Rate Capability of Graphite Negative Electrodes for Lithium-Ion Batteries”. In: *Journal of The Electrochemical Society* 152.2 (2005), A474.

[139] J. Vetter, P. Novák, M. R. Wagner, C. Veit, K. C. Möller, J. O. Besenhard, M. Winter, M. Wohlfahrt-Mehrens, C. Vogler, and A. Hammouche. “Ageing mechanisms in lithium-ion batteries”. In: *Journal of Power Sources* 147.1-2 (2005), pp. 269–281.

[140] M. Wohlfahrt-Mehrens, C. Vogler, and J. Garche. “Aging mechanisms of lithium cathode materials”. In: *Journal of Power Sources* 127.1-2 (2004), pp. 58–64.

[141] P. Niehoff and M. Winter. “Composition and growth behavior of the surface and electrolyte decomposition layer of/on a commercial lithium ion battery LixNi 1/3Mn1/3Co1/3O2 cathode determined by sputter depth profile X-ray photoelectron spectroscopy”. In: *Langmuir* 29.51 (2013), pp. 15813–15821.

[142] A. O. Kondrakov, A. Schmidt, J. Xu, H. Geßwein, R. Mönig, P. Hartmann, H. Sommer, T. Brezesinski, and J. Janek. “On the Anisotropic Lattice Strain and Mechanical Degradation of High- and Low-Nickel NCM Cathode Materials for Li-Ion Batteries”. In: *The Journal of Physical Chemistry C* (2017), acs.jpcc.6b12885.

[143] W. Choi and A. Manthiram. “Comparison of Metal Ion Dissolutions from Lithium Ion Battery Cathodes”. In: *Journal of The Electrochemical Society* 153.9 (2006), A1760.

[144] C. Julien, A. Mauger, K. Zaghib, and H. Groult. “Optimization of layered cathode materials for lithium-ion batteries”. In: *Materials* 9.7 (2016).

[145] J. Xu, E. Hu, D. Nordlund, A. Mehta, S. N. Ehrlich, X. Q. Yang, and W. Tong. “Understanding the degradation mechanism of lithium nickel oxide cathodes for Li-ion batteries”. In: *ACS Applied Materials and Interfaces* 8.46 (2016), pp. 31677–31683.

[146] H. Sun and K. Zhao. “Electronic Structure and Comparative Properties of LiNi _{<i>x</i>} Mn _{<i>y</i>} Co _{<i>z</i>} O ₂ Cathode Materials”. In: *The Journal of Physical Chemistry C* 121.11 (2017), pp. 6002–6010.

[147] G. Gachot, S. Grugeon, M. Armand, S. Pilard, P. Guenot, J. M. Tarascon, and S. Laruelle. “Deciphering the multi-step degradation mechanisms of carbonate-based electrolyte in Li batteries”. In: *Journal of Power Sources* 178.1 (2008), pp. 409–421.

[148] E. Wood, M. Alexander, and T. H. Bradley. “Investigation of battery end-of-life conditions for plug-in hybrid electric vehicles”. In: *Journal of Power Sources* 196.11 (2011), pp. 5147–5154.

[149] Q. Zhai, Z. Dong, K. Meng, and J. Ma. “Modelling and Analysis of Lithium Battery Operations in Spot and Frequency Regulation Service Markets in Australia Electricity Market”. In: *IEEE Transactions on Industrial Informatics* 3203.c (2017), pp. 1–1.

[150] M. Kazemi and H. Zareipour. “Long-term Scheduling of Battery Storage Systems in Energy and Regulation Markets Considering Battery’s lifespan”. In: *IEEE Transactions on Smart Grid* 3053.c (2017), pp. 1–1.

[151] M. Ouyang, Z. Chu, L. Lu, J. Li, X. Han, X. Feng, and G. Liu. “Low temperature aging mechanism identification and lithium deposition in a large format lithium iron phosphate battery for different charge profiles”. In: *Journal of Power Sources* 286 (2015), pp. 309–320.

[152] M. Klett, R. Eriksson, J. Groot, P. Svens, K. Ciosek Högström, R. W. Lindström, H. Berg, T. Gustafson, G. Lindbergh, and K. Edström. “Non-uniform aging of cycled commercial LiFePO4//graphite cylindrical cells revealed by post-mortem analysis”. In: *Journal of Power Sources* 257 (2014), pp. 126–137.

[153] M. Ecker, N. Nieto, S. Käbitz, J. Schmalstieg, H. Blanke, A. Warnecke, and D. U. Sauer. “Calendar and cycle life study of Li(NiMnCo)O2-based 18650 lithium-ion batteries”. In: *Journal of Power Sources* 248 (2014), pp. 839–851.

[154] I Bloom, J. Christophersen, D. Abraham, and K. Gering. “Differential voltage analyses of high-power lithium-ion cells - 3. Another anode phenomenon”. In: *Journal of Power Sources* 157.1 (2006), pp. 537–542.

[155] S. Buller. *Impedance-Based Simulation Models for Energy Storage Devices in Advanced Automotive Power Systems.* Shaker Verlag GmbH Postfach 101818 52018 Aachen, 2003. ISBN: 9783832212254.

[156] D. Andre, M. Meiler, K. Steiner, C. Wimmer, T. Soczka-Guth, and D. U. Sauer. “Characterization of high-power lithium-ion batteries by electrochemical impedance spectroscopy. I. Experimental investigation”. In: *Journal of Power Sources* 196.12 (2011), pp. 5334–5341.

[157] W. Waag, S. Käbitz, and D. U. Sauer. “Experimental investigation of the lithium-ion battery impedance characteristic at various conditions and aging states and its influence on the application”. In: *Applied Energy* 102 (2013), pp. 885–897.

[158] A. Eddahech, O. Briat, and J. M. Vinassa. “Determination of lithium-ion battery state-of-health based on constant-voltage charge phase”. In: *Journal of Power Sources* 258 (2014), pp. 218–227.

[159] M. Abdel Monem, K. Trad, N. Omar, O. Hegazy, B. Mantels, G. Mulder, P. Van den Bossche, and J. Van Mierlo. “Lithium-ion batteries: Evaluation study of different charging methodologies based on aging process”. In: *Applied Energy* 152 (2015), pp. 143–155.

[160] I. Buchberger, S. Seidlmayer, A. Pokharel, M. Piana, J. Hattendorff, P. Kudejova, R. Gilles, and H. A. Gasteiger. “Aging Analysis of Graphite/LiNi 1/3 Mn 1/3 Co 1/3 O 2 Cells Using XRD, PGAA, and AC Impedance”. In: *Journal of The Electrochemical Society* 162.14 (2015), pp. 2737–2746.

[161] M.-S. Wu, P.-C. J. Chiang, and J.-C. Lin. “Electrochemical Investigations on Advanced Lithium-Ion Batteries by Three-Electrode Measurements”. In: *Journal of The Electrochemical Society* 152.1 (2005), A47.

[162] U. Tröltzsch, O. Kanoun, and H. R. Tränkler. “Characterizing aging effects of lithium ion batteries by impedance spectroscopy”. In: *Electrochimica Acta* 51.8-9 (2006), pp. 1664–1672.

[163] B. Stiaszny, J. C. Ziegler, E. E. Krauß, J. P. Schmidt, and E. Ivers-Tiffée. “Electrochemical characterization and post-mortem analysis of aged LiMn 2O4-Li(Ni0.5Mn0.3Co 0.2)O2/graphite lithium ion batteries. Part I: Cycle aging”. In: *Journal of Power Sources* 251 (2014), pp. 439–450.

[164] Y. Barsukov, J. R. Macdonald, Y. Barsukov, and J. R. Macdonald. “Electrochemical Impedance Spectroscopy”. In: *Characterization of Materials*. Hoboken, NJ, USA: John Wiley & Sons, Inc., 2012. ISBN: 9780471266969.

[165] F. La Mantia. “Characterization of Electrodes for Lithium-Ion Batteries through Electrochemical Impedance Spectroscopy and Mass Spectrometry”. PhD thesis. 2008, p. 145.

[166] J.-B. Jorcin, M. E. Orazem, N Pébère, and B Tribollet. “CPE analysis by local electrochemical impedance spectroscopy”. In: *Electrochimica Acta* 51.89 (2006), pp. 1473–1479.

[167] J. W.J. W. Eaton, D. Bateman, and S. Hauberg. *GNU Octave : a high-level interactive language for numerical computations*. Network Theory, 2008, p. 555. ISBN: 095461206X.

[168] E. Peled. “The Electrochemical Behavior of Alkali and Alkaline Earth Metals in Nonaqueous Battery SystemsThe Solid Electrolyte Interphase Model”. In: *Journal of The Electrochemical Society* 126.12 (1979), p. 2047.

[169] J. Christensen and J. Newman. “A Mathematical Model for the Lithium-Ion Negative Electrode Solid Electrolyte Interphase”. In: *Journal of The Electrochemical Society* 151.11 (2004), A1977.

[170] J. Wang, P. Liu, J. Hicks-Garner, E. Sherman, S. Soukiazian, M. Verbrugge, H. Tataria, J. Musser, and P. Finamore. “Cycle-life model for graphite-LiFePO4 cells”. In: *Journal of Power Sources* 196.8 (2011), pp. 3942–3948.

[171] J. Belt, V. Utgikar, and I. Bloom. “Calendar and PHEV cycle life aging of high-energy, lithium-ion cells containing blended spinel and layered-oxide cathodes”. In: *Journal of Power Sources* 196.23 (2011), pp. 10213–10221.

[172] J. Schmalstieg, S. Käbitz, M. Ecker, and D. U. Sauer. “A holistic aging model for Li(NiMnCo)O2 based 18650 lithium-ion batteries”. In: *Journal of Power Sources* 257 (2014), pp. 325–334.

[173] I. Baghdadi, O. Briat, J. Y. Delétage, P. Gyan, and J. M. Vinassa. “Lithium battery aging model based on Dakin’s degradation approach”. In: *Journal of Power Sources* 325 (2016), pp. 273–285.

[174] R. G. Jungst, G. Nagasubramanian, H. L. Case, B. Y. Liaw, A. Urbina, T. L. Paez, and D. H. Doughty. “Accelerated calendar and pulse life analysis of lithium-ion cells”. In: *Journal of Power Sources* 119-121 (2003), pp. 870–873.

[175] L. Lavigne, J. Sabatier, J. M. Francisco, F. Guillemard, and A. Noury. “Lithium-ion Open Circuit Voltage (OCV) curve modelling and its ageing adjustment”. In: *Journal of Power Sources* 324 (2016), pp. 694–703.

[176] J. P. Schmidt, H. Y. Tran, J. Richter, E. Ivers-Tiffée, and M. Wohlfahrt-Mehrens. “Analysis and prediction of the open circuit potential of lithium-ion cells”. In: *Journal of Power Sources* 239 (2013), pp. 696–704.

[177] B. Stiaszny, J. C. Ziegler, E. E. Krauß, M. Zhang, J. P. Schmidt, and E. Ivers-Tiffée. “Electrochemical characterization and post-mortem analysis of aged LiMn 2O4-NMC/graphite lithium ion batteries part II: Calendar aging”. In: *Journal of Power Sources* 258 (2014), pp. 61–75.

[178] P. Röder, B. Stiaszny, J. C. Ziegler, N. Baba, P. Lagaly, and H. D. Wiemhöfer. “The impact of calendar aging on the thermal stability of a LiMn 2O4-Li(Ni1/3Mn1/3Co 1/3)O2/graphite lithium-ion cell”. In: *Journal of Power Sources* 268 (2014), pp. 315–325.

[179] J Bisquert, G Garcia-Belmonte, P Bueno, E Longo, and L. Bulhões. “Impedance of constant phase element (CPE)-blocked diffusion in film electrodes”. In: *Journal of Electroanalytical Chemistry* 452.2 (1998), pp. 229–234.

[180] T. Zheng, A. S. Gozdz, and G. G. Amatucci. “Reactivity of the Solid Electrolyte Interface on Carbon Electrodes at Elevated Temperatures”. In: *Journal of The Electrochemical Society* 146.11 (1999), p. 4014.

[181] R. S. Rubino, H. Gan, and E. S. Takeuchi. “A Study of Capacity Fade in Cylindrical and Prismatic Lithium-Ion Batteries”. In: *Journal of The Electrochemical Society* 148.9 (2001), A1029.

[182] D. A. Stevens, R. Y. Ying, R. Fathi, J. N. Reimers, J. E. Harlow, and J. R. Dahn. “Using High Precision Coulometry Measurements to Compare the Degradation Mechanisms of NMC/LMO and NMC-Only Automotive Scale Pouch Cells”. In: *Journal of the Electrochemical Society* 161.9 (2014), A1364–A1370.

[183] S. F. Schuster, T. Bach, E. Fleder, J. M??ller, M. Brand, G. Sextl, and A. Jossen. “Nonlinear aging characteristics of lithium-ion cells under different operational conditions”. In: *Journal of Energy Storage* 1.1 (2015), pp. 44–53.

[184] D. Mohanty, K. Dahlberg, D. M. King, L. A. David, A. S. Sefat, D. L. Wood, C. Daniel, S. Dhar, V. Mahajan, M. Lee, and F. Albano. “Modification of Ni-Rich FCG NMC and NCA Cathodes by Atomic Layer Deposition: Preventing Surface Phase Transitions for High-Voltage Lithium-Ion Batteries”. In: *Scientific Reports* 6.1 (2016), p. 26532.

[185] R. Fu, S. Y. Choe, V. Agubra, and J. Fergus. “Modeling of degradation effects considering side reactions for a pouch type Li-ion polymer battery with carbon anode”. In: *Journal of Power Sources* 261 (2014), pp. 120–135.

[186] T. C. Bach, S. F. Schuster, E. Fleder, J. M??ller, M. J. Brand, H. Lorrmann, A. Jossen, and G. Sextl. “Nonlinear aging of cylindrical lithium-ion cells linked to heterogeneous compression”. In: *Journal of Energy Storage* 5 (2016), pp. 212–223.

[187] S. Saxena, C. Le Floch, J. Macdonald, and S. Moura. “Quantifying EV battery end-of-life through analysis of travel needs with vehicle powertrain models”. In: *Journal of Power Sources* 282 (2015), pp. 265–276.

[188] S. F. Schuster, M. J. Brand, C. Campestrini, M. Gleissenberger, and A. Jossen. “Correlation between capacity and impedance of lithium-ion cells during calendar and cycle life”. In: *Journal of Power Sources* 305 (2016), pp. 191–199.

[189] K. Xu. “Nonaqueous liquid electrolytes for lithium-based rechargeable batteries”. In: *Chemical Reviews* 104.10 (2004), pp. 4303–4417.

[190] S. S. Zhang and T. R. Jow. “Aluminum corrosion in electrolyte of Li-ion battery”. In: *Journal of Power Sources* 109.2 (2002), pp. 458–464.

[191] T. Ma, G. L. Xu, Y. Li, L. Wang, X. He, J. Zheng, J. Liu, M. H. Engelhard, P. Zapol, L. A. Curtiss, J. Jorne, K. Amine, and Z. Chen. “Revisiting the Corrosion of the Aluminum Current Collector in Lithium-Ion Batteries”. In: *Journal of Physical Chemistry Letters* 8.5 (2017), pp. 1072–1077.

[192] R. Wagner, B. Streipert, V. Kraft, A. Reyes Jiménez, S. Röser, J. Kasnatscheew, D. R. Gallus, M. Börner, C. Mayer, H. F. Arlinghaus, M. Korth, M. Amereller, I. Cekic-Laskovic, and M. Winter. “Counterintuitive Role of Magnesium Salts as Effective Electrolyte Additives for High Voltage Lithium-Ion Batteries”. In: *Advanced Materials Interfaces* 3.15 (2016), pp. 1–11.

[193] J. C. Burns, D. A. Stevens, and J. R. Dahn. “In-Situ Detection of Lithium Plating Using High Precision Coulometry”. In: *Journal of the Electrochemical Society* 162.6 (2015), A959–A964.

[194] E Sarasketa-Zabala, F Aguesse, I Villarreal, L. M. Rodriguez-Martinez, C. M. López, and P Kubiak. “Understanding Lithium Inventory Loss and Sudden Performance Fade in Cylindrical Cells during Cycling with Deep-Discharge Steps”. In: *The Journal of Physical Chemistry C* 119.2 (2015), pp. 896–906.

[195] M. Petzl and M. A. Danzer. “Nondestructive detection, characterization, and quantification of lithium plating in commercial lithium-ion batteries”. In: *Journal of Power Sources* 254 (2014), pp. 80–87.

[196] S. Zhang, M. S. Ding, K. Xu, J. Allen, and T. R. Jow. “Understanding Solid Electrolyte Interface Film Formation on Graphite Electrodes”. In: *Electrochemical and Solid-State Letters* 4.12 (2001), A206.

[197] K. Y. Oh, J. B. Siegel, L. Secondo, S. U. Kim, N. A. Samad, J. Qin, D. Anderson, K. Garikipati, A. Knobloch, B. I. Epureanu, C. W. Monroe, and A. Stefanopoulou. “Rate dependence of swelling in lithium-ion cells”. In: *Journal of Power Sources* 267 (2014), pp. 197–202.

[198] Y. Li, M. Bettge, B. Polzin, Y. Zhu, M. Balasubramanian, and D. P. Abraham. “Understanding Long-Term Cycling Performance of Li1.2Ni0.15Mn0.55Co0.1O2-Graphite Lithium-Ion Cells”. In: *Journal of the Electrochemical Society* 160.5 (2013), A3006–A3019.

[199] M. K. Rahman and Y. Saito. “Investigation of positive electrodes after cycle testing of high-power Li-ion battery cells. III: An approach to the power fade mechanism using FT-IR-ATR”. In: *Journal of Power Sources* 174.2 (2007), pp. 889–894.

[200] F. Lin, I. M. Markus, D. Nordlund, T.-C. Weng, M. D. Asta, H. L. Xin, and M. M. Doeff. “Surface reconstruction and chemical evolution of stoichiometric layered cathode materials for lithium-ion batteries.” In: *Nature communications* 5 (2014), p. 3529.

[201] M. Shikano, H. Kobayashi, S. Koike, H. Sakaebe, Y. Saito, H. Hori, H. Kageyama, and K. Tatsumi. “X-ray absorption near-edge structure study on positive electrodes of degraded lithium-ion battery”. In: *Journal of Power Sources* 196.16 (2011), pp. 6881–6883.

[202] J. W. Kim, J. J. Travis, E. Hu, K. W. Nam, S. C. Kim, C. S. Kang, J. H. Woo, X. Q. Yang, S. M. George, K. H. Oh, S. J. Cho, and S. H. Lee. “Unexpected high power performance of atomic layer deposition coated Li[Ni1/3Mn1/3Co1/3]O2 cathodes”. In: *Journal of Power Sources* 254 (2014), pp. 190–197.

[203] A. Yano, S. Aoyama, M. Shikano, H. Sakaebe, K. Tatsumi, and Z. Ogumi. “Surface Structure and High-Voltage Charge/Discharge Characteristics of Al-Oxide Coated LiNi1/3Co1/3Mn1/3O2 Cathodes”. In: *Journal of the Electrochemical Society* 162.2 (2015), A3137–A3144.

[204] Z. Chen, Y.-K. Sun, and K. Amine. "Electrochemical Properties of Lithium-Rich Li[sub 1+x](MnNiCo)[sub 1x]O[sub 2] at High Potential". In: *Journal of The Electrochemical Society* 153.10 (2006), A1818.

[205] *United Nations Treaty Collection.* 2015. URL: `https://treaties.un.org/` (visited on 06/01/2018).

[206] DNV GL Energy. *Energy Transition Outlook 2017 report.* Tech. rep. 2017.

[207] International Renewable Energy Agency (IRENA). *Electricity Storage and Renewables : Costs and Markets To 2030.* Tech. rep. October. 2017.

[208] H. L. Ferreira, R. Garde, G. Fulli, W. Kling, and J. P. Lopes. "Characterisation of electrical energy storage technologies". In: *Energy* 53 (2013), pp. 288–298.

[209] H. C. Hesse, M. Schimpe, D. Kucevic, and A. Jossen. *Lithium-ion battery storage for the grid - A review of stationary battery storage system design tailored for applications in modern power grids.* Vol. 10. 12. 2017. ISBN: 4989289269.

[210] J. M. Morales, A. J. Conejo, H. Madsen, P. Pinson, and M. Zugno. *Integrating Renewables in Electricity Markets.* Vol. 205. International Series in Operations Research & Management Science. Boston, MA: Springer US, 2014, pp. 313–343. ISBN: 978-1-4614-9410-2.

[211] J. F. Nolten. "Smart integration of battery storage". In: *TU Eindhoven* (2017).

[212] F. Graves, T. Jenkin, and D. Murphy. "Opportunities for Electricity Storage in Deregulating Markets". In: *The Electricity Journal* 12.8 (1999), pp. 46–56.

[213] Entso-e. *Survey on ancillary services procurement, balancingmarket design 2016.* Tech. rep. March. 2017, p. 222.

[214] P. Blechinger, R. Seguin, C. Cader, P. Bertheau, and C. Breyer. "Assessment of the global potential for renewable energy storage systems on small islands". In: *Energy Procedia* 46 (2014), pp. 294–300.

[215] L. Sigrist, E. Lobato, and L. Rouco. "Energy storage systems providing primary reserve and peak shaving in small isolated power systems: An economic assessment". In: *International Journal of Electrical Power & Energy Systems* 53.1 (2013), pp. 675–683.

[216] M. Tamaki, S. Uehara, K. Takagi, and T. Ichikawa. "Demonstration results using Miyako Island Mega-Solar Demonstration Research Facility". In: *Proceedings of the IEEE Power Engineering Society Transmission and Distribution Conference* 2.6 (2012), pp. 3–6.

[217] S. Ericson, E. Rose, H. Jayaswal, W. Cole, J. Engel-Cox, J. Logan, J. Mclaren, K. Anderson, D. Arent, J. Glassmire, S. Klawiter, and D. Rajasekaran. *Hybrid Storage Market Assessment.* Tech. rep. October. 2017.

[218] N. R. Tristan Glenwright, Justin Arakaki. *Renewable Energy Integration for Islands.* Tech. rep. 2016.

[219] D. Frankel and A. Wagner. "Battery storage : The next disruptive technology in the power sector". In: (2016).

[220] P. Kassing, A. Sumper, T. Müller, and M. Heißwolf. "Battery storage systems feasibility study for revenue models in Germany". In: *Proceedings - 2017 International Conference on Modern Power Systems, MPS 2017* Mps (2017), pp. 0–4.

[221] A. Strassheim, J. E. De Haan, M. Gibescu, and W. L. Kling. "Provision of frequency restoration reserves by possible energy storage systems in Germany and the Netherlands". In: *International Conference on the European Energy Market, EEM* (2014).

[222] W. Hur, Y. Moon, K. Shin, W. Kim, S. Nam, and K. Park. "Economic value of Li-ion energy storage system in frequency regulation application from utility firm's perspective in Korea". In: *Energies* 8.6 (2015), pp. 5000–5017.

[223] M. Avendano-Mora and E. H. Camm. "Financial assessment of battery energy storage systems for frequency regulation service". In: *2015 IEEE Power & Energy Society General Meeting* (2015), pp. 1–5.

[224] I. Miranda, N. Silva, and A. M. Bernardo. "Assessment of the potential of Battery Energy Storage Systems in current European markets designs". In: *2015 12th International Conference on the European Energy Market (EEM).* Vol. 2. IEEE, 2015, pp. 1–5. ISBN: 978-1-4673-6692-2.

[225] M Swierczynski, D. I. Stroe, A. I. Stan, and R Teodorescu. "Primary frequency regulation with Li-ion battery energy storage system: A case study for Denmark". In: *ECCE Asia Downunder (ECCE Asia), 2013 IEEE* (2013), pp. 487–492.

[226] B. Zakeri, S. Syri, and F. Wagner. "Economics of energy storage in the German electricity and reserve markets". In: *International Conference on the European Energy Market, EEM* (2017).

[227] M. B. Salles, J. Huang, M. J. Aziz, and W. W. Hogan. "Potential arbitrage revenue of energy storage systems in PJM". In: *Energies* 10.8 (2017).

[228] A. Stock, G. Bourne, L. Brailsford, and P. Stock. *Fully Charged: Renewables And Storage Powering Australia.* 2018. ISBN: 9781925573435.

[229] E. Cajon, S. Size, P. Rating, S. D. Gas, N. Disclosed, S. D. Gas, N. Disclosed, and S. California. *Energy Storage Investments in California.* Tech. rep. Washington D.C.: Federal Energy Regulatory Commission, 2017, pp. 9–13.

[230] B. Zakeri and S. Syri. "Value of energy storage in the Nordic Power market - benefits from price arbitrage and ancillary services". In: *2016 13th International Conference on the European Energy Market (EEM).* Vol. 2016-July. IEEE, 2016, pp. 1–5. ISBN: 978-1-5090-1298-5.

[231] K. Bradbury, L. Pratson, and D. Patiño-Echeverri. “Economic viability of energy storage systems based on price arbitrage potential in real-time U.S. electricity markets”. In: *Applied Energy* 114 (2014), pp. 512–519.

[232] F Heredia, J. Escuer, and J. Romeu. “Economic analysis of battery electric storage systems operating in electricity markets”. In: *2015 12th International Conference on the European Energy Market (EEM)* (2015), pp. 1–5.

[233] K. Spiliotis, S. Claeys, A. R. Gutierrez, and J. Driesen. “Utilizing local energy storage for congestion management and investment deferral in distribution networks”. In: *International Conference on the European Energy Market, EEM* 2016-July (2016), pp. 0–4.

[234] V. Alimisis and N. D. Hatziargyriou. “Evaluation of a hybrid power plant comprising used EV-batteries to complement wind power”. In: *IEEE Transactions on Sustainable Energy* 4.2 (2013), pp. 286–293.

[235] P Wolfs. “An economic assessment of ’second use’ lithium-ion batteries for grid support”. In: *Universities Power Engineering Conference (AUPEC), 2010 20th Australasian* (2010), pp. 1–6.

[236] R. Rezania and W. Prüggler. “Business models for the integration of electric vehicles into the Austrian energy system”. In: *9th International Conference on the European Energy Market, EEM 12* (2012), pp. 1–8.

[237] K. Gur, D. Chatzikyriakou, C. Baschet, and M. Salomon. “The reuse of electrified vehicle batteries as a means of integrating renewable energy into the European electricity grid: A policy and market analysis”. In: *Energy Policy* 113.October 2017 (2018), pp. 535–545.

[238] C. Goebel, H. Hesse, M. Schimpe, A. Jossen, and H. A. Jacobsen. “Model-Based Dispatch Strategies for Lithium-Ion Battery Energy Storage Applied to Pay-as-Bid Markets for Secondary Reserve”. In: *IEEE Transactions on Power Systems* 32.4 (2017), pp. 2724–2734.

[239] R. L. Fares and M. E. Webber. “A flexible model for economic operational management of grid battery energy storage”. In: *Energy* 78 (2014), pp. 768–776.

[240] D. Pelzer, D. Ciechanowicz, and A. Knoll. “Energy arbitrage through smart scheduling of battery energy storage considering battery degradation and electricity price forecasts”. In: *IEEE PES Innovative Smart Grid Technologies Conference Europe* (2016), pp. 472–477.

[241] B. Xu, J. Zhao, T. Zheng, E. Litvinov, and D. S. Kirschen. “Factoring the Cycle Aging Cost of Batteries Participating in Electricity Markets”. In: *IEEE Transactions on Power Systems* 8950.c (2017), pp. 1–12.

[242] G. He, Q. Chen, C. Kang, P. Pinson, and Q. Xia. “Optimal Bidding Strategy of Battery Storage in Power Markets Considering Performance-Based Regulation and Battery Cycle Life”. In: *IEEE Transactions on Smart Grid* 7.5 (2016), pp. 2359–2367.

[243] S. Shafiee, P. Zamani-Dehkordi, H. Zareipour, and A. M. Knight. “Economic assessment of a price-maker energy storage facility in the Alberta electricity market”. In: *Energy* 111 (2016), pp. 537–547.

[244] F. Wankmüller, P. R. Thimmapuram, K. G. Gallagher, and A. Botterud. “Impact of battery degradation on energy arbitrage revenue of grid-level energy storage”. In: *Journal of Energy Storage* 10 (2017), pp. 56–66.

[245] M. Kazemi, H. Zareipour, N. Amjady, W. D. Rosehart, and M. Ehsan. “Operation Scheduling of Battery Storage Systems in Joint Energy and Ancillary Services Markets”. In: *IEEE Transactions on Sustainable Energy* 3029.c (2017), pp. 1–1.

[246] H. Akhavan-Hejazi and H. Mohsenian-Rad. “Optimal operation of independent storage systems in energy and reserve markets with high wind penetration”. In: *IEEE Transactions on Smart Grid* 5.2 (2014), pp. 1088–1097.

[247] A. Hoke, A. Brissette, K. Smith, A. Pratt, and D. Maksimovic. “Accounting for Lithium-Ion Battery Degradation in Electric Vehicle Charging Optimization”. In: *IEEE Journal of Emerging and Selected Topics in Power Electronics* 2.3 (2014), pp. 691–700.

[248] R. Dufo-López, J. L. Bernal-Agustín, and J. A. Domínguez-Navarro. “Generation management using batteries in wind farms: Economical and technical analysis for Spain”. In: *Energy Policy* 37.1 (2009), pp. 126–139.

[249] S. You and C. Rasmussen. “Generic modelling framework for economic analysis of battery systems”. In: *IET Conference on Renewable Power Generation (RPG 2011)* (2011), pp. 1–6.

[250] S. Teleke, M. E. Baran, S. Member, S. Bhattacharya, and A. Q. Huang. “Optimal Control of Battery Energy Storage for Wind Farm Dispatching”. In: *IEEE Transactions on Energy Conversion* 25.3 (2010), pp. 787–794.

[251] I. Duggal and B. Venkatesh. “Short-Term Scheduling of Thermal Generators and Battery Storage With Depth of Discharge-Based Cost Model”. In: *IEEE Transactions on Power Systems* 30.4 (2015), pp. 2110–2118.

[252] X. Tan, Y. Wu, and D. H. Tsang. “A Stochastic Shortest Path Framework for Quantifying the Value and Lifetime of Battery Energy Storage under Dynamic Pricing”. In: *IEEE Transactions on Smart Grid* 8.2 (2017), pp. 769–778.

[253] E. Namor, D. Torregrossa, F. Sossan, R. Cherkaoui, and M. Paolone. “Assessment of battery ageing and implementation of an ageing aware control strategy for a load leveling application of a lithium titanate battery energy storage system”. In: *2016 IEEE 17th Workshop on Control and Modeling for Power Electronics, COMPEL 2016* (2016).

[254] A. Castelo-Becerra, W. Zeng, and M.-y. Chow. “Cooperative distributed aggregation algorithm for demand response using distributed energy storage devices”. In: *2017 North American Power Symposium (NAPS)*. IEEE, 2017, pp. 1–6. ISBN: 978-1-5386-2699-3.

[255] A. Ahmadian, M. Sedghi, B. Mohammadi-ivatloo, A. Elkamel, M. A. Golkar, and M. W. Fowler. “Cost-Benefit Analysis of V2G Implementation in Distribution Networks Considering PEVs Battery Degradation”. In: *IEEE Transactions on Sustainable Energy* 3029.c (2017), pp. 1–10.

[256] P. Fortenbacher, J. L. Mathieu, and G. Andersson. “Modeling, identification, and optimal control of batteries for power system applications”. In: *2014 Power Systems Computation Conference* (2014), pp. 1–7.

[257] L. Thaller. “Expected cycle life versus depth of discharge relationships of well behaved single cells and cell strings”. In: *162nd Meeting of the Electrochem. Soc., Detroit, 17-22 Oct. 1982* (1982), pp. 17–22.

[258] H. Bindner, T. Cronin, P. Lundsager, J. F. Manwell, U. Abdulwahid, and I. Baring-gould. *Lifetime Modelling of Lead Acid Batteries.* Vol. 1515. April. 2005, pp. 1–81. ISBN: 8755034411.

[259] J. Schiffer, D. U. Sauer, H. Bindner, T. Cronin, P. Lundsager, and R. Kaiser. “Model prediction for ranking lead-acid batteries according to expected lifetime in renewable energy systems and autonomous power-supply systems”. In: *Journal of Power Sources* 168.1 SPEC. ISS. (2007), pp. 66–78.

[260] M. Lewerenz and D. U. Sauer. “Evaluation of cyclic aging tests of prismatic automotive LiNiMnCoO2-Graphite cells considering influence of homogeneity and anode overhang”. In: *Journal of Energy Storage* 18.June (2018), pp. 421–434.

[261] I. Laresgoiti, S. Käbitz, M. Ecker, and D. U. Sauer. “Modeling mechanical degradation in lithium ion batteries during cycling: Solid electrolyte interphase fracture”. In: *Journal of Power Sources* 300 (2015), pp. 112–122.

[262] N. G. Paterakis, Y. A. Hugo, and B. V. Elestor. “Investigation of Arbitrage Between the Dutch Day-Ahead and Imbalance Markets as a Business Case for the Hydrogen Bromine Flow Battery”. In: *PowerTech 2017*. 2017.

[263] M. Padberg. “Approximating separable nonlinear functions via mixed zero-one programs”. In: *Operations Research Letters* 27.1 (2000), pp. 1–5.

[264] A. B. Keha, I. R. De Farias, and G. L. Nemhauser. “Models for representing piecewise linear cost functions”. In: *Operations Research Letters* 32.1 (2004), pp. 44–48.

[265] *ENTSO-E Transparency Platform.* URL: `https://transparency.entsoe.eu/` (visited on 06/03/2018).

[266] W. Li, B. Song, and A. Manthiram. “High-voltage positive electrode materials for lithium-ion batteries”. In: *Chem. Soc. Rev.* 46.10 (2017), pp. 3006–3059.

[267] Y. Qin, H. Lin, Y. Liu, and D. Wang. “Investigation of electrolytes utilized for high-voltage LiNi0.5Mn1.5O4batteries”. In: *AIP Conference Proceedings* 1890.2017 (2017), pp. 1–8.

[268] M. Hu, X. Pang, and Z. Zhou. “Review Recent progress in high-voltage lithium ion batteries”. In: *Journal of Power Sources* 237 (2013), pp. 229–242.

[269] A. Casimir, H. Zhang, O. Ogoke, J. C. Amine, J. Lu, and G. Wu. “Silicon-based anodes for lithium-ion batteries: Effectiveness of materials synthesis and electrode preparation”. In: *Nano Energy* 27 (2016), pp. 359–376.

[270] X. Zuo, J. Zhu, P. Müller-Buschbaum, and Y. J. Cheng. “Silicon based lithium-ion battery anodes: A chronicle perspective review”. In: *Nano Energy* 31.October 2016 (2017), pp. 113–143.

[271] A. Fotouhi, D. Auger, L. O’Neill, T. Cleaver, and S. Walus. “Lithium-Sulfur Battery Technology Readiness and ApplicationsA Review”. In: *Energies* 10.12 (2017), p. 1937.

[272] Q. Pang, X. Liang, C. Y. Kwok, and L. F. Nazar. “Advances in lithium-sulfur batteries based on multifunctional cathodes and electrolytes”. In: *Nature Energy* 1.9 (2016), pp. 1–11.

[273] D. Aurbach, B. D. McCloskey, L. F. Nazar, and P. G. Bruce. “Advances in understanding mechanisms underpinning lithium-air batteries”. In: *Nature Energy* 1.9 (2016), pp. 1–11.

[274] N. Imanishi, A. C. Luntz, and P. Bruce. *The lithium air battery: Fundamentals.* Vol. 9781489980. 2014, pp. 1–318. ISBN: 9781489980625.

[275] F. Zheng, M. Kotobuki, S. Song, M. O. Lai, and L. Lu. “Review on solid electrolytes for all-solid-state lithium-ion batteries”. In: *Journal of Power Sources* 389.February (2018), pp. 198–213.

[276] K. Kerman, A. Luntz, V. Viswanathan, Y.-M. Chiang, and Z. Chen. “ReviewPractical Challenges Hindering the Development of Solid State Li Ion Batteries”. In: *Journal of The Electrochemical Society* 164.7 (2017), A1731–A1744.

[277] J. Janek and W. G. Zeier. “A solid future for battery development”. In: *Nature Energy* 1.9 (2016), pp. 1–4.

[278] F. Gschwind, G. Rodriguez-Garcia, D. J. Sandbeck, A. Gross, M. Weil, M. Fichtner, and N. Hörmann. “Fluoride ion batteries: Theoretical performance, safety, toxicity, and a combinatorial screening of new electrodes”. In: *Journal of Fluorine Chemistry* 182 (2016), pp. 76–90.

[279] X. Zhao, S. Ren, M. Bruns, and M. Fichtner. “Chloride ion battery: A new member in the rechargeable battery family”. In: *J. Power Sources* 245 (2014), pp. 706–711.

[280] J. Tang, A. D. Dysart, and V. G. Pol. “Advancement in sodium-ion rechargeable batteries”. In: *Current Opinion in Chemical Engineering* 9 (2015), pp. 34–41.

[281] F. Wang, X. Fan, T. Gao, W. Sun, Z. Ma, C. Yang, F. Han, K. Xu, and C. Wang. “High-Voltage Aqueous Magnesium Ion Batteries”. In: *ACS Central Science* 3.10 (2017), pp. 1121–1128.

[282] H. Zhang, K. Ye, K. Zhu, R. Cang, J. Yan, K. Cheng, G. Wang, and D. Cao. “High-Energy-Density Aqueous Magnesium-Ion Battery Based on a Carbon-Coated FeVO4Anode and a Mg-OMS-1 Cathode”. In: *Chemistry - A European Journal* 23.67 (2017), pp. 17118–17126.

[283] D. Y. Wang, C. Y. Wei, M. C. Lin, C. J. Pan, H. L. Chou, H. A. Chen, M. Gong, Y. Wu, C. Yuan, M. Angell, Y. J. Hsieh, Y. H. Chen, C. Y. Wen, C. W. Chen, B. J. Hwang, C. C. Chen, and H. Dai. “Advanced rechargeable aluminium ion battery with a high-quality natural graphite cathode”. In: *Nature Communications* 8 (2017), pp. 1–7.

[284] D. J. Bradwell, H. Kim, A. H. Sirk, and D. R. Sadoway. “Magnesium-antimony liquid metal battery for stationary energy storage”. In: *Journal of the American Chemical Society* 134.4 (2012), pp. 1895–1897.

[285] T. Schoetz, C. P. de Leon, M. Ueda, and A. Bund. “PerspectiveState of the Art of Rechargeable Aluminum Batteries in Non-Aqueous Systems”. In: *Journal of The Electrochemical Society* 164.14 (2017), A3499–A3502.

[286] X. Zhang, X.-G. Wang, Z. Xie, and Z. Zhou. “Recent progress in rechargeable alkali metalair batteries”. In: *Green Energy & Environment* 1.1 (2016), pp. 4–17.

[287] Y. Li and J. Lu. “Metal-Air Batteries: Will They Be the Future Electrochemical Energy Storage Device of Choice?” In: *ACS Energy Letters* 2.6 (2017), pp. 1370–1377.

List of publications

1. A. Maheshwari, M.A. Dumitrescu, M. Destro, M. Santarelli, Inverse parameter determination in the development of an optimized lithium iron phosphate Graphite battery discharge model, J. Power Sources. 307 (2016) 160-172.
2. A. Maheshwari, M.A. Dumitrescu, M. Destro, M. Santarelli, A Modelling Approach to understand charge discharge differences in thermal behaviour in lithium iron phosphate - graphite battery, Electrochim. Acta. 243 (2017) 129-141.
3. J. Schmitt, A. Maheshwari, M. Heck, S. Lux, M. Vetter, Impedance change and capacity fade of lithium nickel manganese cobalt oxide-based batteries during calendar aging, J. Power Sources. 353 (2017) 183-194.
4. A. De Vita, A. Maheshwari, M. Destro, M. Santarelli, M. Carello, Transient thermal analysis of a lithium-ion battery pack comparing different cooling solutions for automotive applications, Appl. Energy. 206 (2017) 101-112.
5. A. Maheshwari, M. Heck, M. Santarelli, Cycle aging studies of lithium nickel manganese cobalt oxide-based batteries using electrochemical impedance spectroscopy, Electrochim. Acta. 273 (2018) 335-348.
6. A. Maheshwari, N.G. Paterakis, M. Santarelli, M. Gibescu, A MILP Approach to Model the Non-linear Degradation Behaviour of Lithium-ion Batteries for Optimization Studies (manuscript submitted).

Acknowledgements

It has been a delightful journey, the one of these last four years. It has involved a fair bit of moving northward. Physically, the *viaggio* began in Turin, with a (painfully) short *Zwischenhalt* in Freiburg and had Eindhoven as the *eindbestimming.* The mental ride has also been quite intense, reminding me of a facet of what the Upanishads describe in the *pavamana abhyaroha*, *"tamso ma jyotirgamaya"* (from darkness to light). The knowledge gained and the rich variety of experiences had have not only made me understand more about my research topic but also peeled away some layers to my own self and helped me orient myself towards my true north. Even if this journey was only a fraction of the whole, it has given these last years a sense a completeness and of closure and has left behind a pleasant aftertaste. This would not have been the possible if not for the wonderful people I shared this journey with.

I am thankful...

to the committee members and referees for reading and assessing my research and for the constructive and encouraging feedback I received.

to Michael (Dr.rer.nat. Lang), my master thesis supervisor at DLR Stuttgart, for seeding the idea of pursuing a PhD in my head.

to Massimo (Prof. Santarelli), so positively unconventional for an Italian professor, for the level of trust in my work, the un-intrusive style of supervision and the intellectual freedom I was entrusted with. It was really what I needed. It has been a long association with you and looking back, I owe a few important stepping stones in my path to you.

to Madeleine (Prof. Gibescu) for agreeing to supervise my research at TU/e and not abandoning the ship until the end especially with the turn of events on either side of my stay in Eindhoven. You don't only have a way with your words but I also found you a good listener and adviser. Also thanks to you and Nikos (Dr. Paterakis), I managed to give my research the practical bent that I had initially hoped it would take.

to Nikos for being more collaborator than (co-)supervisor, and for rekindling my fascination for mathematics and programming and letting me dabble in it.

to Michael (Dr. Heck), who made the most productive time of my PhD possible. You have inspired me by your clear priorities and how you go about achieving the mythical work-life balance.

to the *bella gente* (Ale, Andrea, Davide, Domenico, Laura, Luca, Marta, Paola, Raffa) of Torino who made the city for me the first place I called home away from home. To you and Italy, I owe the epicurean in me. You have always welcomed me back to the university and the city as if I never left it. I am also grateful to Ale and Paola for putting a roof over my head.

to the warm people I met and befriended in Freiburg (Diana, Julius, Lluis, Michael, *Kommilitonen* at iOR, cooking partners at ISE) who made my short stay in this beautiful and welcoming city more enjoyable and enriching.

to my newest colleagues and friends in Eindhoven, especially to the inconsistent occupants of Flux 3.079 and around (Andy, Maikel, Raoul, Rik, Siddharth). I am grateful for the pauses, discussions, squash sessions and sometimes just your presence in the office on a gloomy day that made it *gezellig*.

to the project partners of Ca(r)vour and MARS-EV especially Lithops and DISAT and especially Aneta, Daniele, Prof.ssa Bodoardo for enabling my research, to the master thesis students I supervised for pushing the boundaries of my work, to the able people managing the PhD programme, who so efficiently and silently keep the ball rolling (Annemarie, Chamindie, Claudia, Guus, Marina).

to my old friends, near and far, who continue to share their lives and experiences with me and keep me connected to my past and my roots.

to my family, who despite at times not sharing the same enthusiasm about my life decisions, have always unconditionally supported me.

to Claudia, for innumerable things, big and small, for being this huge comforting constant amidst all the variability of the last years, for keeping me grounded when I got too dreamy.

Curriculum Vitae

Arpit Maheshwari was born on 02-04-1987 in Bhopal, India. He received his B.E. (Hons.) degree in Chemical Engineering from Birla Institute of Technology and Science, India in 2009. Thereafter, he worked as a project engineer in Indian Oil Corporation. In 2011, awarded with an Erasmus Mundus scholarship, he pursued a dual M.Sc. degree in Mechanical Engineering from KTH Royal Institute of Technology, Sweden and Energy and Nuclear Engineering from Politecnico di Torino, Italy. He completed his master studies in 2013 after performing his thesis work on solid oxide fuel cells at the German Aerospace Center in Stuttgart, Germany. Thereafter, he worked as a research associate for one year at Politecnico di Torino gaining his first experience with lithium-ion batteries. In 2014, he was accepted into the Erasmus Mundus Joint Doctorate Programme "Environomical Pathways for Sustainable Energy Services" and was nominated for a fellowship to pursue his doctoral research at Politecnico di Torino, Italy and Eindhoven University of Technology, the Netherlands. A part of this doctoral research on Modelling, Aging and Optimal Operation of Lithium-ion Batteries was also carried out by him at Fraunhofer Institute for Solar Energy Systems in Freiburg, Germany.